Robust Track Based Alignment

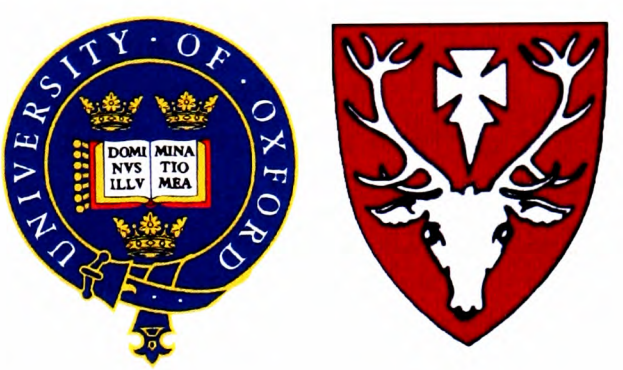
of the ATLAS Silicon Detectors

and

Assessing Parton Distribution Uncertainties

in Drell-Yan Processes

Submitted for the degree of Doctor of Philosophy

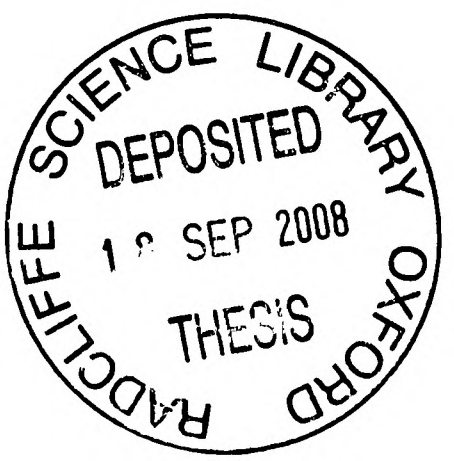


Florian Heinemann

Dipl. Phys. ETH

Hertford College, University of Oxford

2007



Robust Track Based Alignment of the ATLAS Silicon Detectors and Assessing Parton Distribution Uncertainties in Drell-Yan Processes

Florian Heinemann
Hertford College, University of Oxford

Thesis submitted in partial fulfillment of the requirements
for the degree of Doctor of Philosophy.

University of Oxford, Trinity Term 2007.

Abstract

The ATLAS Experiment is one of the four large detectors located at the Large Hadron Collider (LHC) at CERN in Geneva, Switzerland. In summer 2008, ATLAS is expected to start collecting data from proton-proton collisions at 14 TeV centre-of-mass energy. In the centre of the detector, the reconstruction of charged particle tracks is performed by silicon and drift tube based sub-detectors. In order to achieve the ATLAS physics goals the resolutions of the measured track parameters should not be degraded by more than 20% due to misalignment. Thus, the relative positions of the silicon detector elements have to be known to an accuracy of about 10 micrometers in the coordinate with the best measurement precision. This requirement can be achieved by track based alignment algorithms combined with measurements from hardware based alignment techniques. A robust track based alignment method based on track residual and overlap residual optimisation has been developed and implemented into the ATLAS offline software framework. The alignment algorithm has been used to align a test beam setup and also part of the final ATLAS detector using cosmic ray muons. Several simulation studies showed that the algorithm will be able to align the full detector with collision data. In addition to detector misalignments, limitations in the knowledge of the proton structure are going to affect physics discoveries at the LHC. Therefore, parton distribution uncertainties in high-mass Drell-Yan processes have been determined. This study includes the analysis of the forward-backward asymmetry. It has been performed on the level of next-to-leading order in both, Monte Carlo simulation using k-factors and parton distribution functions. This analysis is crucial for new physics searches with the ATLAS detector.

This thesis was typeset with LaTeX.

© Florian Heinemann, 2007.

All rights reserved. No part of this publication may be reproduced, stored in a retrieval system, or transmitted, in any form or by any means, electronic, mechanical, photocopying, recording or otherwise, without express permission of the author.

Published at the University of Oxford, Oxford, United Kingdom.

"The pure and simple truth is rarely pure and never simple."

- Oscar Wilde

ACKNOWLEDGEMENTS

The last three years in Oxford have been very exciting and challenging. I had the chance to meet numerous highly interesting people who helped me to grow academically and personally. I am thankful to the Rhodes Trust which awarded me with a scholarship that gave me, in addition to financial security, access to a community full of bright minds. Especially, I would like to thank Dr. Tony Weidberg for his excellent supervision. He offered me a lot of freedom to develop my own ideas, directed me with the right questions and always supported my plans. It was a great pleasure to work in the Particle Physics Sub-Department. Its students, senior physicists and technical staff continuously supported me. Apart from physics questions they particularly solved uncountable computer problems. It is clear that I would have never finished this thesis without their great help. Additionally, I am thankful to many people in the ATLAS collaboration, especially in the Inner Detector alignment community, for many fruitful discussions and great technical support. Furthermore, I am exceedingly grateful to all my friends from Hertford College, the Oxford University Karate Club, the Oxford University Salsa Team, the Physics Department, within the Rhodes Scholars and, especially, to some out-

side these environments. They made my time in Oxford extremely enjoyable and surely unforgettable. The biggest thanks go to my family who has always supported me with lots of love and keen interest in my activities. They gave me the strength and the values needed to successfully finish this thesis.

AUTHOR'S CONTRIBUTION

This thesis summarises the outcome of my research which was performed between October 2004 and September 2007. All results presented in this document are solely my own contribution unless cited otherwise.

The first year was divided into two parts. Firstly, in lectures and the corresponding course work I deepened my knowledge about theoretical and experimental particle physics. Secondly, I took over the Robust Alignment project from Dr. Danny Hindson which forms the main part of this thesis. Up to this point he had developed a standalone prototype for the silicon barrels which showed the potential of using overlap residuals for alignment. It was my task to analyse the prototype and develop a fully functioning algorithm within the ATLAS offline software.

During the ATLAS Physics Workshop in Rome (June 2005) I initiated a collaboration with Dr. Roberto Petti in order to test the Robust Alignment algorithm on test beam data. Later, the other two algorithms designed for the full detector alignment joined my efforts and for two years numerous analyses were performed which resulted in a 240 pages document.

In May 2006, a similar collaboration started with the community responsible for the commissioning of the SCT barrel. The cosmic ray data collected with a fraction of the real ATLAS detector provided an exciting environment to test and further develop the Robust Alignment algorithm.

In November 2006 data simulated with an "as build" geometry became available. This was the third big challenge for the Robust Alignment algorithm. During these three challenges the Inner Detector alignment community, lead by Dr. Jochen Schieck and Dr. Salva Marti, provided a very fruitful ground for discussions, discoveries and developments.

Also at the workshop in Rome, started a collaboration with Dr. Samir Ferrag which lead to my determination of parton distribution uncertainties and NLO effects in high-mass Drell-Yan processes. This important study was done with the support of Dr. Amanda Cooper-Sakar and Dr. Alessandro Tricoli.

In my third year, I focused on finishing all studies in order to get the most important results published.

Documents and Publications

During the three years of my research I wrote and contributed to the following documents and publications:

- Track Based Alignment of the ATLAS Silicon Detectors with the Robust Alignment Algorithm [1]
- Alignment of the Pixel and SCT Modules for the 2004 ATLAS Combined Test Beam [2]

- ◇ Combined SCT and TRT barrel cosmic run in the SR1 assembly area [3]
- ◇ Dileptons, Diphotons, and Lepton-Photon Resonances at High Masses, CSC note [4]
- ◇ Bulletin of the American Physical Society [5]
- ◇ The ATLAS experiment at the CERN Large Hadron Collider [6]
- ◇ Proceedings of the first LHC Detector Alignment Workshop [7]
- ◇ ATLAS Experiment Silicon Inner Detector Alignment [8]
- ◇ Proceedings of the Workshop on Monte Carlo, Physics and Simulations at LHC [9]
- ◇ Proceedings of the Conference on Deep Inelastic Scattering 2007 [10]
- ◇ 8th International Conference on Large Scale Applications and Radiation Hardness of Semiconductor Detectors [11]

Some parts of my research have also been published on the ATLAS TWiki pages[1].

Furthermore, I gave more than 50 talks at group meetings, international meetings and conferences. All these talks are available on the web[2] and show the progress of my research.

[1] https://twiki.cern.ch/twiki/bin/view/Atlas/

[2] http://agenda.cern.ch, http://indico.cern.ch/, http://www-pnp.physics.ox.ac.uk/~tseng/atlas/, http://florian.e.w.heinemann.googlepages.com/research

CONTENTS

1. Introduction 1
1.1 Theories in Particle Physics 1
1.1.1 Standard Model 2
1.1.2 Supersymmetry 5
1.1.3 Extra Dimensions 9
1.2 Probing Nature At Highest Energies 10
1.2.1 Large Hadron Collider 10
1.2.2 A Toroidal LHC ApparatuS 13

2. The Algorithm: RobustAlignAlg 31
2.1 Residuals and Overlap Residuals 31
2.2 Main Principle 38
2.3 Implementation into Athena 43
2.3.1 Options 45
2.3.2 Initialize 45
2.3.3 Execute 47
2.3.4 Finalize 48
2.3.5 Run the RobustAlignAlg 54
2.4 Uncertainties on Alignment Constants 55
2.5 Distributed Robust Alignment 59
2.5.1 Run Distributed Robust Alignment 61

3. Alignment Limitations, Solutions and Validation 65
3.1 Removal of Edge Channels 65
3.2 Effect of Multiple Scattering on SCT Local Y Residuals 67
3.3 PIXEL Z Overlap Hits 71
3.4 Sagitta Distortions 72
3.5 Validation of Energy and Momentum Measurement inside Athena 74

4. Combined Test Beam Alignment 81
4.1 CTB Data 83
4.2 CTB Simulation 85

4.3 CTB Alignment . . . 85
4.4 PIXEL Local Y Residuals . . . 103
4.5 Ganged PIXEL Hits . . . 103
4.6 CPU Usage for CTB Alignment . . . 105

5. SCT Alignment with SR1 Cosmic Ray Data . . . 107
5.1 Cosmic Muons . . . 108
5.2 SCT Barrel SR1 Setup . . . 109
5.3 SCT Barrel Alignment using Cosmic Ray Data . . . 110
5.4 Residual Bias in SR1 Data . . . 115
5.5 Effect of MCS on SR1 Local X Residuals . . . 117
5.6 Comparison with other Alignment Algorithms . . . 119
5.7 Alignment Results vs. Photogrammetry Measurements . . . 122
5.8 Comparison of Alignment Results with Simulation . . . 124
5.9 Timing of SCT Barrel Cosmic Ray Data . . . 125

6. ATLAS Silicon Detector Alignment Simulation Studies . . . 133
6.1 CSC Alignment Challenge . . . 134
6.2 Error Scaling . . . 137
6.3 Level 3 Alignment . . . 138
6.4 Alignment of all Levels . . . 142
6.5 Using Vertex Fit . . . 146
6.6 Statistical Uncertainty on CSC Constants . . . 147
6.7 Measuring Deformations in the Radii of Detector Rings . . . 149
6.8 CPU Usage for CSC Alignment . . . 149
6.9 Outlook . . . 150

7. Parton Distribution Uncertainties in Drell-Yan Processes . . . 155
7.1 Parton Distribution Uncertainties . . . 158
7.2 The Drell-Yan Processes . . . 161
7.3 Next-to-leading Order Monte Carlo . . . 163
7.4 PDF Uncertainties on the Drell-Yan Cross Section . . . 168
7.5 Forward-backward asymmetry in $Z/\gamma \rightarrow$ee . . . 171

8. Conclusions . . . 183

Glossary . . . 185

Appendix 187

A. Robust Alignment Options . . . 189

B. Robust Alignment Output 191

C. Full Detector Alignment Monitoring 195

D. Runs collecting SR1 Cosmic Rays 203

E. K-Factors 207

Bibliography 220

LIST OF FIGURES

1.1 Schematic view of the LHC at CERN 11
1.2 Schematic view of the ATLAS detector 14
1.3 PIXEL layout 15
1.4 SCT layout 15
1.5 Projection in X and Y of the silicon barrel detectors 16
1.6 PIXEL module 19
1.7 SCT module 19
1.8 Eta range of the silicon tracking detectors 20
1.9 Schematic view of the ATLAS calorimeters 22
1.10 Global and local coordinate system of the ATLAS Inner Detector . 23

2.1 Reconstruction of SCT local Y hit position 33
2.2 Illustration of SCT endcap residual measurement 36
2.3 Effect of misalignment on residuals 39
2.4 Effect of misalignment on overlap residuals 40
2.5 Overlap residuals vs. radius change 42
2.6 Robust Alignment process 45
2.7 Pull distribution 56
2.8 Hits per module for 10 μm precision - G = 10, Range = 100 μm . 57
2.9 Hits per module for 10 μm precision - G = 10, Range = 1000 μm . 57
2.10 Hits per module for 10 μm precision - P = 50, Range = 100 μm . 58
2.11 Hits per module for 10 μm precision - G = 50, Range = 1000 μm . 58

3.1 Edge channel hit 65
3.2 Edge channel bias on overlap residuals 67
3.3 Effect of local Y multiple scattering on local X and Y residuals . . 69
3.4 PIXEL Z overlap hits 72
3.5 Energy to truth energy ratio with release 11.0.3 and 11.0.41 78
3.6 Momentum to truth momentum ratio with release 11.0.3 and 11.0.41 79
3.7 E/p with release 11.0.3 and 11.0.41 80

4.1 CTB setup for PIXEL and SCT 82
4.2 CTB beam profile for PIXEL and SCT 87
4.3 CTB local X residuals after Robust Alignment 89

4.4 Momentum measurement in run 2102442 90
4.5 CTB momentum resolution after alignment 91
4.6 Convergence of CTB PIXEL alignment 92
4.7 Convergence of CTB SCT alignment 93
4.8 CTB local X shifts in 30^{th} iteration 94
4.9 Improvement of track quality with alignment 95
4.10 Pixel local X residuals vs. d_0 after Robust CTB Alignment 96
4.11 Mean CTB PIXEL residuals after alignment 97
4.12 Sigma of CTB PIXEL residuals after alignment 98
4.13 Mean CTB SCT residuals after alignment 99
4.14 Sigma of CTB SCT Residuals after alignment 100
4.15 Track quality of tracks with ganged PIXEL hits 104
4.16 CPU consumption for CTB alignment 105

5.1 SR1 SCT and TRT setup 109
5.2 Cosmic ray track in SCT 110
5.3 SR1 residual and overlap residual improvement 111
5.4 SR1 alignment uncertainty 112
5.5 Robust Alignment iterations - local X shifts 114
5.6 Local Y residuals after alignment 116
5.7 SR1 unbiased residuals 121
5.8 SR1 hit efficiencies 122
5.9 SCT relative barrel rotations and global Z shifts 123
5.10 Cosmic ray scintillator setup 126
5.11 Cosmic ray data unbiased residuals - fast and slow 130
5.12 SCT residuals vs. TDC timing 131
5.13 SCT residuals vs. ϕ and TDC timing 132

6.1 CSC alignment SCT performance 140
6.2 Improvement of impact parameter resolution 147
6.3 Local X statistical alignment uncertainties 152
6.4 Local Y statistical alignment uncertainties 153

7.1 Up quark distribution for CTEQ61, CTEQ6ll, MRST2004NLO and ZEUS2005-ZJ 157
7.2 Distributions of initial partons in the analysed high-mass Drell-Yan processes 160
7.3 Drell-Yan process 161
7.4 Impact of other PDF sets and higher-order effects on the high-mass Drell-Yan invariant mass distribution 165

7.5 Impact of other PDF sets and higher-order effects on the high-mass Drell-Yan η distribution 166
7.6 Impact of other PDF sets and higher-order effects on the high-mass Drell-Yan Y distribution 167
7.7 PDF uncertainty on the high-mass Drell-Yan distribution 171
7.8 PDF uncertainty on the high-mass Drell-Yan lepton η distribution 172
7.9 PDF uncertainty on the high-mass Drell-Yan lepton Y distribution 173
7.10 Impact of other PDF sets and higher-order effects on the high-mass Drell-Yan $\cos(\theta^*)$ distribution 178
7.11 Impact of other PDF sets and higher-order effects on the high-mass Drell-Yan diluted $\cos(\theta^*)$ distribution 179
7.12 PDF uncertainty on the high-mass Drell-Yan $\cos(\theta^*)$ distribution . 180
7.13 PDF uncertainty on the diluted high-mass Drell-Yan $\cos(\theta^*)$ distribution 181
7.14 PDF uncertainties given by the two corresponding error sets on the high-mass Drell-Yan distribution for each of the 20 free PDF parameters 182

C.1 PIXEL barrel local X residuals after CSC alignment 195
C.2 PIXEL endcap local X residuals after CSC alignment 195
C.3 SCT barrel local X residuals after CSC alignment 196
C.4 SCT endcap local X residuals after CSC alignment 196
C.5 PIXEL barrel local Y residuals after CSC alignment 197
C.6 PIXEL endcap local Y residuals after CSC alignment 197
C.7 SCT barrel local Y residuals after CSC alignment 198
C.8 SCT endcap local Y residuals after CSC alignment 198
C.9 PIXEL barrel local X overlap residuals after CSC alignment . . . 199
C.10 PIXEL endcap local X overlap residuals after CSC alignment . . . 199
C.11 SCT barrel local X overlap residuals after CSC alignment 200
C.12 SCT endcap local X overlap residuals after CSC alignment 200
C.13 PIXEL barrel local Y overlap residuals after CSC alignment . . . 201
C.14 PIXEL endcap local Y overlap residuals after CSC alignment . . . 201
C.15 SCT barrel local Y overlap residuals after CSC alignment 202
C.16 SCT endcap local Y overlap residuals after CSC alignment 202

D.1 Runs collecting SR1 Cosmic Rays 206

LIST OF TABLES

1.1 Particle spectrum of the Standard Model 4
1.2 Particle spectrum of the MSSM 6
1.3 Inner Detector modules 21
1.4 Muon trigger rates 26

3.1 Simple mean of electron momentum and energy 77
3.2 Gaussian fit of electron momentum and energy 77

4.1 CTB nominal global geometry 83
4.2 CTB runs 84
4.3 CTB aligned global geometry 101
4.4 CTB aligned local geometry 102

5.1 SR1 alignment constants 120
5.2 CBNT variables in cosmic ray timing analysis 128
5.3 TDC channels 128

6.1 CSC level 1 transformations 135
6.2 CSC level 2 transformations 136
6.3 CSC level 3 transformations 137
6.4 Momentum resolution in level 3 alignment 141
6.5 Momentum resolution in alignment of all levels 144
6.6 Track parameter resolutions 145
6.7 Momentum resolution for TRT-only tracks 146

7.1 PDF uncertainty on forward-backward asymmetry 177
7.2 Forward-backward asymmetry with different PDF sets 177

E.1 MRST k-factors - Y = 0.3 207
E.2 MRST k-factors - Y = 0.9 208
E.3 MRST k-factors - Y = 1.5 208
E.4 MRST k-factors - Y = 2.1 209
E.5 MRST k-factors - Y = 2.7 209
E.6 CTEQ k-factors - Y = 0.3 210
E.7 CTEQ k-factors - Y = 0.9 210

E.8 CTEQ k-factors - Y = 1.5 211
E.9 CTEQ k-factors - Y = 2.1 211
E.10 CTEQ k-factors - Y = 2.7 212
E.11 ZEUS k-factors - Y = 0.3 212
E.12 ZEUS k-factors Y = 0.9 213
E.13 ZEUS k-factors - Y = 1.5 213
E.14 ZEUS k-factors - Y = 2.1 214
E.15 ZEUS k-factors - Y = 2.7 214

1. INTRODUCTION

What are the most fundamental principles of nature? It is one of mankind's central questions and acts as a driving force for scientific research. The interplay between theory and experiment is crucial for the development of knowledge. Experiments unveil the behaviour of nature in certain conditions whereas theories attempt to summarise the discoveries in basic models. It is assumed that the underlying nature of the universe does not change. Therefore, all research performed by past, present and future generations of scientists is constantly leading to a greater understanding about the laws of nature. Particle physics research analyses the interactions of the smallest constituents of matter. It started 110 years ago with the discovery of the electron by J.J. Thomson and is now performed in large international collaborations continuously having a significant influence on society.

1.1 Theories in Particle Physics

Over the last 100 years, particle physicists created a relatively universal description of sub-atomic matter. However, there are large differences in the predictions about future developments in that field. Depending on the outcome of the experi-

ments performed at the Large Hadron Collider staring in 2008, it is even possible that the standard description of nature's smallest constituents may have to be reviewed completely.

1.1.1 Standard Model

The Standard Model (SM) [12, 13, 14] is currently the most widely accepted model describing electroweak and strong interactions. In the last three decades almost all experimental tests of the forces described by the SM have agreed with its predictions. The ability of the SM to successfully predict physical phenomena was first seen with the discovery of neutral weak interactions in 1973 [15]. The production of the intermediate electroweak vector bosons, $W^{\pm}$ and Z^0, in proton-antiproton collisions at the European Organization for Nuclear Research (CERN) in 1983 further increased the general confidence in that model as these particles fulfilled the expected properties. The gluon mediating the strong force was predicted by Quantum Chromodynamics (QCD), a gauge theory which forms part of the SM, also before its discovery in 1979 at the Deutsches Elektronen Synchrotron (DESY) [16, 17]. The electroweak parameters and quantitative predictions from pertubative QCD were finally tested with high precision at the Large Electron Positron Collider (LEP) and the Stanford Linear Collider (SLC). These accurate measurements with electron-positron collisions at the Z^0 resonance showed no evidence for deviations from the SM. Also the W boson and top quark mass measurements performed in proton-antiproton collisions at the Tevatron are consistent

with the SM.

All particles are described by Quantum Field Theories (QFT). The most fundamental principles of nature are explained through particles and their interactions whereas these interactions are also treated as due to exchange of virtual particles. A quantum field is a complex n-dimensional function $\psi(x)$ representing one or more particles where $|\psi(x)|^2$ is the probability of finding that particle at the space-time point x. Since only $|\psi(x)|^2$ is measurable, the phase of $\psi(x)$ is a free parameter. It is natural to assume that at any point in the universe the phase of $\psi(x)$ may be assigned arbitrarily without affecting the physical state of the particle. Thus, all measurables should be invariant under the following transformation:

$$\psi(x) \rightarrow e^{i\theta(x)}\psi(x). \tag{1.1}$$

This is the basis of all gauge theories like the SM and any of its extensions. The direct consequence of this is that only bosons can be responsible for interactions between fermions. In the SM electroweak interactions result from a local $SU(2)_L \times U(1)_Y$ symmetry which is spontaneously broken via the Higgs mechanism and which leads to the existence of four electroweak bosons, $W^{\pm}$, Z^0 and γ. Strong interactions which are mediated by eight gluons arise from a local $SU(3)$ symmetry. Matter fields representing quarks and leptons are organised into families, with left-handed[1] and right-handed[2] fermions transforming as weak

[1] Spin is anti-parallel to momentum in the limit of massless particles.
[2] Spin is parallel to momentum in the limit of massless particles.

isodoublets and weak isosinglets, respectively. Only the left-handed components of particles and right-handed components of antiparticles participate in weak interactions in the SM which is known as parity violation. Masses of particles are introduced by their coupling to a scalar field, the Higgs boson. However, despite intensive searches at LEP and the Tevatron, the Higgs particle has not been discovered yet. It remains as the only missing particle in the SM.

Although the SM has survived numerous tests it is already known that its minimal version with 19 free parameters does not describe nature sufficiently. Recent measurements of neutrino oscillations show that neutrinos have mass. However, the SM can be made consistent with these results by adding 10 more free parameters which are not predicted by any theory and thus need to be determined experimentally. Measurements of the anomalous magnetic moment of the muon in Brookhaven [18] and the WMAP measuring the cold dark matter density in our

Standard Model Particles		
Interaction	*Mass*	*S*
$e^{\pm}_{L/R}, \mu^{\pm}_{L/R}, \tau^{\pm}_{L/R}$	$e^{\pm}, \mu^{\pm}, \tau^{\pm}$	1/2
ν_e, ν_μ, ν_τ	ν_e, ν_μ, ν_τ	1/2
$u'_{L/R}, c'_{L/R}, t'_{L/R}$	u, c, t	1/2
$d'_{L/R}, s'_{L/R}, b'_{L/R}$	d, s, b	1/2
B^0, W^0	γ, Z^0	1
H^0	H^0	0
$W^{\pm}$	$W^{\pm}$	1
g	g	1

Tab. 1.1: Particle spectrum of the Standard Model. Labels "L" and "R" denote left- and right-handed electroweak eigenstates.

universe [19] give a hint that physics even beyond the extended SM may exist. It is for example clear that either our understanding of gravity based on Einstein's theory of General Relativity is wrong or particles forming cold dark matter which so far have escaped our detection must exist. The Axion, which is supposed to explain the non-existence of CP violation in the strong interaction and which could theoretically be an ingredient of cold dark matter, has not been found yet. Furthermore, it might not explain the measured cold dark matter density sufficiently [20] and technically does not belong to the SM. Also, the SM fails to explain the matter-antimatter asymmetry observed in the universe. Additionally, there are theoretical motivations for physics beyond the SM. One such example is the hierarchy problem concerning the quadratically divergent fermion loop corrections to the Higgs mass. New physics at the TeV scale is required to keep the Higgs mass in the area of a few hundred GeV and thus make the SM consistent with W and top mass measurements. Additionally, for reasons of concinnity theorists are aiming for the unification of the gauge couplings. Repeatedly, history has shown that a unification of theories may lead to a better understanding of nature.

1.1.2 Supersymmetry

Mainly theoretical aspects justify the introduction of Supersymmetry. In nature it is often possible to explain its principles and make predictions using symmetries. Since the discovery of the Pauli Principle, particles are divided into two groups, fermions whose spin is an odd multiple of $\frac{1}{2}$ and bosons with integer spin. A

supersymmetric operation on the representation of a particle belonging to one group transforms it to a member of the other group. Thus, the spin changes but the mass and couplings to other particles remain the same. The electron with spin $\frac{1}{2}$ and a mass of 0.511 MeV would have a bosonic partner with spin 0 and the same mass in a supersymmetric world. However, no supersymmetric partner has been discovered until now. It is therefore certain that, if Supersymmetry exists at a high energy scale, it is broken at the electroweak scale which is accessible for experiments at the moment.

The Minimal Supersymmetric Standard Model (MSSM) is the simplest possible supersymmetric extension of the SM with a minimal particle content. The SM

MSSM Particles

Extended Standard Model			Supersymmetric Partners		
Interaction	*Mass*	*S*	*Interaction*	*Mass*	*S*
$e^{\pm}_{L/R}, \mu^{\pm}_{L/R}, \tau^{\pm}_{L/R}$	$e^{\pm}, \mu^{\pm}, \tau^{\pm}$	1/2	$\tilde{e}^{\pm}_{L/R}, \tilde{\mu}^{\pm}_{L/R}, \tilde{\tau}^{\pm}_{L/R}$	$\tilde{e}^{\pm}_{1/2}, \tilde{\mu}^{\pm}_{1/2}, \tilde{\tau}^{\pm}_{1/2}$	0
ν_e, ν_μ, ν_τ	ν_e, ν_μ, ν_τ	1/2	$\tilde{\nu}_e, \tilde{\nu}_\mu, \tilde{\nu}_\tau$	$\tilde{\nu}_e, \tilde{\nu}_\mu, \tilde{\nu}_\tau$	0
$u'_{L/R}, c'_{L/R}, t'_{L/R}$	u, c, t	1/2	$\tilde{u}'_{L/R}, \tilde{c}'_{L/R}, \tilde{t}'_{L/R}$	$\tilde{u}_{1/2}, \tilde{c}_{1/2}, \tilde{t}_{1/2}$	0
$d'_{L/R}, s'_{L/R}, b'_{L/R}$	d, s, b	1/2	$\tilde{d}'_{L/R}, \tilde{s}'_{L/R}, \tilde{b}'_{L/R}$	$\tilde{d}_{1/2}, \tilde{s}_{1/2}, \tilde{b}_{1/2}$	0
B^0, W^0	γ, Z^0	1	$\tilde{B}^0, \tilde{W}^0$	$\tilde{\chi}^0_1, \tilde{\chi}^0_2, \tilde{\chi}^0_3, \tilde{\chi}^0_4$	1/2
H^0_u, H^0_d	$h, H, A^0, A^{\pm}$	0	$\tilde{H}^0_u, \tilde{H}^0_d$		1/2
$W^{\pm}$	$W^{\pm}$	1	$\tilde{W}^{\pm}$	$\tilde{\chi}^{\pm}_1, \tilde{\chi}^{\pm}_2$	1/2
$H^{\pm}$	$H^{\pm}$	1	$\tilde{H}^{\pm}$		1/2
g	g	1	$\tilde{g}$	$\tilde{g}$	1/2

Tab. 1.2: Particle spectrum of the MSSM. The extended SM has instead of only one an additional second Higgs doublet. Labels "L" and "R" denote left- and right-handed electroweak eigenstates. Mass eigenstates $x_{1/2}$ are defined as $x_{1/2} = x_{L/R} \cdot \cos\theta \pm x_{R/L} \cdot \sin\theta$. Since θ is close to zero for electrons, muons, up, down, charm and strange quarks, their mass eigenstates are mostly denoted with "L/R" instead of "1/2", in literature.

Poincaré algebra is expanded to a supersymmetric graduated Lie algebra. The MSSM has an additional second Higgs doublet, describes more than twice as many particles as the SM and solves the following problems:

- One of the main problems of the SM is the *Hierarchy Problem.* Radiative corrections to the Higgs mass including the fermion loops at one-loop-level have an unphysical quadratic divergence. Indeed, this divergence can be canceled by a mass counter term which, however, has to be fine tuned at each order in perturbation theory. In the MSSM, two additional scalar particles S, provided they are in the region of $1 - 10$ TeV, are responsible for the cancellation of that divergence. The remaining divergence is then only logarithmic. Also, the logarithmic term is multiplied with $(m_S^2 - m_f^2)$ which is zero in the supersymmetric limit.

- Within the SM, it is not possible to achieve a *unification of gauge couplings* - at any scale - which would reduce the number of open parameters and therefore be favoured by many theorists. The MSSM provides the possibility of gauge coupling unification at a scale of about 10^{16} GeV.

- Some models within the MSSM provide a *candidate for cold dark matter.* Experiments measuring the rotation velocities of galaxies and observing gravitational lensing [21] have shown that it is very likely that there is more than just visible matter in our universe. One component of the so called dark matter seems to be cold, meaning that it consists of particles moving at

a non-relativistic speed. For example if the lightest supersymmetric particle is a stable neutralino or gravitino it would be an excellent candidate for cold dark matter.

- ◇ In the MSSM, the mechanism of *electroweak symmetry breaking* occurs radiatively at the level of perturbation theory without the need for any new strong interaction. Thus, in contrast to the SM the MSSM gives an explanation for the Higgs mechanism.

However, the MSSM gives neither a hint to the source of CP violation nor is it able to make predictions for any particle mass. Furthermore, the MSSM still is a theory without quantum gravity. String theories may solve some of these problems, but a phenomenologically viable string theory has yet to be constructed [22].

There are two different kinds of superfields in the Minimal Supersymmetric Standard Model at the GUT-scale and above:

- ◇ The *Chiral Scalar Superfields* consisting of a complex scalar field, S, and a 2-component Majorana fermion field, ζ. The SM quarks and leptons and the MSSM higgsinos at the TeV-scale are connected with ζ and its partners, the squarks, sleptons and Higgses, with S.

- ◇ The *Massless Vector Superfields* consisting of a gauge field $F^A_{\mu\nu}$ and a 2-component Majorana fermion field, λ_A. The field $F^A_{\mu\nu}$ is connected with the SM gauge bosons and λ_A with its Superpartners, the gauginos, at the TeV-scale.

These fields respect the same $SU(3) \times SU(2)_L \times U(1)_Y$ gauge symmetries as do the SM fields. In order to confirm or confute the predictions of the MSSM it is first necessary to find the new particles given in Table 1.2 in invariant mass distributions. In the MSSM, each supersymmetric particle has the same gauge couplings as its SM partner. Hence, in a second step the interaction couplings and the spin of the new particles would have to be determined.

1.1.3 Extra Dimensions

Already in the 1920's, first ideas about extra dimensions were developed. Kaluza [23] and Klein [24] tried to unify electromagnetism with Einstein's theory of gravity by introducing a compact fifth dimension. Still today the main motivation for adding extra dimensions is to achieve the unification of gravity with gauge interactions. In general a consistently formulated String Theory needs more than four space-time dimensions. Historically, it was conventional to assume the extra dimensions to be compactified to small radii with magnitudes of approx. the Planck length, $l_P \sim 10^{-33}$ cm. If these extra dimensions do exist, they would be hidden to any currently imaginable experiment. More recently though, theories have been developed which predict extra dimensions being much larger. The upper limit for these dimensions is constrained by experiments to a fraction of a millimeter [25]. In some cases the Large Hadron Collider at CERN will be able to discover that there are more than four space-time dimensions. This would maybe explain why gravity is the weakest of all forces and, a century after Einstein combined space

and time, again change our view on nature fundamentally.

1.2 Probing Nature At Highest Energies

Understanding nature at ever smaller length scales is equivalent to probing particle interactions at ever higher energies. In the past century, technologies have been developed that allow to collide particles at energies which unveil nature at a fraction of a femtometre. These energies correspond to a temperature of 10^{15} Kelvin which existed a fraction of a nano-second after the Big Bang. Experiments of that scale are very expensive and therefore only possible in large global collaborations. In addition to the contribution to fundamental knowledge about nature, these experiments have a far-reaching impact on technological developments which serve society.

1.2.1 Large Hadron Collider

The construction of the Large Hadron Collider (LHC) [26] has been approved by the CERN's Council in December 1994. The LHC, shown in Fig. 1.1, has been installed in a 27 kilometre circumference tunnel which is about 100 metres underground and was used by the Large Electron Positron collider (LEP) until 2001. Starting in summer 2008, the LHC will collide protons at a center-of-mass energy $\sqrt{s}$ of 14 TeV being the highest ever reached in the history of human made particle collisions. The design luminosity $\mathcal{L}$ is $10^{34}\ cm^{-2}s^{-1}$. Furthermore,

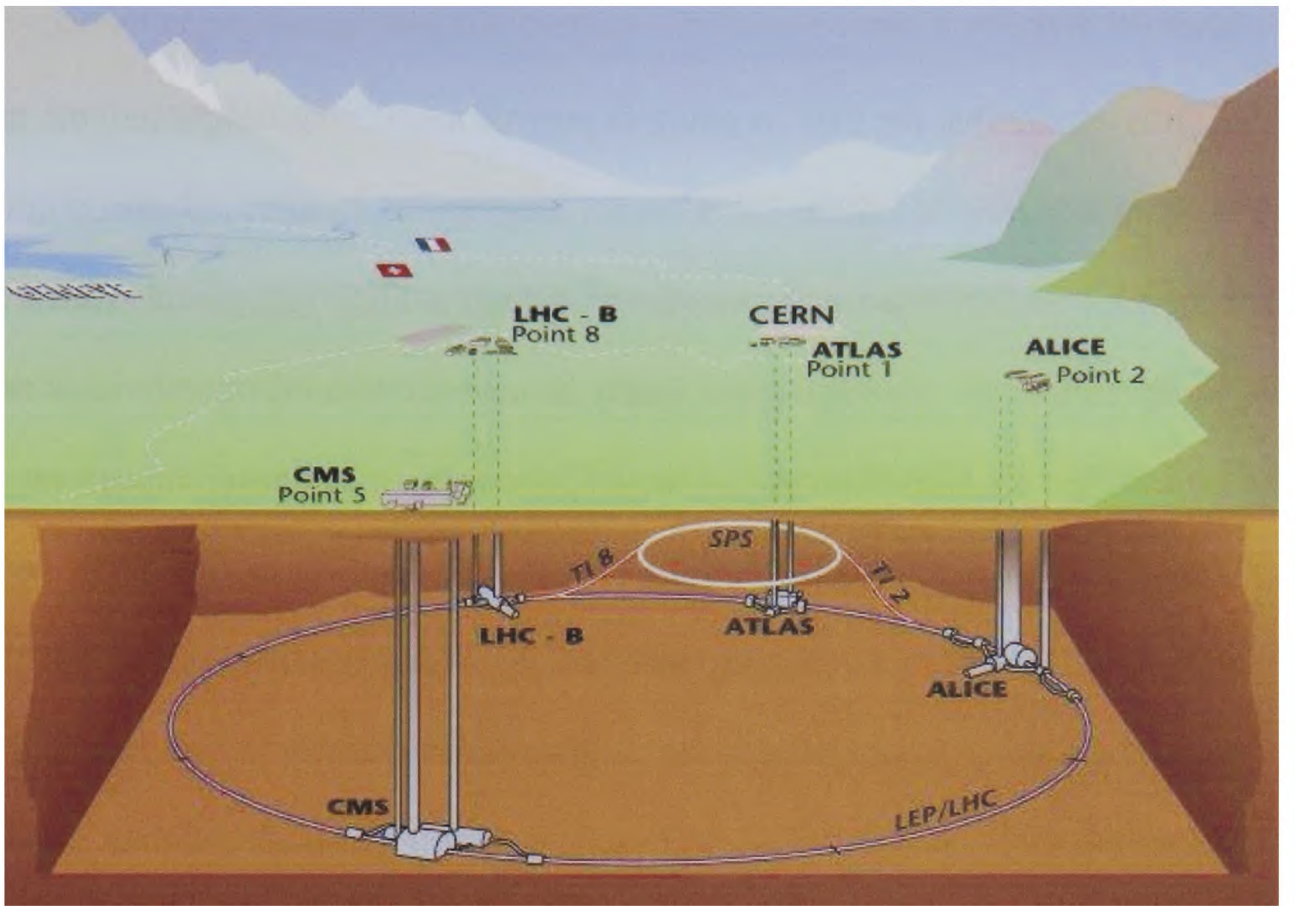


Fig. 1.1: A schematic view of the LHC at CERN near Geneva.

lead-ion collisions are planned with a total $\sqrt{s}$ of 1148 TeV and a luminosity $\mathcal{L}$ of $10^{27}\ cm^{-2}s^{-1}$. The accelerator consists of two interleaved synchrotron rings, whose main elements are 1232 superconducting NbTi dipole and 392 quadrupole magnets operating in superfluid helium at a temperature of 1.9 K. The dipole magnets guide the particles along the ring while the quadrupole magnets are focusing the particle bunches. The nominal field for LHC magnets to handle 7 TeV beams is 8.34 Tesla, and the goal is to achieve 9.0 Tesla. Two 450 GeV beams produced in the Super Proton Synchrotron (SPS) will be injected into the LHC, and then accelerated with superconducting cavities, 8 cavities per ring, operating at 2 MV

and 400 MHz.

It is certain that the LHC is going to provide an exciting insight into the most fundamental laws of nature. There are several possible scenarios of what might or might not be discovered in this new range of energy. The Higgs particle which was predicted over 40 years ago could finally be unveiled. On the other hand, if there is no Higgs, our current understanding of physics might be shaken fundamentally. It is clear that if the SM describes physics at the investigated energy scale the Higgs will be discovered already with an integrated luminosity of 30 fb^{-1} [27]. Its non-existence would mean an immediate end of the validity of the SM. Furthermore, there are numerous theories which predict various different particles within the energy range of the LHC. All these theories can be tested and some of them like most supersymmetric models provide very clear signatures which can be discovered at the LHC. Unfortunately, most theories can adjust their parameters such that they cannot be excluded completely. For example in some areas of the MSSM, in regions of moderate tan β and large values of m_A, the lightest Higgs might be very difficult to detect and all other particles be invisible within the investigated range of energy [27]. History has shown that each step into a new area of physics challenges existing theories and opens our eyes towards better ones. Furthermore, it is clear that the discoveries at the LHC have a strong impact on the future of particle physics, especially on the question whether a linear collider should be build or not. Also the design of such a collider depends on the energy range of the particles which may be discovered. In any case, the LHC will provide

important experimental data for theories which have been developed and worked on in the past decades.

For the discovery of new physics a precise knowledge about the experimental conditions is extremely important. Besides the understanding of various other uncertainties, such as luminosity, alignment and calibration, the knowledge about uncertainties coming from parton distribution functions (PDF) and higher order corrections in the pertubative description of the SM is crucial. A detailed analysis of these uncertainties is presented in Chapter 7.

The experimental program of the LHC will include the dedicated heavy-ion detector ALICE (A Large Ion Collider Experiment), the specialised B-physics spectrometer LHCb and the general purpose detectors CMS (Compact Muon Solenoid) and ATLAS (Section 1.2.2).

1.2.2 A Toroidal LHC ApparatuS

ATLAS is a general-purpose experiment for recording proton-proton collisions at the LHC. It will be run by a collaboration of about 1800 physicists from more than 150 universities and laboratories in 34 countries. The detector design (Fig. 1.2) was optimised to cover the largest possible range of physics: searches for Higgs bosons and alternative schemes for the spontaneous symmetry-breaking mechanism; searches for supersymmetric particles, new gauge bosons, leptoquarks, and other particles indicating physics beyond the SM.

The centre of the ATLAS detector consists of an inner tracking detector in-

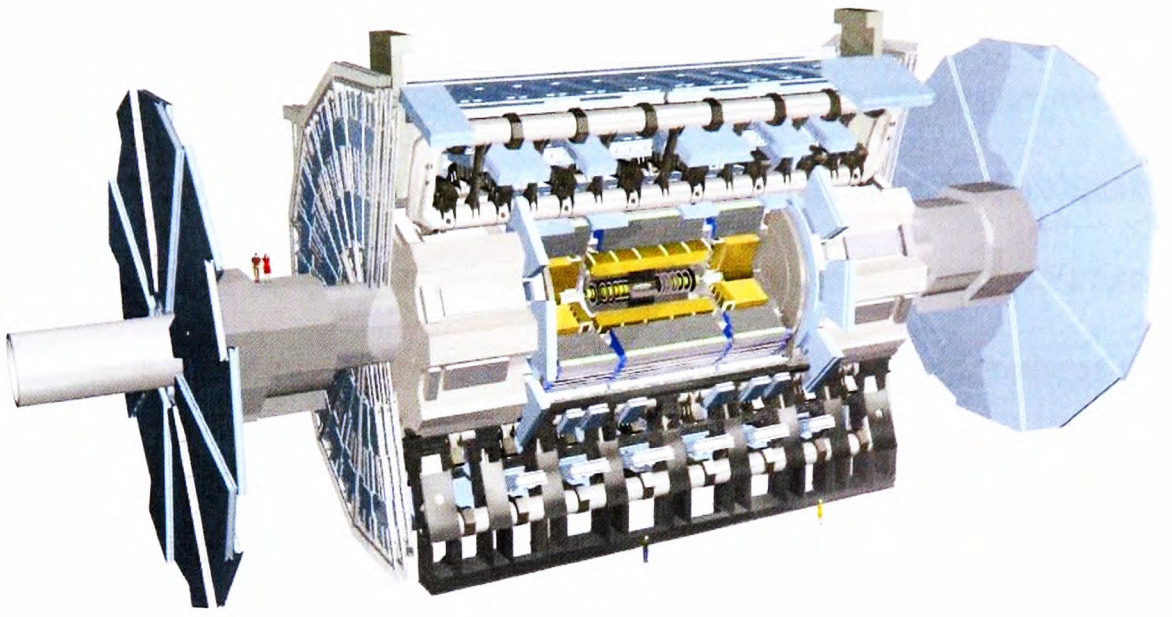


Fig. 1.2: A schematic view of the ATLAS detector is presented. Human beings are added to show the proportions of the image. The overall detector is about 25m in hight and 46m in length. The weight of about 7000 tonnes is similar to that of the Eiffel Tower.

side a 2 T solenoid providing an axial magnetic field. The electromagnetic and hadronic calorimeters are placed outside the solenoid. The air-core-toroid muon spectrometers form the outermost part of the detector. The precision measurements for photons, electrons, muons and hadrons are performed over a range in pseudo-rapidity[3] $|\eta|$ to about 2.5. The complete hadronic energy measurement extends over $|\eta| < 4.7$.

[3] $\eta = -\ln \tan \frac{\theta}{2}$ with θ being the polar angle of the ATLAS detector w.r.t. the beam pipe.

Inner Detector

The Inner Detector consists of three sub-detectors: A silicon pixel detector (PIXEL, Fig. 1.3), a silicon strip detector (SCT, Fig. 1.4) and a transition radiation detector (TRT) [28]. The PIXEL is located inside the SCT (Fig. 1.5) which is placed inside the TRT. Generally, silicon detectors are asymmetric *pn*- or n^+n-doped semiconductor junctions working as a detector for charged particles. A positive voltage is applied on the *n* side of the diode. That way the depletion zone is artificially

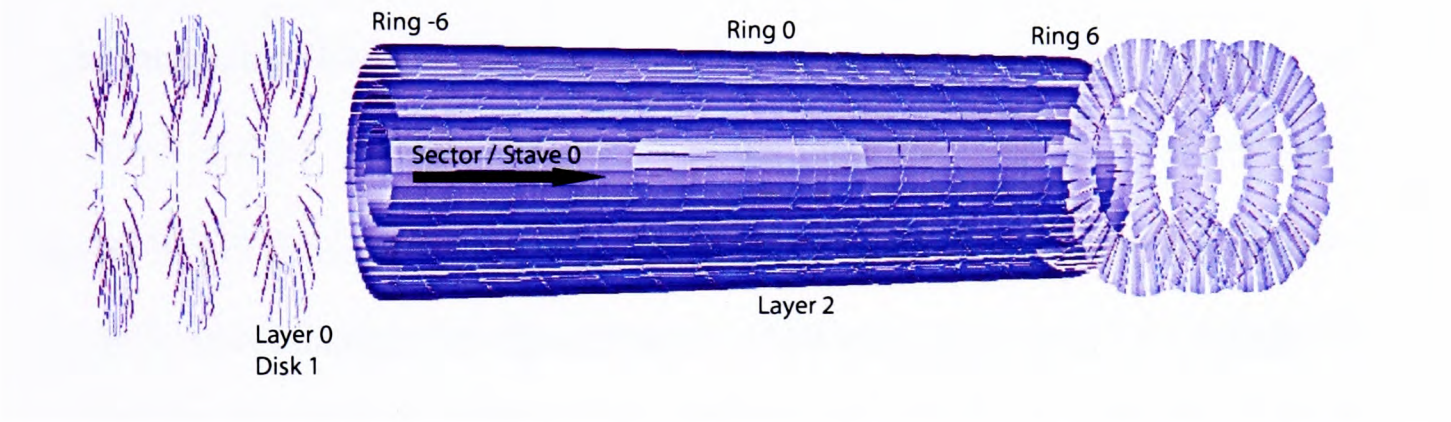


Fig. 1.3: Schematic view of the PIXEL layout. The radius of the outer layer is 122.5 mm.

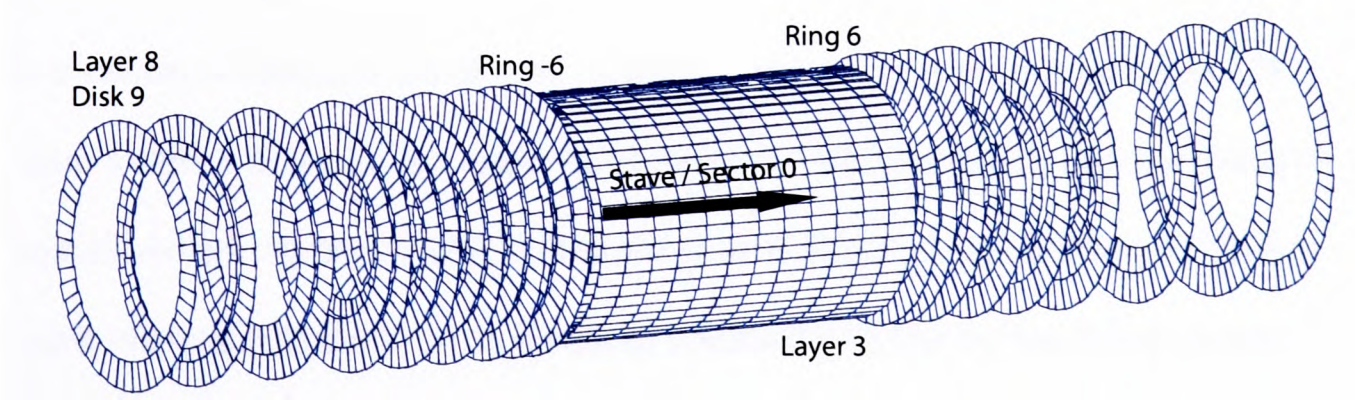


Fig. 1.4: Schematic view of the SCT layout. The radius of the outer layer is 514 mm.

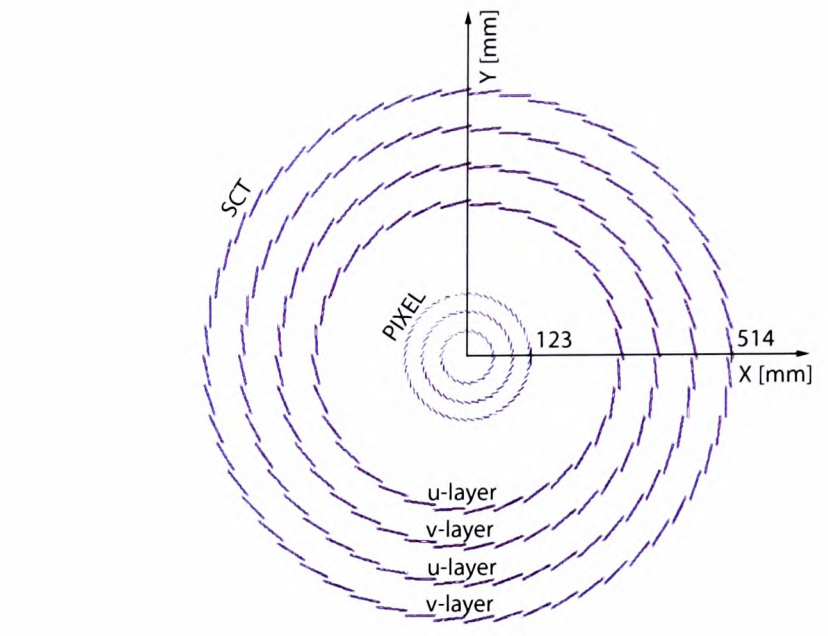


Fig. 1.5: Projection in global X and Y of the PIXEL and SCT barrel detector.

increased and a large volume inside the diode is created which is free of charge carriers. An ionizing particle which passes through the depletion zone produces electron-hole pairs along its path, their number being proportional to the energy loss. The externally applied electric field separates the pairs before they recombine with electrons drifting towards the anode and holes moving to the cathode. The resulting current pulse is then amplified, send to the readout electronics and converted into digital signals. The silicon detectors are operated within a magnetic field of 2 T. Hence, while drifting towards the readout strips, the free charge carriers produced by ionizing radiation in the depletion zone change their direction due to the Lorentz force. This results in an offset of a few microns between readout-position and the actual path of the ionizing particle. However, the ATLAS offline software corrects for this Lorentz-Shift.

The PIXEL is designed for high-precision particle tracking close to the interaction point. It allows finding of relatively long lived particles such as b-quarks and τ-leptons. Each of the 1744 pixel sensors shown in Fig. 1.6 is a 16.4 $\times$ 60.8 mm wafer of silicon with 47268 pixels which are connected to 16 front-end read-out chips. 41984 pixels are having a size of 50 $\times$ 400 μm each, and 5284 each a size of 50 $\times$ 600 μm which is necessary to cover the gap between the read-out chips. Each module has only 46080 read-out channels as there is a 200 μm gap in between read-out chips on opposite sides of the module. In order to get full coverage, the last eight pixels at the gap are connected to only four channels (so called "ganged" pixels). Thus, in 5% of the cases there is a two-fold ambiguity that will be resolved offline [29]. The PIXEL consists of 3 cylindrical barrel layers with radii of 50.5 mm, 88.5 mm and 122.5 mm, respectively. The 1456 barrel modules are glued on carbon staves which are inclined by an azimuthal angle of 20 degrees around the long axis. There are three endcap disks on each side of the forward region. Each disk is made of 8 sectors having 6 modules each.

The aim of the SCT is to provide precision track measurements in the intermediate radial region, contributing to the measurements of momentum, impact parameter and vertex position. The 2112 SCT barrel modules (Fig. 1.7) are mounted on 4 carbon-fibre cylinders with radii of 299 mm, 371 mm, 443 mm and 514 mm symmetric around the interaction point. 1976 further modules are mounted on 18 SCT endcap disks. One module consists of two bipartite wafers of 768 silicon mi-

crostrips[4] which are glued together back-to-back at a 40 mrad stereo angle. This allows to determine the position of the hit along the strips. There are two types of layers in the SCT: u-layers and v-layers (See Fig. 1.5). u-layers consist of modules where the wafers (ϕ) with the smallest distance (side 1) from the beam pipe are parallel to the beam pipe for barrel modules and perpendicular for endcap modules. The wafers (stereo) with the largest distance (side 0) in that layer are rotated anti-clock-wise with respect to the ϕ-wafers by the stereo angle of 40 mrad. v-layers consist of modules where the wafers (ϕ) with the largest distance from the beam pipe are parallel to the beam pipe for barrel modules and perpendicular for endcap modules. The wafers (stereo) with the smallest distance in that layer are rotated clock-wise with respect to the ϕ-wafers by the stereo angle of 40 mrad. The barrel and the endcap detectors consist of alternating u and v layers. The design is a compromise between reducing costs and number of readout channels on the one hand and improving the spatial resolution on the other hand. The spatial resolution is 17 μm in the direction perpendicular to the strips and 580 μm in the direction along the strips [30]. The SCT allows to measure particle tracks up to $|\eta| < 2.5$ (Fig. 1.8). In Table 1.3 an overview of all silicon modules is given. They are sorted by detector type, layer, ring and sector number as they are defined in the ATLAS offline software.

The third part of the ATLAS Inner Detector is a combined straw tracker and

[4] The strips in the barrel modules have each a pitch of 80 μm and strips of the endcap modules a varying pitch in the range from 55 μm to 95 μm.



Fig. 1.6: Picture of a PIXEL Module. The read out electronics is located on top of the silicon. The orange part connects the module to electrical and optical services.

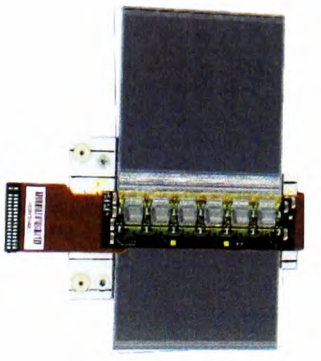


Fig. 1.7: Picture of a SCT barrel module. The read out electronics is located in the middle of the detector module. The brown part connects the module to the electrical and optical services.

transition radiation detector. The TRT barrel is made of 52544 axial straws which are 4 mm in diameter and about 150 cm in length. They are located between 56 cm and 107 cm away from beam pipe. The TRT endcap detectors contain a total of 245760 radial straws at radii between 64 cm and 103 cm. The TRT provides on average 36 two-dimensional measurement points with less than 0.170 mm resolution[5] for charged particle tracks [28]. It facilitates distinguishing electrons and pions.

Calorimeters

The calorimeters of the ATLAS detector which surround the central tracking detectors outside the solenoidal magnet measure the energy of particles originating from the proton-proton interactions inside the detector (Fig. 1.9). They

[5] The resolution depends on the gas mixture.

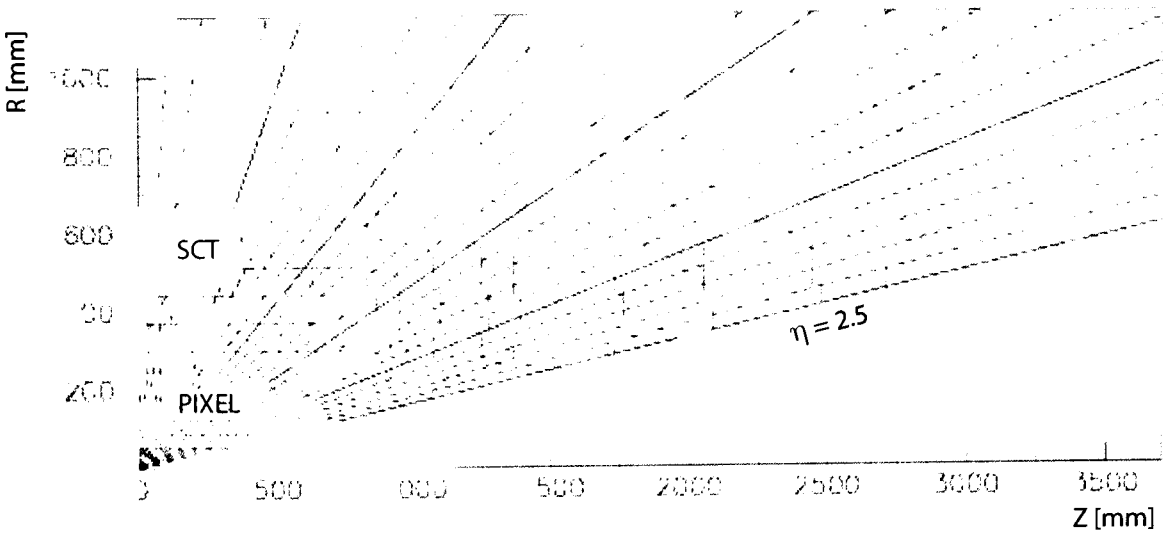


Fig. 1.8: Schematic view of the PIXEL and SCT detector for positive Z including their η range. The other half of the detector is a mirror image of the one presented.

consist of an electromagnetic (EM) calorimeter covering the pseudorapidity region $|\eta| < 3.2$, a hadronic barrel calorimeter covering $|\eta| < 1.7$, hadronic endcap calorimeters covering $1.5 < |\eta| < 3.2$, and forward calorimeters covering $3.1 < |\eta| < 4.9$. Particles are stopped in the material of the calorimeter in order to determine their energies. The main fraction of their energy is absorbed in layers of high density material. The EM calorimeter which is responsible for the absorption of electromagnetically interacting particles like electrons, positrons and photons is based on a lead and stainless steel structure. It is very precise, both in the amount of energy absorbed and in the location of the energy deposited. Angles of particle trajectories can be measured within about 25 mrad [31]. The hadronic calorimeter uses steel (central calorimeter) and tungsten (forward calorimeter) as absorption material to measure the energy of particles interacting via the strong force. It localises particles with a precision of about 100 mrad [31]. Charged

ATLAS Inner Detector Modules				
Detector Type	*Layer*	*Ring*	*Sector*	*Number of modules*
PIXEL Barrel	0	-6,. . .,0,. . .,6	0,. . .,21	286
	1	-6,. . .,0,. . .,6	0,. . .,37	494
	2	-6,. . .,0,. . .,6	0,. . .,51	676
PIXEL Endcap	2 × 0,. . .,2	0	0,. . .,47	288
SCT Barrel	0	-6,. . .,-1,1,. . .,6	0,. . .,31	384
	1	-6,. . .,-1,1,. . .,6	0,. . .,39	480
	2	-6,. . .,-1,1,. . .,6	0,. . .,47	576
	3	-6,. . .,-1,1,. . .,6	0,. . .,55	672
SCT Endcap	2 × 0,. . .,8	0	0,. . .,51	936
	2 × 0,. . .,7	1	0,. . .,39	640
	2 × 1,. . .,5	2	0,. . .,39	400
Total	31 layers	137 rings	5832 modules	

Tab. 1.3: Numbering of all Inner Detector modules in the offline software. The layer, ring and sector numbers are given for each type of detector. Furthermore, the total number of modules is given in the right column. Both SCT wafers are treated as one SCT module. PIXEL layer 0 is often referred to as B-layer. Furthermore, SCT layer 0 to 3 are often called SCT barrel 3 to 6, and the Endcap layers 0 to 8 are commonly referred to as disk 1 to 9. Modules which are in the same barrel and have the same sector number are denoted by being on the same stave.

particles produced in the absorption process of the primary particles ionize the liquid argon which is interleaved between the absorber plates. Due to an applied electric field the electrons drift inducing a current on the electrode structure. The total current is proportional to the energy of the incoming particle. The current is finally measured by an amplifier and is digitized afterwards. The described type of a calorimeter is a sampling calorimeter, because only a small sample of the deposited energy is actually measured in the active medium. The correct calibration of the calorimeters is crucial for their physics performance. It is a complex procedure which is partly based on using particles originating from Z decays.

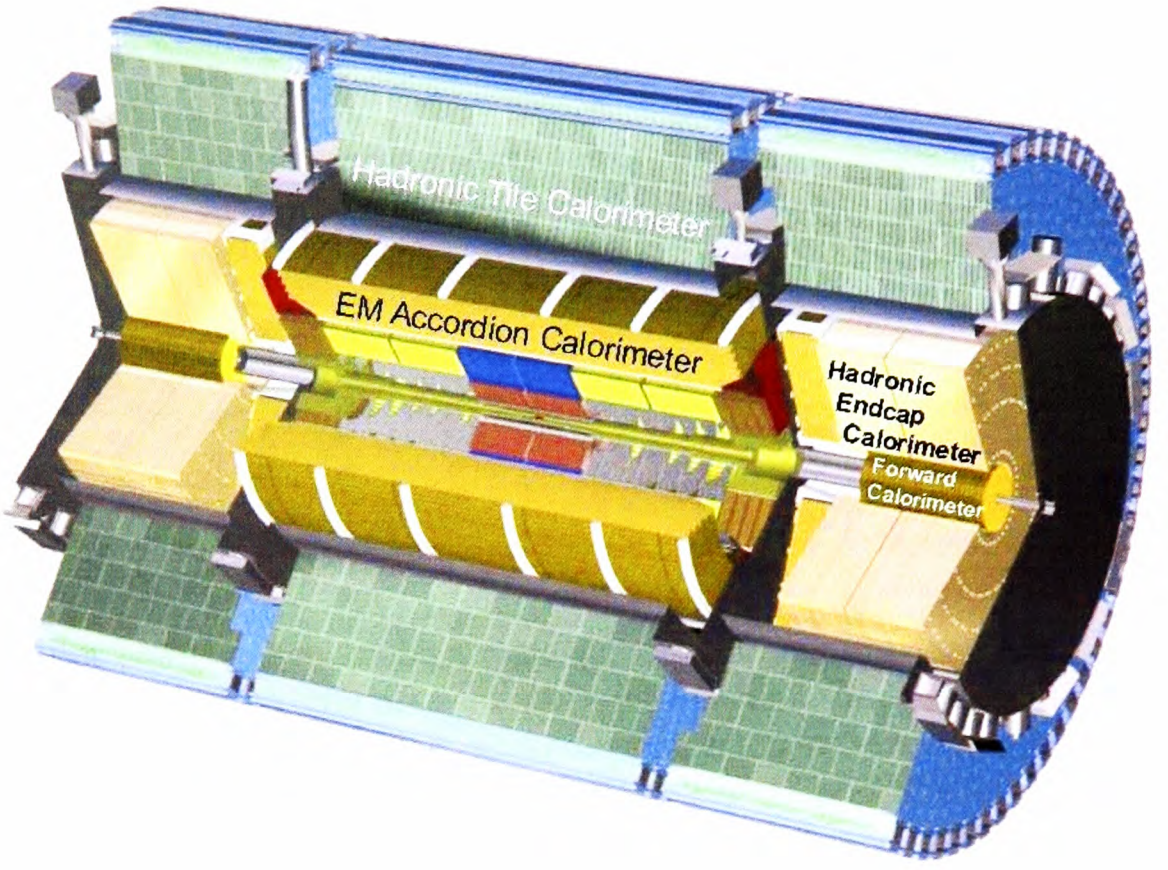


Fig. 1.9: A schematic view of the ATLAS calorimeters.

ATLAS Coordinate Frames

For the description of the ATLAS detector various coordinate frames are used. The three main ones are the Cartesian global, cylindric global and the Cartesian local frame. The Cartesian global frame (blue in Fig. 1.10) is right-handed and has its origin at the centre of the detector. Global X is horizontal, pointing to the centre of the accelerator ring. Global Z is along the nominal beam line and global Y is perpendicular to X and Z. As the accelerator ring is not perfectly parallel to the surface, Y is tilted by about 1.23° from the vertical axis of the ATLAS cavern.

The cylindric global frame which reflects better the shape of the detector is defined by:

$$X = R\,cos(\phi) \tag{1.2}$$

$$Y = R\,sin(\phi) \tag{1.3}$$

$$Z = Z \tag{1.4}$$

In addition to the global frames there is a local frame defined for each silicon module (red in Fig. 1.10). The origin of each Cartesian right-handed frame is in the centre of the module. Local Y is parallel to global Z for PIXEL barrel modules and parallel to global R for PIXEL endcap modules. For SCT modules local Y is parallel to the centre silicon strip. The local X coordinate is always in the module

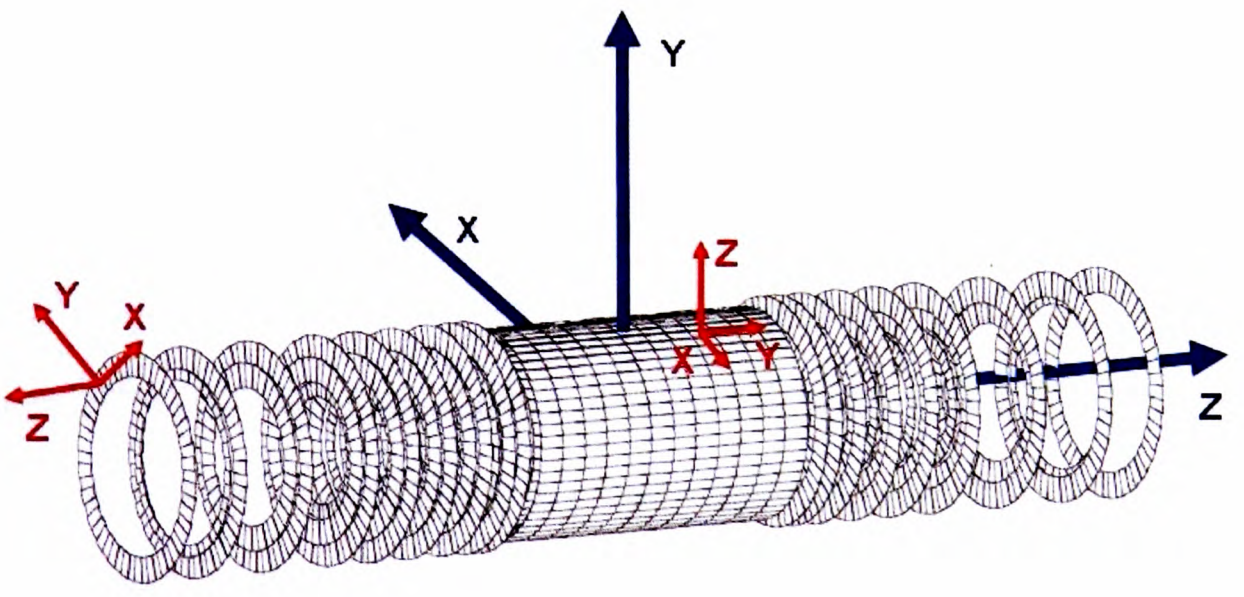


Fig. 1.10: Cartesian coordinate systems: Global coordinate system (blue), two examples of a local frame (red).

plane and perpendicular to the local Y coordinate. The local Z coordinate is thus perpendicular to the module plane by construction. It always points away from the interaction point.

Alignment of the Silicon Detectors

For precision tracking it is absolutely crucial to have a precise knowledge about the location and orientation of the silicon modules. The requirement for the alignment of the ATLAS silicon detectors is that the resolutions of the track parameters are not degraded by more than 20% due to misalignments. Studies have shown that in order to fulfill this requirement the position of the modules has to be known with an accuracy of 7 μm for the PIXEL and 12 μm for the SCT modules in the precision coordinate [28]. For precise W-mass measurements systematic distortions have to be determined to an accuracy of about 1 μm. Furthermore, the measurement of the impact parameter d_0 is crucial for the identification of secondary vertices from long lived particles, such as B-mesons. For example, a random misalignment of 10 μm in the most precise coordinate results in a 10% reduction of the b-tagging efficiency [32].

The positions of the PIXEL barrel modules - which were glued on individual carbon staves - were determined using a coordinate measuring machine (CMM) to a precision of better than 10 μm in $R\phi$ and 20 μm in global Z. However, after mounting the staves on the barrel half-shells they may have bowed in the transverse direction leading to significant displacements of up to 100 μm [33]. The

pixel endcap disks are split into several sectors showing displacements of at most 25 μm from their nominal positions in R and $R\phi$. The estimated bowing is less than 50 μm and the mounting on the larger support structures was surveyed to a precision of 20 μm.

The SCT barrel modules were mounted on brackets which are connected to very precisely built polyketones inserts in the carbon fibre support cylinders. The position of the mounted SCT modules was not surveyed but it is expected to have a precision of 100 μm RMS in $R\phi$ and global Z. The relative positioning of one layer to the next is not expected to be better than 100 μm RMS [33]. The mounting pins of the SCT endcap modules were surveyed to a precision of around 10 μm RMS [34]. Thermal, handling and transport effects are expected to give a misalignment of about 50 μm. The distance between two individual disks is known to a precision of about 100 μm.

The alignment of the ATLAS Inner Detector will be performed by software and purpose-built hardware tools. It is the aim of each tool to determine the alignment parameters that describe the position and if possible the orientation of the modules in the global or local reference frame. A perfect alignment of the silicon detectors is equivalent to the knowledge of the three coordinates that describe the position and the three angles that determine the rotation of each module. For the first alignment of the Inner Detector, when the luminosity is very low, minimum bias events will be used. They will be sent to the alignment algorithms at a rate of 100 Hz. About 10 tracks with a momentum above 1 GeV are expected per event and

an overall efficiency of about 30% may be achieved. Thus, about $2.6 \cdot 10^7$ tracks per 24 hours can be expected. Once the luminosity $\mathcal{L}$ is high enough (above $10^{30}\ cm^{-2}s^{-1}$) the muon trigger is expected to provide a sufficient number of high momentum muons which are suitable for alignment. In Table 1.4 the muon trigger rates are shown. There are three software based methods available which use particle tracks for the alignment of the ATLAS silicon detectors:

- The Global χ^2 algorithm, mainly developed in Oxford, at RAL and in Valencia, provides a measurement of module positions using particle tracks. It is based on a global minimisation of hit residuals, which are defined as the distance between the actual hit and the intercept of the fitted track with the module, with respect to track parameters and module positions. Nearly all degrees of freedom can be determined with this method [35]. However, the achievable precision is not known yet. The main challenge is to solve a linear equation with about 35k degrees of freedom [36].

Muon Trigger Rates [Hz]				
Source	*Low p_T B*	*Low p_T EC*	*High p_T B*	*High p_T EC*
K	7100	5900	680	6400
b	1400	1800	500	1200
c	800	1000	210	600
W	3	0	26	0
t	0	0	0	0
Total	9300	8600	1400	8200

Tab. 1.4: Estimated trigger rates for different muon sources at LHC for Barrel (B) and end-cap (EC) subsystem. The estimated rates are shown for the standard low p_T (6 GeV, $\mathcal{L} = 10^{33} cm^{-2}s^{-1}$) and high p_T (20 GeV, $\mathcal{L} = 10^{34} cm^{-2}s^{-1}$) thresholds [37].

◇ The Local χ^2 algorithm is based on a linearised minimisation of the 3D distance of closest approach between the fitted track and the hit [38]. In contrast to the Global χ^2 algorithm the minimisation is performed on the module level. Correlations are taken into account only through iterations. It is under current development in Munich.

◇ The Robust Alignment method provides a numerically stable[6] alternative to χ^2 minimisation algorithms. It is described in Chapter 2. The alignment of the silicon modules is based on centering residual as well as overlap residual distributions. Overlap residuals can be calculated for tracks which pass through an overlap of two modules. They are defined as the difference between both hit residuals. It was shown that for misalignments up to 40 μm the mean of the overlap residual distribution is about equal to the relative misalignment between these two modules. For larger shifts the mean value is slightly smaller [39]. Overlap residuals correlate modules within the detector rings and staves. The process of correcting module positions needs to be iterated until the relative misalignments converge to zero. The precision of the algorithm depends on the momentum of the input tracks, the intrinsic resolution of the tracking devices and the illumination of the detector. This method successfully aligned the Combined Test Beam setup (Chapter 4) and the SR1 SCT setup (Chapter 5) using real data in both cases. Furthermore, it was used for simulation studies with the full detector (Chapter 6).

[6] For example, there is no requirement that the misalignments have to be relatively small.

It also offers the possibility of distributed alignment which is described in Section 2.5.

There is one hardware alignment tool that will be used during the running of LHC:

- Using tunable lasers, the Frequency Scanning Interferometry (FSI) system is designed to allow 10 μm precision detector shape corrections for the SCT [40]. It provides 842 optical length measurements with an uncertainty of about 1 μm. Its main advantage is the ability of measuring short time scale movements of the detector. However, it addresses only a small, but important, fraction of the 34992 degrees of freedom.

With these four methods it is expected to determine the Inner Detector module positions with sufficient precision.

ATLAS Software

Athena [41] is the ATLAS general purpose software framework being a derivative of the LHCb framework Gaudi. It provides a facility for various needs such as event generation, reconstruction or detector description. Athena is structured in packages which contain services and algorithms. Each package has a defined dependency on other packages. The handling of input and output data as well as the usage of services and algorithms is done in so called jobOption-files which are written in Python, an object-orientated, interpreted scripting language.

The Athena framework is under continuous development. Old classes are often changed to more powerful new ones, new methods are steadily added and also the data flow is regularly modified. Thus, code developed inside this framework needs to be as general as possible, and developers have to be very responsive to new trends. For the reasons given, a detailed documentation is hardly available. Using Doxygen, an automated documentation generator for C++ code, it is possible to gain a good overview of the class structure including their members and methods. Also, the usage of the Concurrent Versions System (CVS) makes code development in the same package by different developers possible.

The offline software contains a generally complete description of the ATLAS detector. This description is used by the simulation and reconstruction and is subject to constant change. Together with this information, the alignment and other conditions which are time dependent are stored. The reconstruction of collision events is performed by a collection of various tools. For the Inner Detector reconstruction, first hit clusters have to be build, space points constructed and finally tracks to be found. The latter step is done by one of the three ATLAS track finding algorithms. The track candidates are then fitted and fed into a transient data store. From there they can be used by various algorithms such as the alignment algorithms. The information provided by the calorimeter and muon chambers is then added to the tracks in order to build particles used in the physics analyses. These analyses may finally unveil the physics laws of the 21^{st} century.

2. THE ALGORITHM: *ROBUSTALIGNALG*

For the alignment of the ATLAS Inner Detector the Robust Alignment algorithm (RobustAlignAlg) has been developed and implemented into the ATLAS offline framework. It provides a simple and stable alternative to the other two algorithms which are based on χ^2 minimisations. The algorithm uses complementary information and does not require the misalignments to be relatively small. In this chapter the algorithm, its implementation as well as its strengths and weaknesses are presented.

2.1 Residuals and Overlap Residuals

The Robust Alignment algorithm is based on hit residual and overlap residual measurements. Before the description of the actual algorithm, these quantities are defined and explained.

The residual calculation slightly differs between the PIXEL and the SCT detector. In general, a residual is defined as the difference between the hit and the

track position in the local frame of the module:

$$res_X = hit_x - track_x \tag{2.1}$$

$$res_Y = hit_y - track_y. \tag{2.2}$$

For the PIXEL, this calculation is straight forward as the 2-dimensional hit position is directly determined. The SCT, however, is a strip detector. Thus, it does not provide a direct measurement of the hit position in the local Y coordinate. It must be constructed from two measurements of two crossing strips within one module. SCT modules consist of two strip detectors which are glued together with a stereo angle of 40 mrad. Both sides of each SCT module are separated by approx. 0.1 mm. The local Y position of the hit depends on the direction of the track which is given through the track fit. First, the hit position is calculated in the global coordinate frame and then it is transformed into the local frame of the respective module. Assuming that there are two strips, A and B, which are hit by the same track which comes from a vertex at the global point $\vec{v}$, and assuming strip A and B lie between the global points a_1 and a_2, and b_1 and b_2 respectively, then the vectors $\vec{q}$ and $\vec{r}$ defined as

$$\vec{q} = \vec{a_1} - \vec{a_2} \tag{2.3}$$

$$\vec{r} = \vec{b_1} - \vec{b_2} \tag{2.4}$$

describe each strip, A and B, in the global frame. A visual representation of the defined quantities is shown in Fig. 2.1. The vectors $\vec{s}$ and $\vec{t}$ which connect the middle of each strip with the vertex v are defined as

$$\vec{s} = \vec{a_1} + \vec{a_2} - 2 \cdot \vec{v} \tag{2.5}$$

$$\vec{t} = \vec{b_1} + \vec{b_2} - 2 \cdot \vec{v}. \tag{2.6}$$

As the track crosses $\vec{v}$ and both strips, the position of the hit on strip A is equivalent to the intersection of strip A with the plane P formed by strip B and the connection $\vec{t}$ to the vertex. The distance of the hit to any other point on the strip, which is

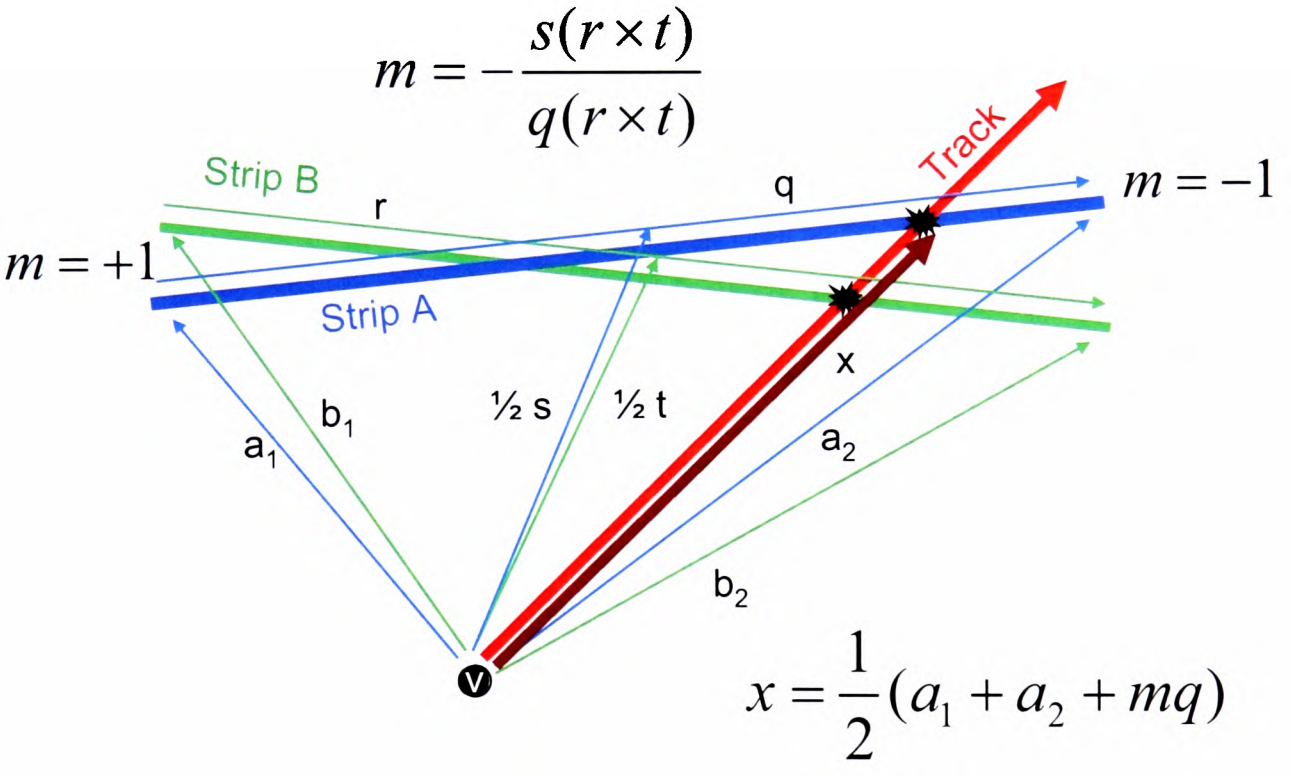


Fig. 2.1: The local Y position of a SCT hit is calculated out of the vertex position and the 3-dimensional directions of the two respective strips. The exact calculation is given in equations 2.3 to 2.9

here chosen to be the middle of the strip, is given by the ratio of two values: the projection of the vector from the middle of the strip ($0.5 \cdot \vec{s}$) onto any vector $\vec{rt}$ perpendicular to the plane P and the projection of the whole strip A onto the same vector $\vec{rt}$. Here, $\vec{rt}$ was chosen to be

$$\vec{rt} = \vec{r} \times \vec{t}. \tag{2.7}$$

Therefore, the distance of the hit to the middle of the strip relative to half of the overall length of the strip can be calculated using the ratio

$$m = -(\vec{s} \cdot \vec{rt})/(\vec{q} \cdot \vec{rt}). \tag{2.8}$$

Knowing m, the global point x on the strip A can finally be constructed:

$$\vec{x} = \frac{1}{2} \cdot (\vec{a_1} + \vec{a_2} + m \cdot \vec{q}) \tag{2.9}$$

Obviously, there are only local Y residuals in the SCT if two crossing strips in a module were hit. If only one strip shows a signal this hit will still be used for the local X residual measurement. This algorithm is the only one inside the ATLAS software which monitors the SCT local Y residual. This measurement is very sensitive to certain biases. In several cases it proved being crucial for detecting problems in the simulation, digitisation or reconstruction software.

Due to the special fan-structure of the SCT endcap modules, special care has to

be taken of the calculation of the local X residual. Generally, a residual is defined as the closest distance of the track to the silicon strip. This distance is given by the following equation:

$$\Delta = (hit_x - track_x)\cos(\alpha) - track_y \sin(\alpha) \tag{2.10}$$

Here, α is the angle between the strip and the y axis of the local coordinate frame. The hit and the track position in the local coordinate system are given by hit and $track$. An illustration of the calculation is shown in Fig. 2.2. For the alignment the distance of the track to the strip in the local frame, the frame in which the alignment is performed, is relevant. This distance gives the residual as:

$$res_X = \frac{\Delta}{cos(\alpha)} \tag{2.11}$$

However, some Athena algorithms define Δ as the residual. In order to facilitate a proper comparison the RobustAlignAlg can switch between both definitions. If useLocalFrameResiduals is set to true in the configuration of the algorithm, res_X is used.

Residuals may be biased or unbiased. For the SCT there is a third option: Fully unbiased residuals. The algorithm allows to choose between all three kinds of residuals:

- Biased residuals show the difference between the hit and the track position

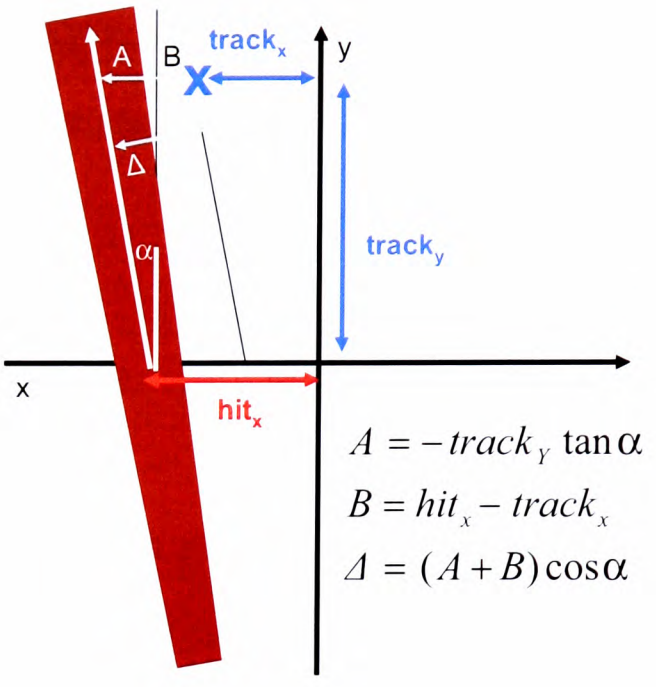


Fig. 2.2: Illustration of the SCT endcap residual calculation. The hit is shown in red, the track is shown in blue.

if the track is fitted using all hits including the one considered in the residual calculation.

- Unbiased residuals are calculated after removing the respective hit and refitting the track.

- The two hits on a SCT module are strongly correlated. Thus, for the calculation of fully unbiased SCT residuals both hits are removed from the track before refitting it.

Using unbiased residuals removes the bias on the track caused by the misalignment of the respective module. Thus, unbiased residuals are a direct measure of the misalignment if only one module position is not known. However, in reality all hits associated with a track come from misaligned modules and the resulting

bias is quite complex. It is controversial whether biased or unbiased residuals should be used for alignment. The Global χ^2 algorithm depends on biased residuals whereas the Local χ^2 algorithm operates on unbiased residuals. In the limit of an infinite number of hits on a track both residuals are exactly the same. However, usually there are less then 10 hits on a particle track which leads to significant differences in the shape and width, but not the mean, of the residual distributions. As the RobustAlignAlg is based on the measurement of the mean residuals only, it can work with both residual types. Studies have shown that the usage of both types of residuals leads to Robust Alignment constants of similar quality.

Once all residuals are determined, overlap residuals can be calculated. Overlap residuals are defined as the difference between two residuals from two overlapping modules:

$$ovres = res_{Module1} - res_{Module2} \tag{2.12}$$

There are two types of residuals, residuals in local X and Y, and two types of overlaps, overlaps in the local X and Y direction. Thus, four different overlap residuals can be constructed. The naming convention is as follows:

$$ovres_{AB};\ \text{A = Residual type, B = Overlap type} \tag{2.13}$$

Similar to residual distributions, the mean of overlap residuals reflects the relative shift between the two overlapping modules. As this measurement is only relative,

it is impossible to determine which module is actually shifted. Thus, it is necessary to allocate each overlap residual to one of the two overlapping modules. In this algorithm the following convention is used: Each overlap is allocated to the module with the

- larger sector number and
- larger ring number.

The 2π symmetry of a ring is taken into account by allocating the overlap between the module with the highest sector number and the module with the lowest sector number to the latter module. Obviously, the SCT detector elements have only overlap residuals in local Y if both modules have each two crossing strips with a signal. In general, overlap residuals are less dependent on multiple scattering effects as the short length between the two tracking surfaces leads to a smaller extrapolation error. Section 2.3.4 explains in more detail how the measured hit residuals and overlap residuals are transformed into measurements of alignment constants.

2.2 Main Principle

The Robust Alignment algorithm is based on two main premises:

- For a perfectly aligned detector all residual and overlap residual distributions are centred around zero.

◇ If only one module is shifted by δx in the direction of the residual measurement, the mean of its unbiased residual and overlap residual distribution is equal to $-\delta x$.

The first point reflects the fact that each silicon strip or pixel being hit by the particle is symmetric around its center. The second principle is illustrated in Fig. 2.3 and 2.4. Reality, however, is more complex and, instead of one, all modules of the detector will be misaligned. Thus, correlations have to be taken into account. The algorithm automatically correlates modules within one ring or stave through overlap residuals. Dependencies on modules which are positioned further away in the detector are taken into account through iterations. Compared with the other

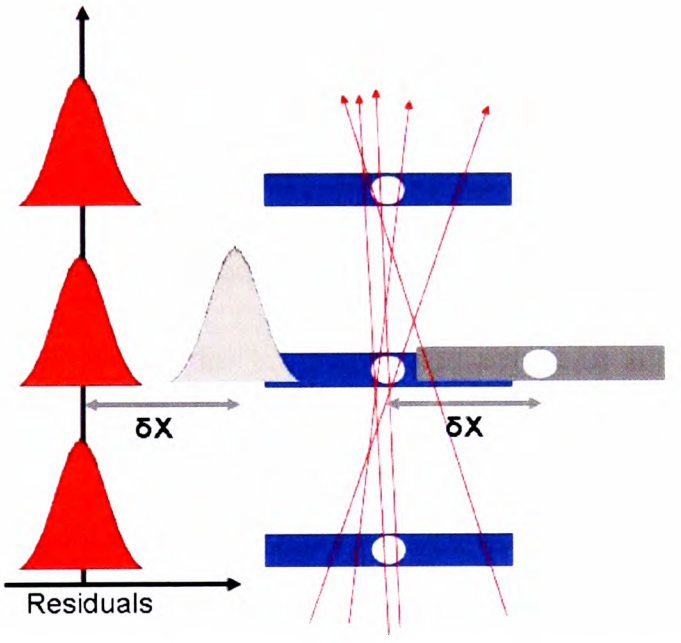


Fig. 2.3: Effect of misalignment on residuals. An example of three modules in three detector layers is given. For simplicity the tracks are assumed to be independent of the misalignment of one module (unbiased residuals or the limit of infinite number of layers). The red distributions show no misalignment, the grey one does. δx is the size of the module shift.

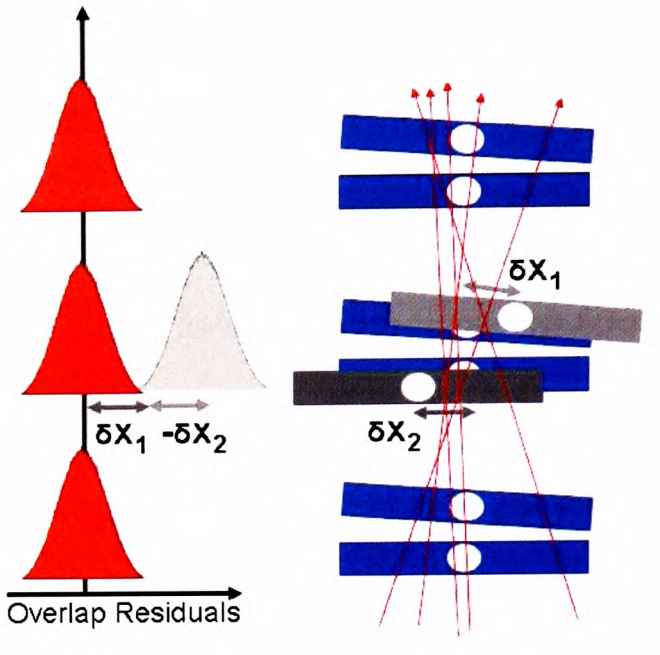


Fig. 2.4: Effect of misalignment on overlap residuals. An example of six overlapping modules in three detector layers is given. For simplicity the tracks are assumed to be independent of the misalignment of one module (unbiased residuals or the limit of infinite number of layers). The red distributions show no misalignment, the grey one does. δx_1 and δx_2 are the sizes of the two module shifts.

two alignment algorithms, the Global χ^2 and the Local χ^2, the Robust Alignment algorithm is numerically very stable as no matrix inversion or χ^2-minimisation is involved. It is thus ideal for performing reliable alignment, especially at the beginning of data taking when the experimental environment is not yet well known. The tests described in Chapters 4, 5 and 6 showed that this algorithm does not require any alignment specific track selection. Furthermore, it provides an independent tool to cross check alignment constants calculated by other algorithms. However, it only corrects for misalignments in the direction of the two most important degrees of freedom; the local X and Y coordinates. These variables are crucial as they have the most impact on the track properties. Tests showed that,

in the local X and Y direction, the Robust Alignment is able to determine alignment constants of similar quality as the other two algorithms [7]. Using overlap residuals it is also possible to take advantage of a third principle:

- ◇ The change of circumference, and therefore the average radial shift of each module, in a ring of overlapping modules is proportional to its sum of overlap residuals.

If the circumference of a detector ring is exactly at its design value the sum of overlap residuals vanishes, even if the modules are generally misaligned. As can be seen in Fig. 2.5, increasing (decreasing) the circumference of a ring shifts the silicon modules away from (towards) each other leading to a positive (negative) sum of the mean overlap residuals. The measurement of deviations in the radial direction is not straight forward for the other two algorithms, as tracks enter the silicon modules mostly perpendicularly leading to a low sensitivity on radial distortions.

Like the other algorithms, the Robust Alignment algorithm assumes that the modules are rigid bodies and that the SCT wafers in each module do not move with respect to each other. Furthermore, the Robust Alignment algorithm does not measure rotations of the modules. This measurement requires very large statistics and will be performed by the Global χ^2 and the Local χ^2 algorithms. It is expected that, applied on real data, the Robust Alignment algorithm is going to provide a very good and stable first set of alignment constants which may be improved with

the other two algorithms. The final precision should be achieved with the Global χ^2. In the following, the implementation of the Robust Alignment algorithm is described in more detail.

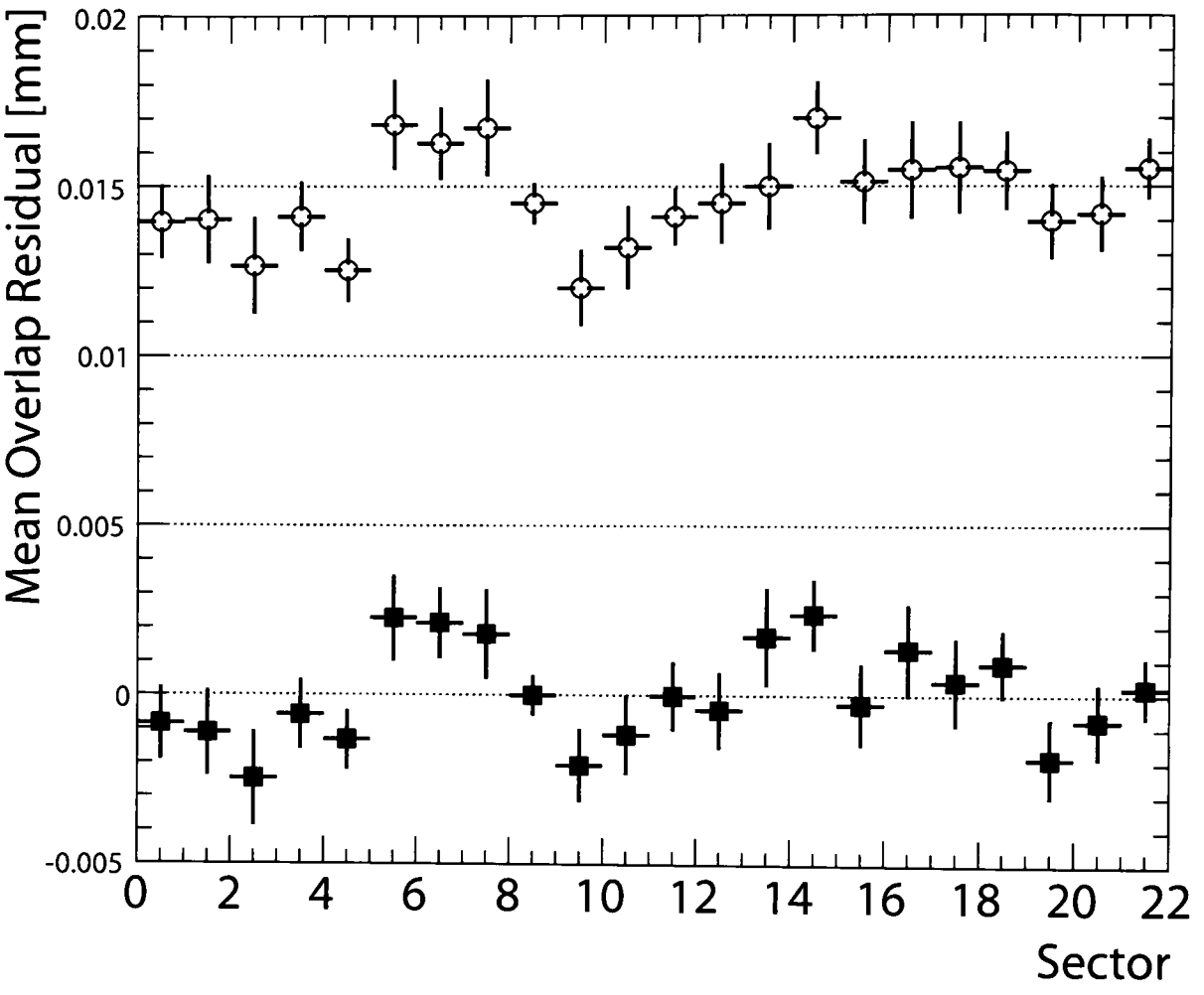


Fig. 2.5: Mean overlap residuals for all modules in a PIXEL ring: A geometry with nominal radius (black squares) and with a radius increased by 50 μm (white circles) are shown. According to Eq. 2.20 each overlap residual receives a bias of on average 14.3 μm.

2.3 Implementation into Athena

The implementation of the Robust Alignment algorithm into the ATLAS offline software is a well structured collection of more than 3000 lines of code excluding comments which is publicly available[1]. The Robust Alignment algorithm requires two main objects: Particle tracks and the module descriptions of all ATLAS Inner Detector silicon modules. Tracks are reconstructed by one of the three currently existing pattern-recognition and track-finding programs which have digitised signals of simulated or real events as an input. They are then fitted by one of the various ATLAS track fitters. More information about the tracking event data model can be found in Ref. [42]. The detector description is stored in the GeoModel library with the service GeoModelSvc providing the interface to Athena.

The software prototype for the silicon barrel detectors written by Danny Hindson [39] was investigated for the migration into Athena. Most of the base classes which are currently used inside Athena were not available at the time when the standalone software was developed. Therefore, it was based on objects which were designed only for its special purpose. It is a requirement, however, that any official ATLAS alignment algorithm is based on Athena classes. Furthermore, the Athena base classes for tracks and also for the interfaces to the conditions database [43] are very powerful and offer many features that are crucial for alignment. For the given reasons it was unavoidable to completely rewrite the Robust

[1] http://atlas-sw.cern.ch/cgi-bin/viewcvs-atlas.cgi/offline/InnerDetector/InDetAlignAlgs/SiRobustAlignAlgs/

Alignment prototype. During that process the structure of the algorithm itself and the calculation of alignment constants improved significantly. Now,

- ◇ residual and overlap residual measurements are combined naturally and applied simultaneously according to their uncertainties,
- ◇ it is possible to apply the algorithm on any kind of detector so that the same code can be used for the alignment of the Combined Test Beam (Chapter 4), the SR1 cosmic data setup (Chapter 5) and the full detector (Chapter 6),
- ◇ not a single line of code has to be changed if more layers of silicon are added for the planned upgrade to the Super LHC (SLHC),
- ◇ the endcap region is now naturally implemented using similar calculations,
- ◇ radial changes can be detected,
- ◇ the user of the algorithm can easily switch between biased and unbiased residuals, different track finders and fitters, and choose to align only certain parts of the detector.

Fig. 2.6 shows an overview of the new Robust Alignment algorithm within the ATLAS software framework. The source code for the RobustAlignAlg is part of the SiRobustAlignAlgs package which is included in official ATLAS offline software. The alignment procedure including the track finding and fitting needs to be iterated until the algorithm has converged to a final solution. The final solution

is defined as a set of alignment constants where no module is shifted in a further iteration if the same data sample is used. Obviously, if another data sample is used statistical fluctuations in the residual distributions will lead to fluctuations in the alignment constants.

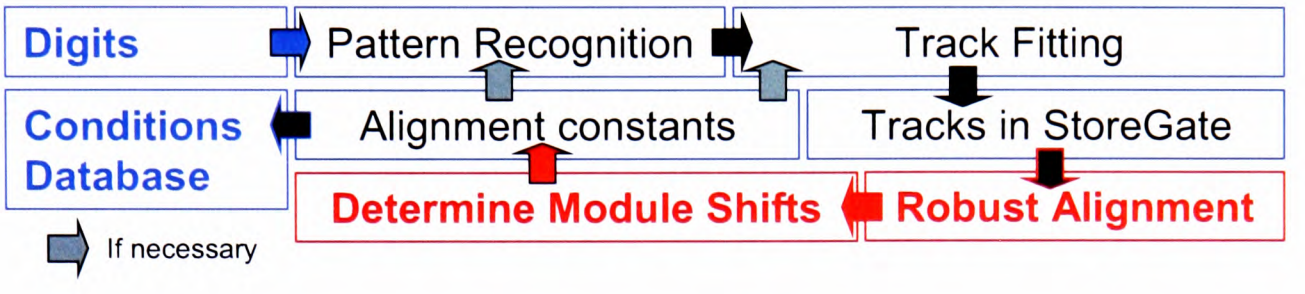


Fig. 2.6: Visualisation of Robust Alignment process inside Athena. Especially if there are large misalignments it is necessary to redo the pattern recognition and track finding after each alignment iteration. For small misalignments which have no effect on the number of reconstructed tracks a simple track refitting is enough.

2.3.1 Options

With the constructor of the algorithm the user has a wide range of options to choose from at the jobOption level. It is, for example, possible to select the degrees of freedom to be aligned, change the requirements on the minimum number of hits per module or choose the type of the residuals to be used for the alignment. A complete list with detailed explanations is given in Appendix A.

2.3.2 Initialize

During the initialisation of the RobustAlignAlg various Athena services are retrieved. The StoreGateSvc is a Gaudi [44] service that allows to record and access

data objects. For example, the StoreGate stores the track collections which contain the track information used by the RobustAlignAlg. The ToolSvc is a service that manages tools[2] inside Athena. It is responsible for creating tools and making them available to algorithms or other services. The ToolSvc tests whether a tool type is available and after having verified that it does not already exist creates the necessary instance. If a tool instance already exists, the ToolSvc does not create a new identical one but passes the existing instance to the algorithm. Only the first algorithm requesting a tool will prompt its creation. The DetectorStore service provides a client interface to conditions data which contains, for example, alignment information.

With the help of the ToolSvc the InDetAlignDBTool is retrieved. This tool is necessary to feed the alignment constants calculated by the RobustAlignAlg back into the Athena software. The GetResidualTool which belongs to the SiRobustAlignTools package is required by the RobustAlignAlg for using unbiased residuals. In this case also an updator tool has to be retrieved which provides the necessary calculations if measured hits get added to or removed from the track. The SiSpacePointMakerTool is necessary for combining two strips from the same SCT module, but different wafers, in order to get a 2-dimensional hit measurement (see Section 2.1). This important measurement is fed into the local Y residual calculation which is fundamental for the RobustAlignAlg. For the correct handling

[2] A tool, in contrast to an algorithm, performs only a very specific task and may be executed multiple times per event.

of silicon modules inside the algorithm the IdDictManager, the ID helper, the PixelManager and the SCT_Manager are retrieved. For example, these tools are used to access the detector information from a certain hit.

Furthermore, all ntuples are initialised at this stage. In these ntuples various test variables are stored which help monitoring the alignment process. They are explained in more detail in Appendix B. At the end of the initialisation two vectors of RobustAlignModule objects are created, one for the PIXEL detector and one for the SCT. These vectors contain representations of all modules defined in the detector description. This feature is the basis of the Robust Alignment algorithm's great flexibility.

2.3.3 Execute

In execute, only one method, readTracksFromSG(), is called. This method reads in a track collection from StoreGate, which is created event by event, and loops over all of tracks in that collection. For each track the method hitLoop() is called which accesses the hits on each track and fills a vector with HitOnModule objects. A HitOnModule object is a combination of an IDHit and IDModule object. The IDHit object contains hit information such as residuals and the global position of the hit. The IDModule object describes the properties of the module such as for example the detector type, the layer number or whether it is a barrel or endcap module. The hitLoop() method forms the basis of the RobustAlignAlg. Here, hit residuals and their errors are calculated. For this process, two main

methods are used, get_localXResidual() which calculates the local X residual, and get_localYResidual() which provides the local Y residual measurement. The latter method uses the SiSpacePointMakerTool in order to combine two 1-dimensional SCT measurements from the two wafers of a module to one 2-dimensional space point. Also, these methods take into account the different module geometries. Thus, they can operate with both, barrel and endcap modules. In fact, they could provide alignment information for any kind of pixel or strip detector module as long as the module geometry is given by the detector description.

2.3.4 Finalize

In finalize, the method doAlign() is called. This method performs the actual calculation of alignment constants out of the collected detector, residual and overlap residual data. If the user selected not to use distributed alignment, this information gets directly fed into two methods doPIXELAlignment() and doSCTAlignment(). The user has also the possibility to align only one of the two detectors. If the user selected to read in text files with alignment information, any new data from the reconstruction is ignored and only that from the text files is fed into the two alignment methods. In both cases the user can write out text files with alignment information. The methods doPIXELAlignment() and doSCTAlignment() calculate the alignment constants using the method getAlignmentTransformation(). The latter method calculates the transformation for each wafer separately and then combines both wafers together. It is expected that the wafers are aligned to a precision of

2 μm in local X and 3 μm in local Y with respect to each other [30]. This uncertainty is too small to be properly detected by the Robust Alignment algorithm. In fact, inside Athena it is currently not even possible to shift wafers separately. The method getAlignmentTransformation() calculates the local alignment transformation which is a 3-dimensional translation (a^X, a^Y, a^Z).

The alignment constants a^X, a^Y and a^Z are determined from the residual and overlap residual measurements on each module. A shift in the mean of the residual distribution of a module and a shift in the mean of the overlap residual distributions is a measure of the same quantity; the displacement of the module. For each local coordinate, X and Y, there is one residual distribution and a maximum of two overlap residual distributions. It is natural to combine these up to three measurements respecting their statistical uncertainties:

$$a^{X/Y} = -\sum_{j=1}^{n} \frac{s_j^{X/Y}}{(\delta s_j^{X/Y})^2} \Big/ \sum_{j=1}^{n} \frac{1}{(\delta s_j^{X/Y})^2}, \; n \leq 3. \tag{2.14}$$

The first summand in this equation comes from the residual measurements on each module. As these are directly correlated with the module displacement, $s_1^{X/Y}$ is given by the mean of the module's residual distribution:

$$s_1^{X/Y} = \overline{res}_{X/Y}. \tag{2.15}$$

Thus, the first summand is given by:

$$\frac{s_1^{X/Y}}{(\delta s_1^{X/Y})^2} = \frac{\overline{res}_{X/Y}}{\delta\overline{res}^2_{X/Y}} \tag{2.16}$$

The statistical uncertainty on the mean residual $\delta\overline{res}_{X/Y}$ is given by the RMS of the residual distribution[3] and the number of entries:

$$\delta\overline{res}_{X/Y} = \frac{RMS_{res}}{\sqrt{n_{Hits}}}, \tag{2.17}$$

If the module has a local X (local Y) overlap to a neighbouring module the second (third) term that has to be considered as well. As shown in Fig. 2.4 overlap residuals are also correlated to the displacement of a module. Furthermore, overlap residual distributions are dependent on displacements of the neighbouring modules. Therefore, these correlations have to be accounted for in the calculations of the alignment constants. From the overlap point of view, where to set the starting point in a ring or stave is an arbitrary choice. The Robust Alignment algorithm begins with the modules which have the smallest sector or ring number. All other module position measurements from the overlap residuals are performed with re-

[3] Biased residual distributions tend to have smaller widths compared to unbiased residual distributions. Therefore, by using biased residuals the statistical uncertainties can be reduced.

spect to the neighbour with the smallest sector or ring number:

$$s_2^X = \sum_{i=0}^{i=N_s} \overline{ovres}_{XX} \tag{2.18}$$

$$s_3^Y = \sum_{i=0}^{i=N_r} \overline{ovres}_{YY} \tag{2.19}$$

Here, N_s is the sector number and N_r the ring number of the module to be aligned. An average increase or decrease in the overall circumference of a detector ring leads to a systematically positive or negative bias in the sum of all overlap residuals. If a detector ring is complete and all overlap residuals are measured with sufficient precision the algorithm is able to perform corrections in the local Z direction:

$$a^Z = -\frac{\sum_{i=0}^{i=N_a} \overline{ovres}_{XX}}{2\pi} \tag{2.20}$$

Here, N_a is the number of all modules in the ring of the module to be aligned. However, this bias has to be removed from s_2^X in the case of local X local X overlap residuals:

$$s_2^X = \sum_{i=0}^{i=N_s} \overline{ovres}_{XX} + \frac{2\pi a^Z}{N_a} \tag{2.21}$$

Thus, for local X measurements the second and third term in Eq. 2.14 are given

by:

$$\frac{s_2^X}{(\delta s_2^X)^2} = \frac{\sum_{i=0}^{i=N_s} \overline{ovres}_{XX} + \frac{2\pi a^Z}{N_a}}{\delta(\sum_{i=0}^{i=N_s} \overline{ovres}_{XX} + \frac{2\pi a^Z}{N_a})^2} \tag{2.22}$$

$$\frac{s_3^X}{(\delta s_3^X)^2} = \frac{\overline{ovres}_{XY}}{\delta \overline{ovres}_{XY}^2} \tag{2.23}$$

As the detector shape is a cylinder, rather than a sphere, there is no 2π-symmetry for the detector staves. Therefore, this correction is not applied for shifts in the local Y direction. The second and third term in Eq. 2.14 for the calculation of the local Y misalignments are given by:

$$\frac{s_2^Y}{(\delta s_2^Y)^2} = \frac{\overline{ovres}_{YX}}{\delta \overline{ovres}_{YX}^2} \tag{2.24}$$

$$\frac{s_3^Y}{(\delta s_3^Y)^2} = \frac{\sum_{i=0}^{i=N_r} \overline{ovres}_{YY}}{\delta(\sum_{i=0}^{i=N_r} \overline{ovres}_{YY})^2} \tag{2.25}$$

The alignment constants are finally given by the following equations:

$$a^X = -\frac{\frac{\overline{res}_X}{\delta \overline{res}_X^2} + \frac{\sum_{i=0}^{i=N_s} \overline{ovres}_{XX} + \frac{2\pi a^Z}{N_a}}{\delta(\sum_{i=0}^{i=N_s} \overline{ovres}_{XX} + \frac{2\pi a^Z}{N_a})^2} + \frac{\overline{ovres}_{XY}}{\delta \overline{ovres}_{XY}^2}}{N^X} \tag{2.26}$$

$$a^Y = -\frac{\frac{\overline{res}_Y}{\delta \overline{res}_Y^2} + \frac{\overline{ovres}_{YX}}{\delta \overline{ovres}_{YX}^2} + \frac{\sum_{i=0}^{i=N_r} \overline{ovres}_{YY}}{\delta(\sum_{i=0}^{i=N_r} \overline{ovres}_{YY})^2}}{N^Y} \tag{2.27}$$

$$a^Z = -\frac{\sum_{i=0}^{i=N_a} \overline{ovres}_{XX}}{2\pi} \tag{2.28}$$

The normalisations N^X and N^Y are defined as

$$N^X = \frac{1}{\delta\overline{res}_X^2} + \frac{1}{\delta(\sum_{i=0}^{i=N_s} \overline{ovres}_{XX} + \frac{2\pi a^Z}{N_a})^2} + \frac{1}{\delta\overline{ovres}_{XY}^2} \quad (2.29)$$

$$N^Y = \frac{1}{\delta\overline{res}_Y^2} + \frac{1}{\delta\overline{ovres}_{YX}^2} + \frac{1}{\delta(\sum_{i=0}^{i=N_r} \overline{ovres}_{YY})^2} \quad (2.30)$$

It is possible to apply damping factors to the alignment corrections. The user of the algorithm has the opportunity to use different values for each degree of freedom. For example, applying a factor of 2 halves the corrections and leads to a smoother convergence. The alignment corrections $a^{X,Y,Z}$ are only applied if they are bigger than n times their respective statistical uncertainties $\delta a^{X,Y,Z}$ (see Section 2.4). Depending on the available statistics the user can chose the appropriate value for n. The analyses presented in this thesis used $n = 1$. Any higher value would have reduced the number of aligned modules significantly. However, once the statistical uncertainties are much smaller than the alignment corrections, the value for n should be increased. The alignment correction a^Z is only applied if the overlaps form a circle. The alignment corrections are local in X, Y and Z. Therefore, from the residual and overlap residual point of view there is no difference between the barrel and the endcaps, and the same calculations are used for both parts of the detector.

Generally, tracking is invariant under global translation and rotation. However, if the real origin (x, y, z) of the tracks is known[4] it can be compared with the mean

[4] Measurements of the beam profile may provide such information.

values, x', y' and z', of the vertex distribution. If (x, y, z) does not match (x', y', z') this algorithm allows to perform a global transformation T to the PIXEL or the whole Inner Detector which is given by

$$T = (x - x', y - y', z - z'). \tag{2.31}$$

Applying this correction is especially important for a correct measurement of the impact parameter d_0. It has been used and is explained in more detail in Section 6.5.

2.3.5 Run the RobustAlignAlg

The Robust Alignment can be configured in any Inner Detector reconstruction jobOption. It is executed after the reconstruction and consumes less than 10% of the total CPU time used for the whole process. Some jobOptions have the Robust Alignment included and only a flag *doRobustAlign* has to be set to true. Digitised signals or extended Event Summary Data (ESD), which contain only hits associated to a track, can be used as input. In a highly misaligned environment it is necessary to use digitised signals and perform the track finding and fitting again in each iteration. As the alignment improves more and more tracks are found. This is not possible using ESD where only refitting may be performed and thus no new tracks are found. Each iteration may be executed in one single process or using distributed alignment. The latter option is explained in more detail in Section 2.5.

In order to monitor the alignment process various ROOT-based [45] macros have been developed. They are used to analyse the convergence of the algorithm or to display the improvement of the track parameters.

2.4 Uncertainties on Alignment Constants

Statistical uncertainties on the alignment constants are determined by the uncertainties on the mean values of the residual and overlap residual distributions which are each given by

$$\delta_{mean} = \frac{RMS}{\sqrt{n_{Hits}}}, \tag{2.32}$$

with n_{Hits} being the number of hits in that particular distribution. Therefore, the exact uncertainty on each module shift depends on the width of the measured distributions and on the illumination of the module. The overall statistical uncertainties for each of the three coordinates are given by:

$$\delta a^X = \frac{1}{\sqrt{N^X}} \tag{2.33}$$

$$\delta a^Y = \frac{1}{\sqrt{N^Y}} \tag{2.34}$$

$$\delta a^Z = \frac{\sqrt{\sum_{i=0}^{i=N_a} \delta\overline{ovres}^2_{XX}}}{2\pi} \tag{2.35}$$

N^X and N^X are defined in Eq. 2.29 and 2.30. For a perfectly aligned detector the pull distribution which is defined as the ratio between the applied module shift and the uncertainty on the respective shift is centered around zero and has a RMS of one as can be seen in Fig. 2.7. The number of hits per module N_{HpM} which is required to reach a certain statistical uncertainty Δ can be estimated by:

$$N_{HpM} = \frac{1}{\Delta^2 \times (\frac{1}{RMS_{res}^2} + \frac{2}{G \times RMS_{ovres}^2})} \quad . \tag{2.36}$$

Here, RMS_{res} and RMS_{ovres} represent the average RMS for the residual and overlap residual distributions, respectively. The geometrical factor G corrects for two considerations. Firstly, depending on the location of the module in the detector there are about ten times fewer overlap residuals than residuals. Secondly, some overlap residual measurements are correlated with others in the same ring or stave. The uncertainties of these measurements have to be taken into account

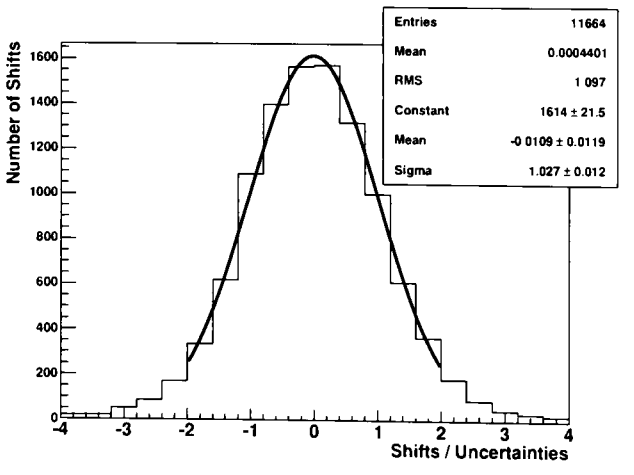


Fig. 2.7: Pull distribution: For each of the 5832 modules and for the alignment in both directions, local X and Y, the ratio between the applied module shift and its uncertainty is shown. A perfectly aligned detector geometry was used.

as well. Thus, G is defined as the product of the number of correlated measurements and the ratio of residual to overlap residual measurements. Values for G are typically between 10 and 300. Four examples are given in Fig. 2.8 to 2.11. With each iteration, the residual and overlap residual distributions get narrower and the tracking efficiency is improved. Therefore, the statistical uncertainties improve significantly in each step. On the whole, the PIXEL detector provides a much better intrinsic resolution compared to the SCT, leading to much better alignment constants. Furthermore, the number of hits per module increases for smaller layer numbers. The innermost layers are expected to have the best precision. Only the outer rings of the innermost PIXEL layer, which are at the kinematic limit of the detector's tracking acceptance, show poor illumination with hits associated to a track.

There are two types of systematic errors. First of all, there are certain global modes which are not determined properly by the alignment algorithm. The most

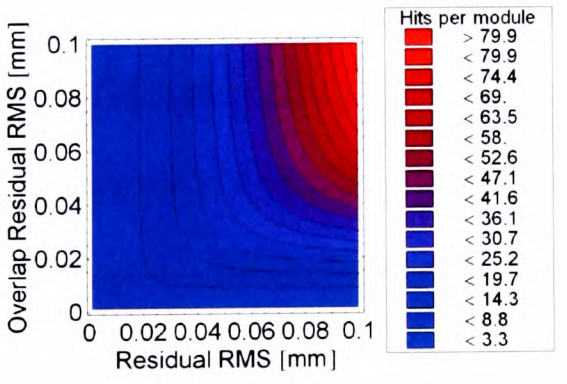


Fig. 2.8: Hits per module required for 10 μm precision - G = 10, Range = 100 μm

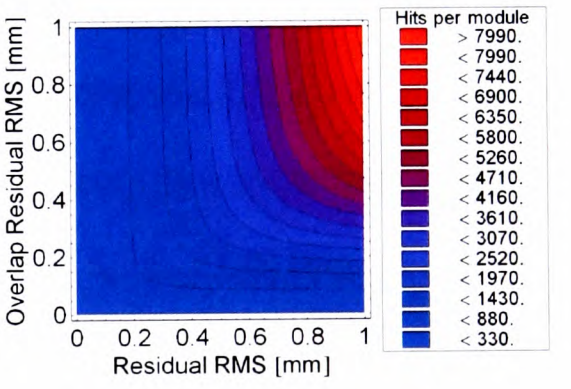


Fig. 2.9: Hits per module required for 10 μm precision - G = 10, Range = 1000 μm

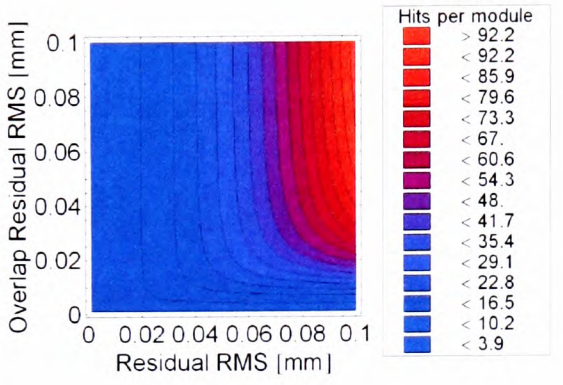


Fig. 2.10: Hits per module required for 10 μm precision - P = 50, Range = 100 μm

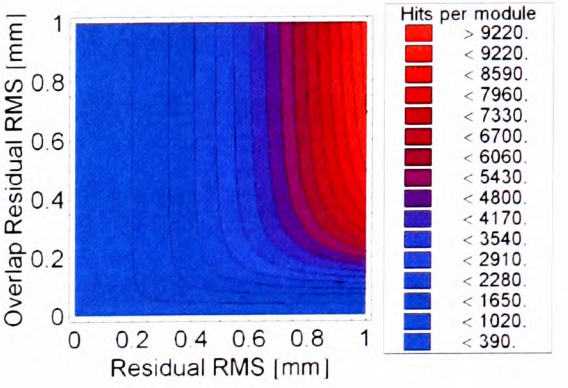


Fig. 2.11: Hits per module required for 10 μm precision - G = 50, Range = 1000 μm

obvious ones are global translations or rotations. In principle the tracking is invariant under these transformations. As described in Section 2.3.4 it is possible to shift the centre of the detector to the beam position. However, the uncertainty on that measurement is expected to be large compared to the uncertainties on relative module positions. There are more subtle, so called weak modes, which lead to properly fitted tracks, however, show significant differences in the module positions from the actual geometry. This challenge is explained in more detail in Section 3.4. Secondly, as the alignment algorithm is located at the end of the data chain, from the actual particle hitting the detector to the reconstructed track, problems in the underlying infrastructure will definitely affect the measurement of the module positions. During the development and tests of the Robust Alignment numerous issues which are independent of the algorithm were found and resolved. In Athena release 12 there are still problems with SCT and PIXEL residuals as they are not precisely centered around zero for a perfectly aligned detector [46].

Indeed most of the shifts are very small. However, it is crucial, not only for the alignment, that these open issues get solved before the start of the LHC.

2.5 Distributed Robust Alignment

Already at the start of LHC a large number of tracks suitable for the Inner Detector alignment is expected to be produced (Section 1.2.2). In order to save time, these tracks may be reconstructed on several computers simultaneously. It is crucial to produce a first set of alignment constants as quickly as possible as these constants can immediately be used by the triggers to improve their performance. It is a requirement for each alignment algorithm to be able to produce alignment constants within 24 hours. With the method described in this section this requirement can be easily achieved if enough computers are available to perform the reconstruction.

The Robust Alignment algorithm calculates alignment constants $a^{X,Y,Z}$ out of all residuals and overlap residuals measured during reconstruction. The more tracks are used for the alignment the better is its precision. More than 90% of the computing time is used for the reconstruction, not for the calculation of alignment constants. It is possible to reconstruct any number of events N on P computers in order to decrease the reconstruction time of the whole data sample. The challenge is to store the alignment information from each sub-sample of M events such that it can be combined later without changing the resulting alignment constants. Hence,

the requirement for a successful solution is:

$$a_{i,d}^{NEvents} = \sum_{j=1}^{P} a_{i,d}^{M_j Events} \bigvee d, i \tag{2.37}$$

with

$$\sum_{j=1}^{P} M_j = N \tag{2.38}$$

$$d \in \{X, Y, Z\} \; and \; i \in All \; modules \tag{2.39}$$

The Robust Alignment solves this challenge by storing all information required for the calculation of alignment constants in purpose built objects which can be written out as text files. As only the mean, the RMS and the number of entries for each residual and overlap residual distribution for each module is used to calculate the alignment constants, only this information is actually stored. The algorithm that performs the distributed alignment is based on simple mathematical equations that ensure the correct addition of the above quantities without any loss of relevant information. It is important that the requirement on the minimum number of hits on each module is only applied at the end when all the sub-samples are combined. Thus, if data instead of input files with alignment information - is used for the calculation of alignment constants and if at the same time text-files for the distributed alignment are written out the minimum number of hits required is automatically set to zero. The lower limit is therefore only applied if either the

whole dataset is used or if different text files with alignment information are read in to produce the final set of alignment constants.

In order to test the distributed alignment algorithm, alignment constants calculated in two ways were analysed. The first set of constants was directly determined from 6k events with each ten muons. A misaligned detector together with error scaling (See Chapter 6) was used. The second set was calculated by combining three sets of 2k events. The three sets of 2k events contain exactly the same events as the first set with 6k events. A comparison of the two alignment constant sets showed differences with an RMS of less than 0.1 nanometres in all module coordinates. These differences are due to rounding errors and clearly negligible.

2.5.1 Run Distributed Robust Alignment

The distributed alignment is very simple to use. In the first step, text-files with the alignment information have to be produced. It is not important how many events are fed into each file. Also, the number of files in not limited. Thus, as many computers as available can be used for the generation of input text files. As it is described in Section 2.3.1, the Robust Alignment input parameters are defined with the configuration of the algorithm. The following parameters are crucial for the distributed alignment:

- ◇ TextFileNameBasis: The basis character string for the files which contain the alignment information for each sub-sample.

- ◇ TextFileWriteNumber: The number of the sub-sample. It has to be different for each sub-sample.

- ◇ DoWriteTextFile: This boolean flag has to be set to true if text files with alignment information are to be written out.

In the second step all text files are read in. With this complete information the alignment constants can be calculated. The same jobOptions as used for the generation of the text files should be used. However, only one arbitrary event is needed for this run in order to initialise the detector description. Also, the configuration of the RobustAlignAlg has to be slightly different:

- ◇ TextFileReadStartNumber: The first number of the sub-sample which is used for the calculation of the final alignment constants.

- ◇ TextFileReadEndNumber: The last number of the sub-sample which is used for the calculation of the final alignment constants.

- ◇ DoReadTextFiles: This boolean flag has to be set to true if text files with alignment information are to be read in for the final calculation of alignment constants. If this flag is set to true, all information coming from events in the event selector is ignored.

For the reasons explained above, the minimum number of hits per module required for the alignment is set to zero if DoReadTextFiles is set to false and DoWriteTextFile is set to true. In all other cases the value given through the configuration

is used.

The distributed alignment has successfully been applied to perform the SR1 and CSC alignment which are described in Chapter 5 and 6. The distributed CSC alignment used the computer farm in Oxford whereas the distributed SR1 alignment was completed on the lxbatch farm at CERN. In both cases a single script was sufficient for the fully automated execution of the alignment.

3. ALIGNMENT LIMITATIONS, SOLUTIONS AND VALIDATION

The performance of any track based alignment algorithms is generally affected by limitations in the detector design, theoretical constraints and problems in the reconstruction software. In this chapter a few of these problems are described and where possible solutions presented. These challenges are not specific, but clearly relevant, to the Robust Alignment.

3.1 Removal of Edge Channels

An edge channel is defined as the strip or pixel that forms the border of an SCT or PIXEL module. Due to the thickness of the silicon the measured interaction point of the track with the silicon may lie outside of the active silicon if the track is not perpendicular to the module surface (Fig. 3.1). This biases the residual measurement. Furthermore, charges generated by the particle may in general induce a signal in the neighbouring strip if the track is close to the edge of the main strip.

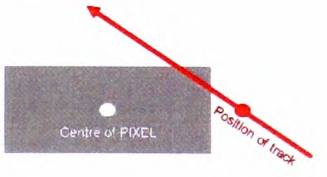


Fig. 3.1: Track hitting an edge channel. The position of the track is outside of the silicon.

For edge channel strips this is, however, not possible and again the residual measurement receives a bias [47]. Tracks that go through two overlapping modules are likely to hit edge channels which affects the overlap residual measurement significantly. Additionally, if there is a bias in both hits of the overlap residual, the biases are of opposite sign. Therefore, the bias of the overlap residual is twice as big as that of the residual measurement. In Fig. 3.2 it can be seen that the outer strip (Strip 0) of the SCT detector has a positive bias in the overlap residual distribution. The same biases can be found in the PIXEL detector. The figure presented was generated with 1000k events, with ten muons each, which were simulated using a perfect geometry. For alignment studies, edge channels must be removed from the calculation of alignment constants even though it reduces the number of overlap hits[1]. In order to study this effect the RobustAlignAlg offers the option to remove or keep edge channel hits.

With the removal of edge channels, overlap residuals should be centered around zero for a perfectly known geometry. However, biases of a few microns have been discovered which are currently being investigated [46]. These biases are smaller than the statistical uncertainties existing in all the analyses presented in this thesis. Therefore, they do not affect the results significantly.

[1] Reduction between 6% for SCT local X overlaps to 100% for the central PIXEL local Y overlaps.

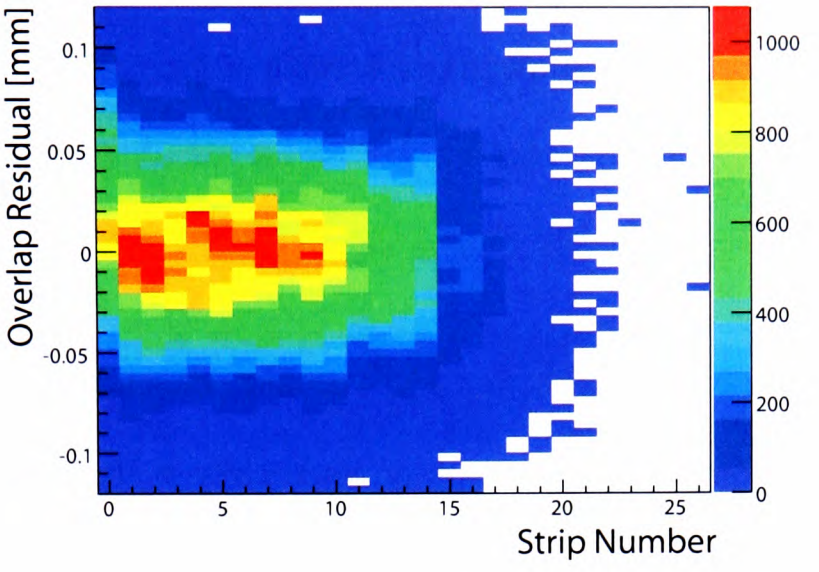


Fig. 3.2: Overlap residual distribution as a function of the SCT strip number for all SCT barrels. The strip number is given for the hit closest to the edge of the module. Only the strips which form overlaps with other strips are presented. Channel 0 shows a positive bias.

3.2 Effect of Multiple Scattering on SCT Local Y Residuals

Each charged particle traversing through the tracking detector is mainly deflected by small-angle Multiple Coulomb Scattering (MCS) off nuclei. MCS affects the tracking resolution and is most significant for low momentum tracks. For a thin layer of traversed material the RMS of the deflection angle can be approximated by [25]:

$$\theta = \frac{13.6MeV}{\beta cp} z\sqrt{x/X_0}[1 + 0.038\ln(x/X_0)] \tag{3.1}$$

Here, p, βc and z are the momentum, velocity, and charge number of the incident particle, and x/X_0 is the thickness of the scattering medium in radiation length. The scattering medium here is either the layer of silicon or other detector material.

Neglecting the uncertainty of the track fit, the measured width σ of the residual distribution is a function of the intrinsic resolution σ_{res} and the average deflection due to MCS σ_{MCS}:

$$\sigma^2 = \sigma^2_{res} + \sigma^2_{MCS} \tag{3.2}$$

The size of the average deflection σ^2_{MCS} does not depend on the direction X or Y as the scattering on the silicon occurs symmetrically in all directions. It is, however, not correct to assume that the SCT detector can be considered as a simple PIXEL-like detector where Eq. 3.2 still holds. Due to the geometry of the modules with the two strip detectors, their particular placement in the different layers of the SCT (see Section 1.2.2) and the design of the tracking algorithm, the effect of MCS is much higher than equation 3.2 would suggest. As the Robust Alignment algorithm is the only ATLAS algorithm analysing local Y residuals, this phenomenon was not known prior to this analysis. In the following, a simple model is presented that correctly predicts the order of the magnitude of the observed increase in the local Y resolution.

The ATLAS tracking algorithms reconstruct particle tracks in the SCT by minimising all 3-dimensional distances between the track and the strips. These strips belong to modules which are rotated alternating from layer to layer by $\pm$ 20 mrad around the local Z axis. In order to estimate the magnitude of this effect it is helpful to make a simple, but general model. Two layers of one module each are enough for this purpose. Both modules are rotated with respect to each other by

an angle α in the plane perpendicular to the track as it is shown in Fig. 3.3. Here, α is equal to the stereo angle between the two wafers of each SCT module.

In this model the particle undergoes MCS between the two hits, $H1$ and $H2$, and its track is assumed to be perpendicular to the module planes. In the following, two cases are discussed: Scatters in the local X direction and scatters in the local Y direction. In the first case, a track fitter minimising the 2-dimensional distances places the track directly between $H1$ and $H2$ at $T1$ as it is shown in Fig. 3.3. However, minimising the 3-dimensional distances to all strips leads to a track at $T2$. In this case, a scatter δ_x in local X leads to a change in the local Y position of

$$\delta_y = \frac{\delta_x}{2 \cdot \tan(\alpha)}. \tag{3.3}$$

Regarding local Y scatters, the two different possibilities of fitting the track lead

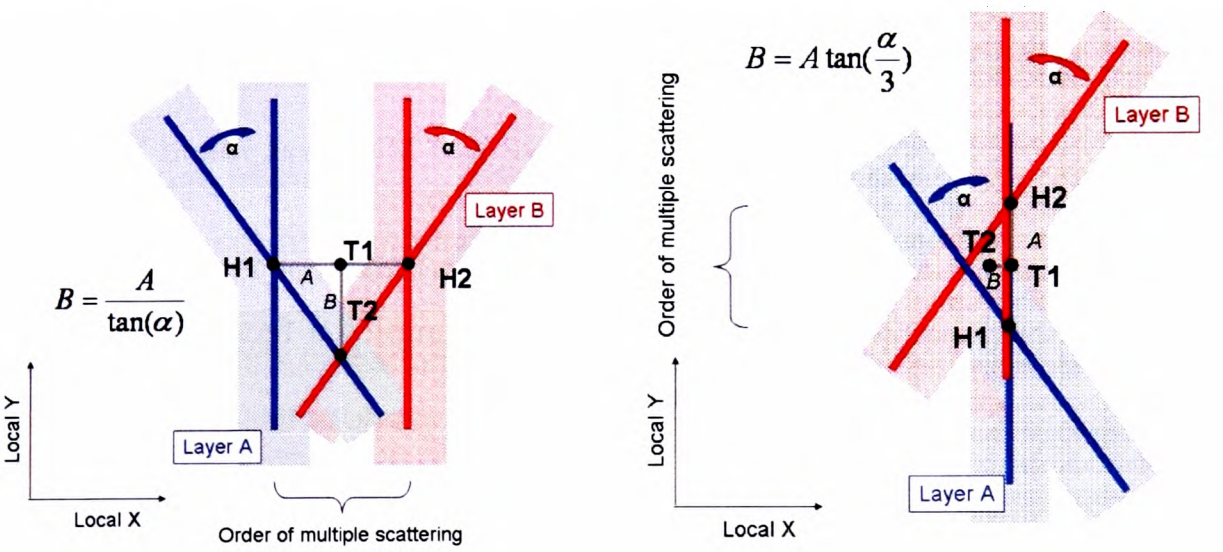


Fig. 3.3: Example for a scatter in the local X (left) and local Y (right) direction. H1 and H2 are the actual hits, T1 the position of the fitted track if the distances to 2-dimensional space points are minimised and T2 the position of the fitted track if the distances to all strips are minimised. The particle is assumed to fly perpendicularly to the projection plane, entering first layer A then layer B.

to the same displacements in the local Y direction as can be seen in Fig. 3.3. Thus, the effect of MCS on the local Y resolution gets magnified by a factor M which can be approximated by

$$M = \sqrt{\frac{1}{4 \cdot \tan^2(\alpha)} + 1}. \tag{3.4}$$

The first term in equation 3.4 arises from actual scatters in the local X direction whereas the second term represents scatters in the local Y direction. For small angles α the first term is much greater than the second. For the ATLAS SCT α is 40 mrad. Therefore, with this model there is an increase of the MCS effect by a factor of approx. 13. Simulation studies with single muon tracks were performed to test this simple model. A low and a high energy sample which contained only muons with momenta greater than 200 MeV and 20 GeV, respectively, were used. Using Eq.3.2 and assuming that MCS above 20 GeV is negligible, an average σ_{MCS} of almost 80 μm for tracks above 200 MeV was found by measuring the local X resolution σ in both samples. Applying then the same calculations to the local Y residual distributions in both samples a factor M of about 14 was measured. Hence, this simple model indeed predicts the order of the magnitude of this effect correctly.

Furthermore, Fig. 3.3 shows that also the residual measurement in the local X direction is slightly magnified due to MCS in the local Y direction. The position of track $T2$ is given by minimising the distances to all four strips. This effect,

however, is only of the order 10^{-5}:

$$M = \sqrt{\frac{tan^2(\frac{\alpha}{3})}{4} + 1}. \tag{3.5}$$

The model presented suggests that the magnification of MCS effects would neither exist if tracks were reconstructed by minimising all 3-dimensional distances between the track and the 2-dimensional space points made out of two strips nor would it be there if the modules had the same orientation in each layer.

3.3 PIXEL Z Overlap Hits

Due to the design of the PIXEL detector the innermost PIXEL barrel rings have no global Z overlaps for tracks coming directly from the origin. This affects the number of overlap hits in that region significantly. Due to the spread of the vertex it is, however, still possible to measure overlap residuals. In Fig. 3.4 the number of overlap hits per PIXEL ring is shown. In the central region of the detector there are far less overlap hits than in the outer regions. Therefore, the contribution from overlap residuals for the local Y alignment in the central PIXEL detector will be negligible.

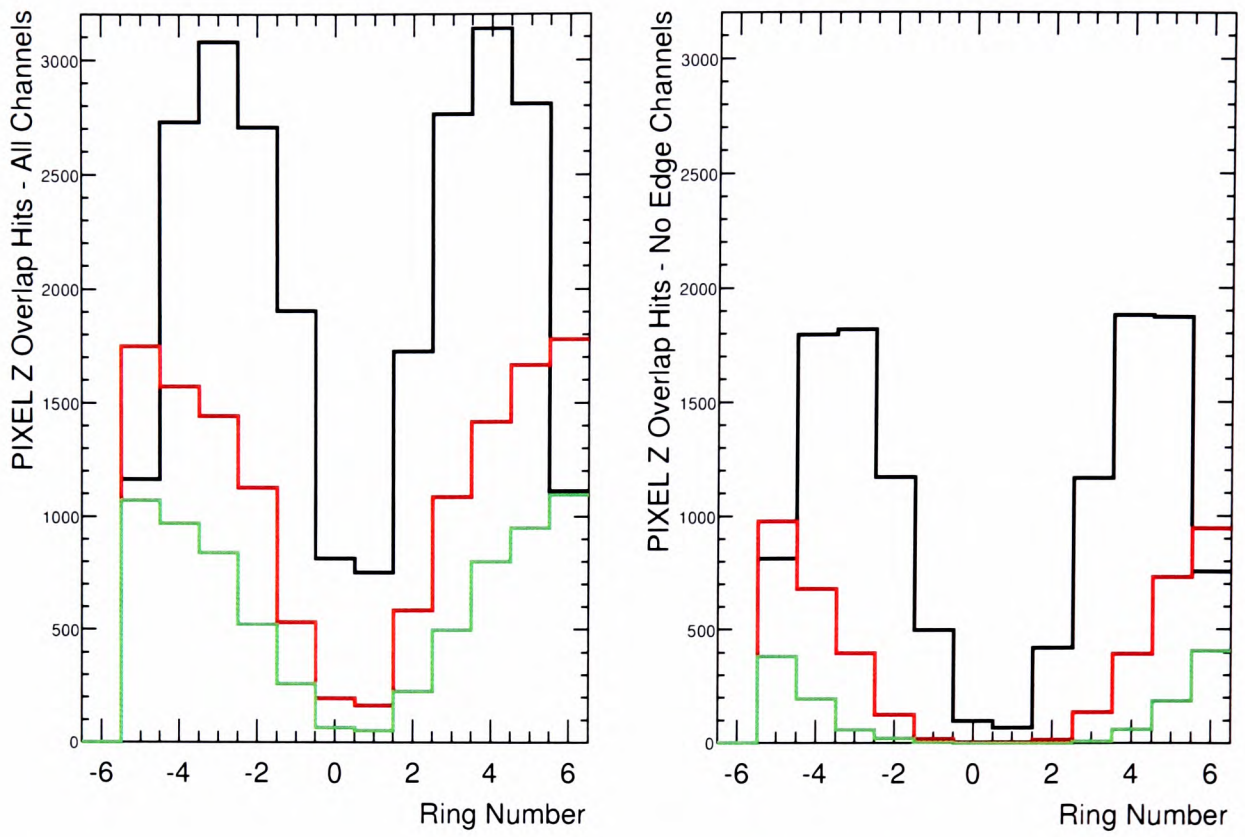


Fig. 3.4: Overlap hits for all three PIXEL layers (layer 0: black, layer 1: red, layer 2: green). The distributions are shown for all channels (left) and excluding edge channels (right). The input for this distribution is 70k simulated multi-muons (perfectly aligned geometry). The convention is that the overlap is associated with the ring with the higher ring number.

3.4 Sagitta Distortions

Any track based alignment algorithm is designed to measure the relative module positions by optimising track parameters. However, it is known that there are global deformations of the detector that do not have any impact on the quality of the track parameters. For example, it is possible to apply systematic rotations to the individual detector barrels such that only the reconstructed momenta of

the individual particles changes, but not any other parameter. More examples of possible modes are described in Ref. [39]. There are generally three classes of solutions to that problem.

Firstly, it is possible to constrain the momentum of the particle tracks used for the alignment. Reconstructing particle tracks, especially those coming from cosmic rays, in runs without magnetic field produces straight tracks which is equivalent to having tracks with infinite momentum. Here, the momentum is naturally constrained. Other suggested solutions include momentum constraints from invariant mass measurements on known resonances and using the muon spectrometer or the TRT to give an estimate about the momentum. The latter option has successfully been tested as can be seen in Chapter 6. Secondly, tracks from cosmic rays, even with magnetic field, correlate the upper and the lower part of the detector and hence, constrain some of the global modes. Thirdly, it is possible to use the calorimeter information to detect global sagitta distortions. By measuring the asymmetry between the E/p distribution[2] from electrons with that from positrons, it is possible to measure certain distortions independent of the calorimeter calibration [39].

The first and the second solution is naturally implemented in the Robust Alignment algorithm. For example, tests with the CTB setup (Chapter 4) have shown that the correct momentum scale can be recovered if the momentum of a certain class of particles is known. The third solution needs a complete independent algo-

[2] E/p is the measured energy to momentum ratio.

rithm that translates the information from the E/p distributions in actual alignment constants. Such an algorithm would need to be used after the alignment constants calculation by one of the three official track based alignment algorithms.

It is clear that each of the methods presented may have a bias in itself. However, the analysis of correlations between all of them should minimise the uncertainty and lead to sufficient constraints for solving the weak modes.

3.5 Validation of Energy and Momentum Measurement inside Athena

As it is described in Section 3.4, alignment algorithms might converge on sagitta distortions. These distortions are systematic shifts of detector parts. One possibility to correct for these shifts is to compare the E/p distributions of positive and negative leptons. During the analysis of simulated $Z^0 \rightarrow e^+e^-$ data in Athena release 10, a significant momentum asymmetry between electrons and positrons was discovered. Careful and systematic analysis with different parts of the detector and iterating the process with different newer software releases (11.0.X) proved that there is no asymmetry in the simulation or digitisation. The analysis finally lead to the discovery of a bug in the tracking package TRT_Rec which was solved from tag 05-01-19 onward. This bug caused a different treatment in the TRT of electrons and positrons which had lost a lot of momentum when passing through the detector material.

The final analysis was performed using the package UserAnalysis-00-04-02 together with 50k single electrons and 50k single positrons which were simulated and digitised with Athena release 11.0.1. The reconstruction was performed with releases 11.0.1, 11.0.2, 11.0.3 and 11.0.41. As the correction in TRT_Rec became available from release 11.0.41 onward, only results generated with this and the previous (11.0.3) release are presented. In the used geometry[3] all silicon modules were placed at their nominal position. Thus, no misalignment was applied. All leptons used for this study were generated in an energy range between 20 and 200 GeV and $|\eta| < 1.5$.

In order to quantify the asymmetry, the mean values of three distributions were analysed: Measured energy to truth energy ratio, measured momentum to truth momentum ratio and measured E/p ratio (Fig. 3.5, 3.6 and 3.7). The differences on the means between the electron and the positron sample is an indicator for an measurement asymmetry if they are much greater than their uncertainties. "Much greater" is usually defined as a factor of 5 greater. Two different methods of measuring the mean were applied. Firstly, the mean of the overall distribution was analysed. The results are shown in Table 3.1. Secondly, a Gaussian fit was performed around the peak region. Using a fit region of 0.99 to 1.02 for the mean energy resolution and 0.95 to 1.05 for the mean momentum and E/p resolution gave reasonable χ^2 to degrees of freedom ratios of around 1. The analysis of different fit regions and binnings with similar χ^2 to degrees of freedom ratios was

[3] The geometry is referred to as "Rome-Final".

used to determine the systematic uncertainties of the measurements. The results are shown in Table 3.2.

The energy resolution distribution has no significant asymmetry. The overall mean as well as the fitted mean are equal for electrons and positrons within the uncertainties. Furthermore, more detailed studies showed that there is no effect on the binning or the chosen range of the distribution. The momentum resolution asymmetry in the overall mean which is significant in release 11.0.3 vanishes in release 11.0.41. Consequently, for release 11.0.41 also the asymmetry in the overall mean of E/p vanishes. The fitted means in the peak region did not show a significant asymmetry in both releases. Thus, the asymmetry was in the tail of the distribution. This is in accordance with the explanation of the bug given above.

Overall Mean				
Quantity	*Release*	*Mean difference*	*Uncertainty*	$\frac{Mean\ difference}{Uncertainty}$
E^m/E^t	11.0.3	0.0010	0.0007	1.4
	11.0.41	0.0010	0.0007	1.4
P^m/P^t	11.0.3	0.0115	0.0014	8.2
	11.0.41	-0.0024	0.0014	-1.7
E^m/P^m	11.0.3	-0.0190	0.0034	5.6
	11.0.41	0.0020	0.0033	0.6

Tab. 3.1: For three quantities - measured energy to truth energy ratio, measured momentum to truth momentum ratio and measured energy to momentum ratio - the difference between the electron and positron overall means is shown with the corresponding uncertainties. The analysed distributions were generated with release 11.0.3 and 11.0.41.

Gaussian Mean					
Quantity	*Release*	*Mean diff.*	*Uncert. (stat)*	*Uncert. (syst)*	$\frac{Mean\ difference}{Uncertainty}$
E^m/E^t	11.0.3	0.0002	0.0002	0.0001	0.9
	11.0.41	0.0002	0.0002	0.0001	0.9
P^m/P^t	11.0.3	-0.0038	0.0011	0.002	1.7
	11.0.41	-0.0056	0.0011	0.002	2.5
E^m/P^m	11.0.3	0.0055	0.0021	0.003	1.5
	11.0.41	0.0078	0.0020	0.003	2.2

Tab. 3.2: For three quantities - measured energy to truth energy ratio, measured momentum to truth momentum ratio and measured energy to momentum ratio - the difference between the electron and positron means obtained with a Gaussian fit between 0.99 and 1.02 (E^m/E^t) or 0.95 and 1.05 (P^m/P^t, E^m/P^m) is shown with the corresponding uncertainties - statistical and systematic. The systematic uncertainty has been obtained by comparing different fit ranges and binnings within an area of reasonable χ^2 to degrees of freedom ratios. The analysed distributions were generated with release 11.0.3 and 11.0.41.

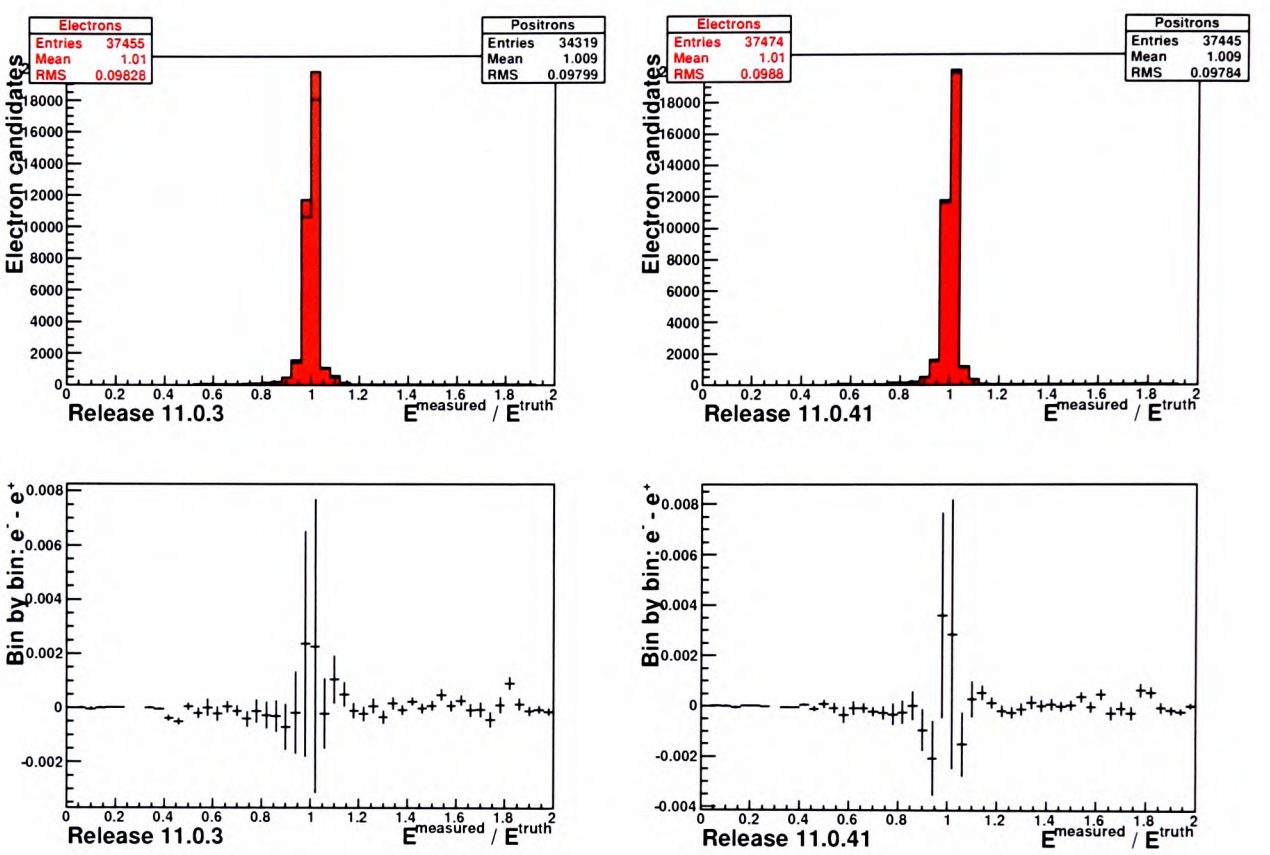


Fig. 3.5: Measured energy to truth energy ratio using Athena release 11.0.3 and 11.0.41. The upper plots show the distributions for electrons (red) and positrons (white) for both releases. The lower plots show the bin by bin difference between the normalised electron and positron distribution. The integral of the lower plots is zero by construction. There is no significant asymmetry.

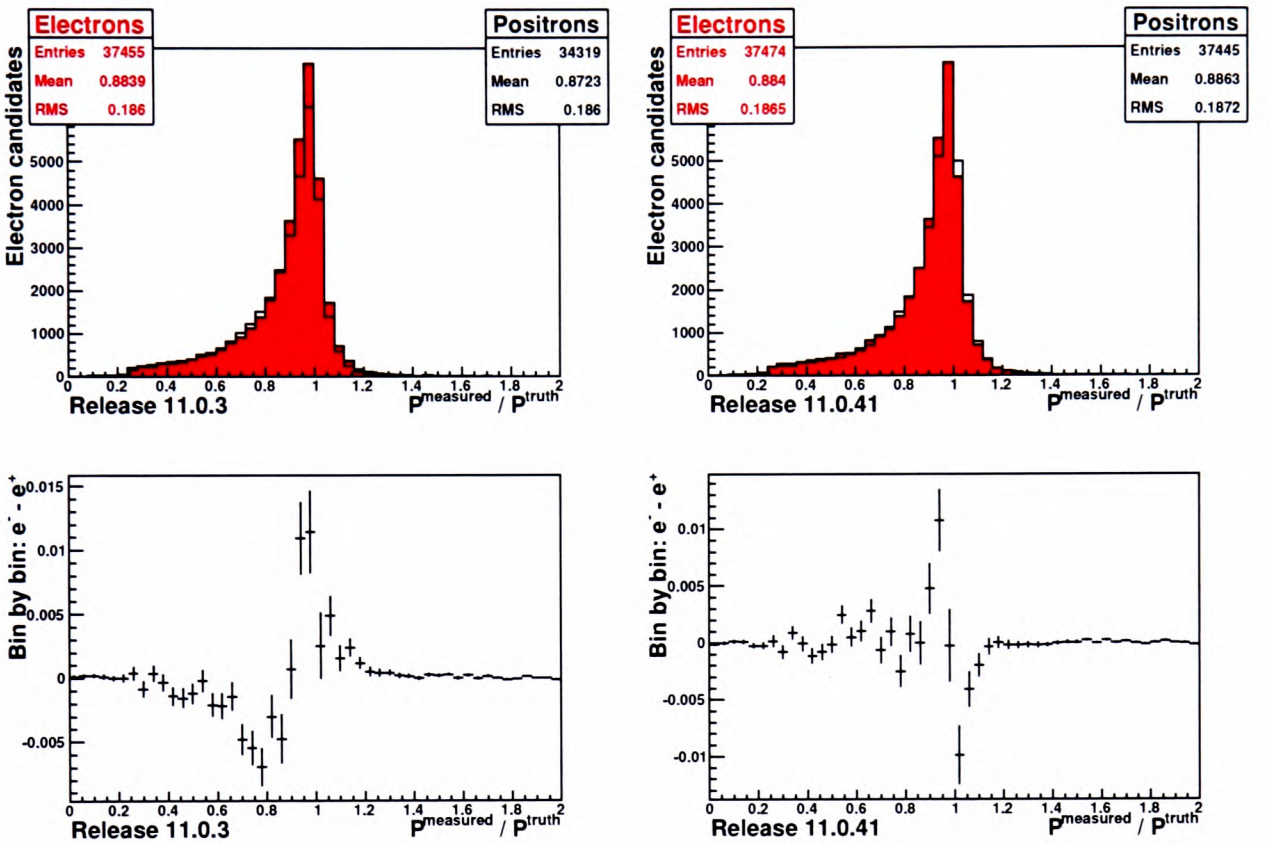


Fig. 3.6: Measured momentum to truth momentum ratio using Athena release 11.0.3 and 11.0.41. The upper plots show the distributions for electrons (red) and positrons (white) for both releases. The lower plots show the bin by bin difference between the normalised electron and positron distribution. The integral of the lower plots is zero by construction. There is a significant asymmetry in the left plot and none in the right one.

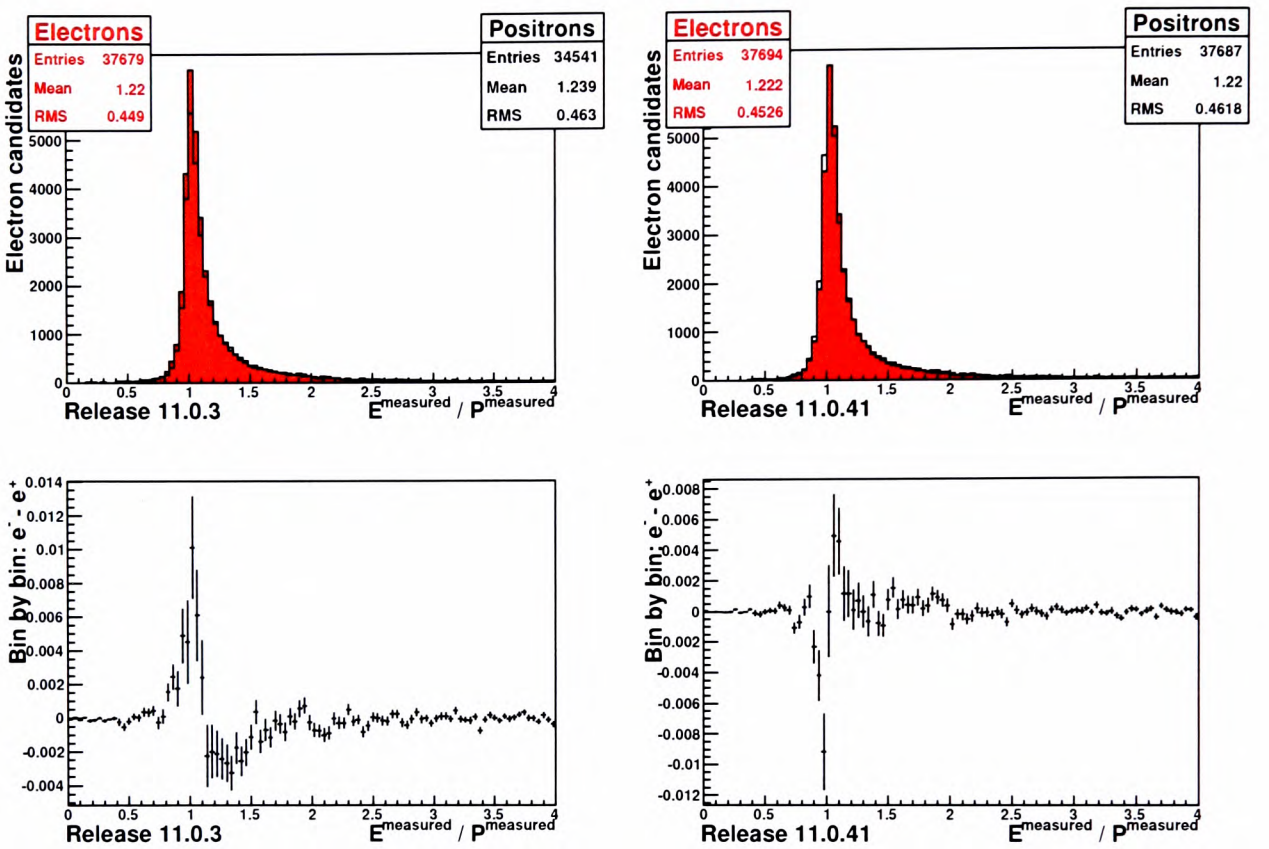


Fig. 3.7: Measured E/p using Athena release 11.0.3 and 11.0.41. The upper plots show the distributions for electrons (red) and positrons (white) for both releases. The lower plots show the bin by bin difference between the normalised electron and positron distribution. The integral of the lower plots is zero by construction. There is a significant asymmetry in the left plot and none in the right one.

4. COMBINED TEST BEAM ALIGNMENT

The ATLAS Combined Test Beam (CTB), which took place at CERN using the H8 beam line, was a test of final prototypes of the detector elements which had similar performances to those installed in the full ATLAS detector. It was meant to represent a slice of the full ATLAS detector at $\phi = 90^o$ and $\eta = 0.0$ containing parts of the Inner Detector, the Calorimeter and the Muon detectors. The data used in this study was taken in October and November 2004 after the installation of the PIXEL and SCT modules. The coordinate system was chosen to be right handed with the x-axis in beam direction and the y-axis vertically towards the sky [48]. The CTB Inner Detector consisted of three sub-detectors: PIXEL, SCT and TRT. The PIXEL detector was made of six modules (Green modules, Fig. 4.1), two in the PIXEL B layer and two each for PIXEL layer 1 and 2. The active surface of each module was $z \times y = 60.8 \times 16.4$ mm^2. There was an overlap of about 2 mm between the two modules in each layer. The SCT detector consisted of four layers with two modules per layer covering each an area of $z \times y = 120.0 \times 60.0$ mm^2 (Red modules, Fig. 4.1). There was a 4 mm overlap between the two modules in each layer. Although the CTB setup approximately represents a slice of the full

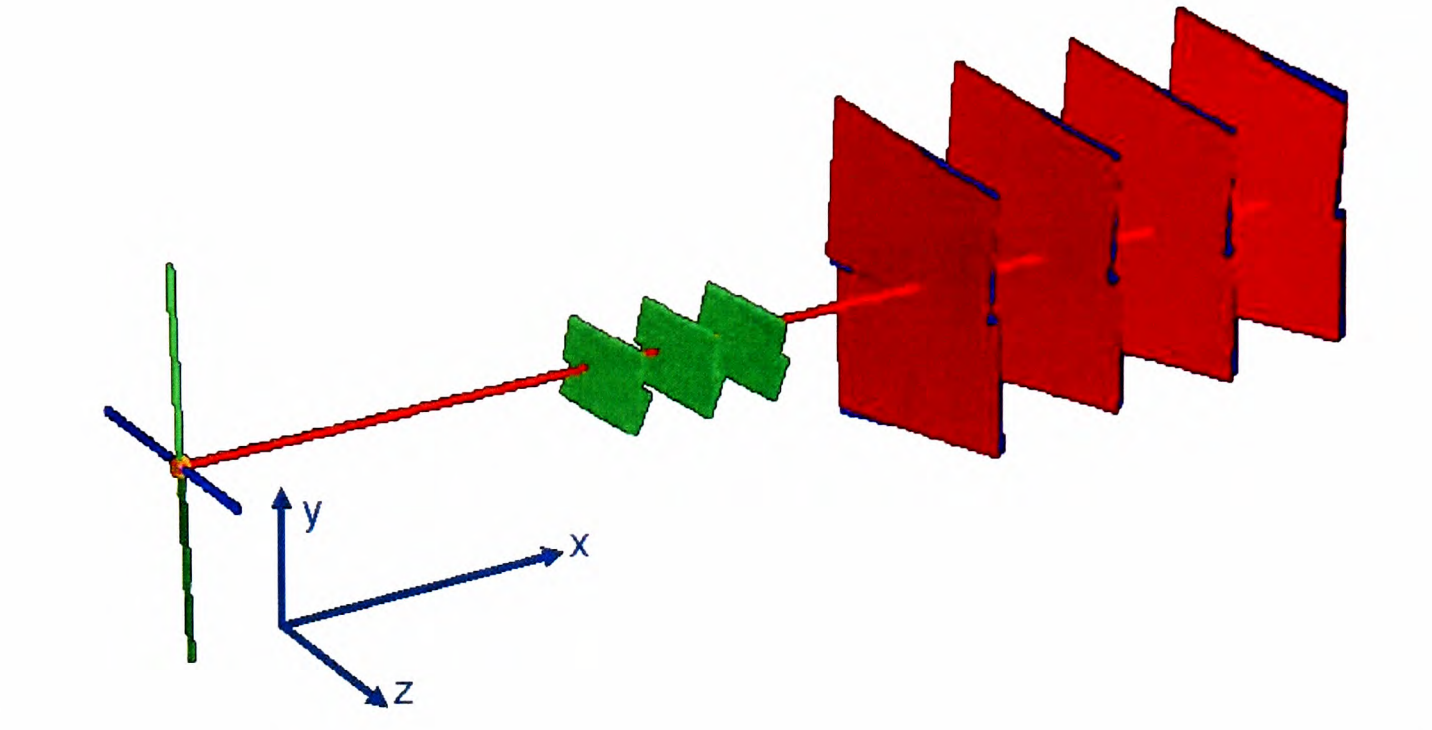


Fig. 4.1: CTB setup for PIXEL (green) and SCT (red).

ATLAS detector, SCT endcap instead of barrel modules were used. During all the CTB runs, the front silicon side of the lower module in the third SCT layer downstream of the beam was not functioning. The initial silicon module positions before the alignment are given in Table 4.1. The TRT setup was made of two barrel wedges. Each barrel wedge was equivalent to 1/16 of the circumference of a cylinder, with inner radius of 558 mm and outer radius of 1080 mm and overall length along the z-axis of 1425.5 mm.

For some of the CTB runs the Inner Detector was exposed to a magnetic field. The MBPS magnet was operated at -850 A corresponding to a 1.4 T magnetic field pointing towards the negative Z direction. The magnetic field was not con-

Nominal CTB Global Module Positions						
Detector Type	*Layer*	*Sector*	*Side*	*X [mm]*	*Y [mm]*	*Z [mm]*
PIXEL	0	0	0	195.986	-7.187	12.295
PIXEL	0	1	0	195.986	7.187	12.295
PIXEL	1	0	0	234.198	-7.308	12.295
PIXEL	1	1	0	234.198	7.308	12.295
PIXEL	2	0	0	268.277	-7.396	12.295
PIXEL	2	1	0	268.277	7.396	12.295
SCT	0	0	0	378.197	25.152	-9.991
SCT	0	0	1	379.163	25.152	-9.991
SCT	0	1	0	383.717	-35.152	-9.991
SCT	0	1	1	384.683	-35.152	-9.991
SCT	1	0	0	449.697	30.152	-9.991
SCT	1	0	1	450.663	30.152	-9.991
SCT	1	1	0	455.217	-30.152	-9.991
SCT	1	1	1	456.183	-30.152	-9.991
SCT	2	0	0	521.697	30.152	-9.991
SCT	2	0	1	522.663	30.152	-9.991
SCT	2	1	0	527.217	-30.152	-9.991
SCT	2	1	1	528.183	-30.152	-9.991
SCT	3	0	0	592.697	35.152	-9.991
SCT	3	0	1	593.663	35.152	-9.991
SCT	3	1	0	598.217	-25.152	-9.991
SCT	3	1	1	599.183	-25.152	-9.991

Tab. 4.1: Nominal CTB geometry in global coordinates. All values are in mm.

stant. However, the track reconstruction software corrected for this effect.

4.1 CTB Data

The main reference CTB data was collected during the period between October and November 2004 when all Inner Detector subsystems were operational. About 22 million events were considered as usable after offline data validation [49]. Four

main parameters were used to distinguish between different runs: Particle type (electrons, pions, muons and photons), energy (2 to 350 GeV), magnetic current (0 and -850 A) and geometry configuration (six different geometry tags, 01, 03, 04, 06, 08 and 09). The CTB beam line instrumentation which was responsible for the trigger, beam position and quality measurements and the particle identification as well as the read-out system are explained in Ref. [50]. Out of about 400 good CTB runs, the eight shown in Table 4.2 are relevant for the analysis presented. They correspond to the geometry setup 04 which was commonly chosen for the alignment. This setup included the PIXEL, SCT and TRT detector. No extra material layer was included. Thus, MCS effects were relatively small. Furthermore, setup 04 corresponds to the last period of running. Therefore, data taking was very stable and a large number of events was recorded.

CTB Runs Geometry 04				
Run Number	*Particle*	*Momentum*	*Magnet*	*Events*
2102355	pion	100 GeV	0A	83995
2102365	pion	100 GeV	-850A	167986
2102399	electron	100 GeV	-850A	231498
2102400	electron	50 GeV	-850A	230983
2102439	electron	20 GeV	-850A	52495
2102442	pion	20 GeV	-850A	91943
2102452	electron	80 GeV	-850A	229636
2102463	electron	180 GeV	-850A	220485

Tab. 4.2: Eight CTB runs which have been used to perform and test the alignment. The calculated alignment constants are valid for at least all those runs.

4.2 CTB Simulation

In order to understand the measurements performed with test beam data, in this case especially to test the quality of the calculated alignment constants, it was necessary to simulate the CTB setup. Initially, the simulation started at the point from where the beam was affected by CTB specific material. A total of 13.2% radiation length was simulated in order to account for effects due to air and the scintillators which were responsible for monitoring and triggering. With increasing tracking precision due to alignment a better description of the actual beam profile was necessary. A more realistic estimate of the beam characteristics was then developed using measurements obtained with test beam data. Also the magnetic field had to be carefully calculated. More details about the simulation can be found in Ref. [2].

4.3 CTB Alignment

The alignment of the CTB [2] had two purposes. Firstly, the precise knowledge of the Inner Detector module positions is necessary for reliable and efficient tracking, and thus affects all other studies. A special CTB alignment software based on residual minimisation had been developed by the IFIC Valencia group [2]. However, this software had problems with magnetic field runs. Furthermore, the calculated alignment constants appeared to be unrealistic. Although these constants did improve the CTB reconstruction, a better calculation of alignment constants

was necessary.

Secondly, CTB data offered the first possibility to test the three different Inner Detector alignment algorithms in a realistic environment. Although the CTB consists of only a few per mill of the full ATLAS detector modules, it was a difficult setup to align. Some of the CTB modules were mounted by hand which introduced much larger misalignments than there are expected for the full ATLAS detector. Furthermore, the narrow beam hit only part of each module which can be seen in Fig. 4.2. This may have introduced a bias in the calculated alignment constants, especially, as edge channels were not yet excluded in the version of the Robust Alignment software which was used for the CTB alignment.

In the following, the procedure of CTB alignment using the RobustAlignAlg is described. Compared to the full ATLAS detector the CTB geometry was very simple. Thus, a straightforward implementation of Eq. 2.26 to 2.28 was used (Eq. 4.4 and 4.5) and additional features were tested. In particular, weights A for overlap residuals and B for residuals were defined which control the influence of each measurement on the alignment corrections in the local X and Y directions. The local X and Y corrections were also weighted with the number of overlap hits $n^{oh}_{X/Y}$ and the number of hits $n^{h}_{X/Y}$, which correspond to applying the factor $1/{\delta s_j}^2$ in Eq. 2.14. The total residual weight $W^{r}_{X/Y}$ and the total overlap residual weight $W^{or}_{X/Y}$ were normalised by $N_{X/Y}$. There is just one overlap for each two modules in a layer. Thus, the overlap residual measurement could only be used for the alignment constant calculations in one sector which has been arbitrarily

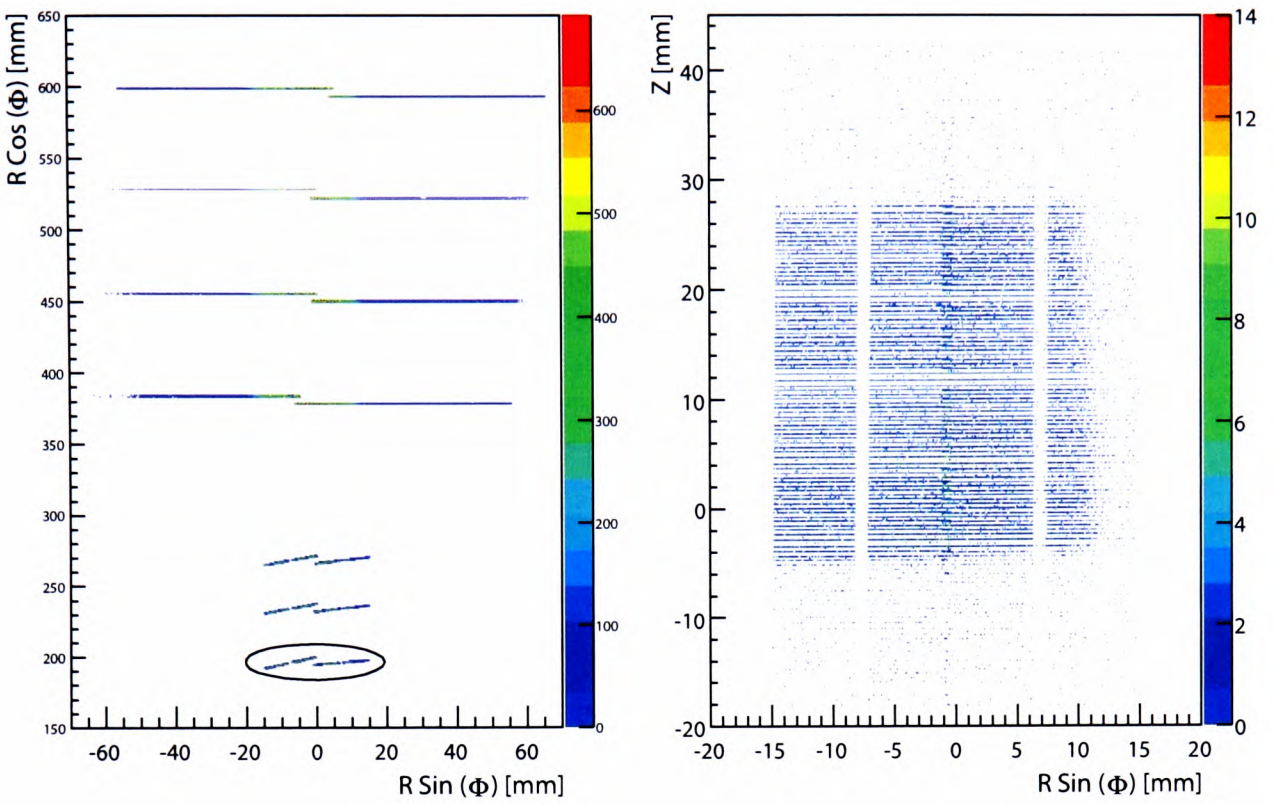


Fig. 4.2: Left: X-Y Projection of the detected CTB beam after alignment with run 2102355 data. Right: First PIXEL layer is shown in the Z-RΦ plane (Ellipse in left plot). The colour shows the number of hits in the given area of the detector.

chosen to be sector 1. The alignment constants $a_{X/Y}$ for modules in sector 1 are given by:

$$a_{X/Y} = -W^{or}_{X/Y} \cdot \overline{ovres}_{X/Y} - W^{r}_{X/Y} \cdot \overline{res}_{X/Y} \tag{4.1}$$

Here, $W^{r}_{X/Y}$ and $W^{or}_{X/Y}$ are the residual and overlap residual weights,

$$W^{r}_{X/Y} = \frac{B \cdot n^{h}_{X/Y}}{N_{X/Y}} \tag{4.2}$$

$$W^{or}_{X/Y} = \frac{A \cdot n^{oh}_{X/Y}}{N_{X/Y}}, \tag{4.3}$$

with the normalisation

$$N_{X/Y} = A \cdot n^{oh}_{X/Y} + B \cdot n^{h}_{X/Y}. \tag{4.4}$$

The alignment constants $a_{X/Y}$ for modules in sector 0 are given by:

$$a_{X/Y} = -\overline{res}_{X/Y} \tag{4.5}$$

With this method, the RobustAlignAlg aligned successfully all 14 CTB modules in the local X and Y direction. The algorithm converged quickly on a stable solution without any alignment specific track selection. It improved the residual distributions significantly as can be seen in Fig. 4.3. The results are comparable with the other three algorithms [2]. None of the major challenges which limited the performance of the RobustAlignAlg during the CTB alignment should affect the alignment of the full detector setup with collision data. The alignment constants are given in Table 4.3 and 4.4.

The reconstruction for the alignment presented was performed in release 11.2.0 together with InDetTBRecExample-00-02-50 and several other packages[1] which contained improvements in the tracking software and the geometry description as well as further developments of the alignment tools. The actual alignment al-

[1] TrkDistributedKalmanFilter-00-00-32, TrkGeometry-00-05-04, TrkDetDescrTools-00-03-04, TrkDetDescrSvc-00-00-06, TrkExInterfaces-00-01-01, TrkExTools-02-13-05, InDetTrackingGeometry-00-06-04, InDetReadoutGeometry-01-30-00, SiRobustAlignTools-00-00-16, InDetAlignGenTools-00-01-09.

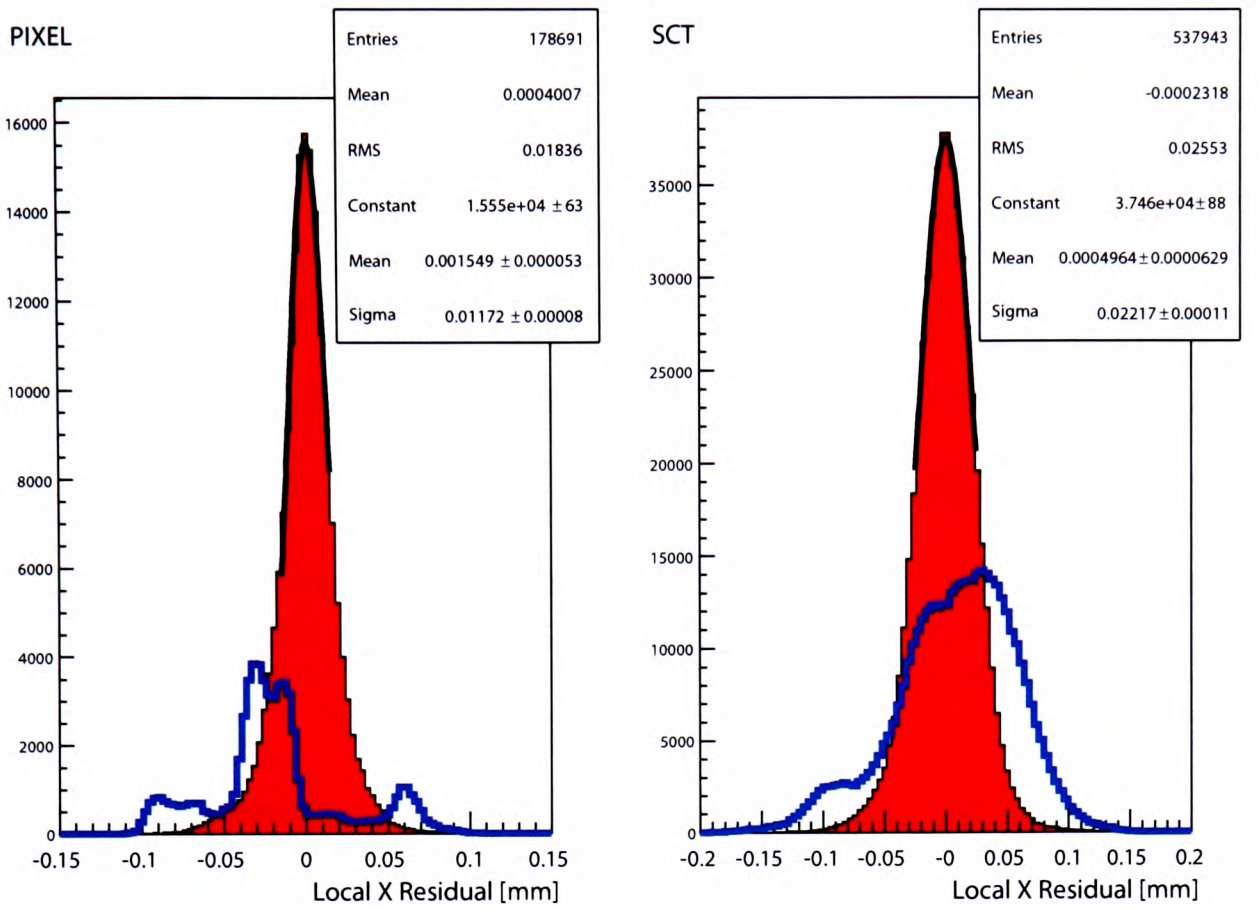


Fig. 4.3: Local X residual distributions for the CTB PIXEL (left) and SCT (right) detectors: Initial alignment (blue) and after Robust Alignment (red with fit) with run 2102355.

gorithm used for the CTB alignment is in SiRobustAlignAlgs-00-00-41. A total of 72 553 events with 100 GeV pions not being exposed to a magnetic field (run 2102355) were reconstructed with the CTBTracking straight line fitter. The CTB alignment was performed with unbiased residuals, thus each hit which was used for the alignment constant calculation had been removed from track fit. Only the central parts of the PIXEL and especially the SCT modules were illuminated in these events. Other runs which used the magnetic field hit other parts of the silicon detector. Although, the alignment was performed only with one run, the final

alignment constants were also valid for all other runs, with or without magnetic field. An example showing the improvement in the momentum measurement of pions after the Robust Alignment is shown in Fig. 4.4. The momentum resolutions, which are shown in Fig. 4.5 for various runs, are up to 50% larger than expected from simulation. Due to bremsstrahlung, the momentum resolution for electrons is slightly larger than for pions. In total, 30 iterations on a single CPU were performed to align the CTB detector elements. However, as can be seen in Fig. 4.6 and 4.7, already after 15 iterations stable results were achieved. As

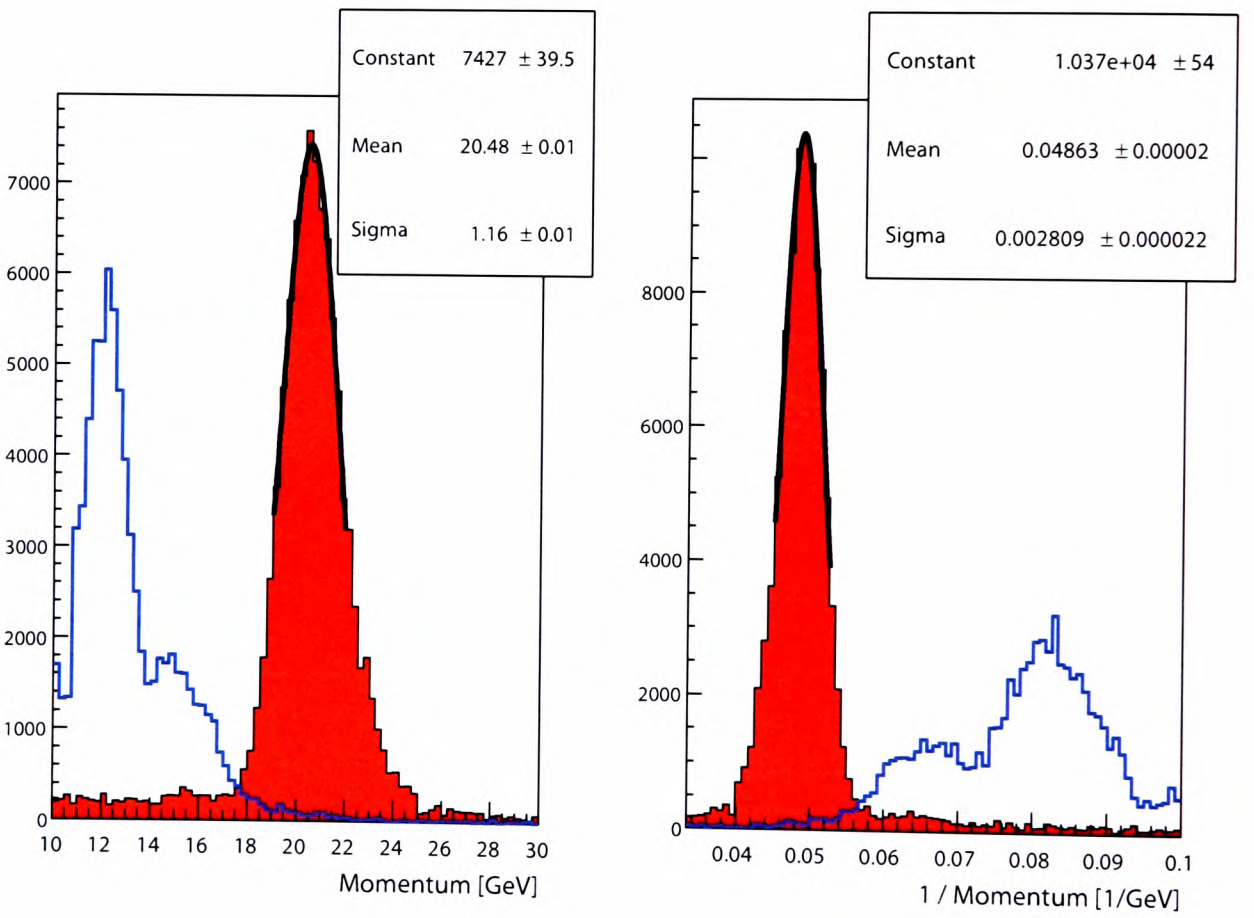


Fig. 4.4: Left: Measured momentum of pions in run 2102442 (20 GeV) before (blue) and after (red with fit) the alignment. Right: Inverse momentum before (blue) and after (red with fit) the alignment. This run was not used for the alignment.

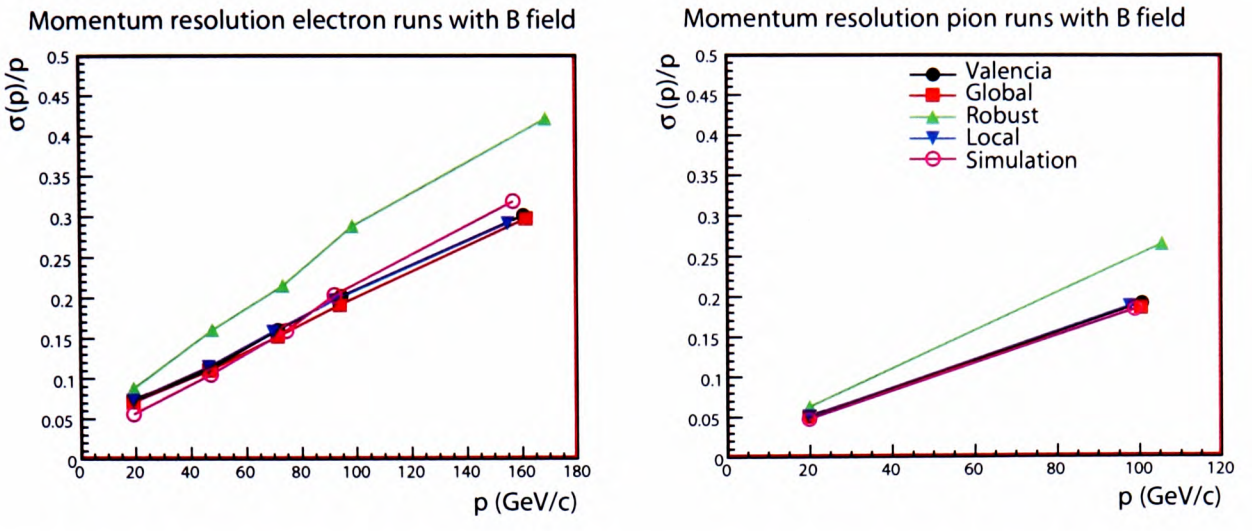


Fig. 4.5: Momentum resolution after alignment for all algorithms for all investigated CTB runs. Left: Runs with electrons. Right: Runs with pions [2].

can be seen in Fig 4.8, after 30 iterations the shifts in the local X direction were of the order of one micron pointing in the same direction. This corresponds to a tiny global shift to which tracking is insensitive. Thus, it can be concluded that the algorithm converged to stable alignment constants. The statistical uncertainty on the module measurement is represented by the error bars in Fig 4.8. It is on average of the order of one micron. As can be seen in Fig. 4.9, the track quality improves significantly already after the first few iterations.

In the CTB run which was used for the alignment, there were about 10 to 50 times more hits than overlap hits depending on the part of the detector and the stage of alignment. Thus, the measurements from residual distributions and overlap residual distributions were weighted such that both types had an almost similar influence[2] on the calculation of the alignment constants. The experience

[2] A equals to 10 and B equals to 1 were used for the final alignment. Other values were tested which, however, only changed the speed of the convergence rather than on the final result itself.

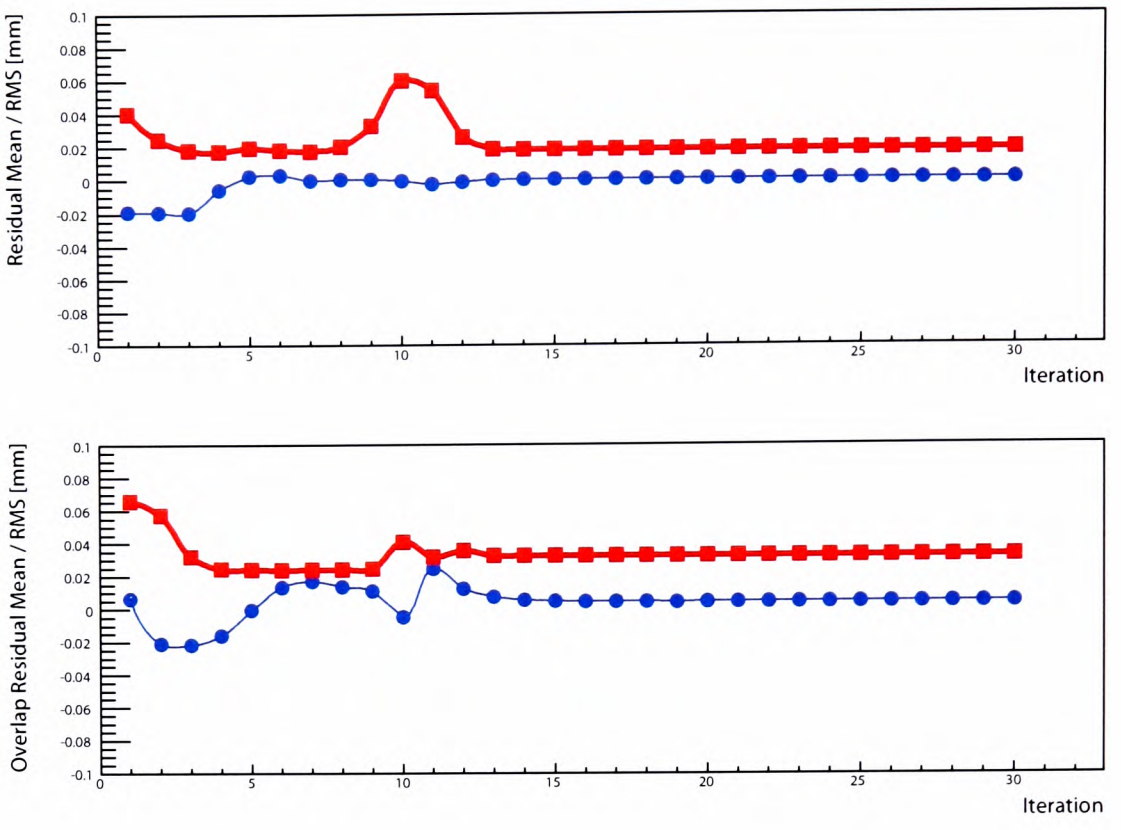


Fig. 4.6: PIXEL detector: Change of mean (blue circles) and RMS (red squares) for local X residuals and overlap residuals as a function of iterations.

from the CTB alignment about combining residuals and overlap residuals led to the more sophisticated algorithm which was used for the alignment of the SR1 and final detector setup.

The final monitoring results presented in this thesis were produced with Athena release 12.0.3. Changes in the offline software between release 11.2.0 and 12.0.3 seemed to affect the alignment slightly. However, time constraints did not allow to redo the alignment with the latter release. Furthermore, there were limitations for the Robust Alignment of the CTB which will not appear with collision data in the full ATLAS detector setup. Firstly, some modules had been mounted by

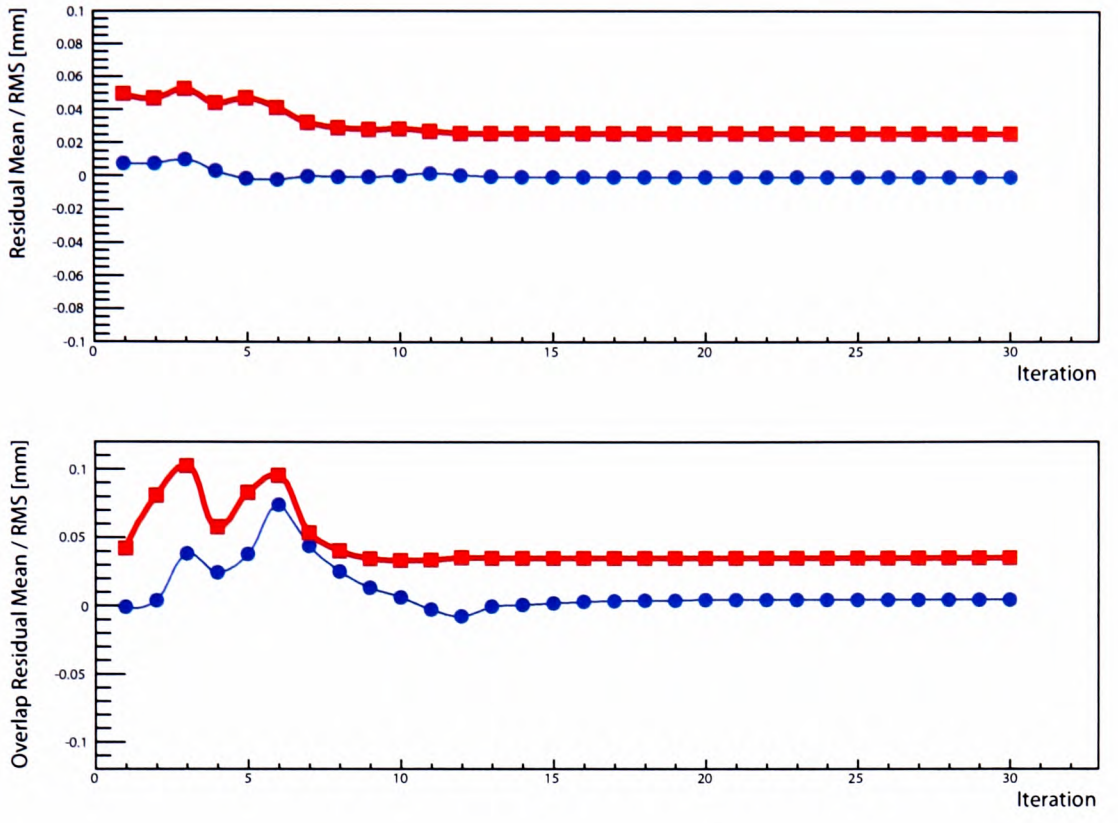


Fig. 4.7: SCT detector: Change of mean (blue circles) and RMS (red squares) for local X residuals and overlap residuals as a function of iterations.

hand. Thus, significant tilts could not have been avoided. In contrast to the other algorithms the RobustAlignAlg does not correct for rotations. Therefore, after alignment there is still a clear linear d_0 dependence on the residuals as can be seen in Fig. 4.10. Studies performed with the Global and the Local χ^2 algorithms showed that, indeed, there were tilts of the order of 10 mrad around the local Y axis. Furthermore, it was shown that this d_0 dependence vanishes if the modules get rotated accordingly [51]. These tilts are the main reason why the residuals achieved by the Robust Alignment are not as small as the ones achieved by the other algorithms (see Fig. 4.11, 4.12, 4.13 and 4.14). The modules with

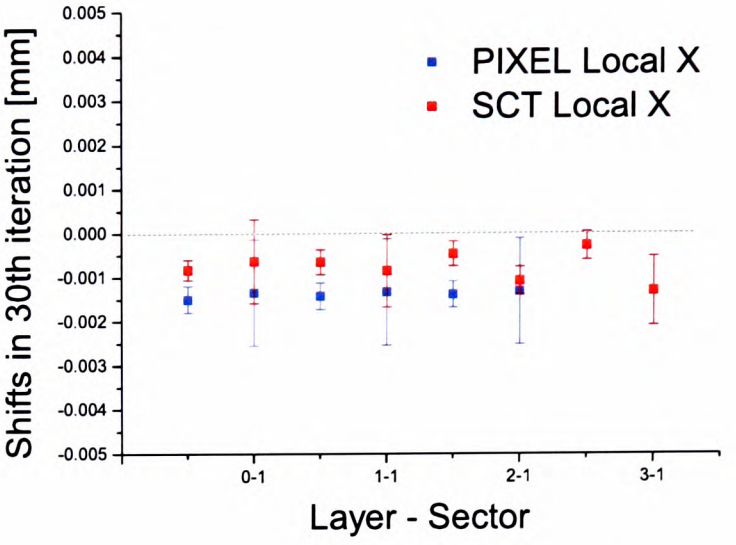


Fig. 4.8: Shifts in the local X direction for the 30^{th} iteration of CTB alignment. The error bars give the statistical uncertainty on that measurement.

the biggest residuals after the Robust Alignment correspond to the modules with the largest rotations. The silicon modules for the final ATLAS detector, however, were mounted on very precise mounting pins which do not allow large displacements. Therefore, much smaller and less significant tilts are expected. Secondly, the PIXEL local Y residuals showed a triple peak structure (Section 4.4) which was an artifact of the CTB setup. This made the mean of the residuals less stable with respect to small shifts. Simulation studies showed that this problem does not exist for the full detector setup. Furthermore, the biases in the means of the residual distributions may be explained by edge-channel effects in the overlap residual calculations. As the algorithm centres both residuals and overlap residuals simultaneously, a bias in the overlap residual distribution introduces an immediate bias

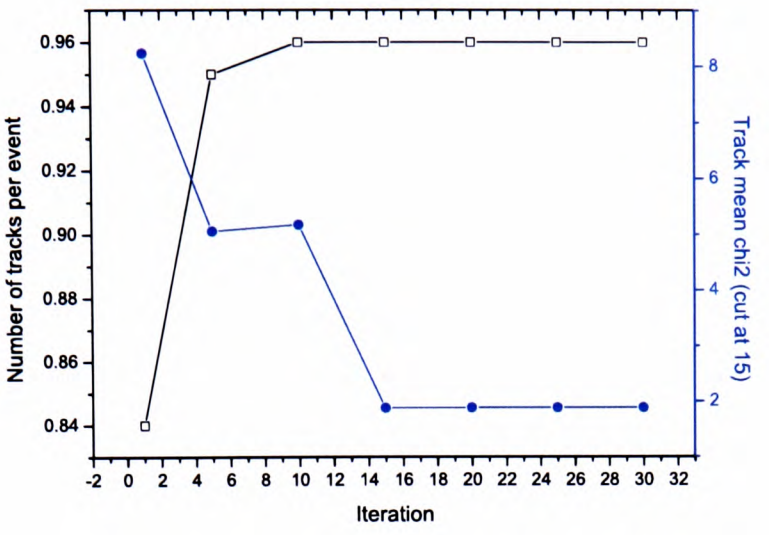


Fig. 4.9: Change in mean track χ^2 over degrees of freedom and reconstruction efficiency as a function of iterations. A minimum track χ^2 of 15 is required in each iteration.

in the residual distribution after alignment. Unfortunately, the Athena releases where edge channels can be removed for the Robust Alignment were not compatible with the releases used for the CTB reconstruction. Therefore, this hypothesis was not tested.

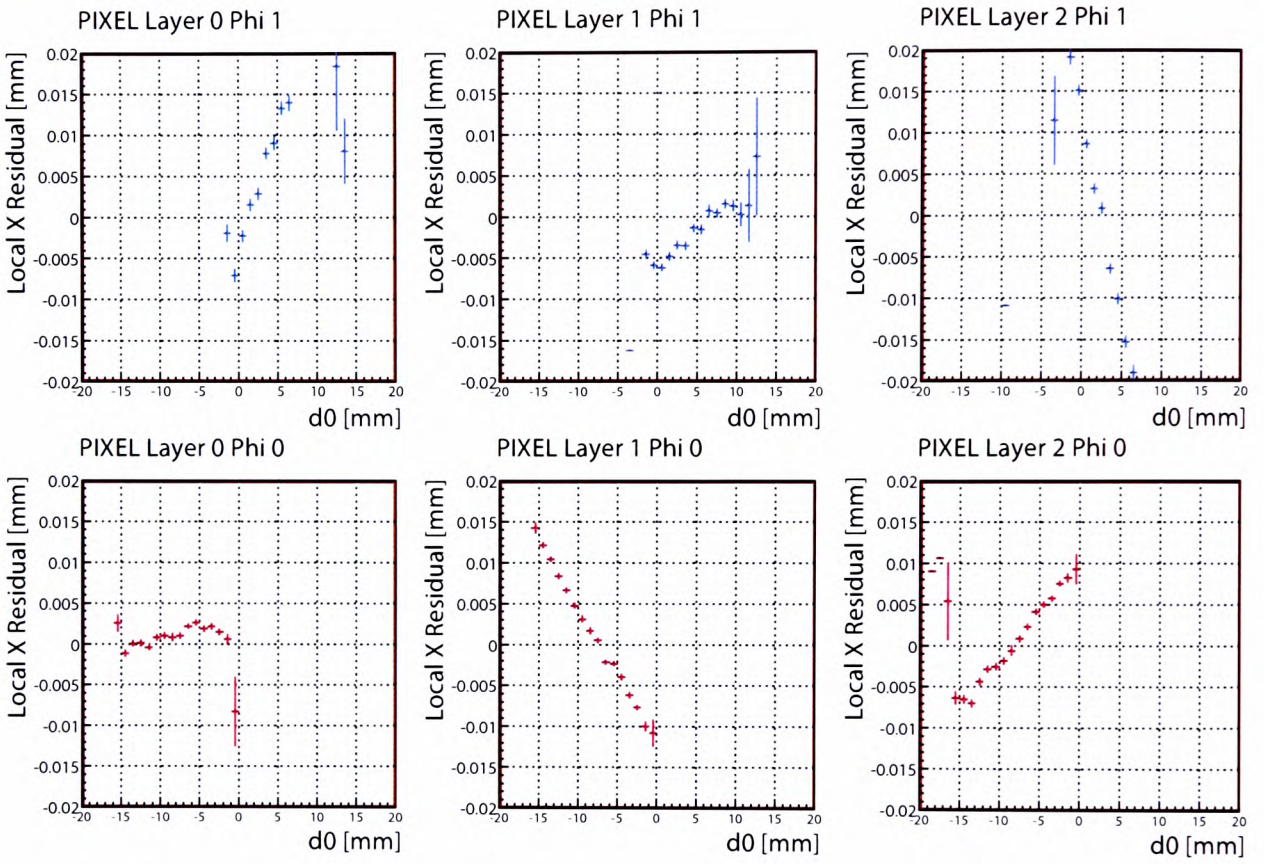


Fig. 4.10: Pixel local X residuals vs. d_0 in run 2102355 after Robust Alignment for each of the six modules [2].

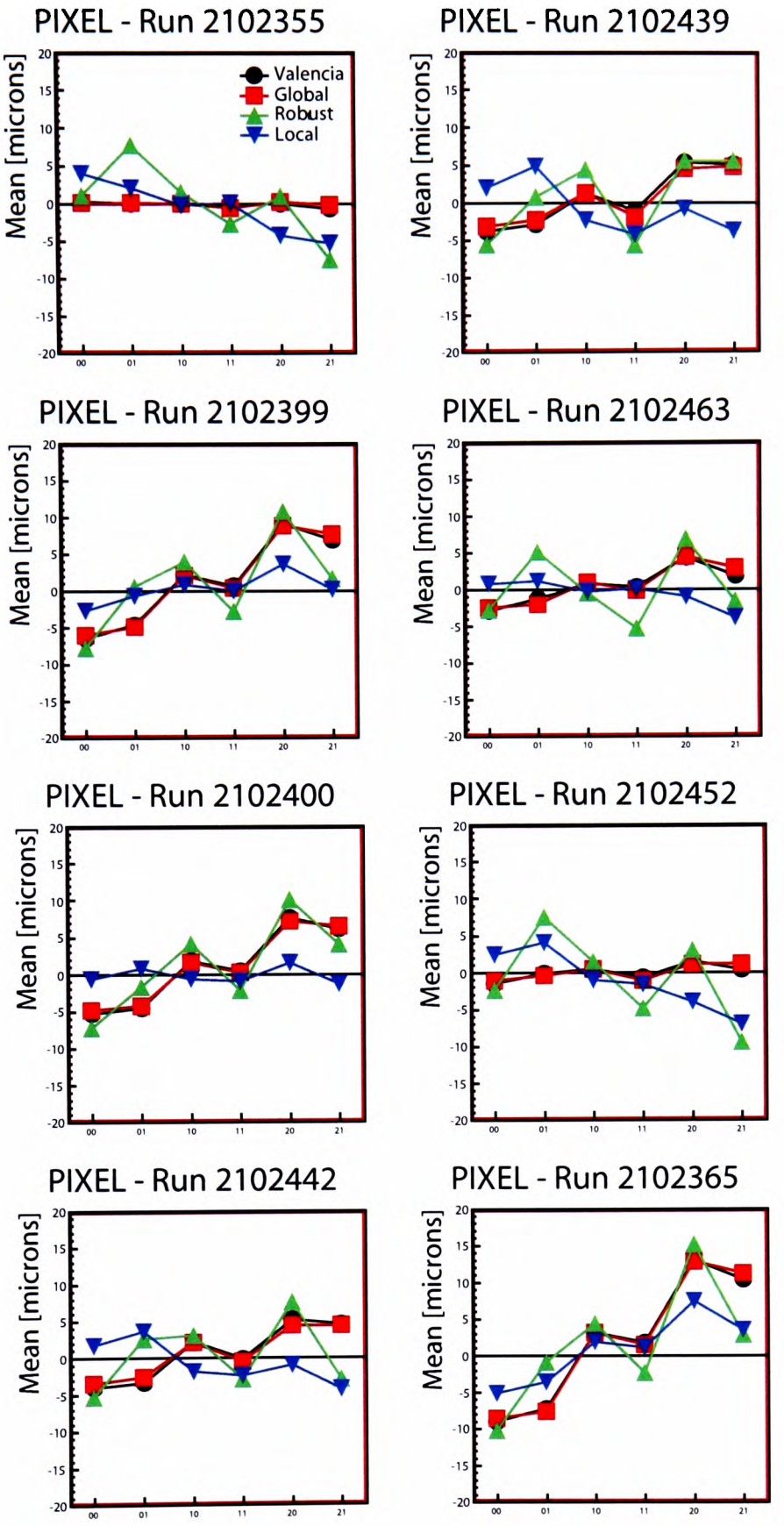


Fig. 4.11: PIXEL mean residuals after alignment for all algorithms for all investigated CTB runs [2]. Module numbering: Layer / Sector.

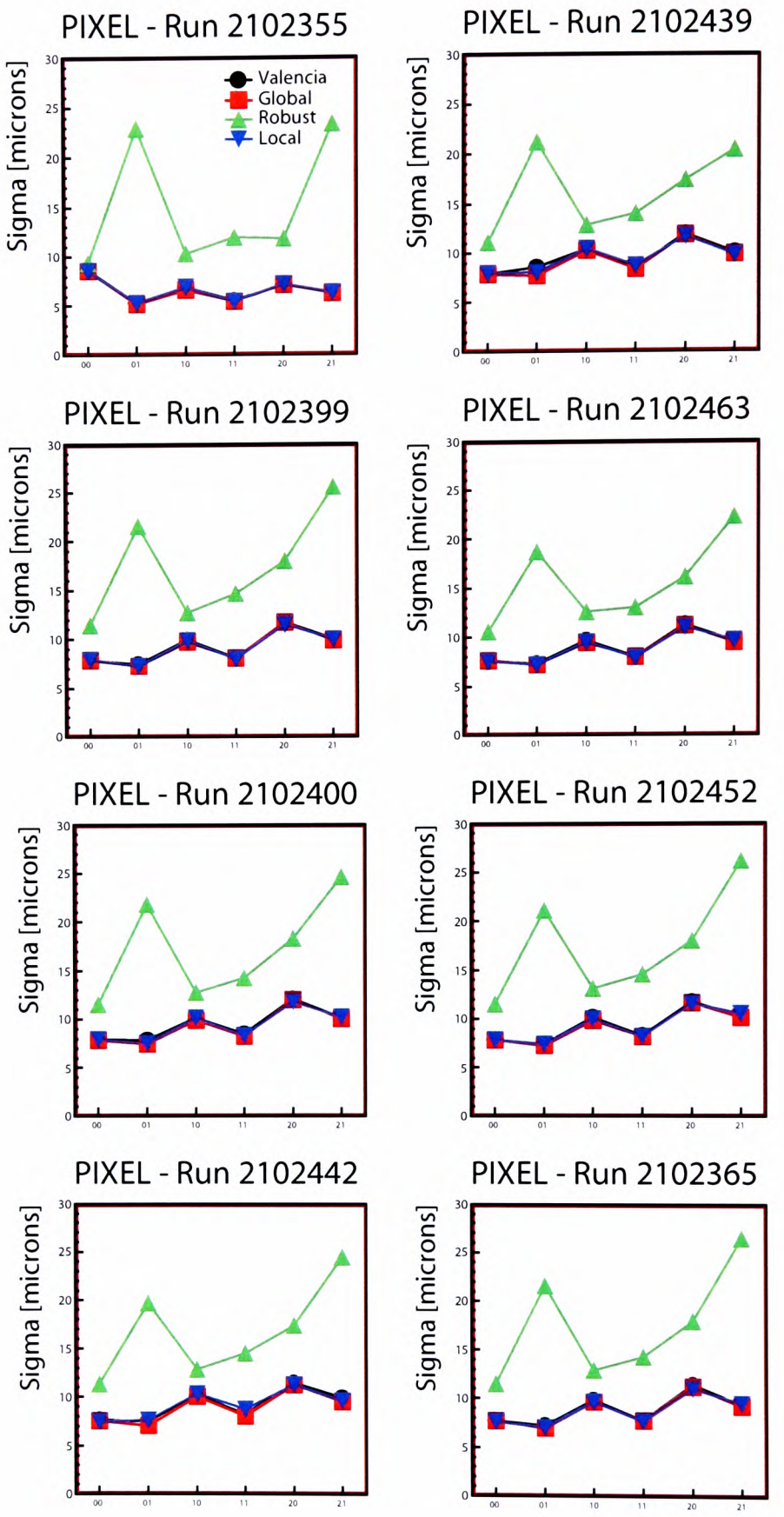


Fig. 4.12: PIXEL residuals sigma after alignment for all algorithms for all investigated CTB runs [2]. Module numbering: Layer / Sector.

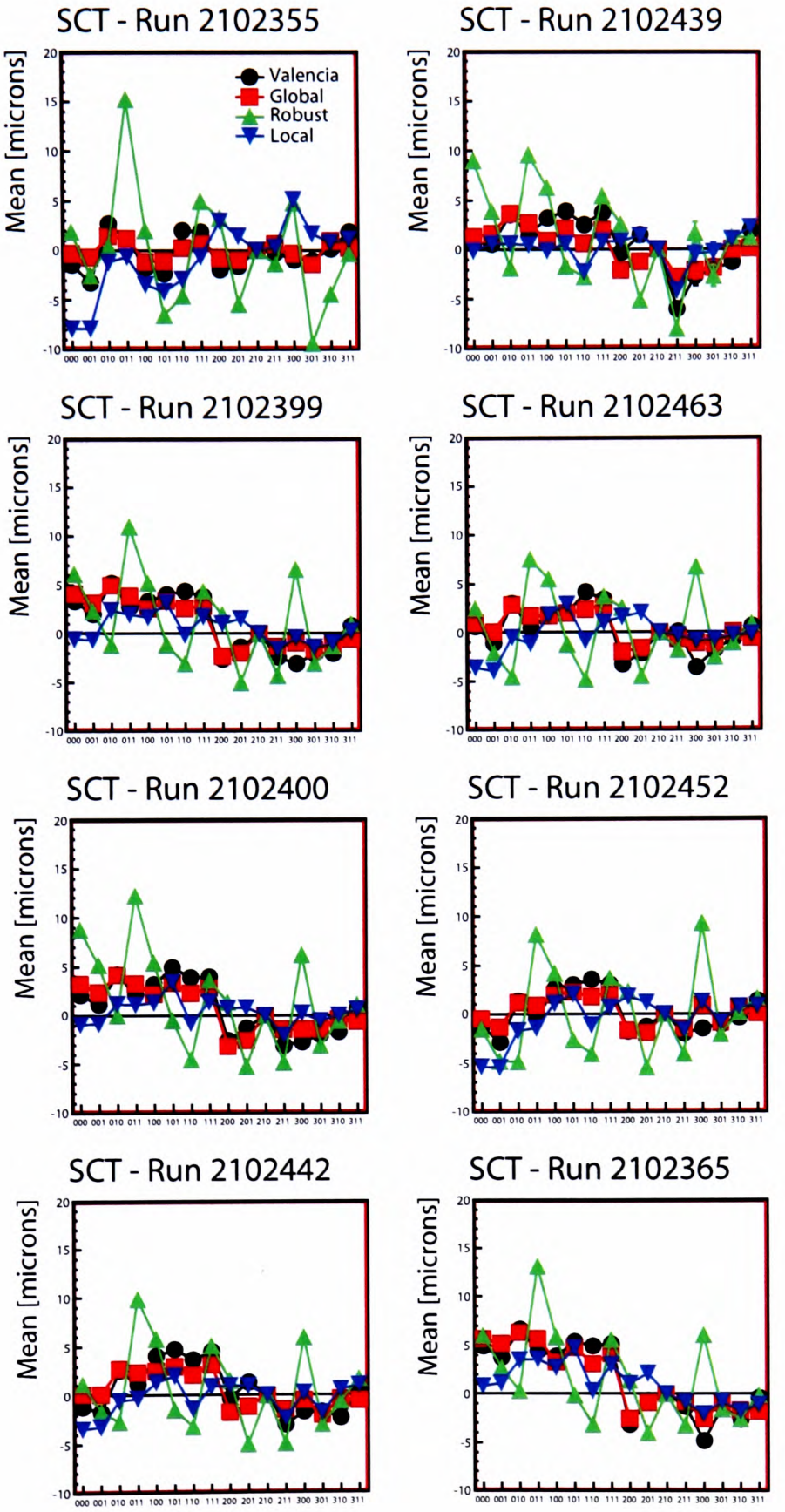


Fig. 4.13: SCT mean residuals after alignment for all algorithms for all investigated CTB runs [2]. Module numbering: Layer / Sector / Side. The wafer 2/1/0 was not functioning.

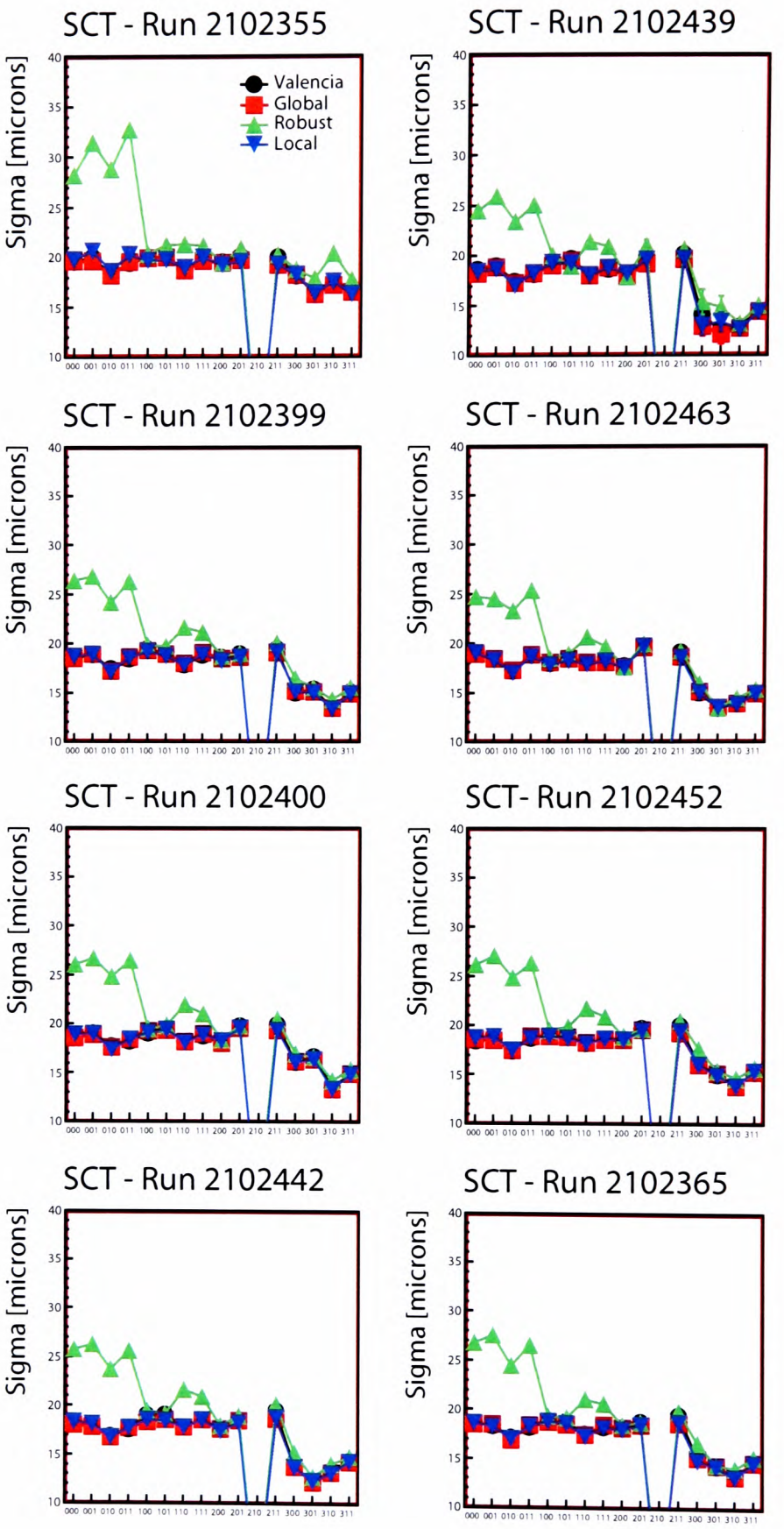


Fig. 4.14: SCT residuals sigma after alignment for all algorithms for all investigated CTB runs [2]. Module numbering: Layer / Sector / Side. The wafer 2/1/0 was not functioning.

CTB Global Module Positions after Alignment						
Detector Type	*Layer*	*Sector*	*Side*	*X [mm]*	*Y [mm]*	*Z [mm]*
PIXEL	0	0	0	195.834	-7.482	12.032
PIXEL	0	1	0	195.948	6.974	11.988
PIXEL	1	0	0	234.207	-7.286	12.344
PIXEL	1	1	0	234.189	7.274	12.246
PIXEL	2	0	0	268.317	-7.295	12.472
PIXEL	2	1	0	268.305	7.500	12.399
SCT	0	0	0	378.197	24.992	-10.295
SCT	0	0	1	379.163	24.992	-10.295
SCT	0	1	0	383.717	-35.330	-9.901
SCT	0	1	1	384.683	-35.330	-9.901
SCT	1	0	0	449.697	30.029	-9.437
SCT	1	0	1	450.663	30.029	-9.437
SCT	1	1	0	455.217	-30.242	-8.933
SCT	1	1	1	456.183	-30.242	-8.933
SCT	2	0	0	521.697	30.074	-8.198
SCT	2	0	1	522.663	30.074	-8.198
SCT	2	1	0	527.217	-30.117	-8.194
SCT	2	1	1	528.183	-30.117	-8.194
SCT	3	0	0	592.697	35.354	-7.481
SCT	3	0	1	593.663	35.354	-7.481
SCT	3	1	0	598.217	-24.931	-6.996
SCT	3	1	1	599.183	-24.931	-6.996

Tab. 4.3: CTB geometry measured with the Robust Alignment in global coordinates. All values are in mm.

CTB Local Module Positions after Alignment					
Detector Type	*Layer*	*Sector*	*X [mm]*	*Y [mm]*	*Z [mm]*
PIXEL	0	0	-0.335	-0.262	0
PIXEL	0	1	-0.219	-0.305	0
PIXEL	1	0	0.021	0.053	0
PIXEL	1	1	-0.039	-0.046	0
PIXEL	2	0	0.106	0.182	0
PIXEL	2	1	0.104	0.110	0
SCT	0	0	-0.174	0.285	0
SCT	0	1	-0.185	-0.095	0
SCT	1	0	-0.102	-0.575	0
SCT	1	1	-0.136	-1.070	0
SCT	2	0	-0.007	-1.816	0
SCT	2	1	-0.041	1.818	0
SCT	3	0	0.302	-2.524	0
SCT	3	1	0.097	-3.026	0

Tab. 4.4: CTB geometry measured with the Robust Alignment in local coordinates. All values are in mm and show the difference to the nominal geometry where all local positions are at zero.

4.4 PIXEL Local Y Residuals

In contrast to the full ATLAS detector, the CTB setup is placed in the beam such that most particles hit the PIXEL detector perpendicularly to the active silicon. Due to the large dimension (400 μm) of each PIXEL in the local Y direction compared to the silicon thickness of 300 μm, the drift of the charge carriers is small in this direction. As a consequence, most of the PIXEL clusters are made of a single PIXEL column. The position of the cluster is then in the middle of the PIXEL which leads to almost discrete residuals. This effect has a significant influence on the alignment and is explained in more detail in Ref. [2].

4.5 Ganged PIXEL Hits

During the alignment of the CTB it was discovered that ganged pixel hits may affect the process significantly. As described in Section 1.2.2, ganged pixels are pixels that are connected to the same readout channel. Due to this connection, information about which pixel actually fired is lost. The CTB implementation of the reconstruction software translates this information into a greater uncertainty on the hit position. In a highly misaligned environment, hits with a large uncertainty on their position reduce the track χ^2 as can be seen in Fig. 4.15. Thus, if there is a limit on the track quality ganged pixel hits are favoured in a misaligned detector. The default CTB tracking which was used for the alignment applied a limit on the ratio of track χ^2 to number of degrees of freedom of 15. With this requirement

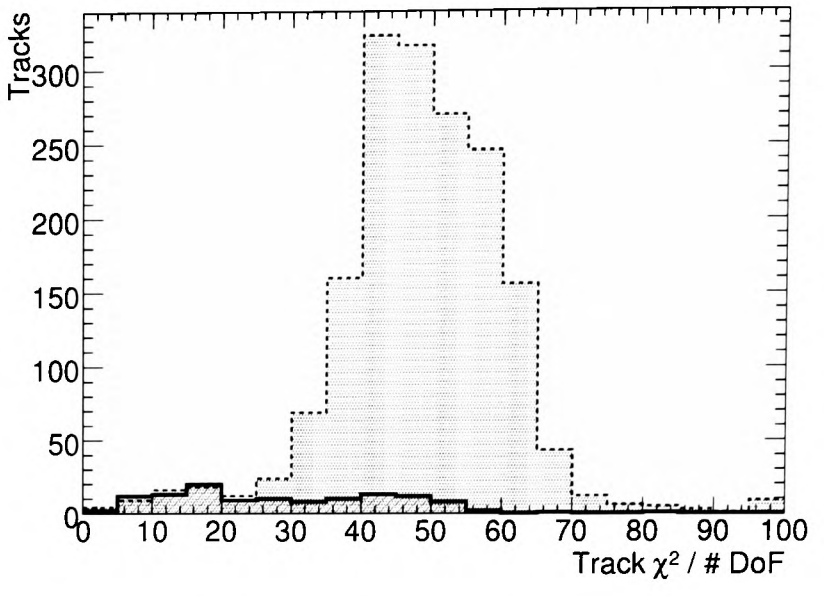


Fig. 4.15: For each track which contains at least one PIXEL hit the track χ^2 / number of DoF's is shown. All tracks which contain at least one ganged PIXEL hit are presented (solid line) and all other tracks (dashed line). The nominal detector geometry has been used. The track quality has been relaxed from 15 to 100. This relaxation increases the number of PIXEL hits per track from 1.1 to 2.2 and the number of SCT hits per track from 7.0 to 7.7.

there were about 50% ganged PIXEL hits and 50% other hits in reconstructed tracks of CTB data, if the detector elements were assumed to be in their nominal position. In order to remove this bias from the alignment constants calculation, ganged PIXEL hits had to be excluded. More detailed studies showed that ganged pixel hits should only be removed from the alignment process if the limit on the track χ^2 has a significant effect on the tracking efficiency. A small ratio of ganged PIXEL hits does not affect the alignment.

4.6 CPU Usage for CTB Alignment

The alignment of the CTB detector elements required 15 to 30 iterations which used 70 to 130 minutes each on a single CPU. With improving alignment, the tracking algorithm spent a decreasing amount of time to reconstruct good tracks. On the other hand the alignment algorithm had to operate with more tracks leading to an increase in CPU time consumption. As can be seen in Fig. 4.16, the RobustAlignAlg's CPU time usage is negligible compared to that of the tracking algorithms. As described in Section 2.5 the RobustAlignAlg offers the possibility of distributed alignment. There was, however, no need to use this option for the alignment of the CTB.

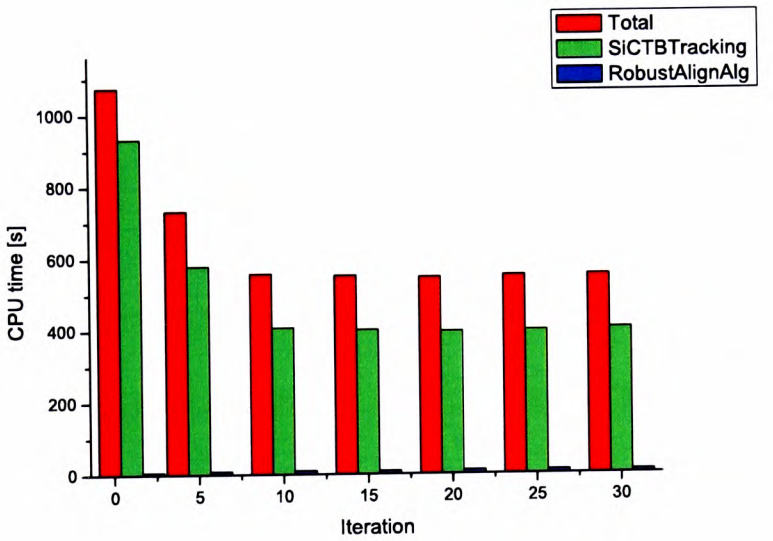


Fig. 4.16: CPU consumption for each iteration in seconds per 10k events: Total (red), SiCTBTracking (green) and RobustAlignAlg (blue).

5. SCT ALIGNMENT WITH SR1 COSMIC RAY DATA

In 2006, tracks from cosmic rays were collected with the SCT barrels and endcap disks in two uncorrelated setups. The statistics for the SCT endcaps runs, however, appeared to be too low for Robust Alignment studies. Therefore, the following chapter only concerns the SCT barrels.

The SCT barrels were designed and built in a collaborative international effort. 2112 SCT barrel modules were produced in different countries before being sent to Oxford for precision assembly. From 2004 to 2005, all SCT modules were mounted onto a carbon fibre support structure using two purpose built robots. During the assembly the robot was measuring the location of the mounting holes in its own frame with a precision of about 40 microns [52]. These 3-dimensional measurements were then converted into the ATLAS coordinate system. However, the systematical uncertainties may have exceeded 100 microns due the fact that the actual position of the robot, which was for example affected by changes in the setup or temperature, was not known [53]. Thus, it was concluded that these measurements should not be used as an input for the SCT alignment. After completion and intensive testing, each of the SCT barrels was shipped to CERN where the fi-

nal assembly took place. In order to measure part of the initial SCT alignment, three photogrammetric surveys were performed which are described in Ref. [54], Ref. [55] and Ref. [56]. Furthermore, part of the SCT was connected to the read out system in order to collect tracks from cosmic rays. This data was used for the SCT barrel alignment. The resulting knowledge about the alignment of the SCT barrel was then compared with the analysis of the photogrammetric surveys.

5.1 Cosmic Muons

The Earth's atmosphere is continuously hit by a flux of protons (90%), α-particles (9%) and electrons (1%). Their energy spectrum spans from a few MeV up to 10^8 GeV. The primary cosmic rays engage in nuclear interactions within the atmosphere and create secondary particles, mostly mesons. These mesons decay in muons, electrons, photons and neutrinos. At sea level mainly muons are detectable as neutrinos hardly interact with matter at all and electrons and photons loose too much energy while traversing through the atmosphere. The mean energy of muons at sea level is about 4 GeV. The energy spectrum is flat below 1 GeV and steepens gradually to reflect the primary spectrum ($\propto E^{-2.7}$) in the 10 to 100 GeV range and asymptotically becomes one power steeper for energies far beyond 1 TeV [25].

5.2 SCT Barrel SR1 Setup

The first test of the SCT barrel with cosmic ray muons was performed on the surface inside the SR1 building at CERN. The whole setup consisted of all four SCT barrels, the TRT and three scintillator layers. The scintillators were used to trigger cosmic ray events and are described in more detail in Section 5.9. Only part of the SCT and TRT (Fig. 5.1) was connected to the read out system. In total 467 SCT modules and 24 TRT modules were used to measure tracks from cosmic rays. A layer of 15cm concrete (Fig. 5.10) prevented muons with a momentum smaller than about 100 to 200 MeV to reach the lower scintillator. The collected data sample contains only tracks which did reach it.

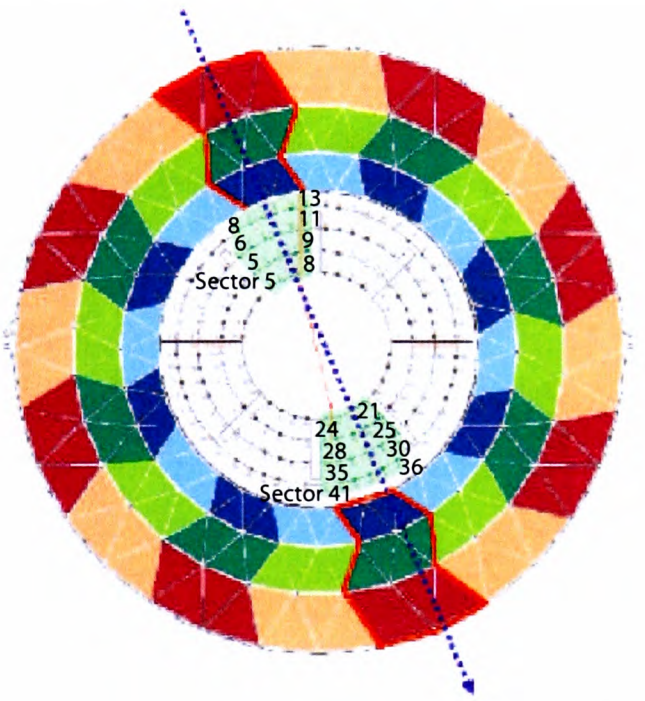


Fig. 5.1: SR1 SCT and TRT setup. The outer three layers show the TRT, the inner four layers the SCT. The marked area around the blue track shows the modules which were active during cosmic ray data taking.

5.3 SCT Barrel Alignment using Cosmic Ray Data

The tracks reconstructed from cosmic data collected in the SR1 building provided the first possibility to align part of the final ATLAS detector. Furthermore, this setup was ideal to test the whole alignment chain as well as to perform detailed analyses in order to understand the performance of the SCT. These tracks were either single muon tracks or multiple particle tracks that arose from showers. Showers were produced through cosmic muons interacting with material near the detector. An example of an event with multiple tracks can be seen in Fig. 5.2. For the alignment, both types of tracks have been used.

The RobustAlignAlg aligned successfully all 467 modules of the SR1 SCT setup in the local X and Y direction. The algorithm converged to a stable solution



Fig. 5.2: Reconstructed track produced during run 2992. White points represent hits in the TRT, yellow points hits in the SCT and red points SCT hits associated with the track. The track fitter assumes the track to be a straight line.

without any alignment specific track selection. The final alignment constants improve the residual and overlap residual distributions (Fig. 5.3) significantly. After alignment, the distributions are much narrower and nicely centered around zero. The layer and side dependence of the residual widths is caused by MCS and also appears in simulated data (see Section 5.5).

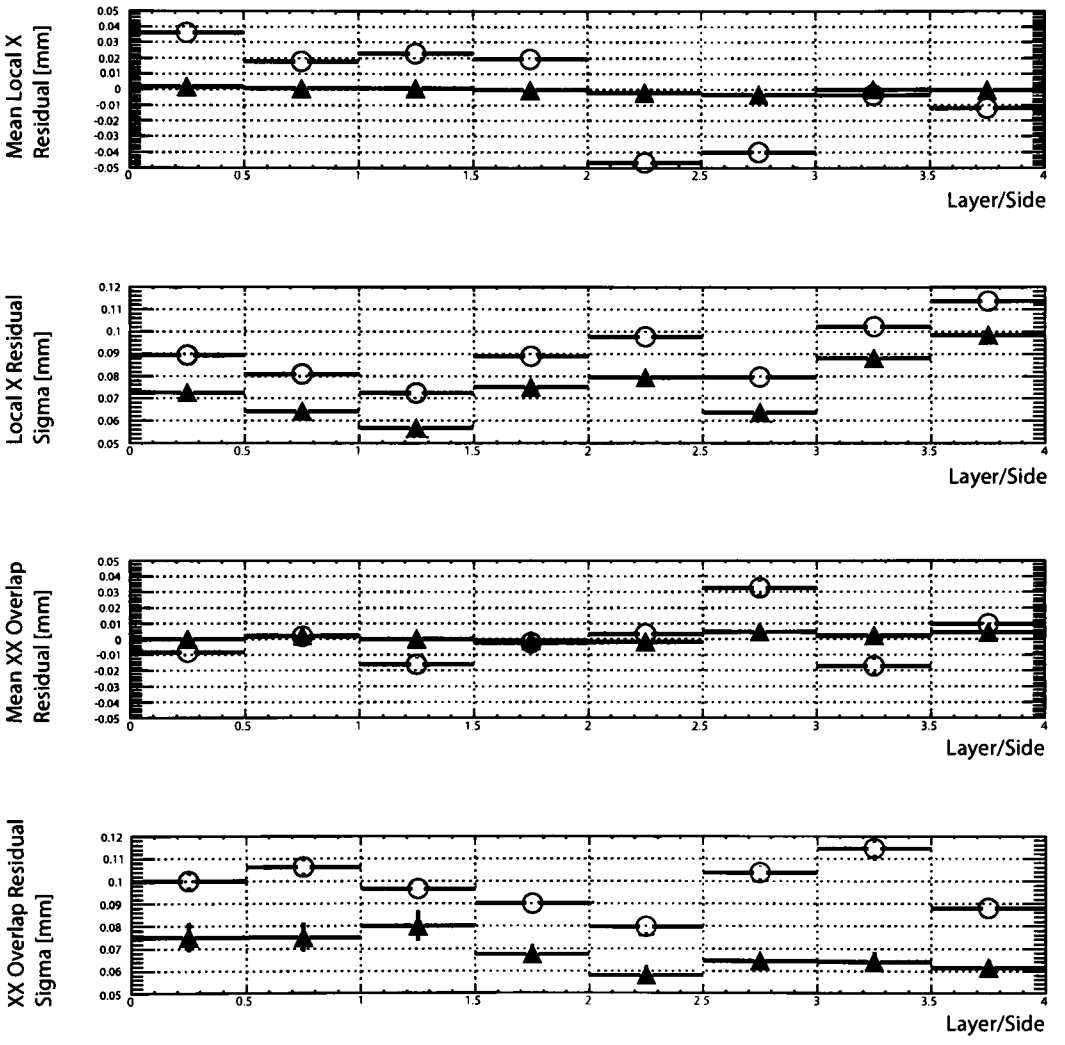


Fig. 5.3: Residuals and overlap residuals (means and widths) for each layer and side before (white circles) and after Robust Alignment (black triangles). Top: Mean SCT local X residuals. Second line: Unbiased SCT local X residual widths. Third line: Mean SCT local X local X overlap residuals. Bottom: Biased SCT local X local X overlap residual widths.

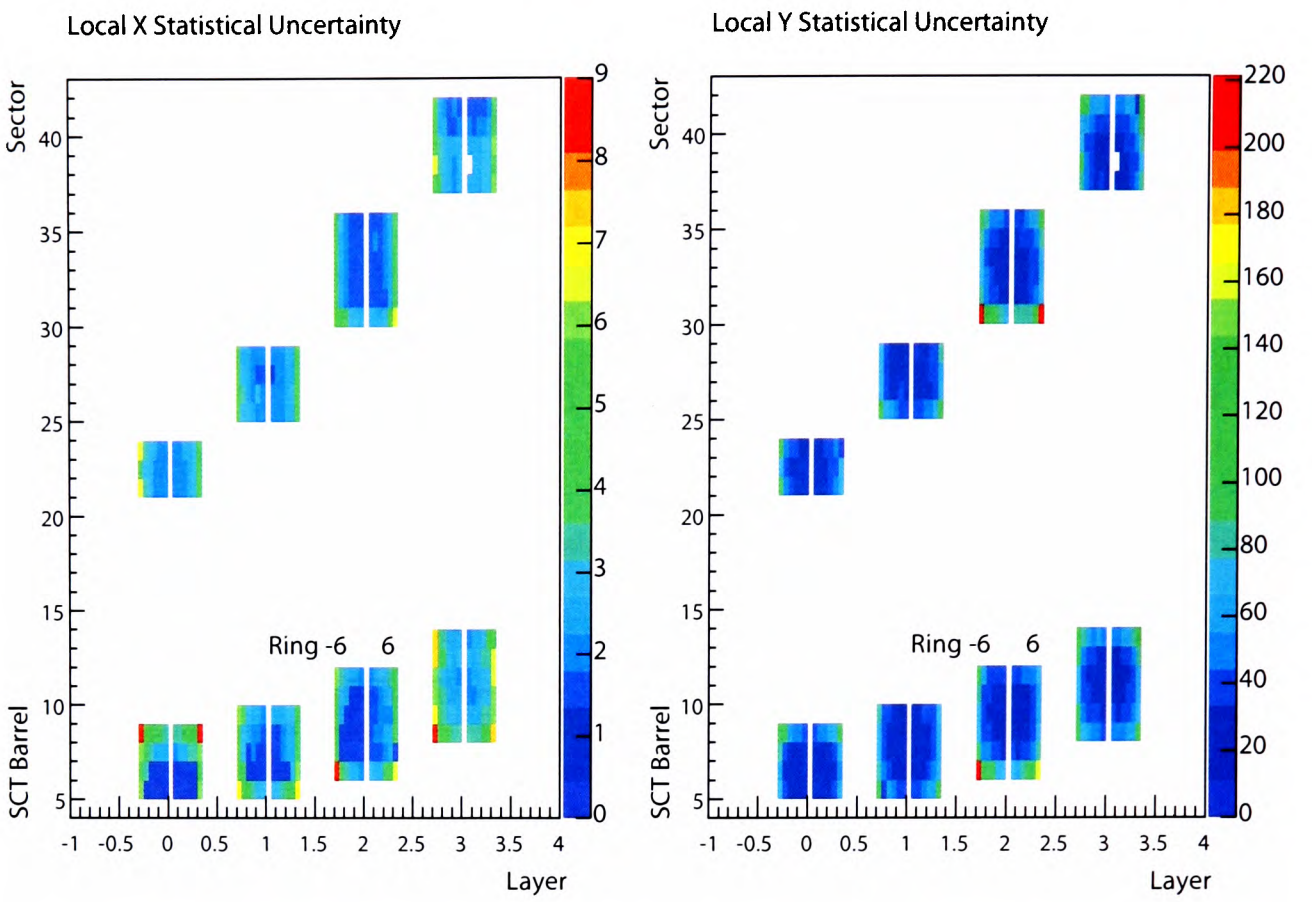


Fig. 5.4: The colours show the statistical uncertainty (in microns) on the alignment constants measurement for the local X (left) and local Y (right) coordinate. "Layer", "Ring" and "Sector" are defined in Table 1.3.

The reconstruction for the alignment presented here was performed in release 12.0.6 together with InDetCosmicRecExample-00-00-87. The actual alignment algorithm used for the SR1 alignment is SiRobustAlignAlgs-00-02-03 together with SiRobustAlignTools-00-00-29. For the alignment presented 200k events collected in 13 runs[1] were used. This dataset is about half of the available sample and is sufficient to produce alignment constants with a statistical uncertainty of mostly

[1] The runs used for the alignment were 2935 (15679 events), 2939 (15127 events), 2986 (7223 events), 2989 (4528 events), 2992 (31897 events), 2996 (21297 events), 2997 (56473 events), 3007 (10045 events), 3013 (16145 events), 3023 (2697 events), 3024 (12764 events), 3026 (3279 events) and 3027 (6623 events). More details about these runs can be found in Appendix D.

1 μm in local X and about 40 μm in local Y as can be seen in Fig. 5.4. The final alignment constants were produced with biased residuals. However, tests showed that performing alignment with unbiased residuals produces alignment constants of similar quality.

Due to the design of the SCT, misalignments in the local X direction also affect residuals in the local Y direction. In order to give the alignment of the precise coordinate more weight at the beginning, the first fourty iterations were performed applying shifts which were reduced by a factor of 2 for the local X direction and 10 for the local Y direction[2]. This leads to a smooth initial alignment when corrections are relatively large. A requirement on the minimum hits per module of 50 was applied in order to align all modules. Already the first 10 iterations lead to quite stable alignment constants. In the 10^{th} iteration, modules were shifted only by less than 10 μm in the precise direction (Fig. 5.5). The final thirty iterations were performed with no damping factor, neither for local X nor for local Y, and a requirement on the minimum hits per module of 1000. This excluded a few modules at the limit of acceptance. The alignment algorithm converged (See Section 2.3) after a total of 68 iterations. Thus, the last few iterations did not shift any module. Repeated problems with data access to the CERN data storage system appeared during the alignment process. Therefore, some of the iterations were performed with less than 200k events. This lead to statistical fluctuations in the alignment constant calculation. Thus, it is very likely that the alignment

[2] Other values only affect the speed of convergence

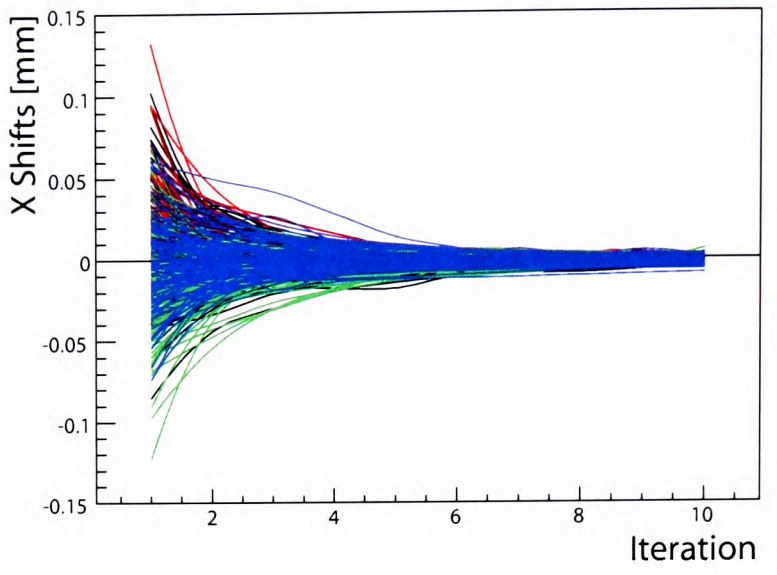


Fig. 5.5: For the first 10 iterations the shifts in the local X direction are shown: layer 0 (black), layer 1 (red), layer 2 (green) and layer 3 (blue).

would have converged within less iterations in a more stable environment. Also, the second part of the alignment procedure could have been performed already at an earlier stage in order to save time.

The alignment with SR1 data was performed with distributed alignment. In each iteration 10 independent computers reconstructed 20k events each and produced files with alignment information. In a second step these files were merged and alignment constants calculated. Each iteration used about 30 minutes of computing time. Neglecting the waiting time for the CERN batch system an overall integrated time of about 34 hours was used for the alignment. However, already after 5 hours good alignment constants were produced. The final 50 iterations which lead to full convergence only improved the residual widths by a few microns.

5.4 Residual Bias in SR1 Data

In the SR1 cosmic ray data, a negative bias of a few microns in the side 0 local X residuals and a positive bias of a few microns in the side 1 local X residuals was discovered. This lead to a global shift in the local Y residual distribution which is equivalent to a global displacement of the whole detector. In principle, tracking should be invariant under systematic global transformations. This effect was not seen in the simulated data sample and it may be explained with systematic misalignments in the local X direction.

As can be seen in Section 5.7, the SCT layers 0 and 2 appear[3] to be rotated in the negative ϕ-direction around the beam-pipe w.r.t. to layer 1 and 3. The fit of a straight line through these layers minimises the sum of distances to the individual strips. In the 2-dimensional projection of the detector onto a plane perpendicular to the beam pipe (as in Fig. 5.2), it is clear that the systematic barrel rotations lead to a positive bias in the residuals of the ϕ-wafers (see Section 1.2.2) in layer 0 and 2, and a negative bias in the residuals of the ϕ-wafers in layer 1 and 3. The geometry of the stereo-wafers, however, allows the residuals in these detector elements to be further optimised by shifting the track along the global Z direction. The biases in the ϕ-wafers are equivalent to the negative residual bias in side 0 and the positive bias in side 1 wafers. In fact, it was further shown that already the alignment in the local X direction partly resolves the observed residual shift.

[3] It is either a real rotation or an apparent rotation caused by a systematic bias in the track reconstruction.

In Fig. 5.6, it can be seen that after Robust Alignment, the mean of the local Y residual distribution is consistent with zero.

Although, the width of the local Y residual distribution improved significantly during the alignment process, it appeared to be much wider than expected. However,

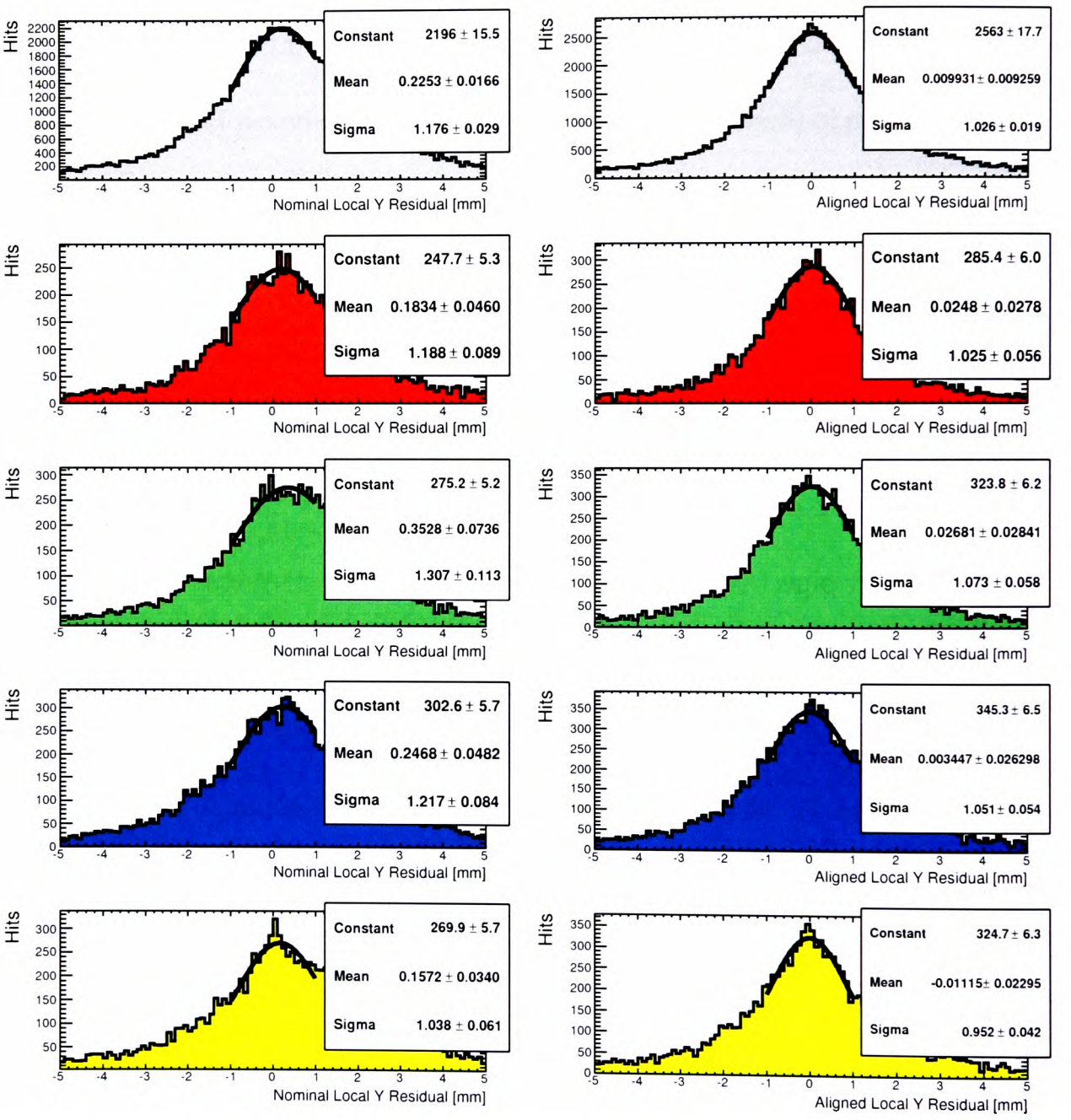


Fig. 5.6: SCT local Y residuals before (left) and after (right) alignment. All barrels together (grey with fit) and the individual layers are shown: layer 0 (red), layer 1 (green), layer 2 (blue) and layer 3 (yellow).

studies have shown that the particular structure of the SCT leads to an amplification of multiple scattering effects by a factor of about 14 compared to PIXEL-like detectors (see Section 3.2).

5.5 Effect of MCS on SR1 Local X Residuals

As can be seen in Fig. 5.3 and 5.7, the magnitudes of the SR1 local X residual widths depend on the layer and the side number of the SCT modules. Both effects are caused by MCS.

The dependence of the residual widths on the layer number can be explained by a simple 2-dimensional model. A cosmic ray that traverses through the SCT causes signals in the upper and the lower part of the detector. In the 2-dimensional projection of the detector onto a plane perpendicular to the beam pipe (see Fig. 5.2), these hits can be described as points. Due to MCS, these points are spread out rather than being located on a straight line. The track fitter reconstructs the track by minimising the distances, i.e. residuals, of a straight line to all of these points. The hits in the upper and the lower part of the detector are separated from each other. Therefore, the track fit can be considered as a fit of a straight line to two separated clouds of points. The track which corresponds to the solution with the minimal sum of residuals goes through the centre of both clouds. Hence, the residuals are the smallest in these centres which correspond to layer 1 and 2. Therefore, on average the residuals in layer 1 and 2 are smaller than in layer 0 and 3.

The dependence of the residuals on the side number can be understood with a 3-dimensional model which describes four layers of the SCT. One module in each of the layers are enough for this purpose. It is important to recall the special design of the SCT as it is described in Section 1.2.2 and that the actual flight path of the cosmic ray muon is not a straight line, but is changed from layer to layer due to MCS. For simplicity it is assumed that the fitted track is perpendicular to the module planes. The track fitter, fitting a straight line, minimises the distances to the hits in the ϕ- and stereo-wafers. If misalignments are neglected, biased local X residuals in the ϕ-wafers directly reflect the magnitude of MCS in that direction. The residuals in the stereo-wafers, however, can be further minimised by shifting the track along the local Y direction. Therefore, biased residuals are generally smaller in stereo- than in ϕ-wafers. Unbiasing residuals reverses the effect. Removing a hit on a ϕ-wafer from the track fit does not change the position of the track significantly. However, removing a hit on a stereo-wafer from the track fit gives the stereo-wafer in the next-but-one layer a large weight on the determination of the track position in the local Y direction. Therefore, the track may be significantly shifted away from its actual position along the local Y direction, leading to a large hit residual for the hit that was removed. Therefore, unbiased residuals are larger in stereo-wafers than in ϕ-wafers.

5.6 Comparison with other Alignment Algorithms

The SCT barrel alignment constants calculated by the Robust Alignment and the other two algorithms give a first hint about the magnitude of the real SCT misalignments. In order to get comparable alignment constants, all analysed sets were transformed into a common coordinate system. Thus, a global translation and rotation was applied to the SCT barrel detector in order to minimise the differences between the three alignment constants sets. As can be seen in Table 5.1, the magnitude of the shifts in the local X direction is on average of the order 100 μm. This value is in accordance with the expectations from the build tolerances. The Robust Alignment algorithm systematically obtains smaller shifts in the local X direction than the other two algorithms. However, the Robust Alignment constants for the local Y direction appear to be generally larger. Module rotations may transform a local X shift partly into a local Y shift. In contrast to the other algorithms, the Robust Alignment does not rotate modules. Thus, the results from the three algorithms may be consistent in the overall magnitude of the shifts. The local Y alignment constants are on average of the order 600 μm. This is much larger than expected. As the statistical uncertainties on these measurements are mostly of the order of 40 μm, the origin for these large shifts is not quite understood. Indeed, it may be that the actual misalignments are that large. However, it is also possible that the large displacements are due to systematic module movements along the global Z direction away from the centre of the detector. Track based alignment

Alignment Constants - RMS [μm] / Mean [μm]						
SCT Layer / Shift	*Robust Alignment*		*Local* χ^2		*Global* χ^2	
	RMS	Mean	RMS	Mean	RMS	Mean
0 / Local X	70	19	97	-23	135	20
1 / Local X	62	-6	84	-44	141	18
2 / Local X	65	73	95	20	128	48
3 / Local X	78	35	95	-21	142	44
0 / Local Y	639	117	559	74	418	90
1 / Local Y	713	69	505	84	450	126
2 / Local Y	743	-138	673	-94	568	-26
3 / Local Y	888	19	687	58	698	100

Tab. 5.1: Means and widths of the Local X and Y SR1 alignment constant distributions for the four SCT detector layers after removing global translations and rotations.

algorithms are not sensitive to all such global distortions and may actually converge on them. Furthermore, if the systematic barrel rotations are different along the global Z direction, the effect described in Section 5.4 may introduce module movements which are equivalent to telescope modes. Indeed, all the sets of alignment constants determined by the three algorithms showed partly telescope-like deformations.

As can be seen in Fig. 5.7 the Robust Alignment produces slightly wider residuals than the other algorithms. However, the overall efficiency[4] (Fig. 5.8) is similar and the residuals are more centered (Fig. 5.7). This result is in accordance with the basic principles of the algorithms. The Robust Alignment centres

[4] The efficiency is defined as the ratio between the numbers of observed and expected hits. For a track, the number of expected hits in each layer or disk is calculated after removing hits, if present, from the detector element, refitting the track with quality requirements and extrapolating the refitted track to the respective element. If the intersection point is within the fiducial area of the module and less than 2.0 mm away from the bond gap a hit is expected.

residuals whereas the other algorithms minimise them.

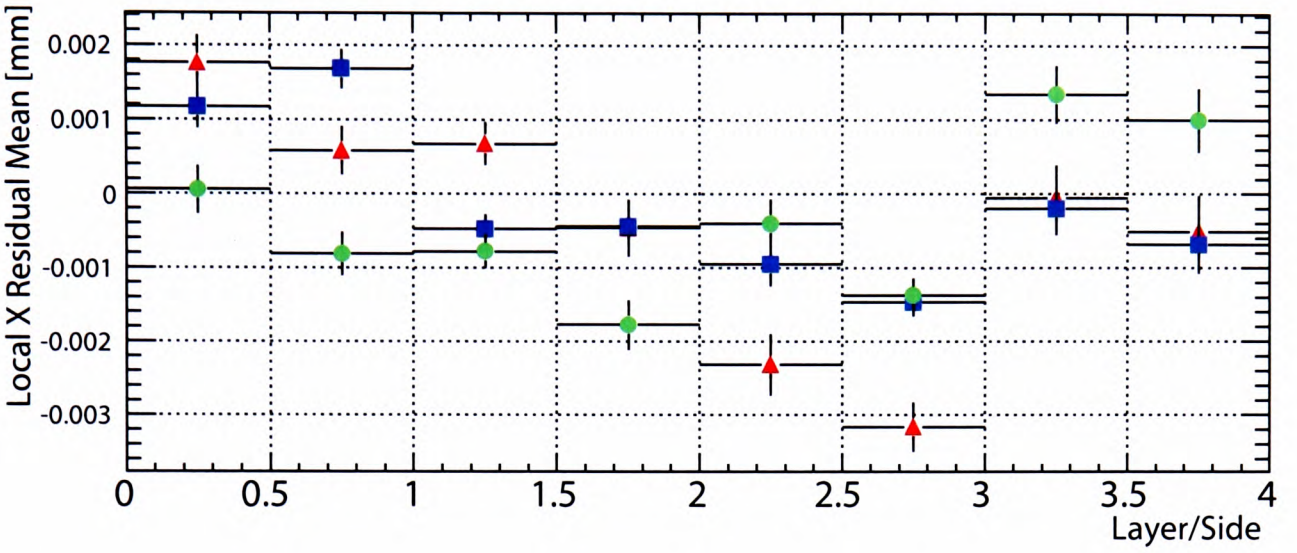


Fig. 5.7: Unbiased hit residuals for three alignment scenarios: Robust Alignment (red triangles), Local χ^2 Alignment (green circles) and Global χ^2 Alignment (blue squares). Upper plot: Mean of local X residual distribution layer by layer. Lower plot: Fitted width of hit residual distributions layer by layer.

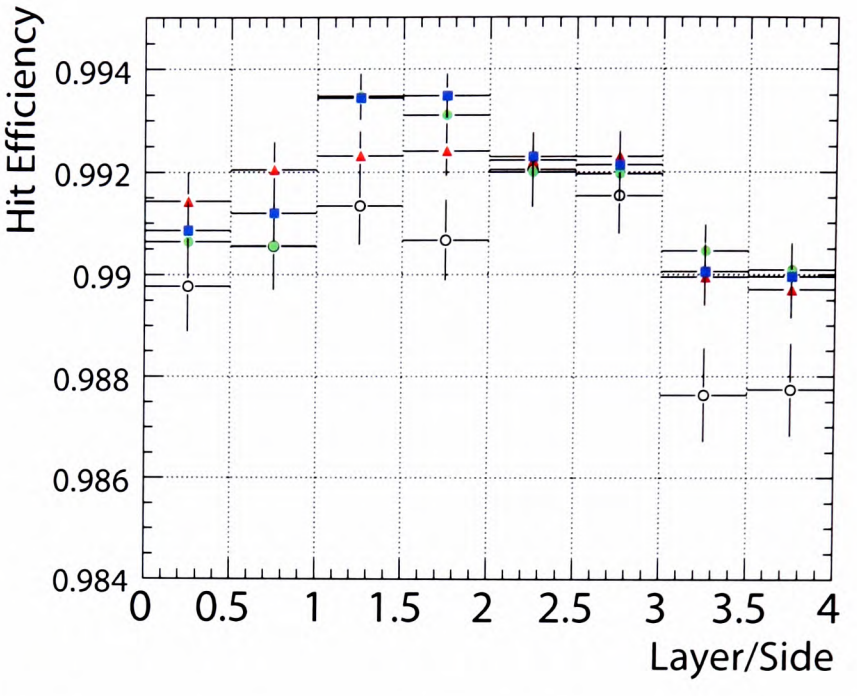


Fig. 5.8: Hit efficiencies for four alignment scenarios: No alignment (white circles), Robust Alignment (red triangles), Local χ^2 Alignment (green circles) and Global χ^2 Alignment (blue squares).

5.7 Alignment Results vs. Photogrammetry Measurements

Due to the absence of a magnetic field during SR1 data taking all tracks coming from cosmic rays are straight lines. Thus, this setup was ideal to determine the relative SCT barrel rotations in ϕ. A similar measurement was performed analysing the photogrammetry data [57]. The first set of the three photogrammetry measurements, which was taken in November 2005 [54], was precise enough to determine relative barrel rotations. However, these measurements were taken before the insertion of the SCT into the TRT. Especially, the mounting of the SCT

on the temporary support was completely different to its mounting on rails inside the TRT which may have lead to significant global distortions of the SCT barrels. This type of distortions may create systematic radius dependent barrel rotations. Fig. 5.9 shows the measurement of the photogrammetry data in comparison with the measurements performed by the three track based alignment algorithms. The track based algorithms measure the same relative barrel rotations within the er-

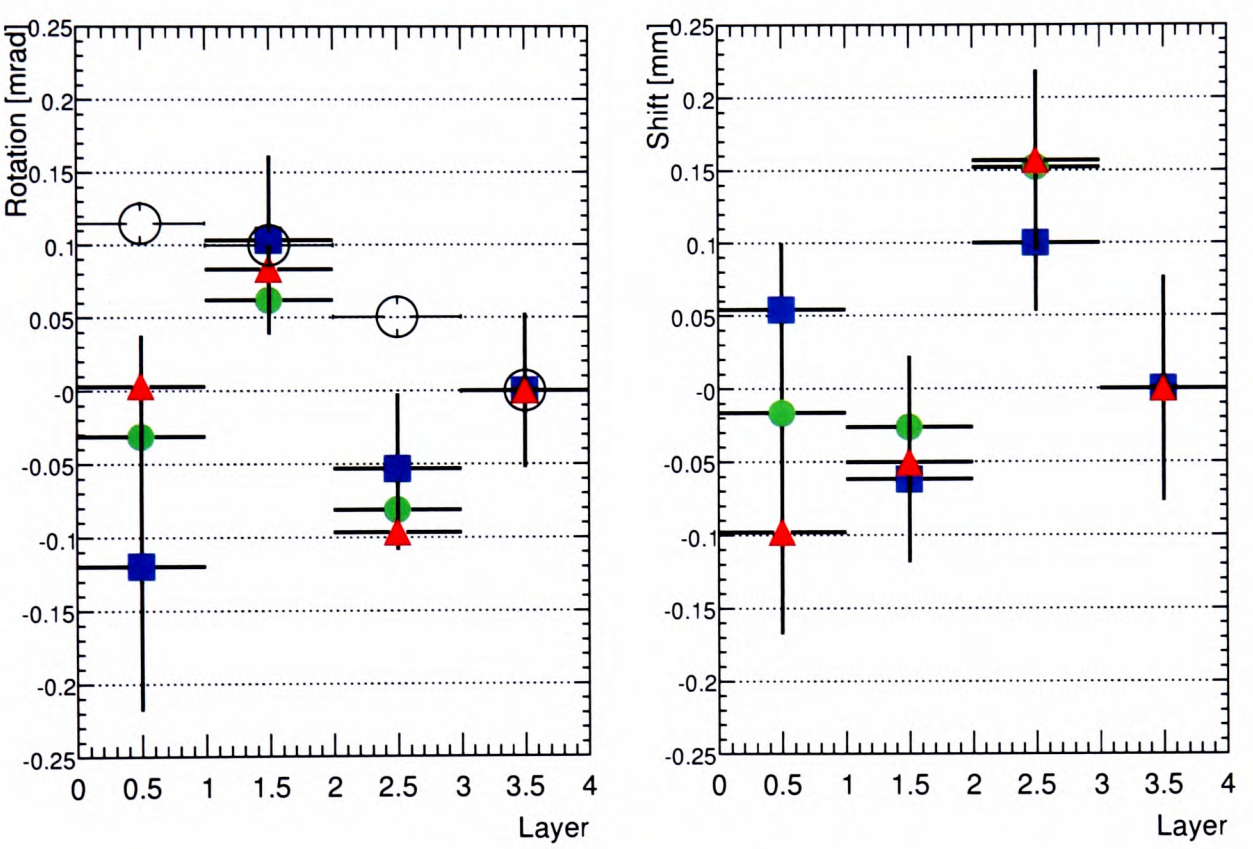


Fig. 5.9: For each SCT Layer the relative rotation of the whole SCT barrel in ϕ is shown in mrad (left) and the relative Z shift in mm (right). White circle: Photogrammetry measurement. Red triangle: Robust Alignment. Green circle: Local χ^2 Alignment. Blue square: Global χ^2 Alignment. The alignment sets have been transformed into a common reference frame and the global shifts normalised to those of layer 3.

rors. The results from the photogrammetry data are different in two layers. It is not quite clear whether this difference arises from actual barrel movements or from systematic uncertainties in the photogrammetry measurements which may not be perfectly understood. The systematic deformations mentioned above may explain the difference. Furthermore, the relative barrel shifts in the global Z direction were analysed. Again, all alignment algorithms determined the same systematic distortions within their uncertainties.

Although, the barrel was shifted between SR1 data taking and its final position in the ATLAS cavern, the alignment constants which have been derived are expected to be valid for the final setup. An analysis of tracks from cosmic rays which will be collected in the detector pit before and also after the start of particle collisions from the LHC may have to confirm this statement.

5.8 Comparison of Alignment Results with Simulation

Usually, comparisons between reconstructed data using the aligned geometry and simulated data give insight about the quality of the obtained alignment constants. These comparisons, however, require that the same physical processes are simulated as there are expected to appear in the actual experiment. Due to the layer of concrete above the lower trigger, the cosmic muon rays were expected to have momenta larger than about 100 to 200 MeV. It is not clear how many cosmic ray tracks in that momentum range are actually present in the collected data sample.

Furthermore, the cosmic ray data sample includes also multiple particle tracks arising from showers. The simulated data sample, however, only consists of single muon tracks with a momentum higher than 200 MeV. Therefore, MCS is less dominant and the track topology much simpler in the latter sample. Residual distributions are a good indicator of the alignment quality. However, at low momenta the widths of these distributions are dominated by MCS. Also, hit efficiencies depend significantly on MCS and the track topology. For the given reasons it was concluded that simulation studies should not be used to determine the SR1 alignment quality. Detailed simulation studies for the full Inner Detector alignment are presented in Chapter 6.

5.9 Timing of SCT Barrel Cosmic Ray Data

The cosmic ray data were triggered using three layers of Eljen EJ-200 scintillators of the size 144 cm $\times$ 40 cm $\times$ 2.5 cm which are shown in Fig. 5.10. The setup and a more detailed analysis is described in Ref. [58]. The three scintillators were arranged such that a wide angular distribution of cosmic ray muons hit the scintillators and the instrumented sectors of the TRT and SCT. One of the scintillators was placed above the SCT, two of them below. In particular, the cosmic ray trigger was formed by taking the coincidence between the top and the middle layers. The time of an output pulse emerging from one of the two Hamamatsu R2150 phototubes attached to both ends of the scintillators differed by a few nanosec-

onds depending upon where the particle hit the scintillator detector. Therefore, a Model 624 Octal Meantimer was used to equalize the photon transit time by providing an output pulse at always a fixed time independent of where the impact occurred. That way a time resolution in the time of flight measurement of 0.5ns was achieved. Also, the charge deposited was measured in order to ensure that the event was triggered by a charged particle.

The timing of the cosmic ray data was analysed for two purposes. Firstly, the impact of the momentum, and thus multiple scattering, on the SCT hit resolu-

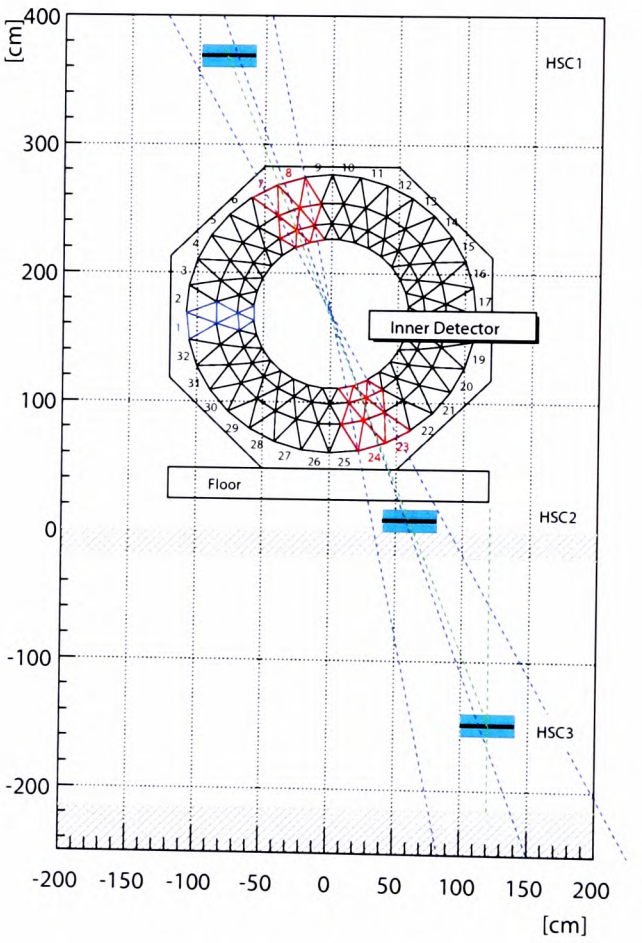


Fig. 5.10: The blue boxes, one above the Inner Detector and two below, show the cosmic ray scintillator setup. Each of the scintillator parts, HSC-1, -2 and -3, consists of two layers. The white box directly below the Inner Detector symbolises the concrete floor.

tion had to be understood. Secondly, in the simulation of cosmic ray events a ϕ-dependence of the mean residuals had been found. A careful analysis showed that in the simulation, timing of the hits had a clear impact on this effect [59]. The time-dependent modeling of the electronic response makes the signal depend on the depth in the silicon at which ionisation is deposited and on the distance from the readout strip. These values depend on the angle of the track with respect to the silicon plane. Thus, tracks which hit the silicon at a relatively large angle may receive a bias in the hit position. It is known that the angular distribution for cosmic ray tracks is quite different from the distribution which is expected to appear in collision data. Indeed, fixing the time in the digitisation to the time which is normally expected for hits coming from collisions at the interaction point solved the problem [59]. However, it is not quite clear whether this solution has the correct physical meaning. For the two reasons given it was necessary to investigate the dependence of residual distributions on the trigger time in real cosmic ray data.

The analysed ntuple is based on 71391 events which were collected in the runs 2939, 3007, 3028 and 3098 (Appendix D). The combined ntuple was produced with the InDetCosmicRecExample package tag 00-00-72 in Athena release 12.0.3. In this analysis six variables in the combined ntuple shown in Table 5.2 were used. The meaning of the various channels is described in Table 5.3. In order to analyse the effect of the momentum on the residuals, a time of flight measurement was performed. The variable tdc_phase contains the time measurement for each channel stored in tdc_channel. The cosmic trigger is random with respect

CBNT Variables	
Variable Name	*Definition*
tdc_ntdcs	Total number of TDC channels that were hit
tdc_channel	Number of TDC channel
tdc_phase	Phase of given TDC channel
trk_SctRes	SCT hit residual
trk_Sct_phi	Sector number in SCT barrel
trk_Sct_layer	SCT layer number

Tab. 5.2: Combined ntuple variables used in the timing analysis.

TDC Channels		
Channel	*Definition*	*Name*
Channel 1	Top scintillator Side 1	HSC-1B
Channel 2	Top scintillator - Side 2	HSC-1A
Channel 3	Middle scintillator - Side 1	HSC-2B
Channel 4	Middle scintillator - Side 2	HSC-2A
Channel 5	Bottom scintillator Side 1	HSC-3B
Channel 6	Bottom scintillator Side 2	HSC-3A
Channel 7	Top scintillator Meantime	HSC-1
Channel 8	Middle scintillator Meantime	HSC-2
Channel 9	Bottom scintillator - Meantime	HSC-3

Tab. 5.3: Definition of TDC channels.

to the 40 MHz system clock, generated by the ATLAS Local Timing Processor. The trigger is synchronised with the clock. The start of the Time to Digital Converter (TDC) was a clocked signal and all the times were measured relative to that. Thus, the time of flight between the upper and the bottom scintillator is the time difference between channel 9 and channel 7. These two channels measure the meantime of both scintillator sides in the bottom and upper scintillator, respectively. The time difference peaks at about 18.5ns. The dependence of the muon incidence angle θ on the geometrical length of flight, and thus on the average time

of flight, is $1/sin(\theta)$. The non-linear propagation of the signal between the two sides of the scintillator leads to an additional θ dependence which is difficult to predict. It was attempted to correct for this effect using different fitting functions. A quadratic fit appeared to be most reasonable. However, this correction led to an improvement in measurement resolution of only about 8ps. Thus, in the following study only the raw time of flight measurement was used. The events were divided in two groups: Events with slow particles which have a time difference between channel 9 and 7 greater than 18.5ns and events with fast particles which have a time difference smaller than 18.5ns. For the fast particles it is furthermore required that the time difference was positive. In Fig. 5.11 it can be seen that the RMS of the SCT residual distribution, trk_SctRes, is about 30 μm smaller for fast particles than it is for slow ones. Unfortunately, this possible selection reduces statistics by about 50%. Thus, it is unlikely that this selection of events would improve the alignment of the SCT using cosmic tracks significantly.

In the simulation, timing had a clear effect on the SCT residuals which led to a significant residual-ϕ-dependence. In order to compare these results with real data, the detector elements in the SR1 setup were divided in three parts: Modules in the upper part with large values of ϕ which are the sectors 8, 9, 11 and 13 in the layers 0, 1, 2 and 3, respectively (Fig. 5.1); modules in the upper part with small values of ϕ which are the sectors 5, 5, 6 and 8 in layers 0, 1, 2 and 3, respectively; and all other modules. The timing dependence was analysed for two channels, channel 8 and 9. In each of the channels most of the hits were in a time window

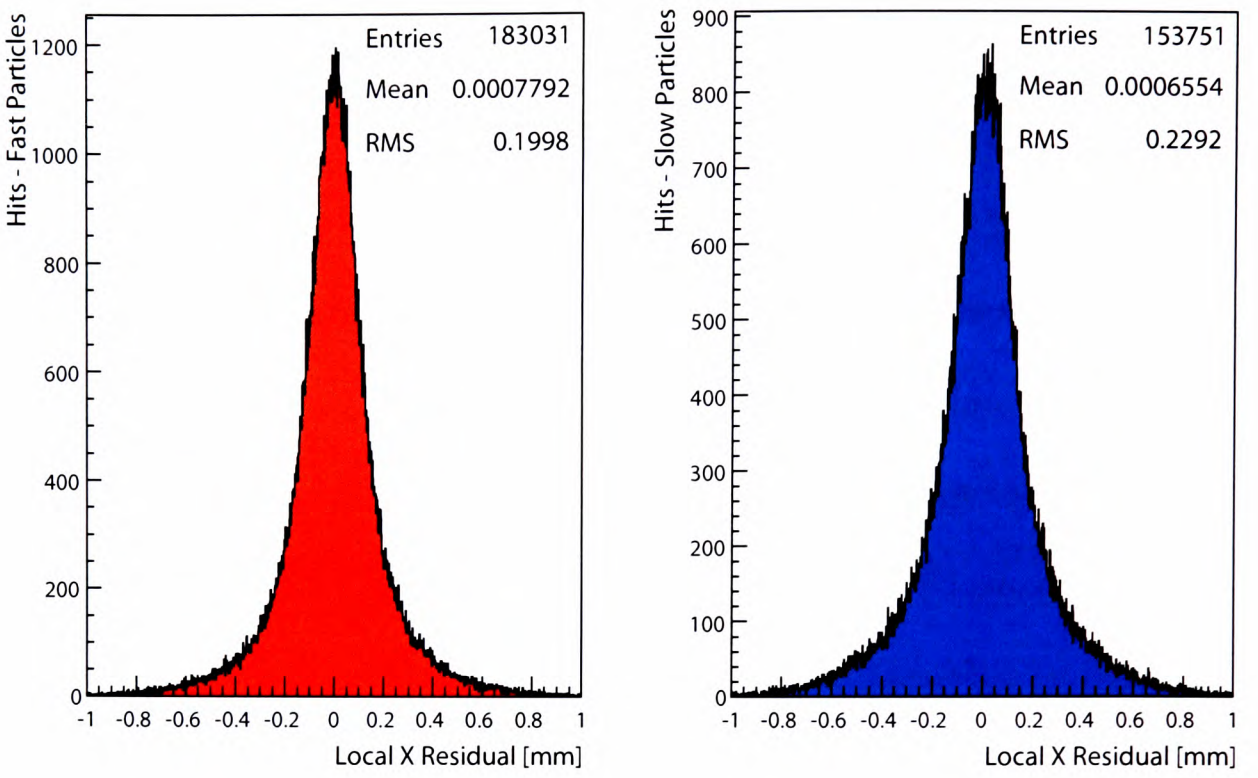


Fig. 5.11: Left: Unbiased SCT residuals for fast particles where the time difference between channel 9 and 7 was positive, but smaller than 18.5ns. Right: Unbiased SCT residuals for slow particles where the time difference between channel 9 and 7 is greater than 18.5ns. No alignment corrections were applied.

of about 24 ns. These 24 ns were divided in 6 equidistant bins. In Fig. 5.12 the resulting mean residuals as a function of the time are shown. In order to measure a time dependence of the mean residuals, all data points have been fitted with a linear fit. In none of the six cases a slope was found which was significantly larger than its error. Furthermore, the ϕ-dependence of the mean residuals in different time bins was analysed. In each layer a significant, but not systematic, ϕ-dependence was found as can be seen in Fig. 5.13. This effect may be explained with the misalignment of the detector. The mean residuals as a function of ϕ are different in each of the three analysed time slices, [74ns,76ns], [86ns,88ns] and

[96ns,98ns] in channel 8. However, no systematic effect was found. Thus, it was concluded that there is no measurable time dependence on the mean residuals in real cosmic ray data.

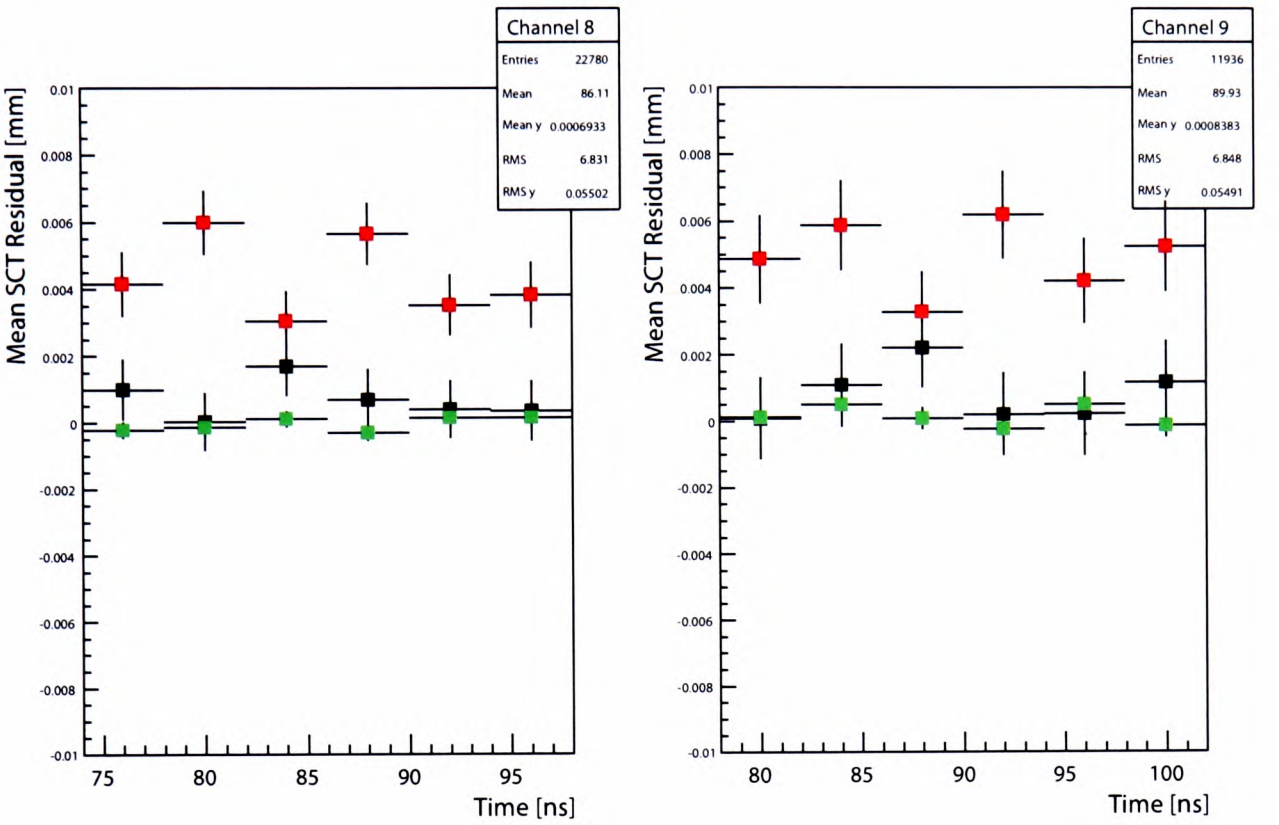


Fig. 5.12: Mean SCT residuals as a function of TDC time. Black: Sector 8, 9, 11 and 13 in layer 0, 1, 2 and 3, respectively. Red: Sector 5, 5, 6 and 8 in layer 0, 1, 2 and 3, respectively. Green: All other modules. Left: Channel 8. Right: Channel 9.

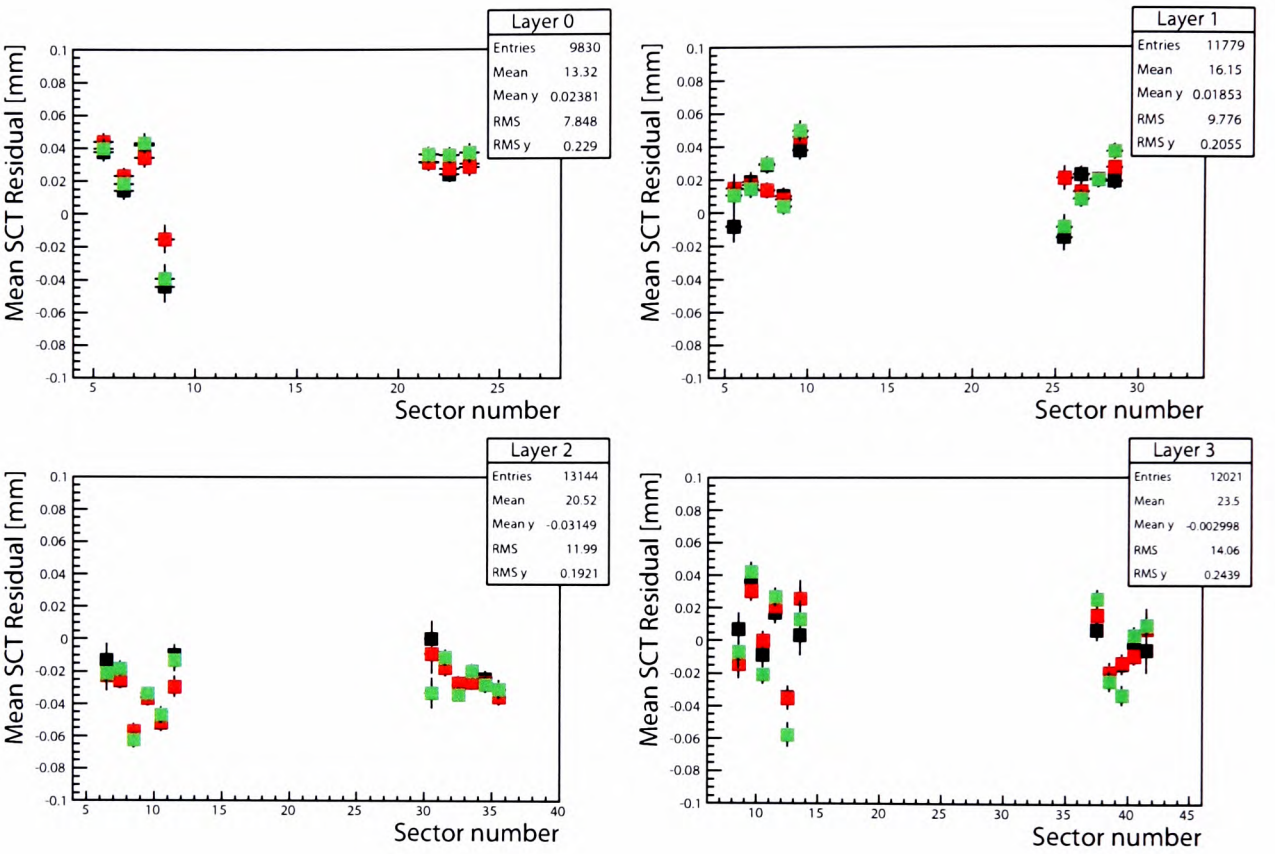


Fig. 5.13: Mean SCT residuals as a function of sector number for all four layers. Black: Early particles in time of channel 8 between 74ns and 76ns. Red: Medium timed particles in time of channel 8 between 86ns and 88ns. Green: Late particles in time of channel 8 between 96ns and 98ns.

6. ATLAS SILICON DETECTOR ALIGNMENT SIMULATION STUDIES

The alignment of all ATLAS silicon detectors is a very difficult challenge. History has shown that it may take many years to measure the positions of silicon modules in tracking detectors to a reasonable precision. It is thus crucial that the ATLAS collaboration is well prepared to align their detector to a sufficient accuracy with real data. As it is described in Section 1.2.2, one of the alignment requirements is that the resolutions of the track parameters are not degraded by more than 20% due to misalignments [60]. A good impact parameter resolution is important for B physics and precise mass measurements depend on the correct determination of the momentum scale. All these requirements need to be addressed and understood before collecting collision data.

Alignment studies on simulated data samples are very useful to understand the behaviour of alignment algorithms in well known environments. In the simplest case only one single module is misaligned. The principle of the Robust Alignment was proven on such studies. More interesting, however, is to study scenarios where all modules are randomly displaced. Furthermore, it is necessary to un-

derstand the effect of systematic distortions to detector subsystems, such as the individual SCT and PIXEL barrels or endcap disks. For this purpose, data samples were simulated with an "as built" geometry and a distorted magnetic field. The alignment studies presented in this chapter are part of the ATLAS Computing System Commissioning (CSC) and Calibration Data Challenge (CDC).

6.1 CSC Alignment Challenge

The aim of the CSC alignment challenge is to prove that the track based ATLAS alignment algorithms are able to determine the silicon module positions to sufficient precision. Furthermore, it is supposed to unveil the main weaknesses of the current algorithms in order to direct their development in the final year before real data taking.

The detector geometry used for the simulation of CSC data samples is significantly distorted on three different levels [61]:

- ◇ On level 1, the transformations represent movements of the main sub-detectors parts, such as the SCT barrel, the two SCT endcaps, the TRT barrel and the two TRT endcaps. The PIXEL barrel and endcaps are moved together as a whole unit. These distortions are applied in the global reference frame.

- ◇ On level 2, the transformations represent movements of the individual silicon barrel layers, silicon endcap disks and TRT barrel modules. These distortions are applied in the global reference frame.

- ◇ On level 3, the transformations represent movements of the individual silicon modules. These transforms are applied in the silicon module local reference frames. In the case of the SCT, all four wafers in a module are shifted together.

It is difficult to estimate how realistic the input parameters, which are shown in Table 6.1, 6.2 and 6.3, are. In addition to using available survey data, it was the general aim to be conservative and assume larger distortions than there are expected for the real ATLAS tracking detector. The analysis of SR1 data (See Chapter 5) gives a good estimate about the validity of this assumption. It was shown (Fig. 5.9) that the relative SCT barrel rotations around the global Z axis are only of the order 0.1 mrad. However, as can be seen in Table 6.2 the relative differences between the SCT barrel layer rotations around that axis in the CSC geometry are up to 1.9 mrad. Furthermore, according to the alignment constants obtained with SR1 data, SCT barrel displacements in the local X direction have an RMS between 62 and 78 μm (Table 5.1, Chapter 5). In the CSC geometry, the

Level 1 Transformations [mm, mrad]						
System	*X*	*Y*	*Z*	*Alpha*	*Beta*	*Gamma*
Pixel detector	+0.60	+1.05	+1.15	-0.10	+0.25	+0.65
SCT Barrel	+0.70	+1.20	+1.30	+0.10	+0.05	+0.80
SCT Endcap A	+2.10	-0.80	+1.80	-0.25	0	-0.50
SCT Endcap C	-1.90	+2.00	-3.10	-0.10	+0.05	+0.40

Tab. 6.1: In the global coordinate system the transformations for the main subdetectors are given. Translations (X, Y and Z) are given in mm. Alpha, beta and gamma are rotations in mrad around the X, Y and Z axis, respectively.

Level 2 Transformations [mm, mrad]							
System	*Layer*	*X*	*Y*	*Z*	*Alpha*	*Beta*	*Gamma*
Pixel Barrel	0	+0.020	+0.010	0	0	0	+0.6
	1	-0.030	+0.030	0	0	0	+0.5
	2	-0.020	+0.030	0	0	0	+0.4
SCT Barrel	0	0	0	0	0	0	-1.0
	1	+0.050	+0.040	0	0	0	+0.9
	2	+0.070	+0.080	0	0	0	+0.8
	3	+0.100	+0.090	0	0	0	+0.7
SCT Endcap A	1	+0.050	+0.040	0	0	0	-0.1
	2	+0.010	-0.080	0	0	0	0
	3	-0.050	+0.020	0	0	0	+0.1
	4	-0.080	+0.060	0	0	0	+0.2
	5	+0.040	+0.040	0	0	0	+0.3
	6	-0.050	+0.030	0	0	0	+0.4
	7	-0.030	-0.020	0	0	0	+0.5
	8	+0.060	+0.030	0	0	0	+0.6
	9	+0.080	-0.050	0	0	0	+0.7
SCT Endcap C	1	+0.050	-0.050	0	0	0	+0.8
	2	0	+0.080	0	0	0	0
	3	+0.020	+0.010	0	0	0	+0.1
	4	+0.040	-0.080	0	0	0	-0.8
	5	0	+0.030	0	0	0	+0.3
	6	+0.010	+0.030	0	0	0	-0.4
	7	0	-0.060	0	0	0	+0.4
	8	+0.030	+0.030	0	0	0	+0.6
	9	+0.040	+0.050	0	0	0	-0.7

Tab. 6.2: In the global coordinate system the transformations for each layer of the main sub-detectors are given. Translations (X, Y and Z) are given in mm. Alpha, beta and gamma are rotations in mrad around the X, Y and Z axis, respectively.

silicon modules are randomly displaced according to a uniform distribution centered at zero with a width of ± 150 μm for the translations in the module plane. This corresponds to an RMS of 87 μm. Thus, the simulated SCT level 3 misalignments are 10% to 40% larger than the ones of the actual SCT detector. It is safe to conclude that, at least for the SCT, the geometry used for the CSC alignment challenge has larger misalignments than are expected for the real silicon detector.

Level 3 Transformations [mm, mrad]						
System	*X*	*Y*	*Z*	*Alpha*	*Beta*	*Gamma*
Pixel Barrel modules	0.030	0.030	0.050	0.001	0.001	0.001
Pixel Endcap modules	0.030	0.030	0.050	0.001	0.001	0.001
SCT Barrel modules	0.150	0.150	0.150	0.001	0.001	0.001
SCT Endcap modules	0.100	0.100	0.150	0.001	0.001	0.001

Tab. 6.3: In the local coordinate system the average transformations for all modules are given. These values represent the half widths of flat top-hat distributions. Translations (X, Y and Z) are given in mm. Alpha, beta and gamma are rotations in mrad around the X, Y and Z axis, respectively.

In addition to the misalignments, a modified magnetic field and distorted material were used in the simulation [61].

The dataset chosen for the first alignment tests consists of 100k events with ten muons in each event. The energy of these muons is equally distributed between 2 and 50 GeV with a η-range of ± 2.7. All ten muons originate from a common vertex which is, however, varying event by event. It is clear that this dataset is unrealistic. However, it offers an excellent opportunity to study the behaviour of the alignment algorithms on a very distorted geometry. Further studies with more realistic samples, such as $Z \rightarrow \mu^+\mu^-$ or minimum bias events, are planned [62].

6.2 *Error Scaling*

Generally, the errors provided by the silicon cluster formation do not include uncertainties from misalignments and mis-calibrations. In a highly misaligned environment the tracking algorithms face difficulties to find most of the tracks if

the errors are not inflated sufficiently. The ATLAS offline software offers the possibility to increase the errors according to estimates about the detector imperfections. In the following analyses error scaling was only applied where it is explicitly stated. Tests showed that it clearly improves the track finding and fitting in the CSC "as built" geometry. Error scaling leads to wider hit residuals and a higher track efficiency. The higher track efficiency is needed in misaligned environments to have enough tracks to start the alignment with. The analysis of the best parameterisation of the error scaling and the most realistic input parameters is ongoing.

6.3 Level 3 Alignment

In principle, the alignment of simulated data offers the opportunity to directly compare the calculated alignment constants with the input geometry. However, numerous tests have shown that this comparison is generally less simple than it seems. The reasons for that are purely geometrical. Relative misalignments are calculated on the micron level. However, the dimensions of the whole detector structure are of the order of metres. Already tiny global rotations and translations lead to large apparent misalignments on the module level even if all modules are perfectly aligned with respect to each other. From the physics and track based alignment point of view perfect alignment means that the tracking performance is not affected due to misalignments. However, in terms of module positions, per-

fect alignment means that the calculated module positions are exactly the same as the ones of the input geometry. These two definitions are separated by systematic global transformations which are difficult to determine. Tools have been developed that attempt to transform one system into another in order to correct for these effects [63]. However, the uncertainties on these transformations are significant compared to the alignment precision and the success of these tools has been limited so far.

Nonetheless, comparing the exact module positions between the calculated alignment constants and the input geometry is an extremely important exercise in order to prove the validity of an alignment algorithm. In order to avoid large global distortions which may dilute the comparison, this test was performed on level 3 only. Thus, the level 1 and 2 misalignments given in Table 6.1 and 6.2, which describe collective shifts of various sub-structures, are assumed to be known. Therefore, only the level 3 misalignments which represent random shifts of the individual silicon modules were determined. After the transformation of the calculated geometry into the centre-of-mass system of the input geometry the difference between the module positions were analysed. In Fig. 6.1 an example of the Robust Alignment performance for the local X alignment of SCT barrel 0 is shown. In the CSC geometry, this SCT barrel has random displacements between $\pm$ 150 μm. After Robust Alignment most of these displacements were recovered. The remaining difference between the actual CSC geometry and the Robust Alignment constants is on average about 20 μm. This difference is caused

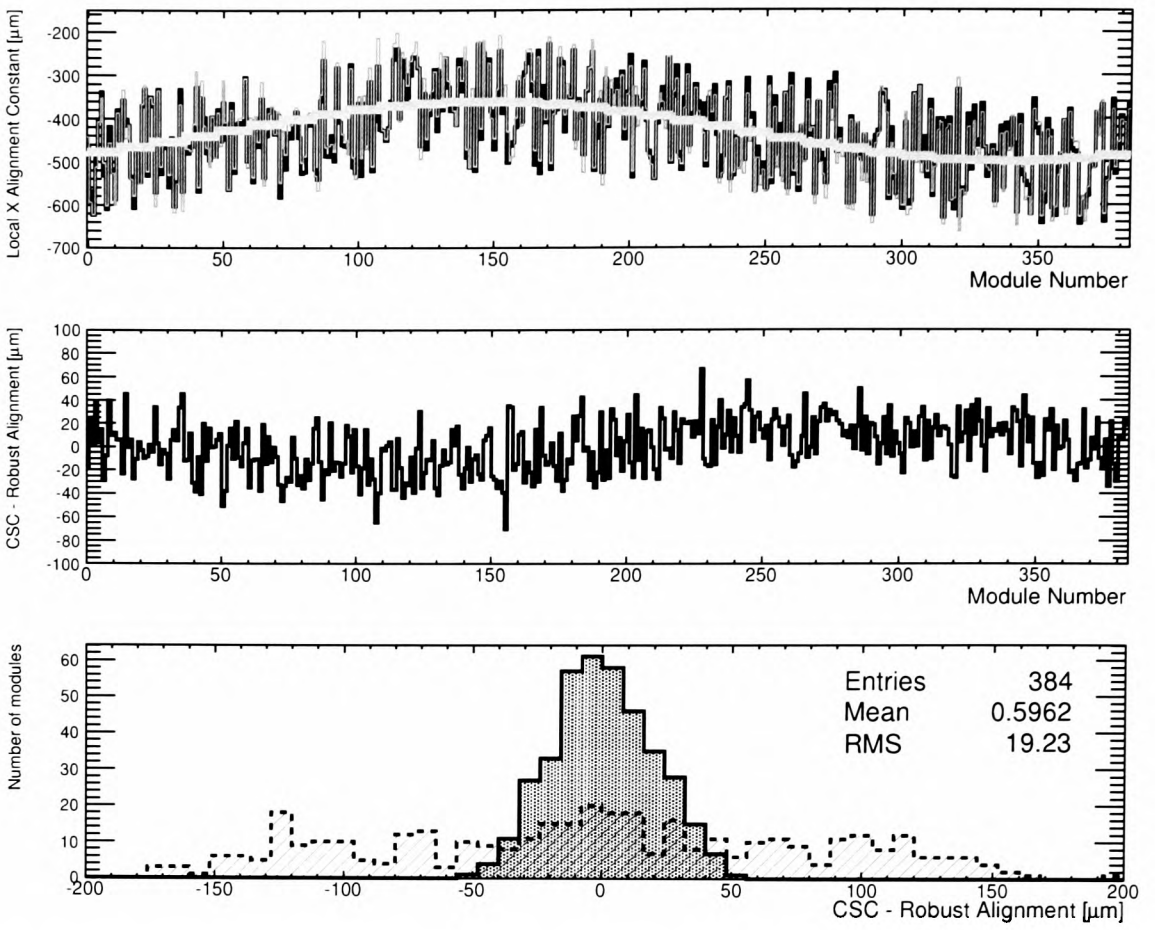


Fig. 6.1: Alignment results for SCT barrel 0. Top: Alignment constants for CSC geometry (black), CSC global misalignments (thick light grey) and Robust Alignment (thin grey). Middle: Difference between CSC geometry and Robust Alignment constants. Bottom: Difference between CSC geometry and Robust Alignment before (dashed) and after (dotted grey area) alignment.

by statistical effects, the distorted magnetic field and remaining systematic global distortions. Furthermore, after alignment the modules in the CSC geometry are still randomly displaced in the local Z direction as only systematic radial shifts can be recovered with the Robust Alignment algorithm (Section 2.2). If the mean incidence angle of tracks hitting a module is not 90°, shifts in the local Z direction are regarded as displacements in the local X and Y direction.

Other regions of the detector showed similar results to the SCT barrel 0. As

can be seen in Fig. C.1 to C.16, the track efficiencies and residual and overlap residual distributions after alignment are almost as good as they are when using the exact CSC geometry. This proves that the Robust Alignment algorithm is able to recover local misalignments properly.

Although, no explicit systematic distortions are modeled into the level 3 misalignments the momentum resolution is affected at that level. As can be seen in Table 6.4, the Robust Alignment improves the momentum resolution significantly with the removal of the random misalignments. In all three geometry setups, the systematic bias of the reconstructed momentum is less than 1% of the particle momentum.

Momentum Resolution [TeV^{-1}*]*			
Momentum	*L3 Misal.*	*L3 Aligned*	*Perfect*
$P < 20$ GeV [RMS]	8.9	4.4	3.3
$P > 20$ GeV [RMS]	6.7	1.8	1.1
$P > 20$ GeV [Mean +]	-0.07 ± 0.04	0.10 ± 0.01	-0.04 ± 0.01
$P > 20$ GeV [Mean -]	-0.01 ± 0.04	0.23 ± 0.01	0.03 ± 0.01
$P < 20$ GeV [Mean +]	-0.30 ± 0.10	-0.05 ± 0.05	-0.14 ± 0.03
$P < 20$ GeV [Mean -]	0.43 ± 0.10	0.69 ± 0.05	0.22 ± 0.03

Tab. 6.4: Improvement of the momentum resolution for level 3 alignment. The RMS and the mean of the difference between the reconstructed momentum and the true MC is shown. The results are presented for positively (+) and negatively (-) charged particles and for three different geometries: no level 3 alignment (level 1 and 2 are known), Robust Alignment of level 3 and the true CSC geometry (perfectly aligned).

6.4 Alignment of all Levels

At the start of LHC the level 1 and 2 misalignments will not be known. Therefore, it is important to understand the Robust Alignment performance for the alignment of all levels. It is clear, that the Robust Alignment algorithm is most powerful for the alignment of relative module misalignments, i.e. level 3, as it uses overlap residuals to correlate neighbouring modules. However, the studies presented in this section showed that the Robust Alignment is also able to significantly improve the tracking performance if none of the global distortions are known.

Similar to the alignment on level 3, first the random module misalignments were removed with 20 iterations using error scaling. This procedure improves the tracking efficiency and track resolution significantly. Already at this level some of the global distortions are removed. In the CSC geometry, as it is also expected for the real ATLAS detector, the endcaps do not have the same systematic distortions as the barrels. Tracks which go through both parts of the detector are therefore able to correct for some of the global weak modes. In order to test this hypothesis five iterations of Robust Alignment were performed once with all tracks and once only with tracks in the barrel region ($\eta < 1.2$). A comparison of the momentum resolutions for barrel tracks in both alignment scenarios showed that using tracks from the whole detector leads to greater improvements in the reconstructed momentum.

In a second step, part of the remaining global misalignments were removed.

In the CSC geometry, the vertex distribution of the reconstructed tracks is not centred around zero. This can be solved by shifting the whole PIXEL detector accordingly (see Section 6.5). After this transformation, 10 more iterations of the Robust Alignment were performed in order to correlate the SCT with the new PIXEL position. These iterations were followed by the alignment of the whole detector using the TRT momentum constraint. This software tool uses the TRT in order to determine the momentum of the particles and refits the tracks in the PIXEL and the SCT detector accordingly. The TRT provides on average 36 two-dimensional measurement points with less than 0.170 mm resolution for charged particle tracks. Therefore, the curvature of the tracks is well measured by the TRT. As the position of the track is measured more precisely with the PIXEL and SCT, only these two detectors were used to determine the remaining track parameters. Unfortunately, due to the large systematic distortions and the misalignments of the TRT on level 1 and 2 [61], most of the tracks get lost if the TRT momentum constraint is used. Also, there are less hits on each track. Therefore, only part of the detector elements get shifted in each iteration. In order to balance this effect, every second iteration was performed without the TRT constraint. That way, the modules move continuously in the right direction without leaving out certain parts of the detector.

As can be seen in Table 6.5 the TRT momentum constraint improves the momentum measurement significantly. Also, the resolutions of the other four track parameters improve significantly with this alignment method (Table 6.6). How-

Momentum Resolution [TeV^{-1}]			
Momentum	*Full Misal.*	*Aligned*	*Al.+ TRT*
$P < 20$ GeV [RMS]	59.2	10.5	6.4
$P > 20$ GeV [RMS]	66.1	10.0	5.7
$P > 20$ GeV [Mean +]	-9.6 ± 0.4	-1.55 ± 0.06	-0.8 ± 0.04
$P > 20$ GeV [Mean -]	-5.8 ± 0.4	-1.25 ± 0.06	-0.6 ± 0.04
$P < 20$ GeV [Mean +]	-15.0 ± 0.8	-1.39 ± 0.11	-0.8 ± 0.08
$P < 20$ GeV [Mean -]	-8.2 ± 0.7	-0.33 ± 0.12	0.3 ± 0.08

Tab. 6.5: Improvement of the momentum resolution for all levels alignment. The RMS and the mean of the difference between the reconstructed momentum and the true MC is shown. The results are presented for positively (+) and negatively (-) charged particles and for three different geometries: full misalignment, Robust Alignment and Robust Alignment including the TRT momentum constraint.

ever, the determined resolutions are much larger than the acceptable 20% increase due to misalignment which is the final goal. Part of the discrepancy may be explained with distortions of the magnetic field which are not addressed in this study. Also, the individual TRT barrel modules are misaligned on level 1 and 2 which affects the TRT momentum measurement. As can be seen in Table 6.7, the momentum resolution of the TRT-only tracks with the misaligned TRT is similar to the momentum resolution obtained for the full detector after alignment using the TRT momentum constraint. However, as there are no systematic distortions built into level 3 of the TRT CSC geometry, it is unclear whether the same improvements may be obtained with collision data in the real ATLAS Inner Detector. Only with a combination of all the solutions presented in Section 3.4 is it expected to be able to achieve the goal of not degrading the track parameter resolutions by more than 20%.

Track Parameter Resolutions [RMS]			
Parameter	*Full Misal.*	*Aligned*	*Perfect*
d_0 [μm],$P < 20$ GeV	4653	99	57
d_0 [μm],$P > 20$ GeV	6960	103	29
ϕ_0 [mrad],$P < 20$ GeV	23.8	1.9	1.0
ϕ_0 [mrad],$P > 20$ GeV	38.4	1.8	0.4
θ_0 [mrad],$P < 20$ GeV	5.8	1.5	0.9
θ_0 [mrad],$P > 20$ GeV	6.3	1.1	0.4
z_0 [μm],$P < 20$ GeV	6068	396	253
z_0 [μm],$P > 20$ GeV	10650	590	223

Tab. 6.6: Track parameter resolutions for three geometries: full misalignment, Robust Alignment with TRT constraint and true CSC geometry (perfectly aligned). d_0 is measured with respect to the point (0,0,0).

For the PIXEL detector, the residual and overlap residual distributions obtained with the alignment of all levels are of almost the same quality as the ones determined with the alignment of level 3 only. However, due to the remaining global distortions the SCT residuals and overlap residuals are wider for the alignment of all levels. The contribution from overlap residuals in the calculation of SCT alignment constants is relatively low as in this part of the detector not enough overlap hits associated to a track are available. Therefore, it is expected that the overlap residual distributions will improve further once the global distortions are removed and more data can be used for the Inner Detector alignment. A summary of all residual and overlap residual distributions is shown in Fig. C.1 to C.16.

Momentum Resolution [TeV^{-1}]		
Momentum	*Full Misal., TRT only*	*Perfect, TRT only*
$P < 20$ GeV [RMS]	7.8	3.1
$P > 20$ GeV [RMS]	5.9	0.8

Tab. 6.7: Impact of the TRT misalignment on the momentum resolution: The momentum resolution is shown for TRT-only tracks with full misalignment and for the perfectly known geometry.

6.5 Using Vertex Fit

As can be seen in Table 6.1 the centre of mass of the PIXEL detector is significantly shifted with respect to the origin. This shift is clearly visible in the impact parameter distribution. In order to correct for this global shift vertices have to be fitted and compared with the position of the beam. The tracks in the simulated data samples used for the CSC alignment have their vertices centred around the global coordinate (0,0,0). Therefore, it was enough in this case to measure the vertex distributions and shift the PIXEL detector such that the final vertex distributions are also centred around the global coordinate (0,0,0). This procedure has been applied after 20 iterations of full detector alignment. In Fig. 6.2 the improvement of the d_0 distribution and its dependence on ϕ can be seen. For the alignment of the real ATLAS detector, the centre of the beam profile, which will be measured with the start of the LHC, has to be used to define the global origin of the detector.

It is controversial whether only the PIXEL detector, which has the most impact on the vertex measurement, should be shifted, or the Inner Detector as a

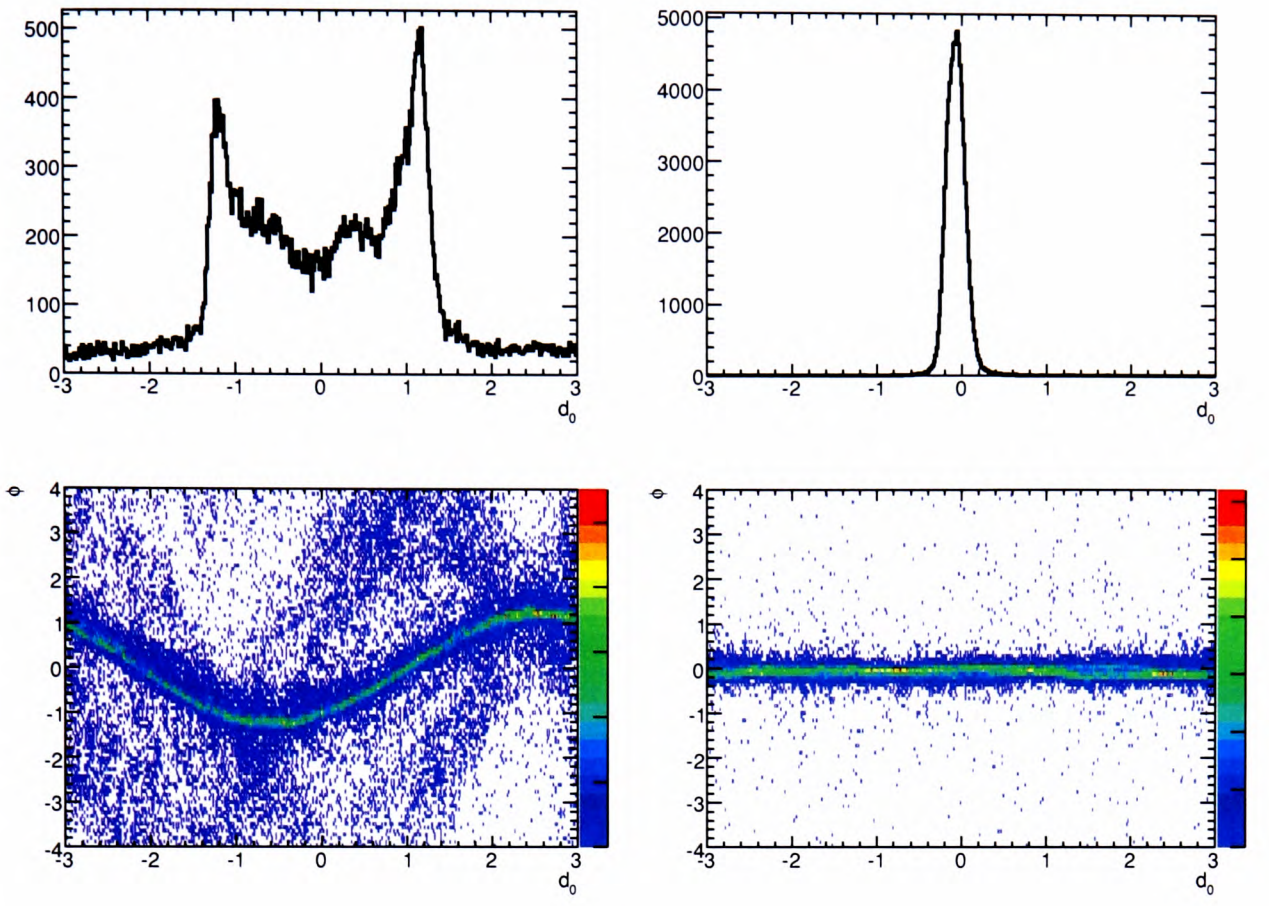


Fig. 6.2: Improvement of the impact parameter resolution with CSC alignment. Top: d_0 distributions. Bottom: d_0 vs. ϕ. Left: Alignment not known. Right: After Robust Alignment including vertex shift.

whole. With both methods improvements in the impact parameter resolution were achieved. Shifting only the PIXEL detector, however, lead to the best results. The Robust Alignment algorithm allows to perform both.

6.6 Statistical Uncertainty on CSC Constants

The statistical uncertainties on the CSC alignment constants in local X and Y can be seen in Fig. 6.3 and Fig. 6.4, respectively. The dependence of the statistical alignment uncertainty on the area in the detector, as is it described in Section 2.4,

was indeed observed.

The uncertainties in local X are up to 1.2 μm for the PIXEL endcap, 3.5 μm for the PIXEL barrel, 3.0 μm for the SCT endcap and 4.5 μm for the SCT barrel detectors. The uncertainties in local Y are up to 3.5 μm for the PIXEL endcap, 18 μm for the PIXEL barrel, 50.0 μm for the SCT endcap and 70.0 μm for the SCT barrel detectors. However, most of the modules have smaller statistical uncertainties. Due to the variation in the illumination of the modules, barrel modules with smaller layer numbers show generally a better alignment precision. Only the modules with very large ring numbers, which are either at the limit of the detector acceptance or in the region between the barrel and the endcap where the performance of the track reconstruction is slightly inferior, have a reduced alignment precision. Furthermore, modules with smaller sector numbers have smaller statistical uncertainties if there are enough overlap hits to increase the alignment precision. As it is explained in Section 2.4, contributions from overlap hits in a module with a larger sector number are affected by the correlations, and therefore the uncertainties, from the detector elements between that module and the module with sector 0 (see Section 2.3.4). This effect can be seen especially in the PIXEL endcap disks where large overlaps are present.

6.7 Measuring Deformations in the Radii of Detector Rings

As it is described in Section 2.3.4, the Robust Alignment allows to perform corrections in the radii of the detector rings using overlap residuals. In the CSC geometry, no systematic changes of the barrel radii were applied. Therefore, a special geometry was generated where the radius of ring 0 in the PIXEL detector was inflated by 50 μm. Measuring changes of ring radii is limited by statistics as each overlap of the ring is required to be sufficiently illuminated. The data sample which was used for the CSC alignment just provides enough statistics to measure the central PIXEL rings to a precision of approx. 2 μm. After two iterations of Robust Alignment the radius of the inflated PIXEL ring was reduced to the design value within the statistical uncertainty.

6.8 CPU Usage for CSC Alignment

The alignment of the CSC geometry was performed using distributed alignment on 40 sub-samples of the 100k events with each 10 muons. Each iteration required about 40 to 60 minutes to finish. More than 90% of the CPU is used for the reconstruction. Using the TRT constraint doubled the CPU time per iteration. The TRT constraint requires extra processes which determine the momentum inside the TRT and perform the refitting of the tracks. The CPU usage for the vertex shift is negligible.

It is a requirement that the Robust Alignment algorithm is able to perform

alignment within 24 hours. The analysis of the CSC alignment showed that, if a sufficient sample of high-momentum muons and enough computers are available, this requirement can be fulfilled even if there is no knowledge about the alignment. However, with the start of the LHC the alignment procedure will be different. As described in Section 1.2.2, the first alignment constants will be produced with minimum bias events before enough high-momentum muons become available. Therefore, the iterations necessary for the Robust Alignment will be performed on an increasing number of good tracks. With each day of data taking the alignment constants improve and only a few iterations of Robust Alignment will be required to get even more precise alignment constants. Thus, for a data sample which is comparable to the one used for the CSC alignment, fewer iterations and therefore fewer computers will be required to improve the alignment within 24 hours.

6.9 Outlook

The alignment of the CSC geometry showed that the Robust Alignment algorithm is functioning properly. With the used data sample the statistical uncertainties on the alignment constant calculations are relatively small compared to the systematic ones. The most important of the remaining challenges, which is the same for all track based alignment algorithms, is to control the systematic distortions which degrade the track parameter resolutions. The ATLAS Inner Detector alignment collaboration is aware of this challenge and is planning to develop and test

the necessary software tools, which solve the remaining weak modes, until the start of collision data taking. As it is shown in Section 6.4, the TRT momentum constraint already proved to be useful, but it is only one of the many suggested solutions. For the real ATLAS detector, a combination of all available momentum constraints will be needed to achieve the ambitious goal to not degrade any of the track parameter resolutions by more than 20%.

Additionally, more realistic data samples including minimum bias events, high-p_T muons from b-decays and muons from Z boson decays have to be used to redo the CSC alignment. Further problems may arise which have to be solved before the start of the LHC. Also the infrastructure for the alignment data stream which is currently being developed has to be completed and tested.

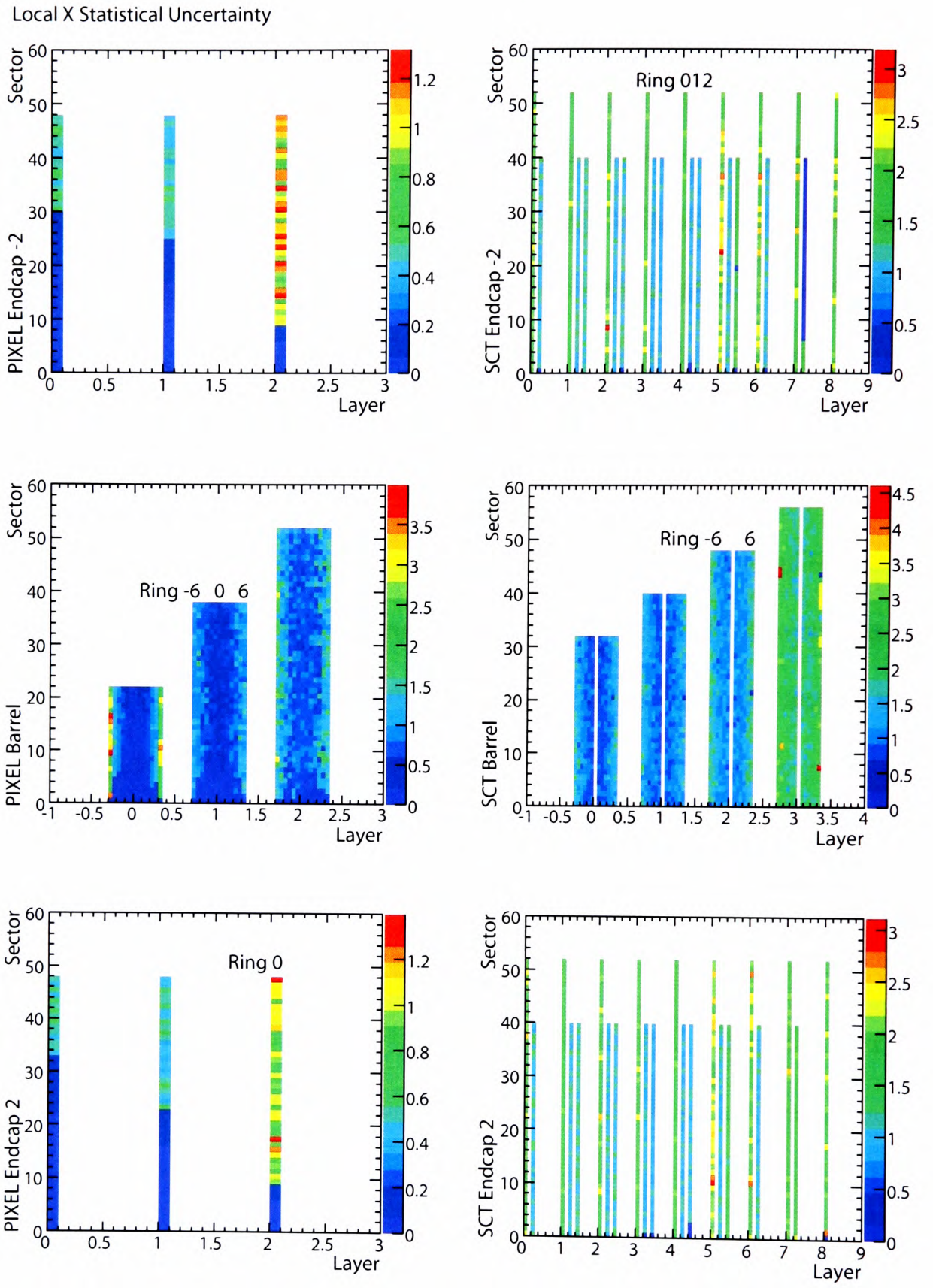


Fig. 6.3: The colours show the statistical alignment uncertainties in local X for all sub-detectors in microns.

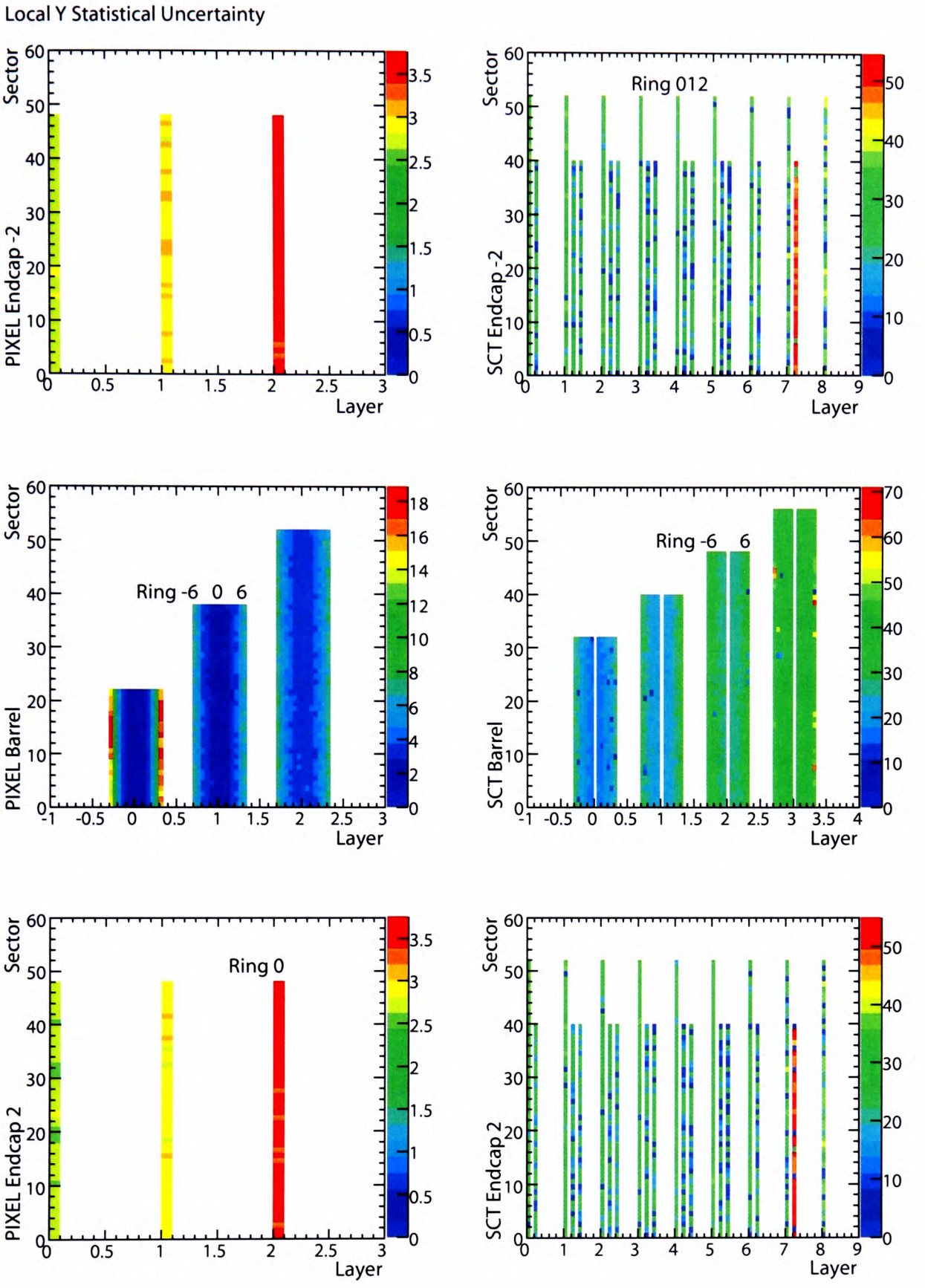


Fig. 6.4: The colours show the statistical alignment uncertainties in local Y for all sub-detectors in microns.

7. PARTON DISTRIBUTION UNCERTAINTIES IN DRELL-YAN PROCESSES

One of the main goals of the LHC experiments is to search for new physics beyond the Standard Model. Presently, there are many possible theories which might succeed it. The two main ones are Supersymmetry (SUSY) [64], introducing a new symmetry between fermions and bosons, and Extra Dimensions (ED) [65], adding at least two more dimensions to the four in space-time. For the discovery of new physics it is very important to understand the predictions of the Standard Model. At the beginning of LHC simple signatures such as the invariant mass of two opposite-sign leptons will be studied first. It is known that the dilepton channel offers many possibilities for new physics searches such as, for example, searches for the Randal-Sundrum graviton [66]. In the SM, these leptons will be mainly produced in Drell-Yan processes and through Z production. SM predictions for various dilepton distributions in these processes are, in addition to statistical and experimental uncertainties, limited by uncertainties arising from higher-order calculations in the pertubative approximation of the SM.

Furthermore, the sub-structure of the proton is not sufficiently known. The

QCD evolution of parton distribution functions (PDF) to large energies is determined through the DGLAP equations. However, the shapes of the input distributions at a certain energy scale are non-pertubative functions which are not calculable from theory. Therefore, these distributions have to be determined using real data coming from deep inelastic scattering (DIS), in fixed target experiments or at HERA, or from proton-antiproton collisions at the Tevatron. Generally, these functions describe the probability of finding a gluon or a quark with a certain flavour inside a proton. This quark or gluon carries a fraction x of the proton momentum. The model used to describe the PDF is typically of the form:

$$xf(x, Q_0) = A_0 x^{A_1} (1 - x)^{A_2} P(x; A_3, \ldots). \tag{7.1}$$

The energy scale Q_0 is usually in the range of 1 to 2 GeV. The function P may depend on one or more parameters and differs between the various groups, like CTEQ, MRST and ZEUS, that determine the PDF sets (Figure 7.1). A_i are the parameters which are determined through a χ^2 fit to experimental data. In this analysis mainly CTEQ PDF sets [67] are used. A detailed description of the particular input data and used methodology can be found in Ref. [68]. Further PDF sets used in this analysis are described in Ref. [69] (ZEUS) and Ref. [70] (MRST). Unfortunately, due to experimental and theoretical limitations none of the groups has been able yet to determine PDF sets to very high precision. The least well measured parton distribution is also the most important one at the LHC: The gluon

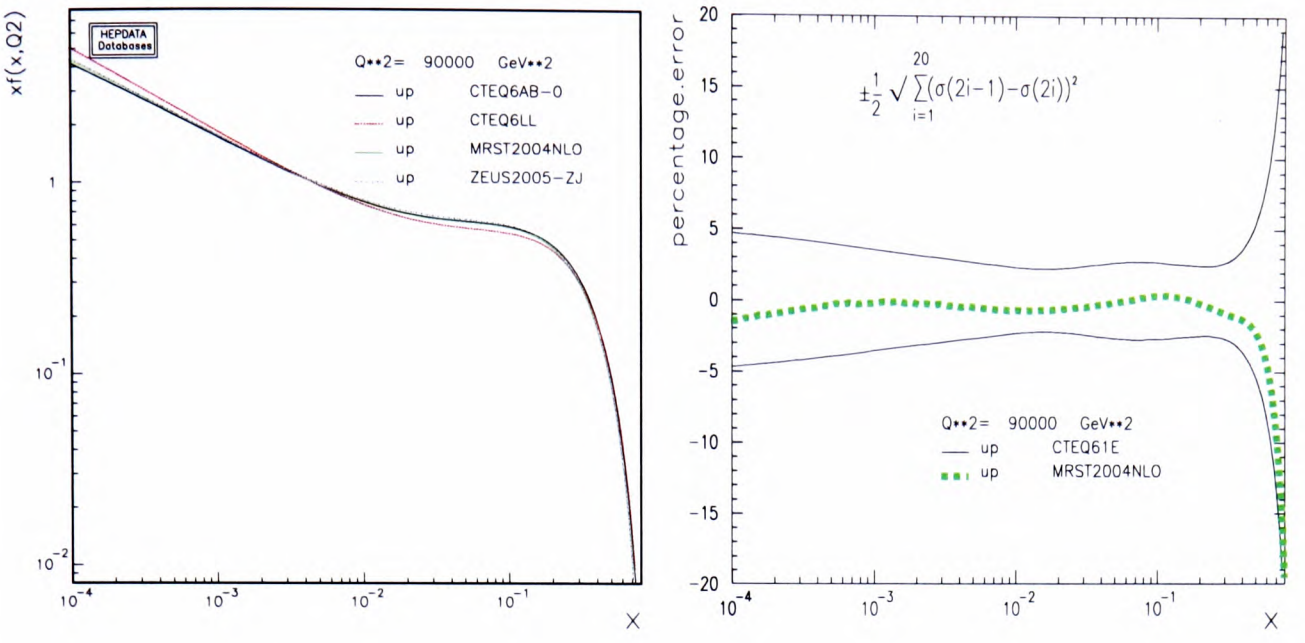


Fig. 7.1: Left: Up-quark distribution for CTEQ61, CTEQ6ll, MRST2004NLO and ZEUS2005-ZJ at $Q^2 = 90\ \mathrm{GeV}^2$. Right: A comparison between the CTEQ uncertainties on that particular up-quark distribution and the MRST central value.

distribution, which is mainly determined from jet production measurements at Tevatron and DIS at HERA, has an uncertainty of order 15% up to $x \sim 0.3$ and clearly dominates the valence and sea quark distributions for low values of x [68]. It is thus known that the PDF uncertainties are going to have a significant affect on physics analyses at LHC.

Every significant deviation from SM predictions gives a hint to physics beyond this widely accepted theory. However, it is crucial to understand their systematic uncertainties first. This analysis presents NLO effects and especially PDF uncertainties in high-mass Drell-Yan processes. The estimation of NLO effects is necessary as most currently available data samples are based on LO calculations only. Furthermore, better calculations of PDF uncertainties have become available recently. Both studies use well established reweighting techniques of

the hard processes. The analyses contribute to the general understanding of SM uncertainties which define the magnitude of the deviations from SM predictions which are required for new physics discovery.

7.1 Parton Distribution Uncertainties

Determining PDF uncertainties is very challenging, and subject of current research. It is known that some of the experimental data samples used to determine PDF sets are not fully compatible with each other. Also, part of the input data is not completely consistent with the theoretical framework. Some theorists, like Alekhin [71], are selecting experimental data such that proper consistency is achieved and that the global fit has a $\chi^2/N^{d.o.f}$ of about one. However, the bias of such selection is not fully understood. Most other groups, such as CTEQ, ZEUS and MRST, use a wider set of experimental data together with more flexible parametric forms for the PDF sets. However, inconsistent data influences the quality of the fit. Also, correlated systematic uncertainties are frequently not Gaussian. Thus, it is not possible to require $\Delta\chi^2$ to be of the order of one for the PDF error band. With a suitable parameterisation of each correlated error source, CTEQ defines the range of the χ^2 such that all used data sets match the PDF sets with a confidence level of 90%. This is equivalent to a $\Delta\chi^2$ of 100. MRST chose a value of 50 which corresponds to a confidence level of 68%.

Two different approaches are generally used for the χ^2 minimisation and error

estimation. The more conservative offset method fixes the systematic uncertainty parameters to zero for the minimal χ^2 fit, but varies these parameters to their minima and maxima, respectively, for the error calculation. The Hessian method, allows the systematic uncertainty parameters to vary during the minimisation process. The errors on the resulting theoretical parameters are calculated using the inverse of a single Hessian matrix expressing the variation of the χ^2 with respect to both theoretical and systematic offset parameters. In order to estimate the error on the PDF set, the behaviour of the global χ^2 in the neighborhood of the minimum in the N-dimensional PDF parameter space has to be analysed. N is the number of free PDF parameters. It is chosen to be 20 for CTEQ and 15 for MRST. By diagonalising the Hessian matrix, N eigenvectors are obtained. Each of the eigenvectors produces two error sets, one in the positive and one in the negative direction of the PDF parameter space along this eigenvector. Each set describes the PDF uncertainty for a certain combination of measurements. For example the CTEQ error sets 1 and 2 describe mainly the behaviour of the u-valance quark whereas the error sets 3 and 4 contain mostly information about the d-valence and sea-quark distributions. However, all of these error sets also contain a linear combination of other measurements. In general it is not possible to assign a certain error set to a certain parton distribution. A more detailed description can be found in Ref. [72].

The estimation of a reasonable error is maybe the most controversial aspect in the analysis of PDF sets. So far the different groups have neither been able to agree

on a common set of parton distributions nor on a generally accepted error set. Estimated errors published by CTEQ are more conservative than errors given by MRST. Furthermore, the central values of ZEUS2005-ZJ and MRST2004NLO are almost consistent with the errors around the central value of CTEQ61 (Fig. 7.1) in the region of x between 10^{-3} and 10^{-1} (Fig. 7.2) which is relevant for this study. Therefore, a sole analysis of uncertainties provided by CTEQ is considered to be sufficient.

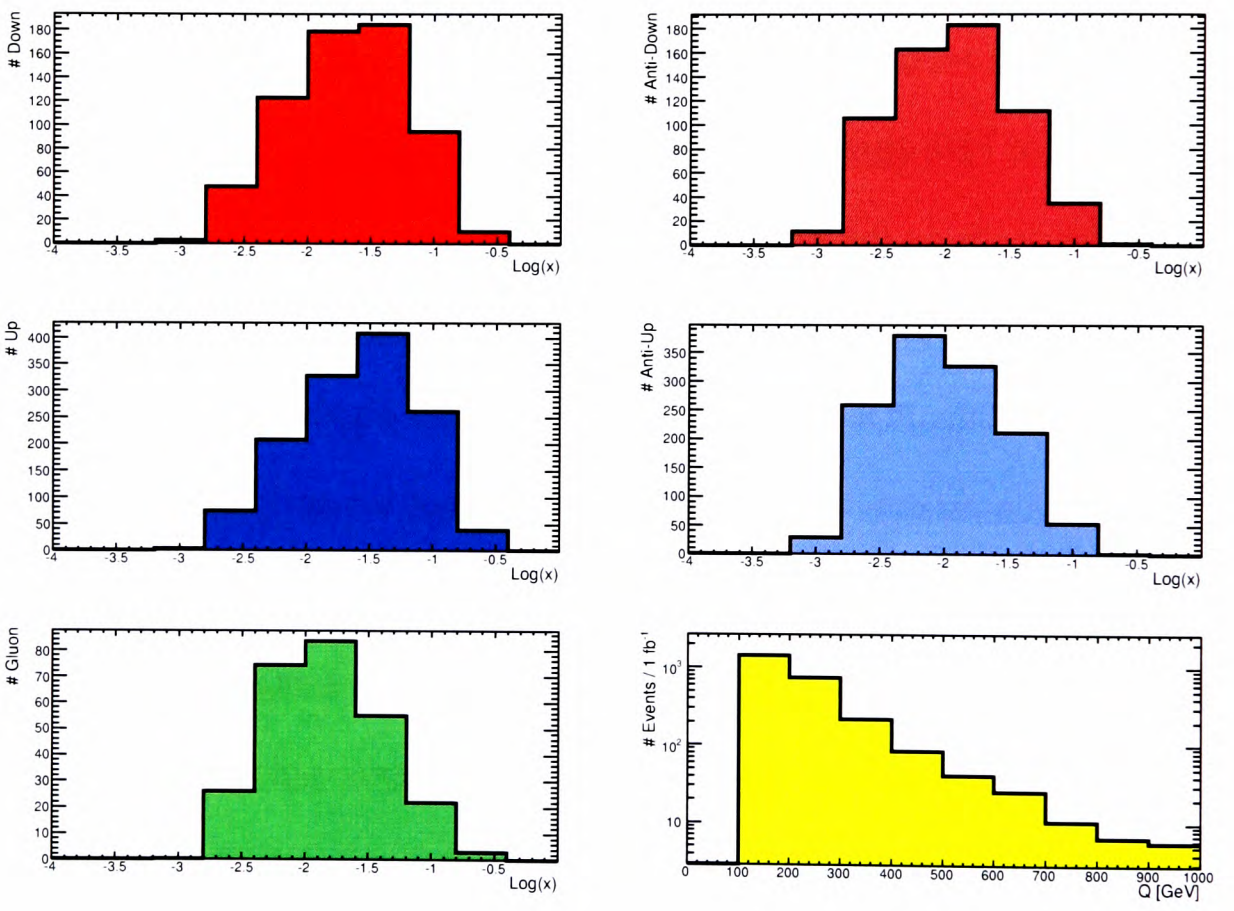


Fig. 7.2: Distributions of initial partons in the simulated data sample of the analysed high-mass Drell-Yan processes: Downs, anti-downs, ups, anti-ups and gluons. Bottom right: Q distribution for this process.

7.2 The Drell-Yan Processes

The Drell-Yan process shown in Fig. 7.3 is the production of a lepton pair through quark-antiquark annihilation at high energies [73]:

$$q\bar{q} \rightarrow \gamma^* \rightarrow l^+ l^- \tag{7.2}$$

In proton-proton collisions the range of partonic centre of mass energies varies from almost zero to the proton-proton center of mass energy which is 14 TeV at the LHC. In the leading order approximation of the SM the partonic cross-section for the annihilation via a virtual intermediate photon is given by

$$\hat{\sigma}(q\bar{q} \rightarrow \gamma^* \rightarrow l^+ l^-) = \frac{4\pi\alpha^2}{3\hat{s}} \frac{1}{N_c} e_q^2. \tag{7.3}$$

In this equation α is the fine structure constant, e_q is the charge of the quark

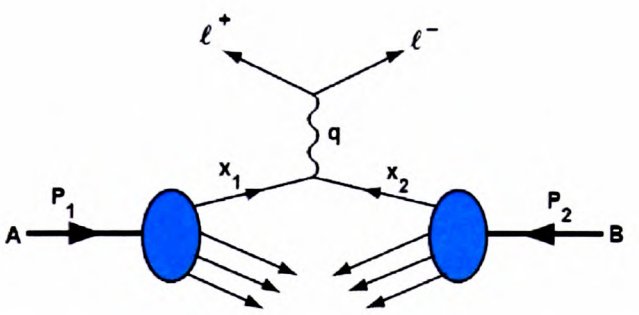


Fig. 7.3: Drell-Yan process. Proton A with momentum P_1 carries a quark with momentum fraction x_1 which is annihilating with an antiquark with momentum fraction x_2 coming from proton B with momentum P_2. The resulting photon γ with momentum q decays to two leptons, l^+ and l^-.

and $\hat{s}$ is the square of the partonic centre of mass energy which is related to the proton-proton centre of mass energy s via

$$\hat{s} = sx_1x_2. \tag{7.4}$$

In Drell-Yan processes $\hat{s}$ is equal to the square of the dileptonic mass M_{ll}. In the parton model, x_1 and x_2 are the momentum fractions of the proton carried by the individual parton. The overall colour factor $1/N_c$ in Eq. 7.3 takes into account that the colour of the quark has to match the colour of the antiquark in order to get a colour-singlet final state. For three colours three out of nine combinations are valid. Hence, N_c is equal to three.

In addition to the Drell-Yan process a lepton pair can be produced via the exchange of a Z boson of mass M_Z with a decay width Γ_Z. The differential cross-section for the dilepton production via this process is given by:

$$\frac{d\hat{\sigma}}{dM_{ll}^2}(q\bar{q} \to Z^0 \to l^+l^-) = \frac{M_Z^6 G_F^2}{18\pi} \frac{(a_i^2 + v_i^2)(a_l^2 + v_l^2)}{(M_{ll}^2 - M_Z^2)^2 + \Gamma_Z^2 M_Z^2} \tag{7.5}$$

G_F is the Fermi constant[1], a the axial couplings[2] and v the vector coupling[3]. The Z boson also interferes with the γ which leads to a third term in addition to the cross-sections given in Eq. 7.3 and 7.5. The contribution from Z exchanges, and their

[1] $G_F/(\hbar c)^3 = 1.166037(1) \times 10^{-5} GeV^{-2}$

[2] $a_{l^-} = -0.5$, $a_{u,c,t} = 0.5$, $a_{d,s,b} = -0.5$

[3] $v_{l^-} = -\frac{1}{2} + 2\sin^2\theta_W \simeq -0.03$, $v_{u,c,t} = \frac{1}{2} - \frac{4}{3}\sin^2\theta_W \simeq 0.19$, $v_{d,s,b} = -\frac{1}{2} + \frac{2}{3}\sin^2\theta_W \simeq -0.34$

interferences with the γ, are responsible for a forward-backward asymmetry in the electron distribution which is discussed in more detail in Section 7.5. Historically, the Drell-Yan process contained only the γ exchange as the Z was unknown at the time. Nowadays, however, both processes are often analysed together and referred to as "Drell-Yan processes".

It is possible that further quarks and gluons radiate from the colliding quarks before or after their annihilation. Also, virtual gluons may be exchanged. These processes have to be added to the above calculations. They correspond to next-to-leading order corrections in pertubative QCD. Unfortunately, an all-orders calculation of the Drell-Yan cross section is not possible. However, it has been shown that next-to-next-to-leading order corrections are relatively small, especially for high masses where they are of the order of 1% [74]. It is generally assumed, though not proven, that even higher orders are negligible.

7.3 Next-to-leading Order Monte Carlo

In perturbation theory, calculations get more precise the more orders are used. In the past, most of the simulations of particle collisions have been performed on the level of leading-order (LO), but next-to-leading-order (NLO) calculations have become increasingly available. The analysed simulated data set had been generated with LO MC and a LO-PDF set. The uncertainty studies which are presented in this analysis however, have been performed with NLO PDF sets. There is a

significant difference in PDF sets, and thus in the invariant mass distribution, depending on whether the hard matrix elements that enter into the pertubative QCD calculations are LO or NLO.

In order to be consistent and in order to take advantage of the newest calculations, k-factors describing the change in cross-section between LO and NLO MC have been applied. The k-factors (Appendix E) used for this analysis have been determined [75] using a Fortran code [76] that calculates the Drell-Yan cross section $d\sigma/dYdM_{ll}^2$ including the Z exchange in proton collisions at the leading and next-to-leading order as a function of mass and dilepton rapidity[4] Y. Various PDF sets can be used with this code. The k-factors used in this analysis have a granularity of 10 bins in Y and 10 bins in invariant mass M_{ll}. As can be seen in Fig. 7.4, NLO effects lead to a mass dependent increase in cross section of about 22 - 36%. Fig. 7.5 and 7.6 show the change of the η and Y distribution through NLO effects.

[4] The rapidity Y is defined by the energy E and the longitudinal momentum p_z of the dilepton pair:

$$Y = \frac{1}{2} ln(\frac{E + q_z}{E - q_z}). \tag{7.6}$$

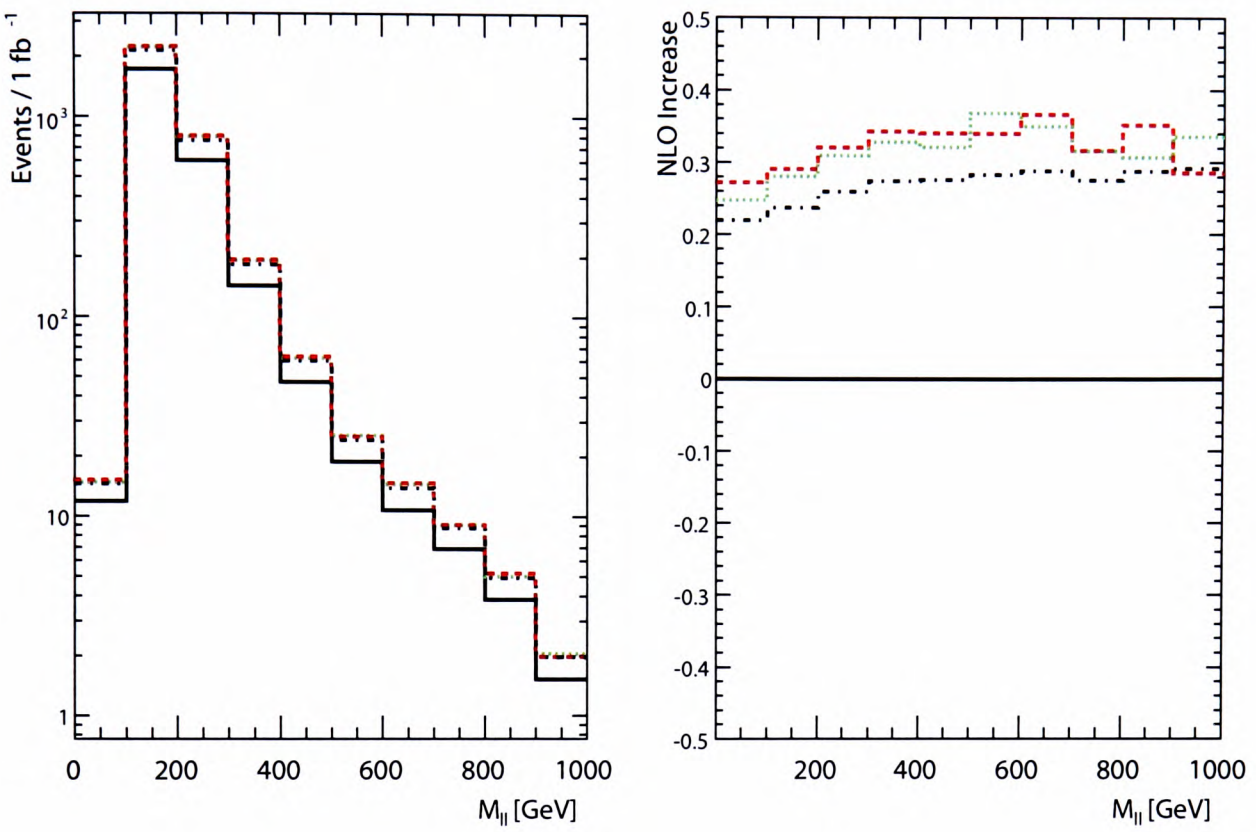


Fig. 7.4: Left: Four reweighted invariant mass distributions up to 1 TeV for high-mass Drell-Yan dielectron final states: CTEQ6ll (LO, solid black), CTEQ61 (NLO, dashed-dotted black), MRST2004NLO (NLO, dotted green) and ZEUS2005-ZJ (NLO, dashed red). For the NLO PDF sets the distributions have also been reweighted with analytical k-factors describing NLO Monte Carlo. Right: The relative differences of the reweighted distributions compared to the original one: CTEQ6ll (solid black), CTEQ61 (dashed-dotted black), MRST2004NLO (dotted green) and ZEUS2005-ZJ (dashed red).

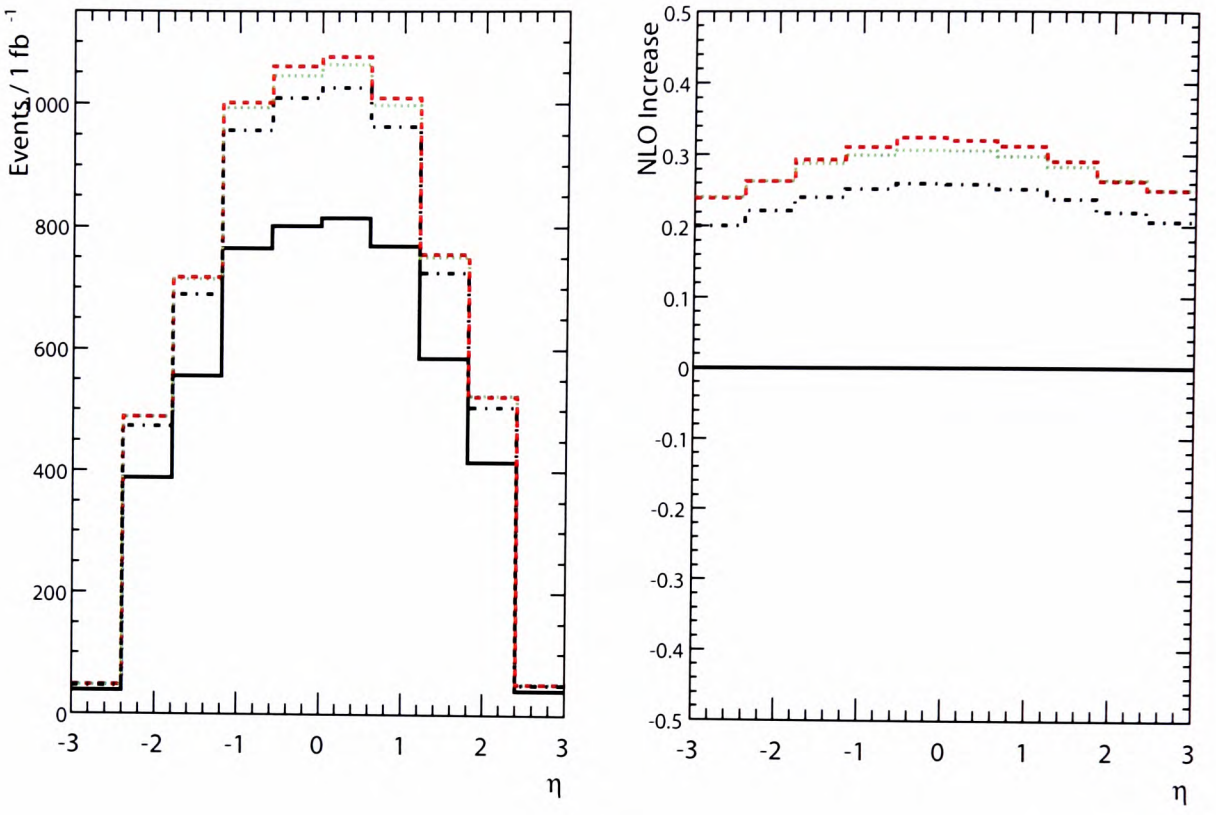


Fig. 7.5: Left: Four reweighted η distributions for high-mass Drell-Yan dielectron final states: CTEQ6ll (LO, solid black), CTEQ61 (NLO, dashed-dotted black), MRST2004NLO (NLO, dotted green) and ZEUS2005-ZJ (NLO, dashed red). For the NLO PDF sets the distributions have also been reweighted with analytical k-factors describing NLO Monte Carlo. Right: The relative differences of the reweighted distributions compared to the original one: CTEQ6ll (solid black), CTEQ61 (dashed-dotted black), MRST2004NLO (dotted green) and ZEUS2005-ZJ (dashed red).

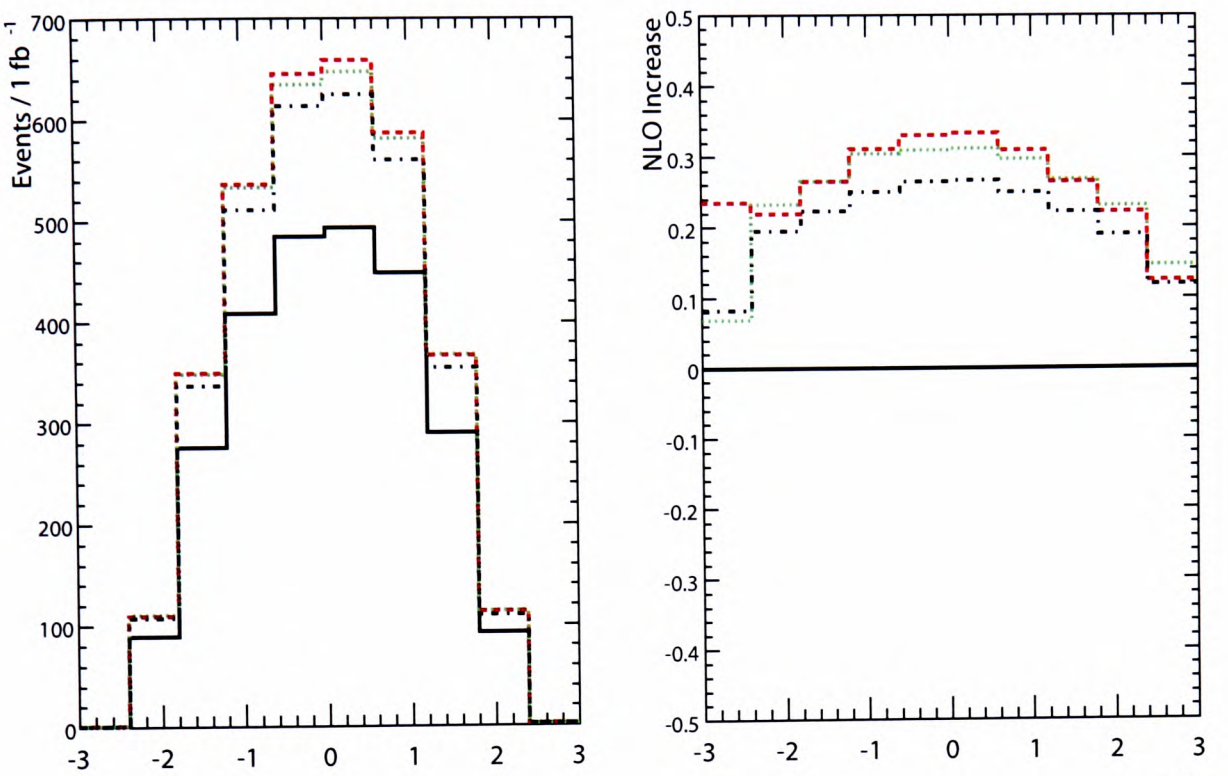


Fig. 7.6: Left: Four reweighted Y distributions for high-mass Drell-Yan dielectron final states: CTEQ6ll (LO, solid black), CTEQ61 (NLO, dashed-dotted black), MRST2004NLO (NLO, dotted green) and ZEUS2005-ZJ (NLO, dashed red). For the NLO PDF sets the distributions have also been reweighted with analytical k-factors describing NLO Monte Carlo. Right: The relative differences of the reweighted distributions compared to the original one: CTEQ6ll (solid black), CTEQ61 (dashed-dotted black), MRST2004NLO (dotted green) and ZEUS2005-ZJ (dashed red).

7.4 PDF Uncertainties on the Drell-Yan Cross Section

In addition to NLO effects, the precision of the Standard Model prediction for the dileptonic cross-section at the LHC is limited by PDF uncertainties. The measured cross-section σ_X for any given event with the momentum transfer Q depends on the parton distribution functions f for parton a and b with flavour $flav$, each carrying the momentum fraction x, and the partonic cross-section $\sigma_{ab\to X}$ as follows [25]:

$$\sigma_X = \sum_{a,b} \int_0^1 dx_a dx_b f(x_a, flav_a, Q^2) f(x_b, flav_b, Q^2) \cdot \sigma_{ab\to X}(x_a, x_b, Q^2). \tag{7.7}$$

The analysed data set is a collection of Drell-Yan dielectron final states which were simulated with the full response of the ATLAS detector and the requirement that the invariant mass of the two electrons is greater than 150 GeV. The complete simulated sample contains data equivalent to an integrated luminosity of 2.7 fb^{-1}. In the first year of data taking with the ATLAS detector, an integrated luminosity of about 1 fb^{-1} is expected. In order to be consistent with other analyses which show the discovery potential for new physics in the first year, all distributions in this chapter were normalised to that value. The simulated data sample was generated with a LO PDF set, CTEQ6ll. The Monte Carlo (MC) generators for the Drell-Yan processes were Herwig [77] and Jimmy [78]. Herwig is a MC code for simulating hadron emission reactions, which include interfering gluons,

and Jimmy is a generator of multiple parton scattering events in hadron-hadron, photon-photon or photon-hadron events which is linked to Herwig.

Available computing power did not allow regeneration of the simulated data samples with all 40 PDF error sets. Thus, it was necessary to reweight the analysed events generated with set $PDF1$ according to set $PDF2$. This is, however, only possible for the hard process. The new weight is given by:

$$Weight = \frac{f_a^{PDF2}(x_a, flav_a, Q^2) \cdot f_b^{PDF2}(x_b, flav_b, Q^2)}{f_a^{PDF1}(x_a, flav_a, Q^2) \cdot f_b^{PDF1}(x_b, flav_b, Q^2)}. \tag{7.8}$$

This method of reweighting is common for the analysis of PDF uncertainties and was tested and used successfully for other processes [79]. The CTEQ error sets [67] are only available at the level of next-to-leading order. Thus, the hard processes generated with leading-order PDF sets were first reweighted to the central values of the next-to-leading order CTEQ61 PDF sets. The uncertainty on the resulting distribution was then evaluated by reweighting the events to the 40 corresponding error sets provided by the CTEQ collaboration. The 20 pairs of error sets are independent by construction. Thus, it is necessary to combine the relative uncertainties quadratically. However, special care has to be taken with asymmetric error sets. In this study the uncertainties have been added as follows [80]:

$$\sigma^+ = \sqrt{\sum_{i=1}^{20} [max(\sigma_i^+, \sigma_i^-, 0)]^2} \tag{7.9}$$

$$\sigma^{-} = \sqrt{\sum_{i=1}^{20} [max(-\sigma_i^{+}, -\sigma_i^{-}, 0)]^2} \tag{7.10}$$

Here, $\sigma_i^{\pm}$ is defined as the relative difference of the histogram with the reweighted histogram h_i and the central value h_0:

$$\sigma_i = \frac{h_i - h_0}{h_0}. \tag{7.11}$$

As can be seen in Fig. 7.7, the overall PDF uncertainty of the dileptonic cross section up to an invariant mass of 1000 GeV is between 4 and 8%. In Fig. 7.8 it can be seen that the PDF uncertainty for leptons in the central rapidity region is significantly higher than the uncertainty for larger η values. Here, η is given for the individual leptons. Furthermore, it is interesting to analyse the rapidity distribution Y of the combined dilepton pair. The uncertainty in Y is, in addition to its local maximum at the centre of the detector, also large at extreme values (Fig. 7.9). This is due to the fact that at least one quark needs to have a fairly large x in order to create a dilepton pair in this region of the phase space. PDF sets are generally poorly constrained for large x above about 0.1 (Fig. 7.1). Furthermore, the impact of different error eigenvectors was investigated. For low invariant masses up to 400 GeV eigenvector 30, which is dominated by the gluon uncertainty, is the most significant one (Fig. 7.14). For higher masses eigenvectors 21 and 7 become more important. These eigenvectors contain mainly contributions from the gluon

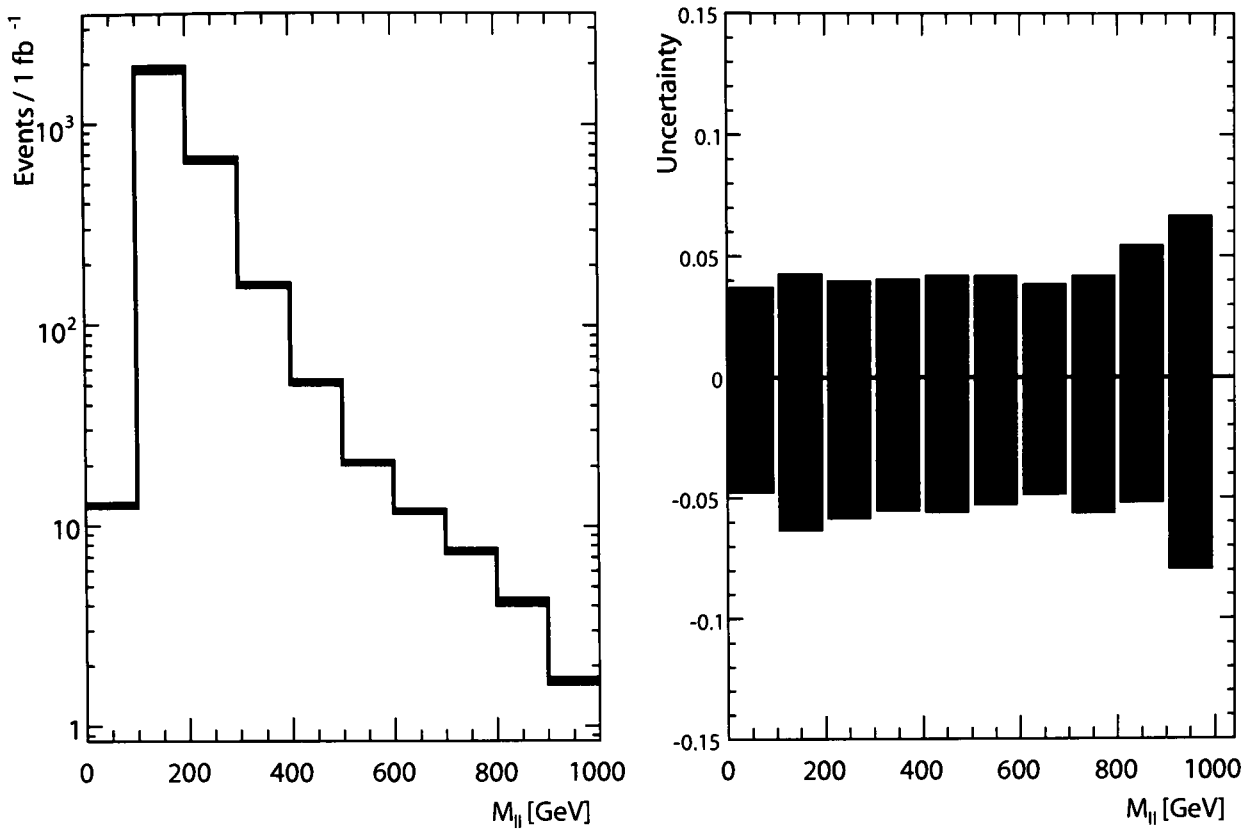


Fig. 7.7: Left: Fourty-one reweighted invariant mass distributions up to 1 TeV for high-mass Drell-Yan dielectron final states. Right: Overall uncertainty on the high-mass Drell-Yan distribution after quadratically adding all uncertainties.

and d-valence uncertainties, respectively.

7.5 Forward-backward asymmetry in $Z/\gamma \rightarrow ee$

Historically, measurements of forward-backward charge asymmetries A_{FB} were mainly performed at e^+e^--collider experiments. First evidence for γ-Z interference came from the observation of a non-vanishing asymmetry at PETRA (DESY) [81] and also at SLAC in elastic scattering experiments with polarised electrons [82]. Furthermore, this type of asymmetry was studied in proton-antiproton col-

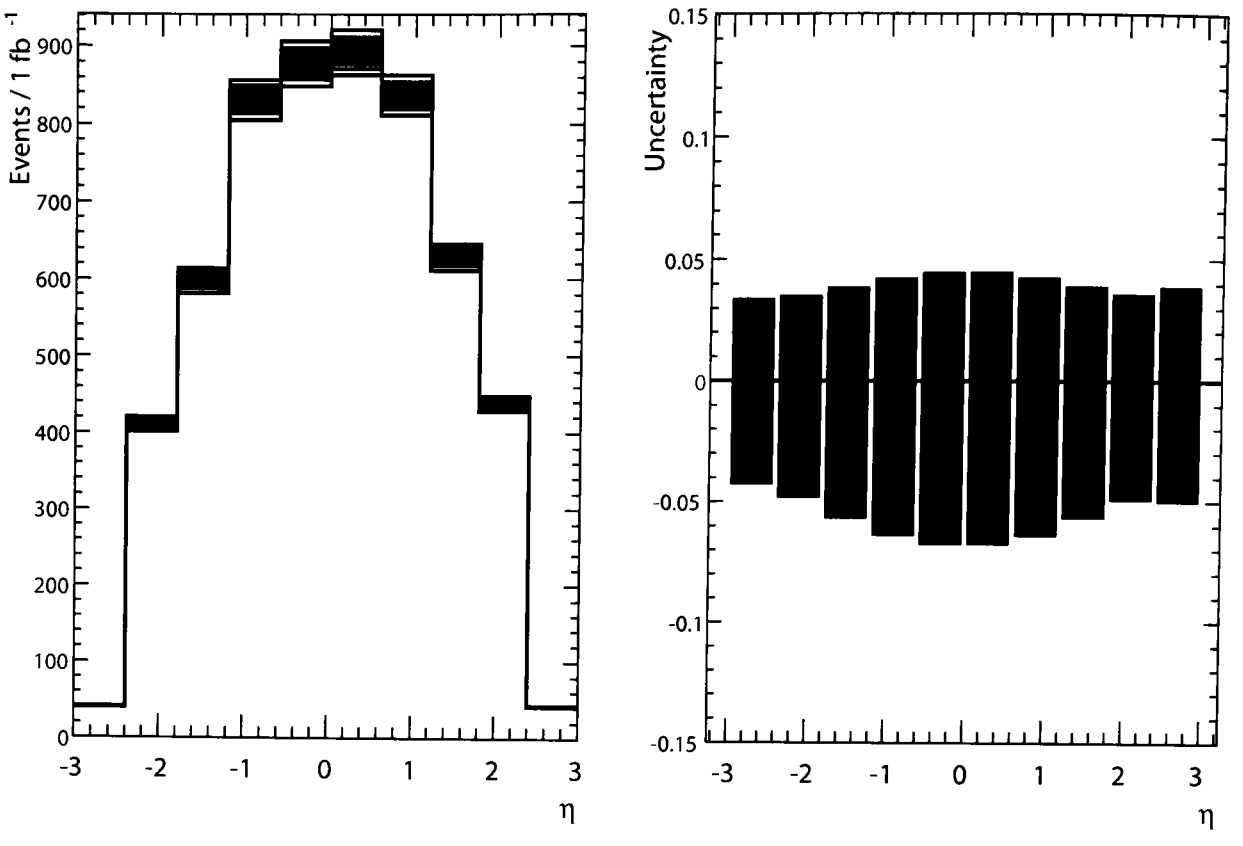


Fig. 7.8: Left: Fourty-one reweighted η distributions for high-mass Drell-Yan dielectron final states. Right: Overall uncertainty on the lepton η distribution after quadratically adding all uncertainties.

lisions at the Tevatron. It was for example crucial for Z'-studies [83]. In exotics searches the magnitude of the forward-backward asymmetry in the $\cos(\theta^*)$-distribution is generally used to measure spin-properties of new particles. It is known that also at LHC these studies will be important for new physics searches [84].

The scattering angle between the incoming quark and the negatively charged lepton in the centre-of-mass fame of the dilepton pair is defined as θ^*. However, since in proton-proton collisions the direction of the quark is not known a priori,

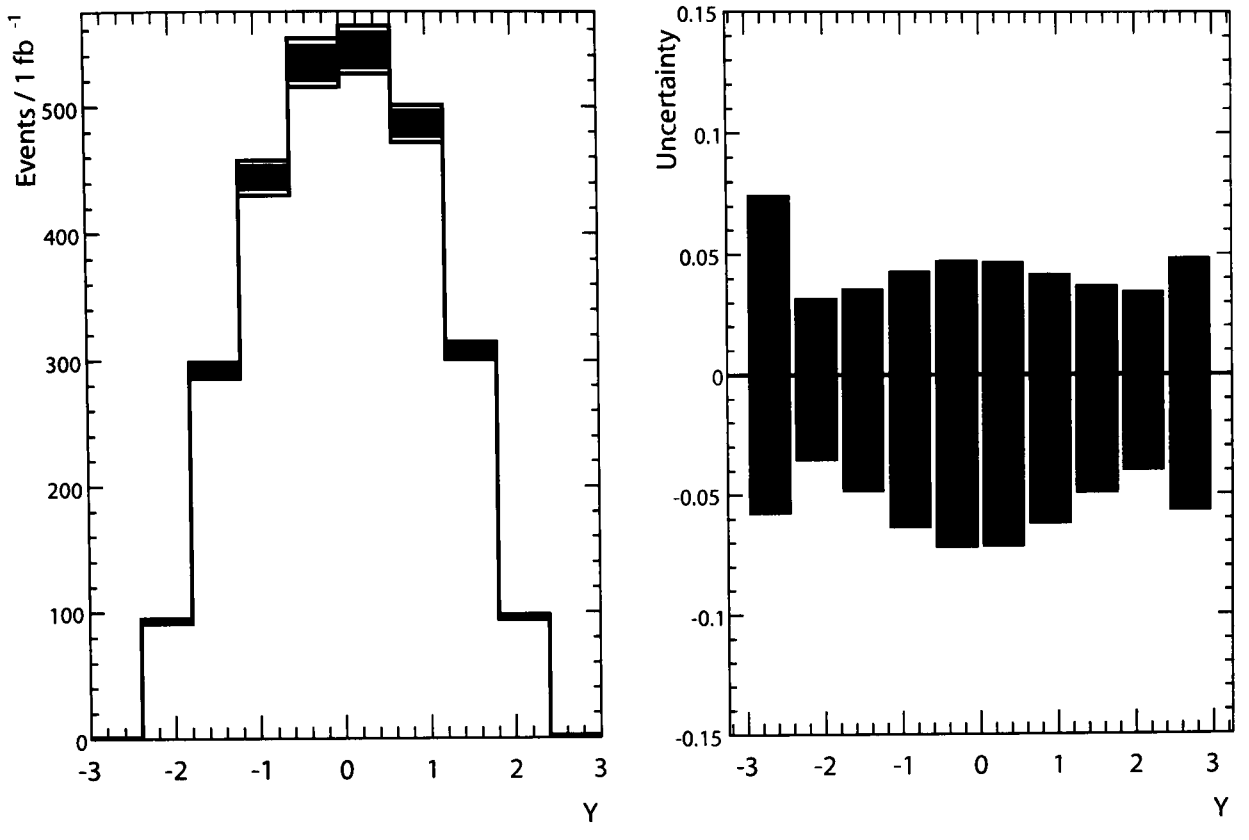


Fig. 7.9: Left: Fourty-one reweighted Y distributions for high-mass Drell-Yan dielectron final states. Right: Overall uncertainty on the lepton Y distribution after quadratically adding all uncertainties.

there is a two fold ambiguity in the measurement of θ^*. Due to the contributions from valance quarks inside the protons, the dominant up and down quarks have on average higher values of x than their corresponding anti-quarks. Therefore, a diluted $\cos(\theta^*)$-distribution can be measured by assuming the quark direction to be equal to that of the dilepton system. The larger the x, the larger the probability of finding a quark rather than an anti-quark in a proton. Thus, the above assumption is valid especially in events with large values of dilepton rapidity Y or with large invariant masses, as in these events one of the quarks must have a large value of x.

In the SM, Z/γ interferences results in a non-zero forward-backward asymmetry in the cos(θ^*)-distribution. There are two different methods to determine the forward-backward asymmetry. Firstly, it can be measured with an maximum likelihood fit to the cos(θ^*)-distribution given by:

$$\frac{d\sigma}{d\cos(\theta^*)} \propto \frac{3}{8}(1+\cos^2\theta^*) + A_{FB}\cos\theta^* \tag{7.12}$$

This methods is ideal for studies at Monte Carlo level. However, limits in the acceptance of the detector lead to a significant drop in the cos(θ^*)-distribution around 1 and -1. As the acceptance function is not a priori known a more simple definition of the forward-backward asymmetry [85] was used. With

$$F = \sigma(\theta^* > \pi/2) \tag{7.13}$$

$$B = \sigma(\theta^* < \pi/2) \tag{7.14}$$

the forward-backward asymmetry can be defined by the following equation:

$$A_{FB} = \frac{F-B}{F+B} \tag{7.15}$$

The statistical uncertainty on the A_{FB} measurement is given by:

$$\delta A_{FB} = \sqrt{(\delta_F A_{FB} \cdot dF)^2 + (\delta_B A_{FB} \cdot dB)^2} \quad (7.16)$$

$$= \frac{2}{(F+B)^2}\sqrt{B^2F + F^2B}. \quad (7.17)$$

In the SM, the forward-backward asymmetry is zero for very low invariant masses where the γ dominates, negative around the Z mass and about 0.61 for large invariant masses. However, due to the dilution arising from the unknown quark direction and due to detector effects, it is impossible to measure directly the theoretical values [84]. The dependence of the PDF uncertainties on these effects was studied by analysing four different scenarios which are explained below.

Using the reweighting techniques as described in Section 7.4, the PDF uncertainty on the $\cos(\theta^*)$ distribution was determined. In Fig. 7.12 and Fig. 7.13 (Fig. 7.10 and 7.11 show the corresponding NLO effects) it can be seen that neither the real $\cos(\theta^*)$-distribution nor the diluted distribution show a significant variation in their uncertainties over the whole range of phase space. In order to obtain the PDF uncertainty on the forward-backward asymmetry measurement, Eq. 7.15 was applied to all fourty reweighted $\cos(\theta^*)$-distributions. The RMS of the resulting A_{FB} distribution gives the uncertainty on that measurement. This method was applied to four distributions which all include detector effects:

- Non-diluted distribution which assumes the quark direction to be known

- ◇ Diluted distribution in the full range of kinematics
- ◇ Diluted distribution requiring $Y > 1.5$
- ◇ Diluted distribution requiring $M_{ll} > 300$ GeV

In Table 7.1, the results for these four measurements are shown. The non-diluted distribution (Fig. 7.12), which is not measurable, just shows the detector effects on the asymmetry measurement. The asymmetry is about 0.1 smaller than it is expected from theory which is in accordance with similar studies presented in Ref. [84]. As expected, the diluted distribution (Fig. 7.13) has a comparatively small asymmetry. Due to kinematics, the asymmetry increases for large values of Y or invariant mass. However, in these regions of phase space not much statistics will be available during the first year of data taking. As can be seen in Table 7.1, the PDF uncertainty $\delta_{PDF}A_{FB}$ is significantly higher in the mass range below 300 GeV, even for large values of Y, than in the rest of the phase space. However, in all four cases the PDF uncertainty on the forward-backward asymmetry is more than one order smaller than the statistical uncertainty. Furthermore, measurements performed with PDF sets from MRST and ZEUS showed only differences within 5 times the CTEQ uncertainty as can be seen in Table 7.2.

It can thus be safely concluded that the PDF uncertainty on the measurement of the forward-backward asymmetry is negligible compared to statistical uncertainties in the first year of data taking. This conclusion confirms an observation made in Ref. [84] which, however, did not analyse PDF uncertainties systematically.

Forward-backward asymmetry			
Sample	A_{FB}^{Mean}	$\delta_{PDF}A_{FB}$	$\delta_{stat}A_{FB}$
Non-diluted	0.4916	0.0004	0.0164
Diluted	0.1259	0.0015	0.0187
Diluted, $Y > 1.5$	0.1774	0.0018	0.0461
Diluted, $M_{ll} > 300$ GeV	0.4690	0.0004	0.0607

Tab. 7.1: The mean value, the PDF and statistical uncertainty of the forward-backward asymmetry measurement is shown for four different scenarios.

Forward-backward asymmetry				
PDF Group	*Non-dil.*	*Dil.*	*Dil.*, $Y > 1.5$	*Dil.*, $M_{ll} > 300$ GeV
MRST2004NLO	0.4912	0.1229	0.1732	0.4680
ZEUS2005_ZJ	0.4927	0.1295	0.1865	0.4692
CTEQ6l	0.4912	0.1261	0.1776	0.4689

Tab. 7.2: Forward-backward asymmetry for MRST2004NLO, ZEUS2005_ZJ and CTEQ6l.

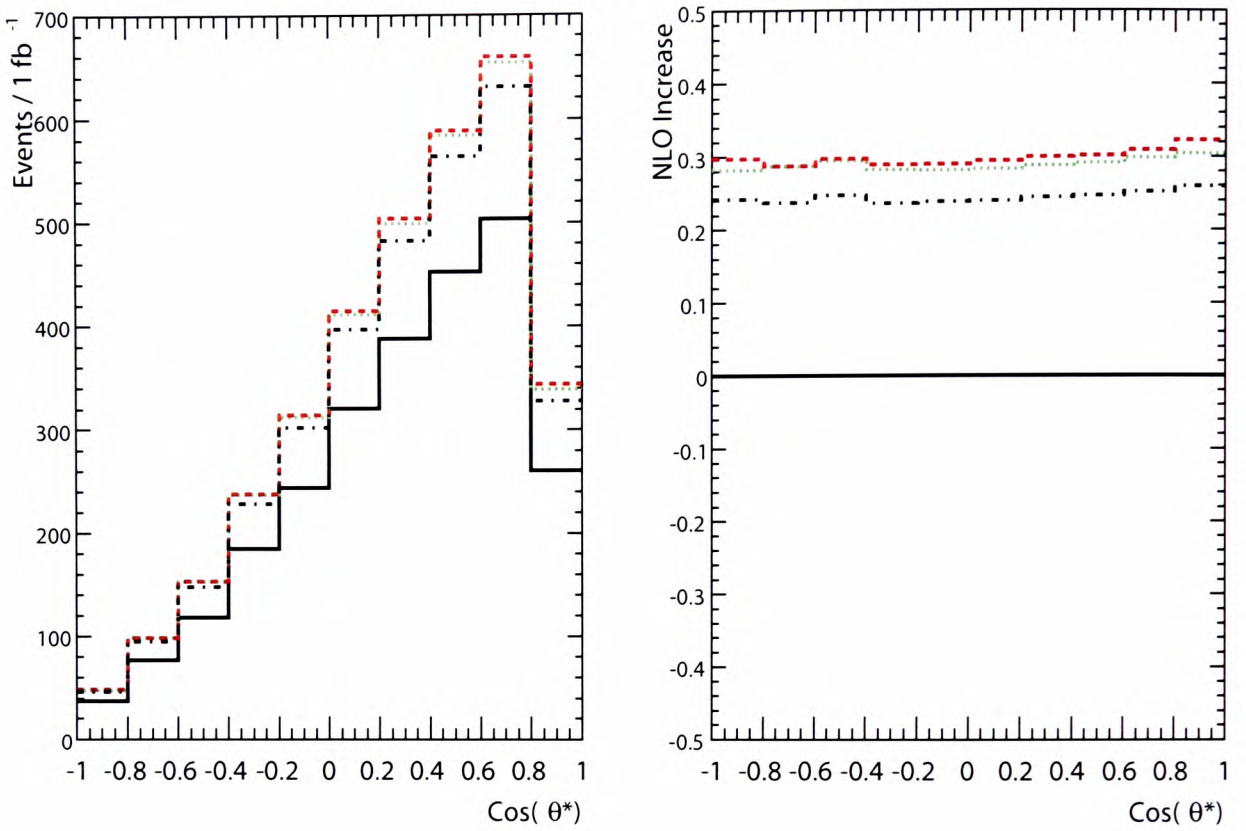


Fig. 7.10: Left: Four reweighted cos(θ^*) distributions for high-mass Drell-Yan dielectron final states: CTEQ6ll (LO, solid black), CTEQ61 (NLO, dashed-dotted black), MRST2004NLO (NLO, dotted green) and ZEUS2005-ZJ (NLO, dashed red). For the NLO PDF sets the distributions have also been reweighted with analytical k-factors describing NLO Monte Carlo. Right: The relative differences of the reweighted distributions compared to the original one: CTEQ6ll (solid black), CTEQ61 (dashed-dotted black), MRST2004NLO (dotted green) and ZEUS2005-ZJ (dashed red).

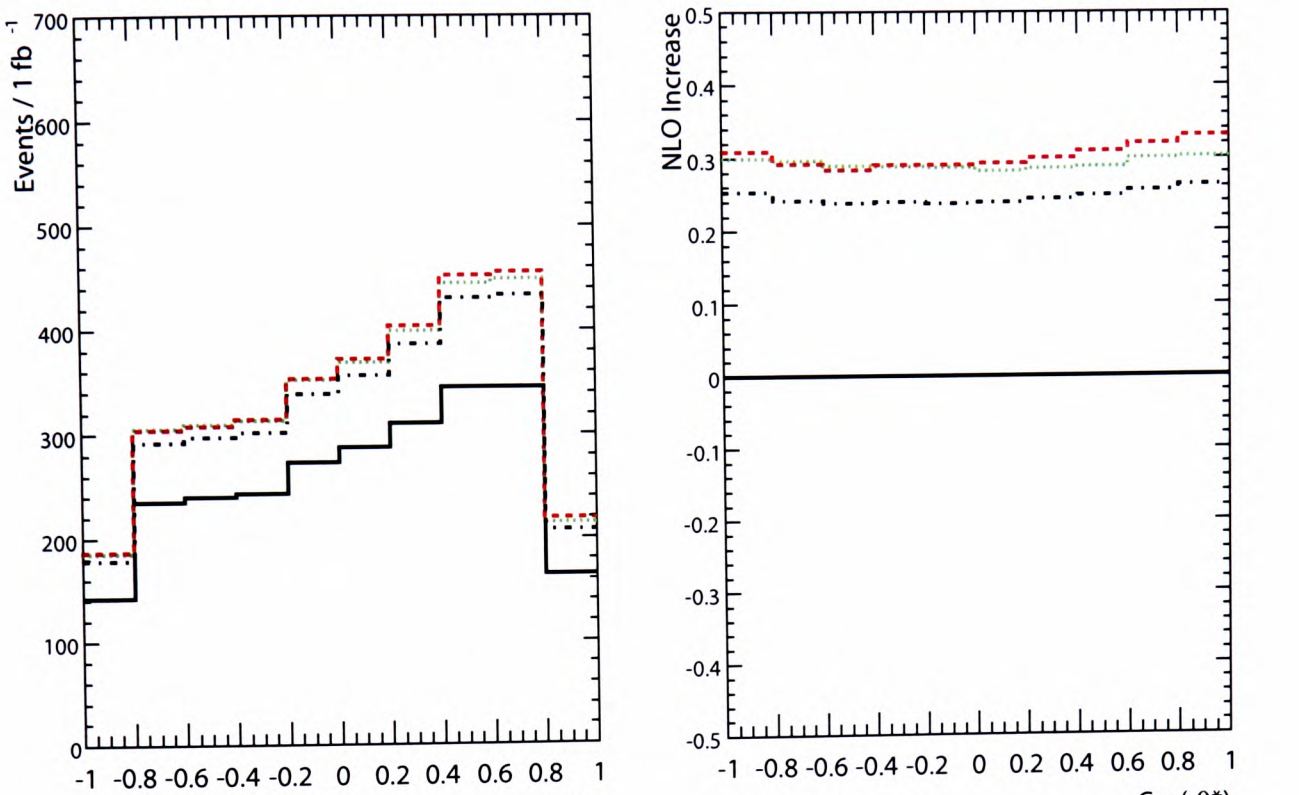


Fig. 7.11: Left: Four reweighted diluted cos(θ^*) distributions for high-mass Drell-Yan dielectron final states: CTEQ6ll (LO, solid black), CTEQ61 (NLO, dashed-dotted black), MRST2004NLO (NLO, dotted green) and ZEUS2005-ZJ (NLO, dashed red). For the NLO PDF sets the distributions have also been reweighted with analytical k-factors describing NLO Monte Carlo. Right: The relative differences of the reweighted distributions compared to the original one: CTEQ6ll (solid black), CTEQ61 (dashed-dotted black), MRST2004NLO (dotted green) and ZEUS2005-ZJ (dashed red).

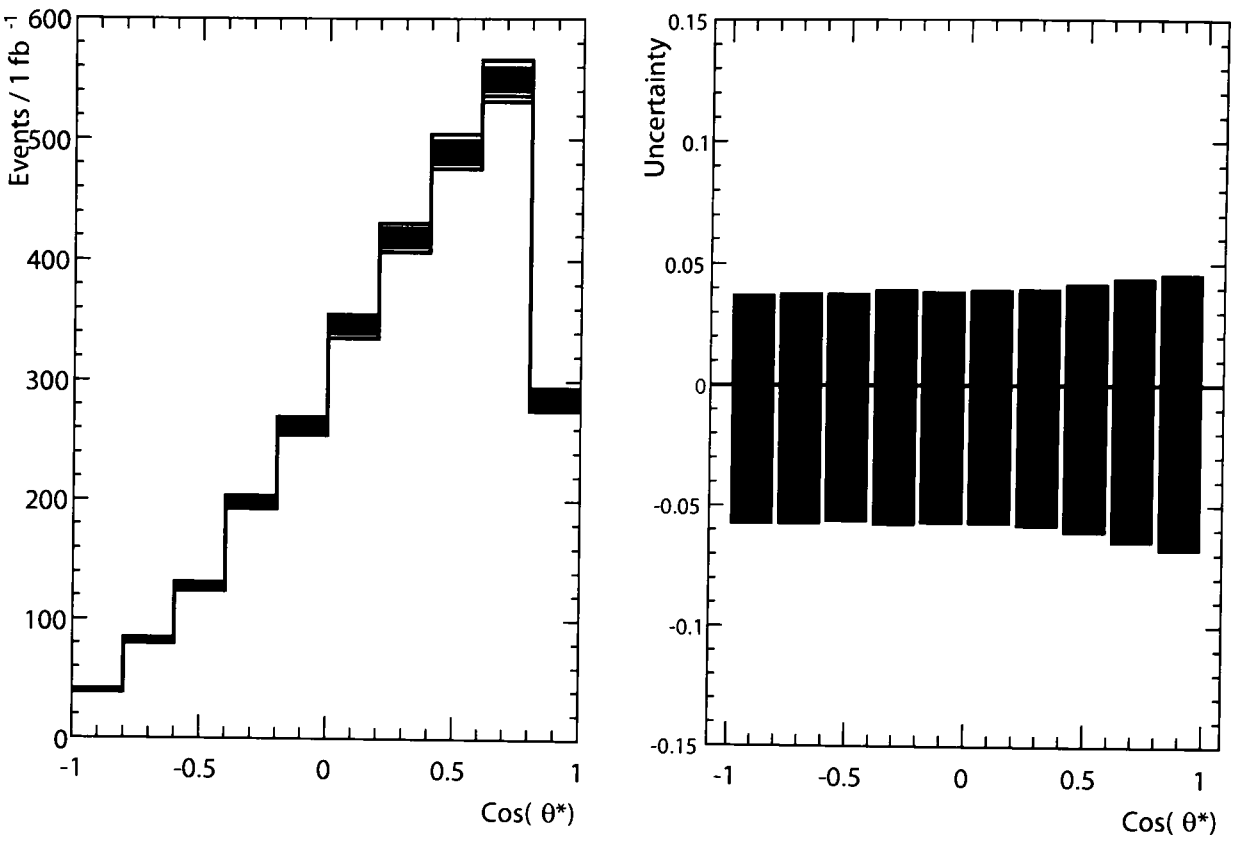


Fig. 7.12: Left: Fourty-one reweighted cos(θ^*) distributions for high-mass Drell-Yan dielectron final states. Right: Overall uncertainty on the cos(θ^*) distribution after quadratically adding all uncertainties (Eq. 7.9 and 7.10). This distribution assumes the knowledge of the quark direction and is thus not measurable.

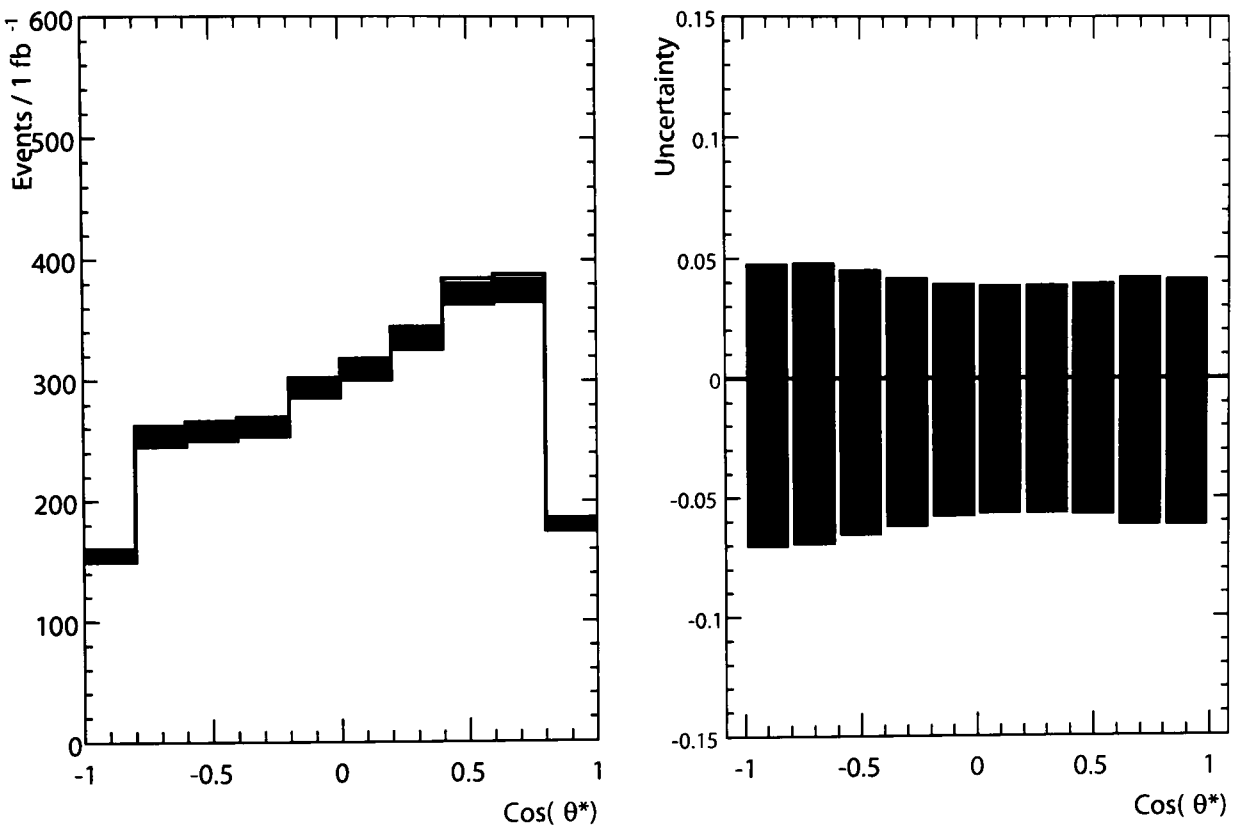


Fig. 7.13: Left: Fourty-one reweighted diluted $\cos(\theta^*)$ distributions for high-mass Drell-Yan dielectron final states. Right: Overall uncertainty on the diluted $\cos(\theta^*)$ distribution after quadratically adding all uncertainties (Eq. 7.9 and 7.10). This distribution is measurable.

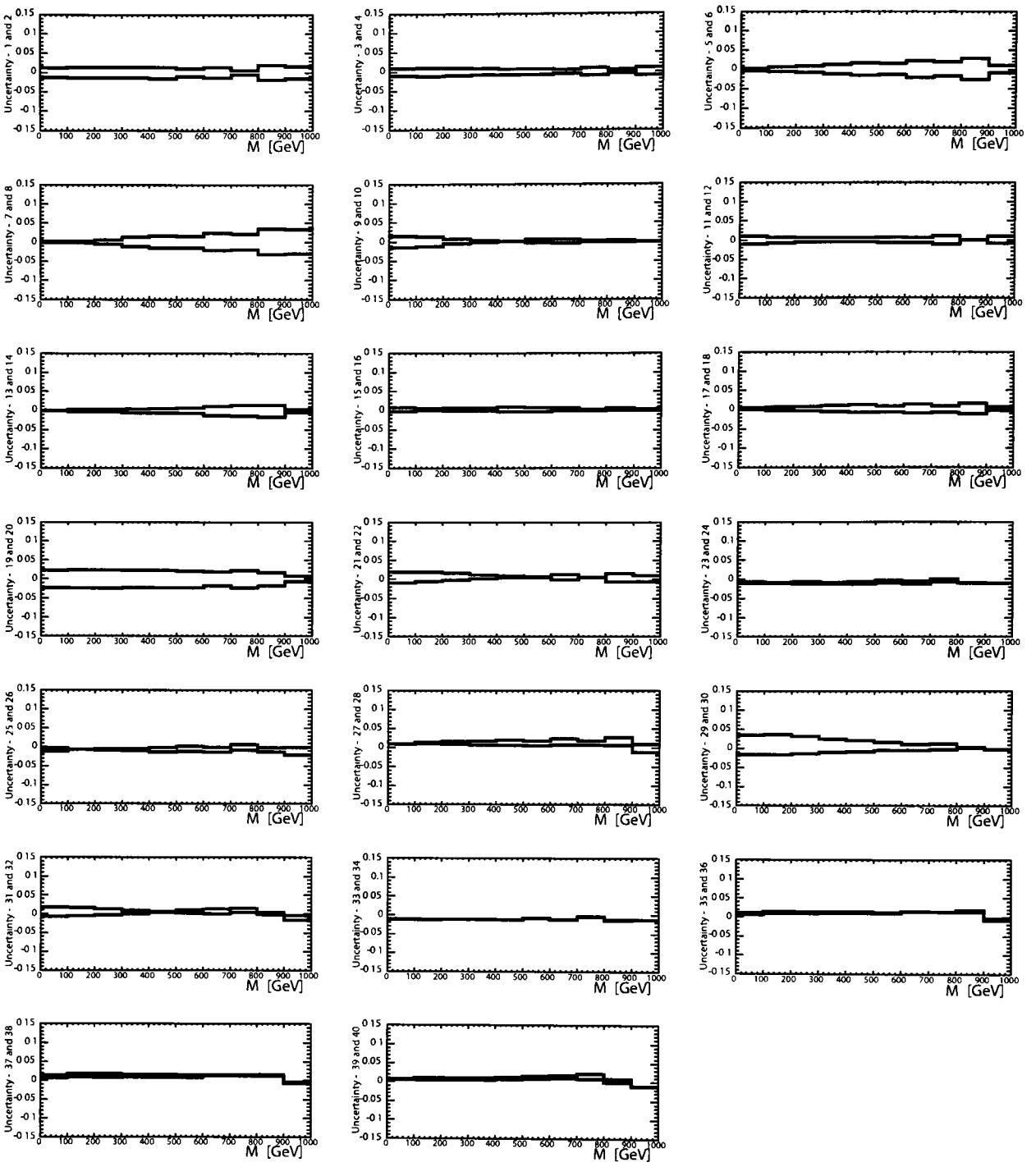


Fig. 7.14: For the 20 free PDF parameters, uncertainties on the high-mass Drell-Yan distribution are presented for each of the two corresponding error sets. For example error set 1 and 2 belong to the first PDF parameter.

8. CONCLUSIONS

The start of the Large Hadron Collider commences an exciting new period of particle physics research. The ATLAS detector is ideally suited for the discovery of new physics which has been predicted by various theories. At the beginning of data taking the main focus will be on two aspects: The understanding of the ATLAS detector performance and searches for new physics in simple signatures. This thesis contributes to both.

Firstly, a robust track based alignment algorithm has been developed and implemented into the ATLAS software framework. It was used to successfully align the silicon modules in the Combined Test Beam setup. Furthermore, the algorithm was applied in order to align part of the SCT silicon modules with tracks from cosmic rays. The alignment constants that were produced can be used at the start of LHC in order to reduce systematic distortions right from the beginning. In addition, simulation studies were performed that prove that the Robust Alignment algorithm will be able to align all ATLAS silicon detectors. The precision of the algorithm depends on the statistics used. It is expected that even with early data a statistical uncertainty of the order of 1 μm in the precise coordinate may be

achieved. However, it has been shown that systematic uncertainties dominate the alignment process. The main challenge will be to control systematic distortions which are weakly constrained by track based alignment algorithms.

Secondly, the parton distribution uncertainties for high-mass Drell-Yan processes were estimated. The uncertainty on the invariant mass distribution is between 4% and 8%. The central η regions and the regions of large dilepton rapidities Y have the largest PDF uncertainties. The PDF uncertainty for the measurement of the forward-backward asymmetry is negligible compared to the statistical uncertainty on that measurement, at least for the first years of data taking. NLO contributions in the Monte Carlo simulation lead to 24% to 36% larger cross-sections with the most significant effects in the central η region.

ATLAS	A Toroidal LHC ApparatuS, 1.2
CDC	Calibration Data Challenge, 6.0
CERN	European Organization for Nuclear Research, 1.1
CMM	Coordinate Measuring Machine, 1.2
CP	Charge-Parity-Symmetry, 1.1
CPU	Central Processing Unit, 2.3
CSC	Computing System Commissioning, 6.0
CTB	ATLAS Combined Test Beam, 4.0
CTEQ	Coordinated Theoretical-Experimental project on QCD, 7.1
DESY	Deutsches Elektronen Synchrotron, 1.1
DGLAP	Dokshitzer-Gribov-Lipatov-Altarelli-Parisi Equations, 7.0
DIS	Deep Inelastic Scattering, 7.0
ED	Extra Dimensions, 7.0
ESD	Event Summary Data, 2.3
FSI	Frequency Scanning Interferometry, 1.2
HERA	Hadron Electron Ring Accelerator Facility, 7.0
jobOption	Python script to define input and output data as well as configure Athena services and algorithms, 1.2
LEP	Large Electron Positron Collider, 1.1
LHC	Large Hadron Collider, 1.2
LO	Leading order calculations, 7.3
MC	Monte Carlo, 7.3
MCS	Multiple Coulomb Scattering, 3.2

MRST	Martin Roberts Stirling Thorne - PDF global fitting team, 7.1
MSSM	Minimal Supersymmetric Standard Model, 1.1
NLO	Next-to-leading order calculations, 7.3
PIXEL	Silicon Pixel Detector, 1.2
QCD	Quantum Chromodynamics, 1.1
QFT	Quantum Field Theories, 1.1
RAL	Rutherford Appleton Laboratory, 1.2
RMS	Root Mean Square, 1.2, 3.2
RobustAlignAlg	Name of the Robust Alignment algorithm, 2.0
SCT	Semi-Conductor Tracker, silicon strip detector, 1.2
SLC	Stanford Linear Collider, 1.1
SLHC	Super Large Hadron Collider, 2.3
SM	Standard Model, 1.1
SUSY	Supersymmetry, 7.0
TDC	Time to Digital Converter, 5.9
TRT	Transition Radiation Tracker, transition radiation detector, 1.2
WMAP	Wilkinson Microwave Anisotropy Probe, 1.1
ZEUS	Collaboration at HERA, 7.1

APPENDIX

A. ROBUST ALIGNMENT OPTIONS

trackfitter	Name of the track fitter
updator	Name of the updator tool
propagator	Name of the propagator tool
extrapolator	Name of the extrapolator tool
inputname	Name of the input track collection
ROOToutput	Write ROOT output
ReadDBPoolFile	Read in alignment constants
WriteDBPoolFile	Write out alignment constants
UseTrackCuts	Use cuts on tracks
useCTB	Align CTB setup with particular CTB algorithm
usePIXEL	Align PIXEL detector in any setup
useSCT	Align SCT detector in any setup
useLocalFrameResiduals	Use residuals in each local frame of the SCT strip
usePIXELLocalX	Align PIXEL detector in local X direction
usePIXELLocalY	Align PIXEL detector in local Y direction
usePIXELLocalZ	Align PIXEL detector in local Z direction
useSCTLocalX	Align SCT detector in local X direction
useSCTLocalY	Align SCT detector in local Y direction
useSCTLocalZ	Align SCT detector in local Z direction
locXPIXELResidualMax	Use only PIXEL local X residuals smaller than given value
localYPIXELResidualMax	Use only PIXEL local Y residuals smaller than given value
locXSCTResidualMax	Use only SCT local X residuals smaller than given value
locYSCTResidualMax	Use only SCT local Y residuals smaller than given value

residualWeight	Relative weight of residuals, only for useCTB
overlapResidualWeight	Relative weight of overlap residuals, only for useCTB
xShiftDamping	Reduce applied correction in local X by a factor of given value
yShiftDamping	Reduce applied correction in local Y by a factor of given value
zShiftDamping	Reduce applied correction in local Z by a factor of given value
minimumHitsPerModule	Only consider modules with more hits than given value for alignment
UnbiasedResiduals	Use unbiased residuals
TrueUnbiasedResiduals	Make both SCT strips unbiased simultaneously
removeEdgeChannels	Remove edge channels for PIXEL and SCT
FilenameBasis	File name basis for alignment constants file
IterationNumber	Number of iteration
TextFileNameBasis	Name basis of files for distributed alignment
TextFileWriteNumber	Number of file for writing distributed alignment information
TextFileReadStartNumber	Start with this file when reading in
TextFileReadEndNumber	End with this file when reading in
DoWriteTextFile	Do write text file and set minimum hits per module to zero
DoReadTextFiles	Read in text files - Ignores all events, so one event is enough
DoWriteConstantsTextFile	Do write constants in standard text-file
ShiftVertex	Shift the whole detector
VertexXShift	Value for the shift in global X
VertexYShift	Value for the shift in global Y
VertexZShift	Value for the shift in global Z
NSigmaCut	Cut on the acceptance for the ratio of calculated shift to its uncertainty

B. ROBUST ALIGNMENT OUTPUT

The **Residuals** tree contains information about the hit residuals and their corresponding modules.

Residuals/BEc	Hit is in barrel (0) or endcap (± 2)
Residuals/DetType	Hit is in PIXEL (1) or SCT (2)
Residuals/Layer	Layer number of hit
Residuals/Ring	Ring number of hit
Residuals/Sector	Sector number of hit
Residuals/Side	Side number of hit
Residuals/Z	Global Z coordinate of hit
Residuals/Phi	Global ϕ coordinate of hit
Residuals/R	Global R coordinate of hit
Residuals/LocalXRes	Local X residual
Residuals/LocalYRes	Local Y residual
Residuals/LocalXResE	Error on local X residual
Residuals/LocalYResE	Error on local Y residual
Residuals/Momentum	Momentum of track associated to the hit
Residuals/PT	P_T of track associated to the hit
Residuals/Eta	η of track associated to the hit

The **Tracks** tree contains information about all reconstructed tracks that have been used for alignment.

Tracks/Momentum	Momentum of reconstructed tracks
Tracks/Charge	Charge of reconstructed tracks
Tracks/PT	Transverse momentum of reconstructed tracks
Tracks/Eta	η of reconstructed tracks
Tracks/D0	Impact parameter reconstructed tracks
Tracks/Z0	Z_0 reconstructed tracks
Tracks/Phi	ϕ reconstructed tracks
Tracks/Theta	θ reconstructed tracks
Tracks/QOverP	Charge over momentum reconstructed tracks

The **Shifts** tree contains information about the actual shifts applied to the modules.

Shifts/ShiftsX	Applied module shift in local X
Shifts/ShiftsY	Applied module shift in local Y
Shifts/ShiftsZ	Applied module shift in local Z
Shifts/BEc	Barrel (0) or endcap (± 2) shifted module
Shifts/DetType	Shifted module is in PIXEL (1) or SCT (2)
Shifts/Layer	Layer number of shifted module
Shifts/Ring	Ring number of shifted module
Shifts/Sector	Sector number of shifted module
Shifts/Side	Side number of shifted module

The **OverlapResiduals** tree contains information about all overlap residuals and their corresponding modules.

OverlapResiduals/OvBEc	Overlap hit is in barrel (0) or endcap (± 2)
OverlapResiduals/OvDetType	Overlap hit is in PIXEL (1) or SCT (2)
OverlapResiduals/OvLayer	Layer number of overlap hit
OverlapResiduals/OvRing	Ring number of overlap hit
OverlapResiduals/OvSector	Sector number of overlap hit
OverlapResiduals/OvSide	Side number of overlap hit
OverlapResiduals/OvZ	Global Z coordinate of overlap hit
OverlapResiduals/OvPhi	Global ϕ coordinate of overlap hit
OverlapResiduals/OvR	Global R coordinate of overlap hit
OverlapResiduals/Overlap	Overlap type is local X (1) or local Y (2)
Ov.Res./LocalYOverlapResidual	Local X overlap residual
Ov.Res./LocalXOverlapResidual	Local Y overlap residual
Ov.Res./OvMomentum	Momentum of track associated to the overlap hit
OverlapResiduals/OvPT	P_T of track associated to the overlap hit
OverlapResiduals/OvEta	η of track associated to the overlap hit

The **Contributions** tree contains information about the individual contributions from residuals and overlap residuals. It can be used to calculate the overall uncertainty on the module shifts.

Contributions/ContributionsLocalX	Local X (Y) residual contribution to the module shift
Contributions/ContributionsLocalXE	Local X (Y) residual contribution to the error on the module shift
Contr./ContributionsLocalXOverlap	Local X overlap residual contribution to the module shift
Contr./ContributionsLocalXOverlapE	Local X overlap residual contribution to the error on the module shift
Contr./ContributionsLocalYOverlap	Local Y overlap residual contribution to the module shift
Contr./ContributionsLocalYOverlapE	Local Y overlap residual contribution to the error on the module shift
Contr./ContributionsLocalXAllOverlap	Contribution from local X overlap residuals that form a ring
Contributions/BEc	Barrel (0) or endcap (± 2) shifted module
Contributions/DetType	Shifted module is in PIXEL (1) or SCT (2)
Contributions/Layer	Layer number of shifted module
Contributions/Ring	Ring number of shifted module
Contributions/Sector	Sector number of shifted module
Contributions/Side	Side number of shifted module
Contributions/XY	Shift in local X (1) or Y (2)

The **Phi** tree is a special tree used for the analysis of ganged PIXEL hits.

Phi/Phi0	Global ϕ-coordinate for hit in PIXEL layer 0
Phi/Phi1	Global ϕ-coordinate for hit in PIXEL layer 1
Phi/Phi2	Global ϕ-coordinate for hit in PIXEL layer 2
Phi/Ganged	Ganged (1) or normal (0) PIXEL hit
Phi/FitQuality	Fit quality of track with hits in each PIXEL layer

C. FULL DETECTOR ALIGNMENT MONITORING

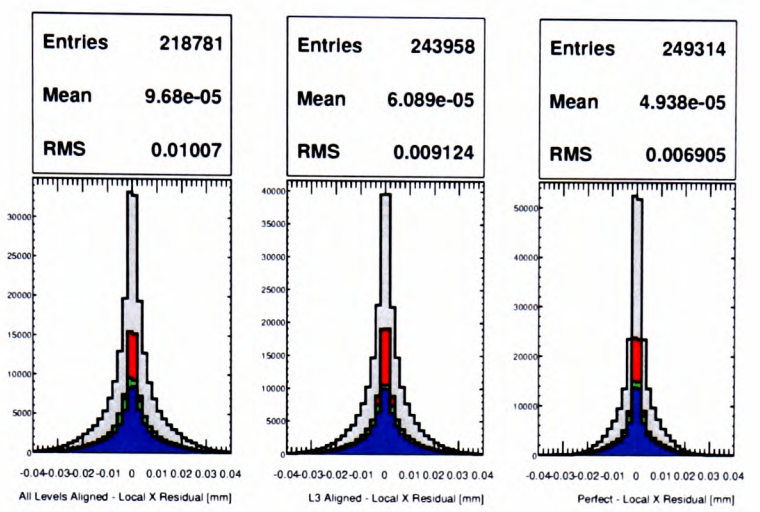


Fig. C.1: Biased PIXEL barrel local X residuals after CSC alignment on all levels (left), on level 3 (middle) and with the true geometry (right). All barrels together (grey) and the individual layers are shown: layer 0 (red), layer 1 (green) and layer 2 (blue).

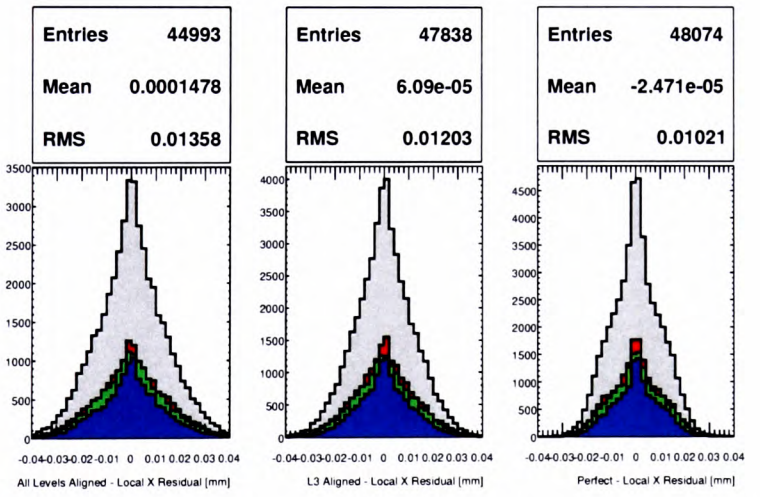


Fig. C.2: Biased PIXEL endcap local X residuals after CSC alignment on all levels (left), on level 3 (middle) and with the true geometry (right).All endcap disks together (grey) and the individual layers are shown: layer 0 (red), layer 1 (green) and layer 2 (blue).

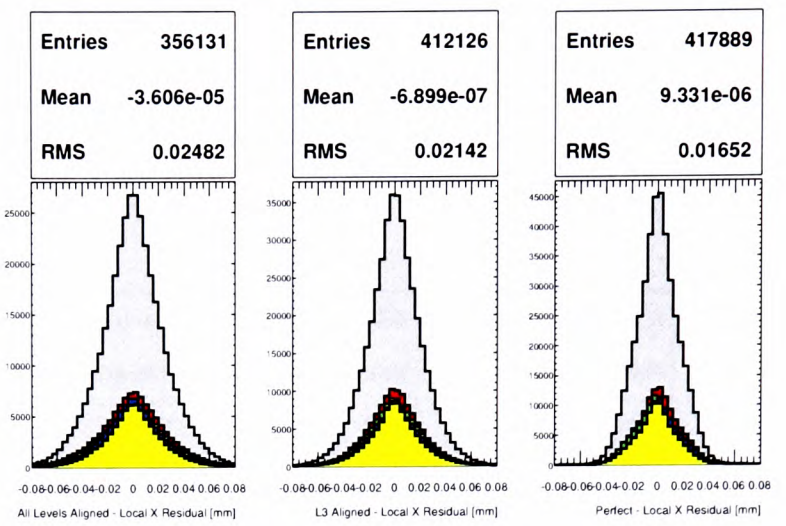


Fig. C.3: Biased SCT barrel local X residuals after CSC alignment on all levels (left), on level 3 (middle) and with the true geometry (right). All barrels together (grey) and the individual layers are shown: layer 0 (red), layer 1 (green), layer 2 (blue) and layer 3 (yellow).

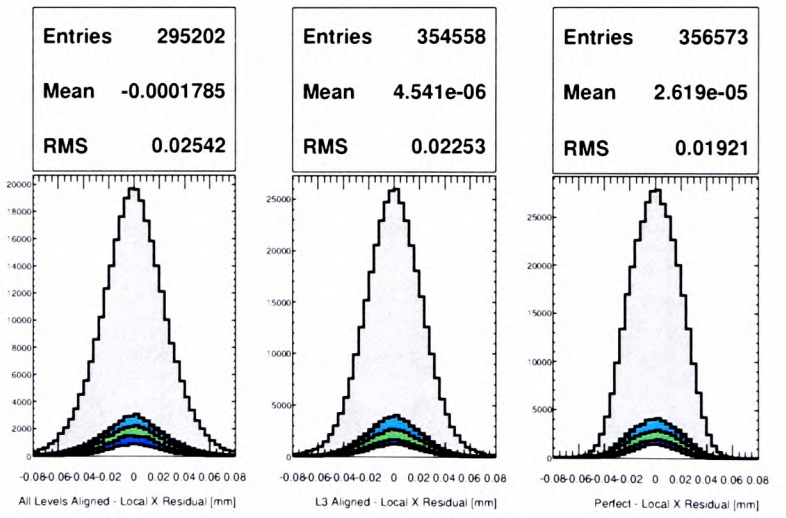


Fig. C.4: Biased SCT endcap local X residuals after CSC alignment on all levels (left), on level 3 (middle) and with the true geometry (right). All endcap disks together (grey) and the individual layers are shown: layer 0 (red), layer 1 (green), layer 2 (blue), layer 3 (yellow), layer 4 (magenta), layer 5 (light blue), layer 6 (dark green), layer 7 (purple) and layer 8 (white).

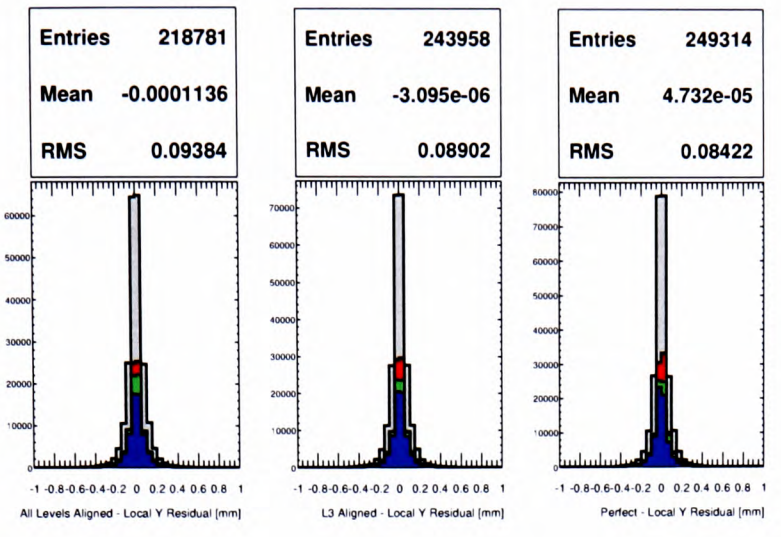


Fig. C.5: Biased PIXEL barrel local Y residuals after CSC alignment on all levels (left), on level 3 (middle) and with the true geometry (right). All barrels together (grey) and the individual layers are shown: layer 0 (red), layer 1 (green) and layer 2 (blue).

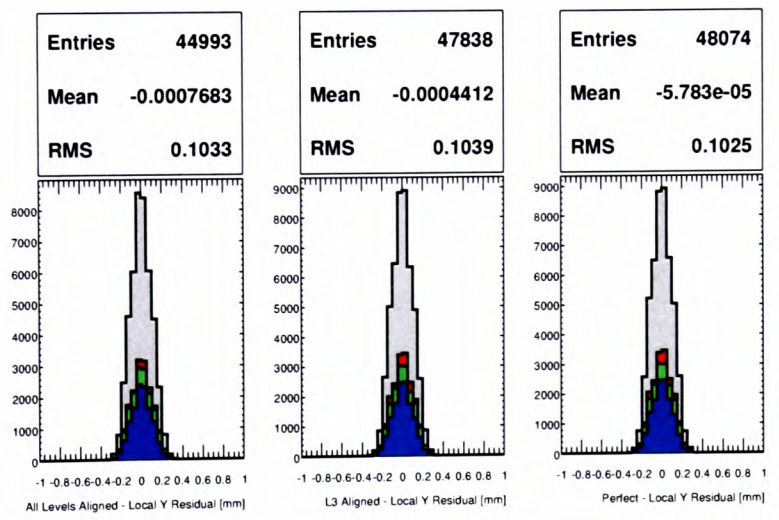


Fig. C.6: Biased PIXEL endcap local Y residuals after CSC alignment on all levels (left), on level 3 (middle) and with the true geometry (right).All endcap disks together (grey) and the individual layers are shown: layer 0 (red), layer 1 (green) and layer 2 (blue).

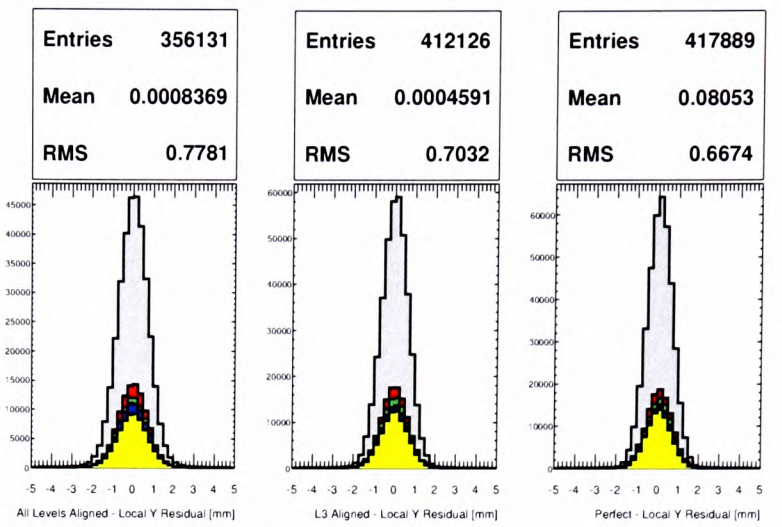


Fig. C.7: Biased SCT barrel local Y residuals after CSC alignment on all levels (left), on level 3 (middle) and with the true geometry (right). All barrels together (grey) and the individual layers are shown: layer 0 (red), layer 1 (green), layer 2 (blue) and layer 3 (yellow).

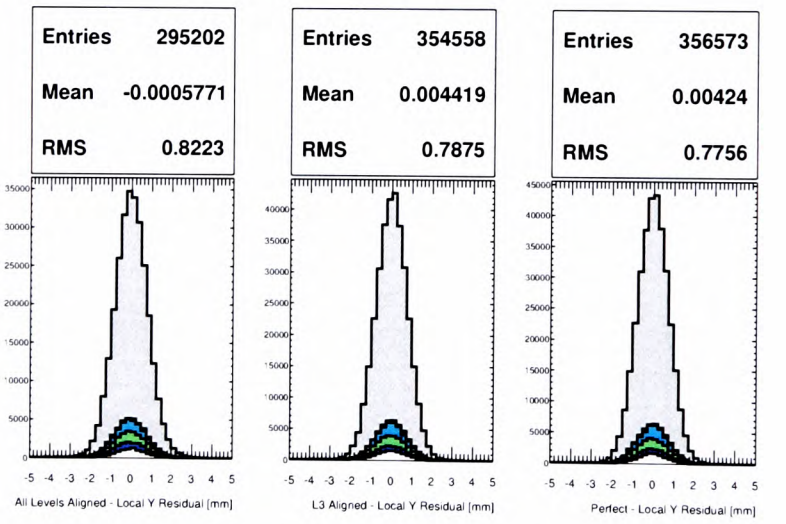


Fig. C.8: Biased SCT endcap local Y residuals after CSC alignment on all levels (left), on level 3 (middle) and with the true geometry (right). All endcap disks together (grey) and the individual layers are shown: layer 0 (red), layer 1 (green), layer 2 (blue), layer 3 (yellow), layer 4 (magenta), layer 5 (light blue), layer 6 (dark green), layer 7 (purple) and layer 8 (white).

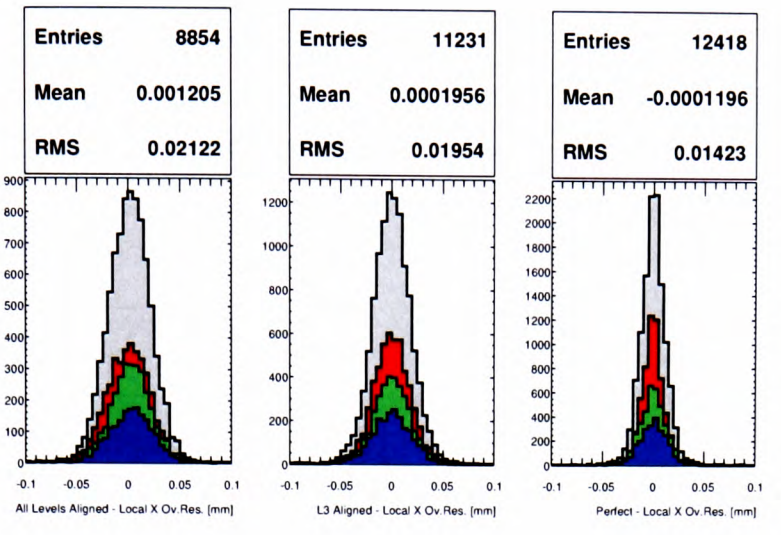


Fig. C.9: Biased PIXEL barrel local X overlap residuals after CSC alignment on all levels (left), on level 3 (middle) and with the true geometry (right). All barrels together (grey) and the individual layers are shown: layer 0 (red), layer 1 (green) and layer 2 (blue).

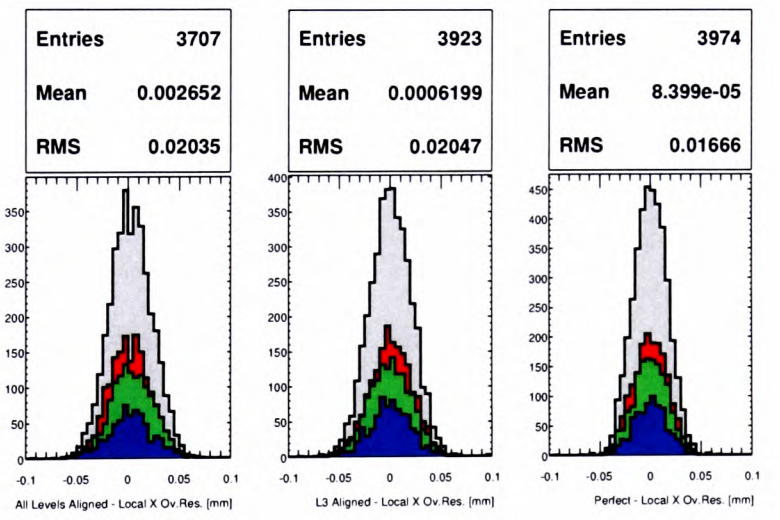


Fig. C.10: Biased PIXEL endcap local X overlap residuals after CSC alignment on all levels (left), on level 3 (middle) and with the true geometry (right).All endcap disks together (grey) and the individual layers are shown: layer 0 (red), layer 1 (green) and layer 2 (blue).

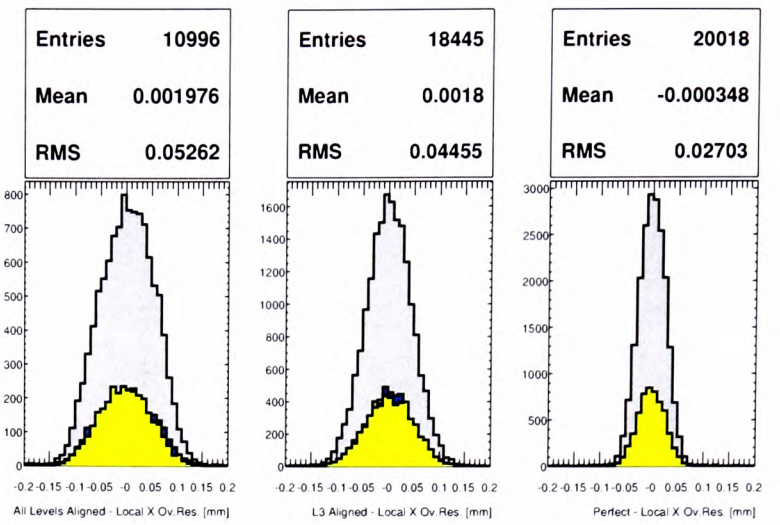


Fig. C.11: Biased SCT barrel local X overlap residuals after CSC alignment on all levels (left), on level 3 (middle) and with the true geometry (right). All barrels together (grey) and the individual layers are shown: layer 0 (red), layer 1 (green), layer 2 (blue) and layer 3 (yellow).

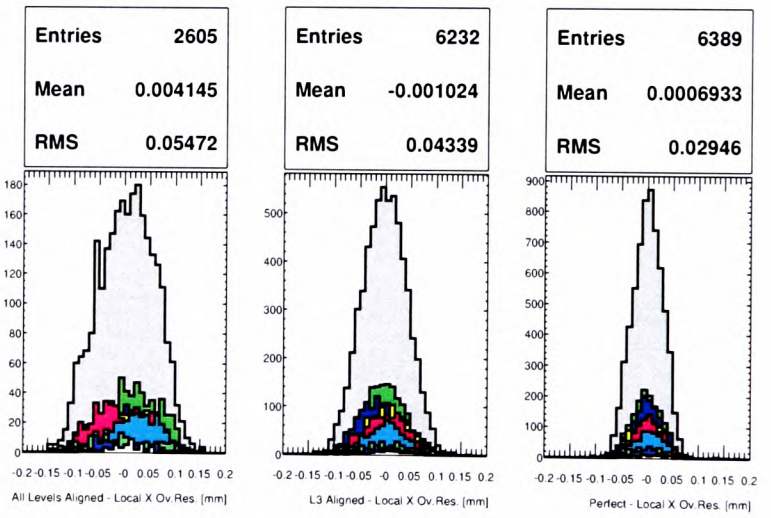


Fig. C.12: Biased SCT endcap local X overlap residuals after CSC alignment on all levels (left), on level 3 (middle) and with the true geometry (right). All endcap disks together (grey) and the individual layers are shown: layer 0 (red), layer 1 (green), layer 2 (blue), layer 3 (yellow), layer 4 (magenta), layer 5 (light blue), layer 6 (dark green), layer 7 (purple) and layer 8 (white).

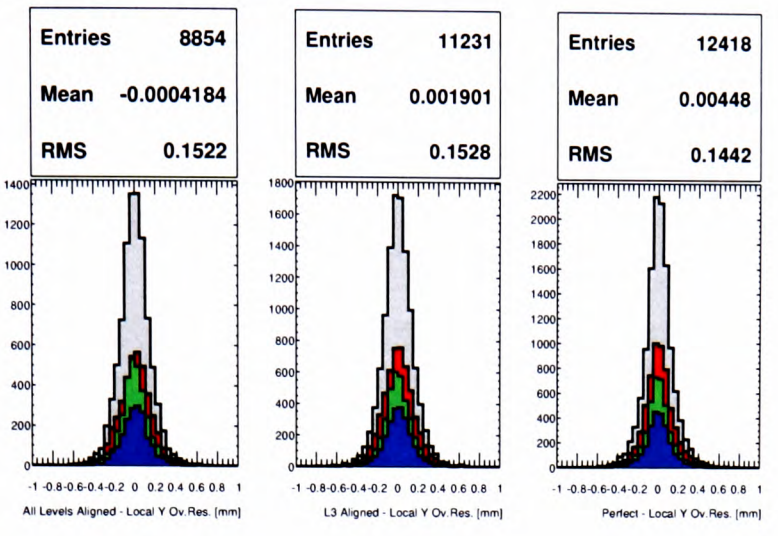


Fig. C.13: Biased PIXEL barrel local Y overlap residuals after CSC alignment on all levels (left), on level 3 (middle) and with the true geometry (right). All barrels together (grey) and the individual layers are shown: layer 0 (red), layer 1 (green) and layer 2 (blue).

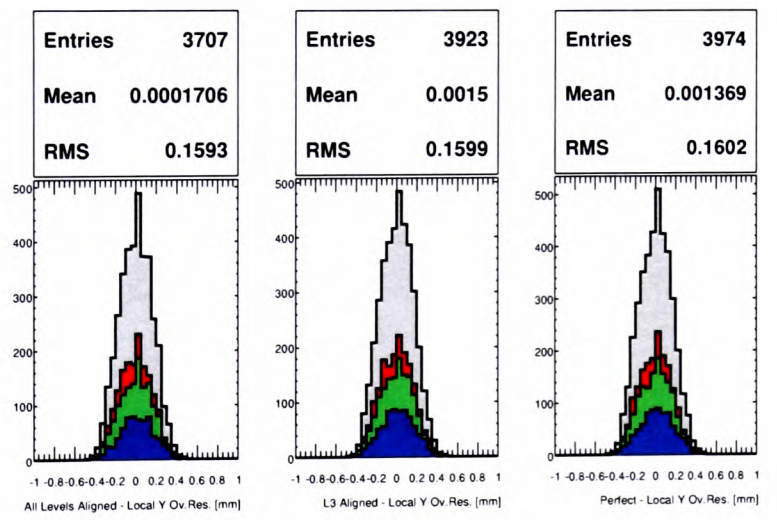


Fig. C.14: Biased PIXEL endcap local Y overlap residuals after CSC alignment on all levels (left), on level 3 (middle) and with the true geometry (right).All endcap disks together (grey) and the individual layers are shown: layer 0 (red), layer 1 (green) and layer 2 (blue).

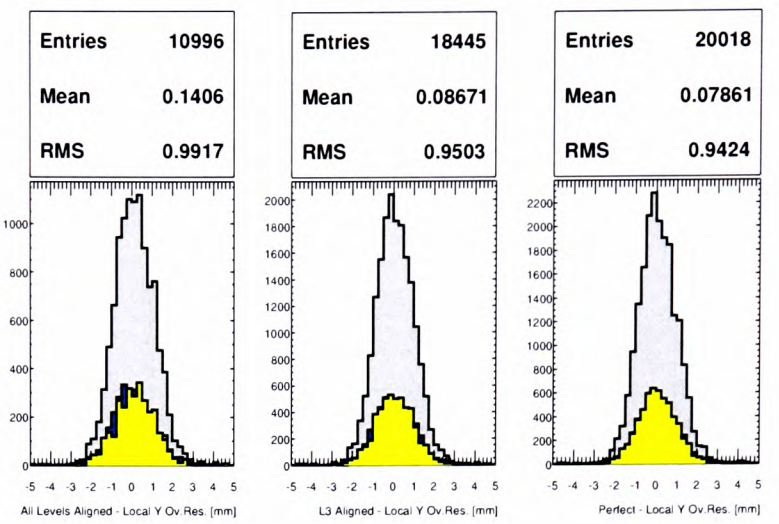


Fig. C.15: Biased SCT barrel local Y overlap residuals after CSC alignment on all levels (left), on level 3 (middle) and with the true geometry (right). All barrels together (grey) and the individual layers are shown: layer 0 (red), layer 1 (green), layer 2 (blue) and layer 3 (yellow).

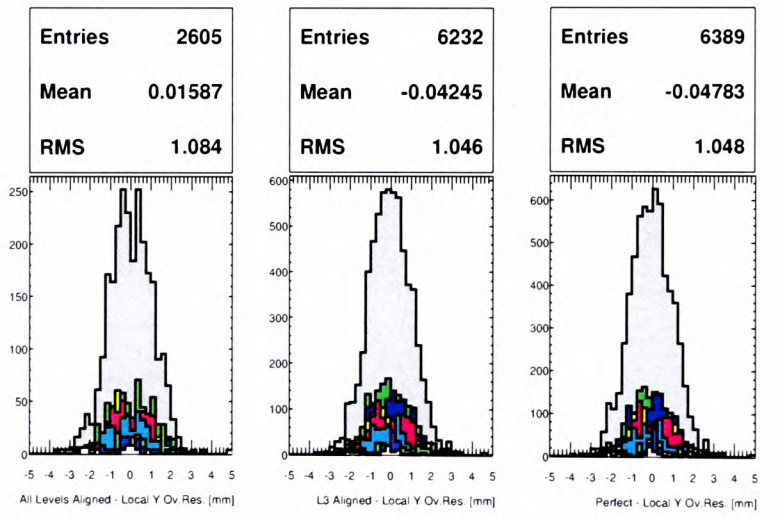


Fig. C.16: Biased SCT endcap local Y overlap residuals after CSC alignment on all levels (left), on level 3 (middle) and with the true geometry (right). All endcap disks together (grey) and the individual layers are shown: layer 0 (red), layer 1 (green), layer 2 (blue), layer 3 (yellow), layer 4 (magenta), layer 5 (light blue), layer 6 (dark green), layer 7 (purple) and layer 8 (white).

D. RUNS COLLECTING SR1 COSMIC RAYS

The given set of cosmics runs was available for the SCT alignment. It consists of about 400k events. The first 200k events were used for Robust Alignment. The full sample was used for monitoring. In addition to these runs there were noise runs or runs with low statistics or major hardware failures which have not been used for alignment purposes.

SR1 Runs SCT at trim target thresholds or SCT thresholds set to 1fC		
Run Number	*Number of Events*	*Online Comments*
2935	15679	SCT in expanded, any hit mode, with thresholds set to trim targets. SCT timing with 8ns fine TX delay.
2939	15127	SCT in expanded, any hit mode. Thresholds set to trim target. Fine delay 8ns. SCT module 20220170200954 (barrel 6, row 10, module 4) HV was off for the first 600 triggers
2986	7223	SCT using trim target thresholds PT application failed after 100 events, due to parameters in DB ... fixed
2989	4528	SCT at trim target thresholds. SCT module Japan 20220170200908 had HV off for the first 350 events Finished abnormally: /tmp was filling up on SBCs and other machines; moved log files to /data/logs

continued on next page

continued from previous page

Run Number	*Number of Events*	*Online Comments for SCT and TRT*
2992	31897	Cosmics run (physics mode) at trim target for SCT. 30k events. Finished ok.
2996	21297	Cosmics run with SCT at trim target and TRT at 0.5%. Got to about 20K events, then DAQ died. Last few events are probably garbage. TRT comments: Noticed one TRT DTMROC that has low efficiency; can't seem to fix it. Probably the ROD not setting the edge correctly.
2997	56473	Thresholds to trim targets. Approx 56K events Long run; noticed PT application dies after sampling 8K events; SCT lost half a module at end
3007	10045	SCT set to 1fC thresholds using new RC fits
3013	16145	SCT set to trim target thresholds. PT application crashed again, removed from partition 20220040200111 HV and LV tripped - around event 3800 - errors from this module. At some point - ¿event 10000 - disabled this module in the ROD formatter (so no more errors, but no data either)
3023	2697	SCT thresholds at trim target Stopped after 3K events due to TRT BUSY (TRT LV trip)
3024	12764	Trim thresholds. TRT LV keeps tripping because of temperature alarms; set limits 5C higher
3026	3279	Trim thresholds. Crashed after 3K events due to SCT ROS failure

continued on next page

continued from previous page

Run Number	*Number of Events*	*Online Comments for SCT and TRT*
3027	6623	Trim thresholds. TRT LV tripped after 6k events. TRT: Increased temperature limits for the rest of the channels; now all lines are 5C higher
3028	25852	SCT at trim thresholds. module 20220040200079 lost HV at some point before 01h32 (event 8130) recovered. module 20220040200101 lost LV and HV around 03h30. (event 25000) Attempt to recover this module caused ROS to crash, so end of run. About 25k good events
3030	17078	Run at trim target. 17k good events before ROS falls over
3031	10584	SCT at trim target. Terminated due to SCT ROS failure
3033	14055	SCT Thresholds to trim targets. Four modules had HV trip, corrected from event 10100: 20220040200211 20220040200218 20220040200220 20220040200226 Terminated due to SCT ROS failure
3039	17104	After DCSPP1 shield connected to ISSS ground. Thresholds at trim target
3042	3189	SCT using 1fC thresholds
3055	4777	Ended with more TRT readout problems at event 4624. TRT ROD failure - Problem seems to have returned after being dormant for many weeks. Maybe caused by crate power cycle. Last few hundred events (200) may not be very good for TRT

continued on next page

continued from previous page		
Run Number	*Number of Events*	*Online Comments for SCT and TRT*
3057	4262	SCT using 3055 start run configuration at 1.0 fC. In retrospect, this probably was not using the new response curve. AJB Terminated due to TRT ROD failure. Last few hundred events (200) may not be very good for TRT
3080	10142	Standard SCT (1fC, new RC) + TRT Cosmic (0.5%) run with TDC/ADC
3098	51625	SCT + TRT cosmics with new SCT ROD firmware. SCT Module 20220040200414 (B6 LMT10 Z-3) had a HV trip around event 4300 for a while. Recovered with HV on. Firmware evidently did not work... got an SCT ROS buffer overflow from ROL 11 at event 51629
3099	32430	Standard settings. Ended with SCT ROS failure again, on ROL 8
3100	4460	Standard settings (1fC). Ended cleanly.

Fig. D.1: Runs, collecting SR1 cosmic rays, which were available for the alignment are shown. The comments represent the entries from the SR1 online logbook. Despite the failures stated all these runs were considered as usable for the SCT alignment.

E. K-FACTORS

The concept of k-factors is generally used to reweight cross-sections according to higher order calculations. There are various definitions of k-factors. Here, they are defined as the ratio between MC NLO and MC LO cross-sections:

$$K = \frac{\sigma_{NLO}}{\sigma_{LO}} \tag{E.1}$$

NLO PDFs are used for both MC LO and MC NLO calculations. The given k-factors depend on the invariant mass of the dilepton pair and the rapidity Y as it is defined in Eq. 7.6.

MRST2004 - Y = 0.3 NLO PDFs used for both LO and NLO calculation		
Mass	*NLO Cross-Section*	*k-Factor*
50.0000	0.775777	1.14511
150.0000	0.366166E-01	1.14558
250.0000	0.393199E-02	1.15322
350.0000	0.106572E-02	1.15863
450.0000	0.415243E-03	1.16208
550.0000	0.198833E-03	1.16511
650.0000	0.108485E-03	1.16729
750.0000	0.649001E-04	1.16955
850.0000	0.414598E-04	1.17164
950.0000	0.278571E-04	1.17371

Tab. E.1: MRST k-factors for Y = 0.3 and a invariant mass range of 0 to 1000 TeV in 10 bins.

MRST2004 - Y = 0.9 NLO PDFs used for both LO and NLO calculation		
Mass	*NLO Cross-Section*	*k-Factor*
50.0000	0.769136	1.14748
150.0000	0.362728E-01	1.14782
250.0000	0.390376E-02	1.15524
350.0000	0.105186E-02	1.16051
450.0000	0.404766E-03	1.16429
550.0000	0.189979E-03	1.16775
650.0000	0.101224E-03	1.17105
750.0000	0.588115E-04	1.17433
850.0000	0.364083E-04	1.17800
950.0000	0.236160E-04	1.18165

Tab. E.2: MRST k-factors for Y = 0.9 and a invariant mass range of 0 to 1000 TeV in 10 bins.

MRST2004 - Y = 1.5 NLO PDFs used for both LO and NLO calculation		
Mass	*NLO Cross-Section*	*k-Factor*
50.0000	0.756787	1.15181
150.0000	0.355404E-01	1.15121
250.0000	0.380637E-02	1.15764
350.0000	0.997369E-03	1.16254
450.0000	0.366494E-03	1.16745
550.0000	0.161874E-03	1.17305
650.0000	0.801404E-04	1.17930
750.0000	0.428059E-04	1.18609
850.0000	0.241019E-04	1.19340
950.0000	0.140850E-04	1.20108

Tab. E.3: MRST k-factors for Y = 1.5 and a invariant mass range of 0 to 1000 TeV in 10 bins.

MRST2004 - Y = 2.1 NLO PDFs used for both LO and NLO calculation		
Mass	*NLO Cross-Section*	*k-Factor*
50.0000	0.743945	1.15823
150.0000	0.339914E-01	1.15291
250.0000	0.346035E-02	1.15772
350.0000	0.819502E-03	1.16467
450.0000	0.261448E-03	1.17448
550.0000	0.966404E-04	1.18610
650.0000	0.386780E-04	1.20019
750.0000	0.160680E-04	1.21573
850.0000	0.673672E-05	1.23325
950.0000	0.278028E-05	1.25313

Tab. E.4: MRST k-factors for Y = 2.1 and a invariant mass range of 0 to 1000 TeV in 10 bins.

MRST2004 - Y = 2.7 NLO PDFs used for both LO and NLO calculation		
Mass	*NLO Cross-Section*	*k-Factor*
50.0000	0.731937	1.16381
150.0000	0.297785E-01	1.14994
250.0000	0.247518E-02	1.15787
350.0000	0.421289E-03	1.17584
450.0000	0.847786E-04	1.20096
550.0000	0.166901E-04	1.23362
650.0000	0.272137E-05	1.27938
750.0000	0.277578E-06	1.35257
850.0000	0.768870E-08	1.76317
950.0000	0.0000	nan

Tab. E.5: MRST k-factors for Y = 2.7 and a invariant mass range of 0 to 1000 TeV in 10 bins.

CTEQ6.1M - Y = 0.3 NLO PDFs used for both LO and NLO calculation		
Mass	*NLO Cross-Section*	*k-Factor*
50.0000	0.778778	1.13189
150.0000	0.357354E-01	1.13698
250.0000	0.382211E-02	1.14800
350.0000	0.103299E-02	1.15497
450.0000	0.403121E-03	1.15924
550.0000	0.193398E-03	1.16254
650.0000	0.105857E-03	1.16491
750.0000	0.634911E-04	1.16711
850.0000	0.406903E-04	1.16927
950.0000	0.273885E-04	1.17109

Tab. E.6: CTEQ k-factors for Y = 0.3 and a invariant mass range of 0 to 1000 TeV in 10 bins.

CTEQ6.1M - Y = 0.9 NLO PDFs used for both LO and NLO calculation		
Mass	*NLO Cross-Section*	*k-Factor*
50.0000	0.768036	1.13447
150.0000	0.352372E-01	1.14069
250.0000	0.379577E-02	1.15060
350.0000	0.102525E-02	1.15663
450.0000	0.395851E-03	1.16089
550.0000	0.186486E-03	1.16460
650.0000	0.996751E-04	1.16786
750.0000	0.581526E-04	1.17138
850.0000	0.361176E-04	1.17495
950.0000	0.234943E-04	1.17854

Tab. E.7: CTEQ k-factors for Y = 0.9 and a invariant mass range of 0 to 1000 TeV in 10 bins.

CTEQ6.1M - Y = 1.5 NLO PDFs used for both LO and NLO calculation		
Mass	*NLO Cross-Section*	*k-Factor*
50.0000	0.750118	1.14019
150.0000	0.343443E-01	1.14496
250.0000	0.371309E-02	1.15254
350.0000	0.981204E-03	1.15823
450.0000	0.362964E-03	1.16311
550.0000	0.161409E-03	1.16884
650.0000	0.803179E-04	1.17505
750.0000	0.430897E-04	1.18209
850.0000	0.243687E-04	1.18982
950.0000	0.142713E-04	1.19747

Tab. E.8: CTEQ k-factors for Y = 1.5 and a invariant mass range of 0 to 1000 TeV in 10 bins.

CTEQ6.1M - Y = 2.1 NLO PDFs used for both LO and NLO calculation		
Mass	*NLO Cross-Section*	*k-Factor*
50.0000	0.730986	1.14883
150.0000	0.330332E-01	1.14777
250.0000	0.341092E-02	1.15185
350.0000	0.816781E-03	1.15834
450.0000	0.262926E-03	1.16809
550.0000	0.978151E-04	1.18011
650.0000	0.393221E-04	1.19455
750.0000	0.163887E-04	1.20978
850.0000	0.689954E-05	1.22690
950.0000	0.287124E-05	1.24590

Tab. E.9: CTEQ k-factors for Y = 2.1 and a invariant mass range of 0 to 1000 TeV in 10 bins.

CTEQ6.1M - Y = 2.7 NLO PDFs used for both LO and NLO calculation		
Mass	*NLO Cross-Section*	*k-Factor*
50.0000	0.719860	1.15778
150.0000	0.293189E-01	1.14301
250.0000	0.247779E-02	1.14993
350.0000	0.425649E-03	1.16781
450.0000	0.862346E-04	1.19206
550.0000	0.172512E-04	1.22292
650.0000	0.293203E-05	1.26451
750.0000	0.331192E-06	1.32636
850.0000	0.119783E-07	1.44209
950.0000	0.0000	0 nan

Tab. E.10: CTEQ k-factors for Y = 2.7 and a invariant mass range of 0 to 1000 TeV in 10 bins.

ZEUS - Y = 0.3 NLO PDFs used for both LO and NLO calculation		
Mass	*NLO Cross-Section*	*k-Factor*
50.0000	0.776116	1.14377
150.0000	0.371941E-01	1.14149
250.0000	0.404905E-02	1.14857
350.0000	0.110150E-02	1.15403
450.0000	0.429287E-03	1.15799
550.0000	0.205191E-03	1.16127
650.0000	0.111911E-03	1.16392
750.0000	0.668877E-04	1.16635
850.0000	0.427266E-04	1.16859
950.0000	0.287140E-04	1.17079

Tab. E.11: ZEUS k-factors for Y = 0.3 and a invariant mass range of 0 to 1000 TeV in 10 bins.

ZEUS - Y = 0.9 NLO PDFs used for both LO and NLO calculation		
Mass	*NLO Cross-Section*	*k-Factor*
50.0000	0.773236	1.14527
150.0000	0.366818E-01	1.14295
250.0000	0.398053E-02	1.15059
350.0000	0.107480E-02	1.15644
450.0000	0.414179E-03	1.16075
550.0000	0.194902E-03	1.16463
650.0000	0.104188E-03	1.16811
750.0000	0.607849E-04	1.17153
850.0000	0.377771E-04	1.17520
950.0000	0.246058E-04	1.17884

Tab. E.12: ZEUS k-factors for Y = 0.9 and a invariant mass range of 0 to 1000 TeV in 10 bins.

ZEUS - Y = 1.5 NLO PDFs used for both LO and NLO calculation		
Mass	*NLO Cross-Section*	*k-Factor*
50.0000	0.767723	1.14786
150.0000	0.355877E-01	1.14596
250.0000	0.382146E-02	1.15388
350.0000	0.100679E-02	1.15993
450.0000	0.373258E-03	1.16514
550.0000	0.166569E-03	1.17076
650.0000	0.833302E-04	1.17691
750.0000	0.449418E-04	1.18366
850.0000	0.255130E-04	1.19090
950.0000	0.150095E-04	1.19858

Tab. E.13: ZEUS k-factors for Y = 1.5 and a invariant mass range of 0 to 1000 TeV in 10 bins.

ZEUS - Y = 2.1 NLO PDFs used for both LO and NLO calculation		
Mass	*NLO Cross-Section*	*k-Factor*
50.0000	0.760173	1.15191
150.0000	0.336397E-01	1.14938
250.0000	0.346177E-02	1.15615
350.0000	0.833688E-03	1.16321
450.0000	0.270673E-03	1.17260
550.0000	0.101511E-03	1.18414
650.0000	0.409817E-04	1.19818
750.0000	0.170650E-04	1.21382
850.0000	0.712641E-05	1.23201
950.0000	0.290260E-05	1.25212

Tab. E.14: ZEUS k-factors for Y = 2.1 and a invariant mass range of 0 to 1000 TeV in 10 bins.

ZEUS - Y = 2.7 NLO PDFs used for both LO and NLO calculation		
Mass	*NLO Cross-Section*	*k-Factor*
50.0000	0.749571	1.15622
150.0000	0.297022E-01	1.14965
250.0000	0.253528E-02	1.15749
350.0000	0.439552E-03	1.17463
450.0000	0.885819E-04	1.19983
550.0000	0.170235E-04	1.23348
650.0000	0.261692E-05	1.27957
750.0000	0.236264E-06	1.34568
850.0000	0.505443E-08	1.47728
950.0000	0.00000	n.a.

Tab. E.15: ZEUS k-factors for Y = 2.7 and a invariant mass range of 0 to 1000 TeV in 10 bins.

BIBLIOGRAPHY

[1] F. Heinemann. Track based alignment of the ATLAS silicon detectors with the Robust Alignment algorithm. *ATL-INDET-PUB-2007-011*, 2007.

[2] F. Heinemann with S. Gonzalez-Sevilla et al. Alignment of the pixel and SCT modules for the 2004 ATLAS combined test beam. *ATL-COM-INDET-2007-013*, 2007.

[3] F. Heinemann with M.J. Costa et al. Combined SCT and TRT barrel cosmic run in the SR1 assembly area. In preparation for 2007.

[4] F. Heinemann with K. Black et al. Dileptons, diphotons, and lepton-photon resonances at high masses. In preparation for 2007.

[5] American Physical Society. Bulletin of the american physical society. *APR07-2007-000546*, 52, No 3, 2007.

[6] ATLAS Collaboration. The ATLAS experiment at the CERN Large Hadron Collider. In preparation for 2007.

[7] S. Blusk et al. Proceedings of the first LHC detector alignment workshop. *CERN-2007-004*, 2007.

[8] M. Karagoz Unel. ATLAS experiment silicon inner detector alignment. *Nucl. Phys. B (Proc. Suppl.) 172C*, pages 194–197, 2007.

[9] A. Tricoli et al. Proceedings of the workshop on monte carlo, physics and simulations at LHC (MCWS), LNF frascati 2006, In preparation for 2007.

[10] A. Cooper-Sakar et al. Proceedings of the conference on deep inelastic scattering 2007. *Science Wise Publishing, ISBN 978-3-935702-23-2*, 2007.

[11] S. Blusk et al. Proceedings of the 8th international conference on large scale applications and radiation hardness of semiconductor detectors. In preparation for 2007.

[12] S. L. Glashow. Partial symmetries of weak interactions. *Nucl. Phys.*, 22:579, 1961.

[13] S. Weinberg. A model of leptons. *Phys. Rev. Lett.*, 19:1264, 1967.

[14] A. Salam. *Weak and Electromagnetic Interactions*, page 367. Almquist and Wiksells, Stockholm, 1968.

[15] F. J. et al. Hasert. Observation of neutrino-like interactions without muon or electron in the gargamelle neutrino experiment. *Phys. Lett.*, B46:138–140, 1973.

[16] Mark-J Collaboration and D.P. Barber et al. Discovery of three-jet events and a test of quantum chromodynamics at PETRA. *Phys. Rev. Lett. 43*, page 830, 1979.

[17] Tasso Collaboration and R. Brandelik et al. Evidence for planar events in e^+e^- annihilation at high energies. *Phys.Lett. B86*, page 243, 1979.

[18] G.W. Bennett and Muon g 2 Collaboration. Measurement of the negative muon anomalous magnetic moment to 0.7 ppm. *Phys. Rev. Lett.*, 92:161802, 2004.

[19] D. N. Spergel et al. First-year wilkinson microwave anisotropy probe (WMAP), observations: Determination of cosmological parameters. *The Astrophysical Journal Supplement Series 148*, pages 175–194, 2003.

[20] S.J. Asztalos et al. Experimental constraints on the axion dark matter halo density. *The Astrophysical Journal*, 571:L27, 2002.

[21] D. Clowe et al. A direct empirical proof of the existence of dark matter. *astro-ph/0608407*, 2006.

[22] S. Dawson. The MSSM and why it works. *hep-ph/9712464*, 1997.

[23] T. Kaluza. Zum Unitätsproblem der Physik. *Sitz. Preuss. Akad. Wiss. Phys. Math. K1*, 1921.

[24] O. Klein. Quantentheorie und fünfdimensionale Relativitätstheorie. *Zeits. Phys. 37*, 1926.

[25] W.-M. Yao at al. Review of Particle Physics. *Journal of Physics G*, 33:1+, 2006.

[26] O. Bruening et al. LHC design report volume 1, 2004.

[27] ATLAS Collaboration. *ATLAS Detector and Physics Performence, Technical Design Report Volume 2*. CERN/LHCC 99-15, 1999.

[28] ATLAS Collaboration. *ATLAS Inner Detector, Technical Design Report Volume 1*. CERN/LHCC 97-16, 1997.

[29] F. Huegging. The ATLAS pixel detector. *IEEE Transactions on Nuclear Science*, 53:1732, 2006.

[30] A. Abdesselam et al. The barrel modules of the ATLAS semiconductor tracker. *Nucl. Inst. & Meth. in Phys. Res. A*, 568:642–671, 2006.

[31] ATLAS Collaboration. *ATLAS Detector and Physics Performence, Technical Design Report Volume 1*. CERN/LHCC 99-14, 1999.

[32] S. Correard et al. b-tagging with DC1 data. *ATL-COM-PHYS-2003-049*, 2003.

[33] R. Hawkings. Initial alignment of the ATLAS SCT and pixel detectors and its effect on track-finding. *CERN-PH/ATT*, 2005.

[34] J. Foster, P.S. Miyagawa, and S. Snow. SCT endcap geometry and surveys. *ATL-INDET-PUB-2007-004*, 2007.

[35] P. Bruckman de Renstrom et al. Global χ^2 approach to the alignment of the ATLAS silicon tracking detectors. *ATL-INDET-PUB-2005-002*, 2005.

[36] M. Karagoz Unel et al. Parallel computing studies for the alignment of the ATLAS silicon tracker. *CHEP06*, 2006.

[37] A. Aloisio et al. The RPC level-1 muon trigger of the ATLAS experiment at the LHC. *ATL-DAQ-CONF-2006-004*, 2006.

[38] R. Haertel. Iterative local χ^2 alignment approach for the ATLAS SCT detector. *Dimploma thesis, MPI*, 2005.

[39] D. Hindson. A robust procedure for alignment of the ATLAS inner detector using tracks. *DPhil thesis, Oxford University*, 2004.

[40] P. Coe et al. Frequency scanning interferometry in ATLAS: remote, multiple, simultaneous and precise distance measurements in a hostile environment. *Meas. Sci. Technol*, 15:2175–2187, 2004.

[41] ATLAS Computing group. *ATLAS Computing, Technical Design Report*. CERN/LHCC 2005-22, 2005.

[42] F. Akesson et al. ATLAS tracking event data model. *ATL-SOFT-PUB-2006-004*, 2006.

[43] A. Amorim et al. Conditions Databases: the interfaces between the different ATLAS systems. *CERN-2005-002*, pages 575–578, 2005.

[44] G. Barrand et al. Gaudi - a software architecture and framework for building HEP data processing applications. *International Conference on Computing in High Energy Physics (CHEP)*, 2000.

[45] R. Brun and F. Rademakers. ROOT - an object oriented data analysis framework. *Nucl. Inst. & Meth. in Phys. Res. A*, 389:81–86, 1997.

[46] K. Stoerig. Private communication, 2007.

[47] F. Campabadal et al. Beam tests of ATLAS SCT silicon strip detector modules. *Nucl. Inst. & Meth. in Phys. Res. A*, 538:384–407, 2005.

[48] B.D. Girolamo, M. Gallas, and T. Koffas. ATLAS barrel combined run in 2004, test beam setup and its evolutions. *EDSM Note: ATC-TT-IN-0001*, 2005.

[49] T. Koffas and R. Petti. Inner detector reference CTB data. *http:// atlas.web.cern.ch/Atlas/GROUPS/INNER_DETECTOR/SOFTWARE/TestBeam/IDgoodruns.ps*, 2005.

[50] B. Di Girolamo et al. Beam line instrumentation in the 2004 combined ATLAS test beam. *ATL-TECH-PUB-2005-001*, 2005.

[51] P. Bruckman de Renstrom. Private communication, 2006.

[52] R. Nickerson et al. Robotic mounting of ATLAS barrel SCT modules. *Nucl. Inst. & Meth. in Phys. Res. A*, 568:686–691, 2006.

[53] S. Gibson. Private communication, 2005.

[54] D. Mergelkuhl and A. Wiart. ATLAS - SCT barrel detector photogrammetric measurement of SCT barrel, FSI and pixel JIG. *EDMS document ATL-IS-UR-0004 id 681215*, 2005.

[55] A. Behrens et al. ATLAS - SCT barrel detector external reference points transfer. *EDMS document ATL-IS-UR-0007 id 705191*, 2006.

[56] D. Mergelkuhl and D. Grimm. ATLAS - TRT & SCT insertion of the SCT barrel on the TRT barrel position control. *EDMS document ATL-I-UR-0003 id 708009*, 2006.

[57] E. Dobson. Photogrammetric measurement of SCT barrel: Analysis. *ATL-COM-INDET-2007-004*, 2007.

[58] B. Demirkoz et al. Atmospheric muon based trigger setup for the integration of the ATLAS inner detector, In preparation for 2007.

[59] R. Batley. Private communication, 2007.

[60] S.Snow and A.Weidberg. The effect of inner detector misalignments on track resolution. *ATL-INDET-97-160*, 1997.

[61] A. Ahmad et al. Inner detector as-built detector description validation for CSC. *ATL-COM-INDET-2007-012*, 2007.

[62] O. Brandt. Private communication, 2007.

[63] T. Golling. Private communication, 2007.

[64] Stephen P. Martin. A supersymmetry primer. *hep-ph/9709356v4*, 1997.

[65] T.G. Rizzo. Pedagogical introduction to extra dimensions. *hep-ph/0409309*, 2004.

[66] B. C. Allanach, K. Odagiri, M. A. Parker, and B. R. Webber. Searching for narrow graviton resonances with the ATLAS detector at the large hadron collider. *JHEP*, 0009:019, 2000.

[67] M. R. Whalley, D. Bourilkov, and R. C. Group. The les houches accord PDFs (lhapdf) and Lhaglue. *hep-ph/0508110*, 2005.

[68] J. Pumplin et al. New generation of parton distributions with uncertainties from global QCD analysis. *JHEP*, 0207:012, 2002.

[69] ZEUS Collaboration. An NLO QCD analysis of inclusive cross-section and jet-production data from the ZEUS experiment. *European Physical Journal C*, 42:1, 2005.

[70] A. D. Martin, W. J. Stirling, and R. S. Thorne. MRST partons generated in a fixed-flavour scheme. *Phys. Lett. B*, 636:259, 2006.

[71] S. Alekhin, K. Melnikov, and F. Petriello. Fixed target Drell-Yan data and NNLO QCD fits of parton distribution functions. *Phys. Rev. D*, 74:054033, 2006.

[72] J. Huston et al. Inclusive jet production, parton distributions, and the search for new physics. *JHEP*, 0310:046, 2003.

[73] S. Drell and T.M. Yan. Massive lepton-pair production in hadron-hadron collisions at high energies. *Phys. Rev. Lett.*, 25:316, 1970.

[74] C.Anastasiou, L. Dixon, K. Melnikov, and F. Petriello. High-precision QCD at hadron colliders: electroweak gauge boson rapidity distributions at NNLO. *Phys. Rev. D*, 69:094008, 2004.

[75] A. Cooper-Sakar. Private communication, 2006.

[76] W.J.Stirling. Private communication, 2006.

[77] G. Corcella et al. HERWIG 6.5 release note. *hep-ph/0210213*, 2002.

[78] J. Butterworth et al. JIMMY generator, multiparton interactions in HERWIG. *http://hepforge.cedar.ac.uk/jimmy/*, 2007.

[79] A. Tricoli. Constraining the proton structure at ATLAS. *DPhil thesis, Oxford University*, 2006.

[80] J. M. Campbell, J. W. Huston, and W. J. Stirling. Hard interactions of quarks and gluons: a primer for LHC physics. *Rept. Prog. Phys.*, 70:89, 2007.

[81] S.L. Wu. e^+e^- physics at PETRA - the first five years. *Physics Reports 107*, pages 59–324, 1984.

[82] C. Y. Prescott et al. Parity non-conservation in inelastic electron scattering. *Phys. Lett. B*, 77:347–352, 1978.

[83] CDF Collaboration. Search for $z' \rightarrow e^+e^-$ using dielectron mass and angular distribution. *Phys. Rev. Lett.*, 96:211801, 2006.

[84] M. Dittmar. Neutral current interference in the tev region: The experimental sensitivity at the CERN LHC. *Phys. Rev. D*, 55(1):161–166, 1997.

[85] R. Devenish and A. Cooper-Sakar. *Deep Inelastic Scattering*, page 167. Oxford University Press, 2004.